TRAVERSING HOT JET IGNITION DELAY OF HYDROCARBON BLENDS IN A CONSTANT VOLUME COMBUSTOR

A Thesis

Submitted to the Faculty

of

Purdue University

by

M Arshad Zahangir Chowdhury

In Partial Fulfillment of the

Requirements for the Degree

of

Master of Science in Mechanical Engineering

August 2018

Purdue University

Indianapolis, Indiana

THE PURDUE UNIVERSITY GRADUATE SCHOOL
STATEMENT OF COMMITTEE APPROVAL

Dr. M. Razi Nalim, Chair

Department of Mechanical Engineering

Dr. Carlos Larriba-Andaluz

Department of Mechanical Engineering

Dr. Likun Zhu

Department of Mechanical Engineering

Approved by:

Dr. Sohel Anwar

Head of the Graduate Program

Bismillahirrahmanirrahim

To my parents-Aziza Akhtar Momotaz Banu Pradhan and *S M Abul Kalam Chowdhury* for their love, support and guidance

and

To my brothers-Md. Shamim Ahasan Chowdhury and *Md. Omar Faruk Chowdhury* for their love, understanding and encouragement.

ACKNOWLEDGMENTS

Throughout my time at Indianapolis, I have met a lot of people, who have left an impression on me and on this work. To all of them I express my warmest gratitude.

First and foremost, my deepest gratitude goes out to my major professor and mentor, Prof. Mohamed Razi Nalim for his support and guidance over the past two years. His patience, wisdom, insight and guidance was incumbent in completion of this thesis.

I thank my committee members, Prof. Likun Zhu and Prof. Carlos Larriba-Andaluz for their time, support, encouragement and valuable suggestions.

A very special thanks goes out to my colleagues at the Combustion and Propulsion Research Laboratory-Ali Tarraf Kojok, Mohammed Ebrahim Feyz, Siddarth Basu and Glen Patterson. My appreciation also goes out to Department of Mechanical Engineering and its stuff, especially Michael Golub, Joseph Derrick and Avinash Mumbarradi for their suggestions and help with machining and Debbie Bennett, Linda Wright, Monica Stahlhut and Jerry Mooney for help with purchasing of equipments and preparation of this thesis.

I also greatly appreciate the financial support provided by the National Science Foundation (Award No. CBET-1235696) and the university for the fellowship that made my study possible.

Finally, I thank my family and friends, living near and far, whose love and support I cherish every moment. You know who you are.

TABLE OF CONTENTS

Page

LIST OF TABLES

LIST OF FIGURES

Figure Page

SYMBOLS

m	mass
Φ	equivalence ratio
Φ_{pre}	pre-chamber equivalence ratio
τ_{id}	ignition delay
τ_{idP}	ignition delay estimated from pressure traces
τ_{idC}	ignition delay estimated from high speed Schlieren camera
$\tau_{jet-trav}$	jet traverse time
$\tau_{trav-jet}$	jet traverse time
τ_{rup}	rupture moment
τ_{mix}	Mixing time
P_{rup}	rupture pressure
P_r	room pressure
P_{pre}	pre-chamber initial filling pressure
P_{max}	Maximum differential pressure
N	revolutions per minute
P	pressure
T	temperature
T_r	room temperature

ABBREVIATIONS

AC	Alternating Current
AMR	Adaptive Mesh Refinement
CPRL	Combustion and Propulsion Research Laboratory
CVC	Constant-Volume Combustion
DAQ	Data Acquisition
DC	Direct Current
DTC	Discharge Time Constant
fps	frames per second
ID	Ignition Delay
MFC	Mass Flow Controller
NASA	National Aeronautics and Space Administration
PCC	Phantom Camera Control Software
PID	Proportional Integral Derivative Control
PT	Pressure Transducer
PWS	Pressure Wave Supercharger
RPM	Revolution Per Minute
SCCM	Standard Cubic Centimeter Per Minute
VI	Virtual Instrument
VFD	Variable Frequency Drive
WRCVC	Wave Rotor Constant Volume Combustor
TC	Thermocouple

ABSTRACT

Chowdhury, M Arshad Zahangir. M.S.M.E., Purdue University, August 2018. Traversing Hot Jet Ignition Delay of Hydrocarbon Blends in a Constant Volume Combustor. Major Professor: M. Razi Nalim.

A chemically reactive turbulent traversing hot-jet issued from a pre-chamber to a relatively long combustion chamber is experimentally investigated. The long combustion chamber represents a single channel of a wave rotor constant-volume combustor. The issued jet ignites the fuel-air mixture in the combustion chamber. Fuel-air mixtures are prepared with different hydrocarbon fuels of different reactivity, namely, methane, propane, methane-hydrogen blend, methane-propane blend and methane-argon blend. The jet acts as a rapid, distributed and moving source of ignition, traversing across one end of the long combustion chamber entrance, induces complex flow structures such as a train of counter rotating vortices that enhance turbulent mixing. In general, a stationary hot-jet ignition process lack these structures due to absence of the traversing motion. The ignition delay of the fuels and fuel blends are measured in order to obtain insights about constant-volume pressure-gain combustion process initiated by a moving source of ignition and also to glean useful data about design and operation of a wave rotor combustor.

Reactive hot-jets are useful to ignite fuel-air mixtures in internal combustion engines and novel wave rotor combustors. A reactive hot-jet or puff of gas issued from a suitably designed pre-chamber can act as rapid, distributed and less polluting ignition source in internal combustion engines. Each cylinder of the engine is provided with its own pre-chamber. A wave rotor combustor has an array of circumferentially arranged channels on a rotating drum. Each channel acts as a constant-volume combustor and produces high pressure combustion products. Implementation of hot-jet igniter in a wave rotor combustor offers utilization of available high temperature and

high pressure reactive combustion products residing in each of the wave rotor channels as a distributed source of ignition for other channels, thus requiring no special pre-chamber in ultimate implementation. Such reactive products or partially combusted and radical-laden gases can be issued from one or more channels to ignite the fuel-air mixture residing in another channel. Due to the rotation of the rotor channels, the issued hot-jet would have relative motion with respect to one end of the channels and traverse across it. This thesis aims to investigate the effects of jet traverse time experimentally on ignition delay along with other important factors that affect the hot-jet ignition process such as fuel reactivity, fuel-air mixture preparation quality and stratification and equivalence ratio.

In this study, the traversing motion of the hot-jet at one end of the main combustion chamber is implemented by keeping the main combustion chamber stationary and rotating a pre-chamber at speeds of 400 RPM, 800 RPM and 1200 RPM. The rotational speeds correspond to jet traverse times of 16.9 ms, 8.4 ms and 5.6 ms respectively. The fuel-air mixture inside the channel is at room temperature and pressure initially and its equivalence ratio is varied from 0.4 to 1.3. The cylindrical pre-chamber is initially filled with a 50%-50% methane-hydrogen blend fuel and air mixture at room pressure and temperature and at an equivalence ratio of 1.1. These conditions were chosen based on prior evidence of ignition rapidity with the jet properties. The hot-jet is issued by rupturing a thin diaphragm isolating the chambers.

Using high frequency dynamic pressure transducer pressure histories, the diaphragm rupture moment and onset of ignition is measured. Pressure traces from two transducers are employed to measure the initial rupture shock speed and ignition delay. Schlieren images recorded by a high speed camera are used to identify ignition moment and validate the measured ignition delay times. Ignition delay is defined as time interval from the rupture moment to onset of ignition of fuel-air mixture in the main combustion chamber. The ignition system is designed to produce diaphragm rupture at almost exactly the moment when jet traverse begins. Ignition delay times are measured for methane, propane, methane-hydrogen blends, methane-

propane blend and methane-argon blend. The equivalence ratio of the fuel-air mixtures varied from 0.4 to 1.3 in steps of 0.1 for stationary-hot jet ignition experiments and in steps of 0.3 for traversing hot-jet ignition experiments.

Hot-jet ignition delay of fuel-air mixtures, for both stationary hot-jet ignition process and traversing hot-jet ignition process, generally increased with increasing equivalence ratio. For stationary hot-jet ignition delay, the minimum ignition delay occurs between $\phi = 0.4$ to $\phi = 0.6$ for the tested fuel-air mixtures. Both stationary and traversing hot-jet ignition delay depended on fuel reactivity. In particular, the shortest ignition delay times were observed for a fuel blend containing hydrogen. Among pure fuels propane exhibited slightly shorter ignition delay times, on average, compared to pure methane fuel. The addition of argon to pure methane, intended to control fuel density and buoyancy, increased the ignition delay. The traversing hot-jet ignition delay generally increased with increasing jet traverse times.

To explain the variations in the measured hot-jet ignition delay and investigate qualitatively the effect of buoyancy on flame propagation and mixture stratification, the fuel-air mixture inside the main combustion chamber was ignited using a spark plug to generate a propagating laminar flame. The laminar flame propagated within the flammable regions of the channel in ways that sensitively reveal variations in local fuel-air mixture equivalence ratio. Flame luminosity images from a high speed camera and schlieren images revealed the fuel-air mixture being highly stratified depending on the density difference between the fuel and air and provided mixing time (0 s, 10s ,30s for most fuels). The lack of buoyancy-driven spreading caused the fuel to remain in the vicinity of the fuel injector resulting in significant longitudinal stratification of the fuel-air mixture. Lighter fuels stratified to the top of the chambers and heavier fuel stratified to the bottom of the chamber. Increasing the mixing time, which is defined as the time interval from end of fuel injection into the chamber to the triggering of the spark plug, improved the buoyancy-driven spreading and extended the flammable region as evidenced by the schlieren and flame luminosity images.

The maximum pressure developed in the combustor for the three ignition processes, namely, stationary hot-jet ignition, traversing hot-jet ignition and spark ignition process in laminar flame propagation experiments were compared. Stationary hot-jet ignition process generally exhibited the highest pressure being developed in the chamber. Variations in heat loss, fuel-air mixture leakage and mass addition mechanisms reduced the maximum pressure for spark ignition and traversing hot-jet ignition process.

1. INTRODUCTION

Depletion of existing fossil fuel reserves due to rise in fuel consumption coupled with increased demand of electrical power is a concern for the past half century. Existing energy conversion devices, particularly, combustion engines such as gas turbines, internal combustion engines engines etc. have reached to a point where their improvements are dependent on incremental efficiency gains and robust operations. Moreover, harmful pollutants and greenhouse gas emission have become a major concern due to their potential of global warming. Addressing these major concerns requires evolving our understanding of fundamental combustion processes and consequently innovative design and production of thermodynamically superior energy conversion systems or subsystems for efficiency, maximum power output and emission reduction benefits.

This thesis aims to contribute to our current understanding of ignition in a confined volume by a traversing hot-jet or puff of gas carrying chemically active radicals. The uniqueness of the thesis arises from the scarcity of experimental investigation into ignition phenomena where there is relative motion between the ignition source and the combustion chamber. Although analytical, numerical and computational studies of traversing hot-jet ignition exists, experimental data for validation is required. Validation quality experimental data exists mostly for hot-jet ignition by a centered stationary hot-jet, the physics of which is significantly different compared to traversing hot-jet ignition due to the absence of large scale vortices that enhance mixing between the reactants and the hot-jet over a large surface area. Chemically active radicals residing in the hot-jet with the support of enhanced mixing over a large surface area opens up more reaction pathways compared to conventional spark ignition. [1]. Moreover, in wave rotor combustors, the expulsion of high temperature and pressure gases, containing chemically active radicals, from a transfer passage to rotor channels, has similarities to the phenomenon being studied here.

1.1 Pressure-Gain Combustion

Pressure-gain combustion provides substantial energy efficiency and emission reduction benefits. This is due to the fact that continuous constant-pressure combustion processes are accompanied by free expansion of surrounding. This results in wasted energy, spent in the expansion process. Whereas, cyclic confined constant-volume combustion is thermodynamically superior to continuous constant-pressure combustion [2].

According to Kentfield et al., "Pressure-gain combustors have substantially steady inflow and outflow, although nonsteady processes occur within the combustor system in order to generate a higher stagnation pressure at the outlet than at the inlet [3]." Therefore, the increased stagnation pressure at the exit of a pressure-gain combustor could be delivered to a gas turbine inlet and increase the output of the turbine. In a wave-rotor combustor, this rise in stagnation pressure is delivered by repeating the constant-volume combustion process in cold channels intermittently along with compression and expansion processes by gas dynamic waves. Other examples of pressure-gain combustion are reciprocating internal combustion engines, pulsed jets, pulse detonation engines, rotating detonation engines etc. Pressure-gain combustion can be achieved in both flame or deflagration mode and detonation mode [4].

1.1.1 Wave Rotors

Wave rotors are unsteady flow pressure wave machines. Pressure waves are used to transfer energy in such machines. Depending on the geometry of the device, a pressure wave machine is capable of directly exchanging energy between different fluids by utilizing compression and expansion waves [5]. Furthermore, no mechanical components such as impellers or vanes are required for the compression and expansion process. A great advantage of these machines is their capability of generating large pressure rise in a very short distance or time [2]. Essentially, a wave rotor is an arrangement of a number of channels around the axis of a cylindrical drum sealed by

two stationary end plates with a number of flow control ports or manifolds. Sudden opening and closing of the ports, due to rotation of the drum, generates expansion and compression wave respectively in the channels akin to a piston. Fig. 1.1 shows a schematic configuration of a wave rotor combustor.

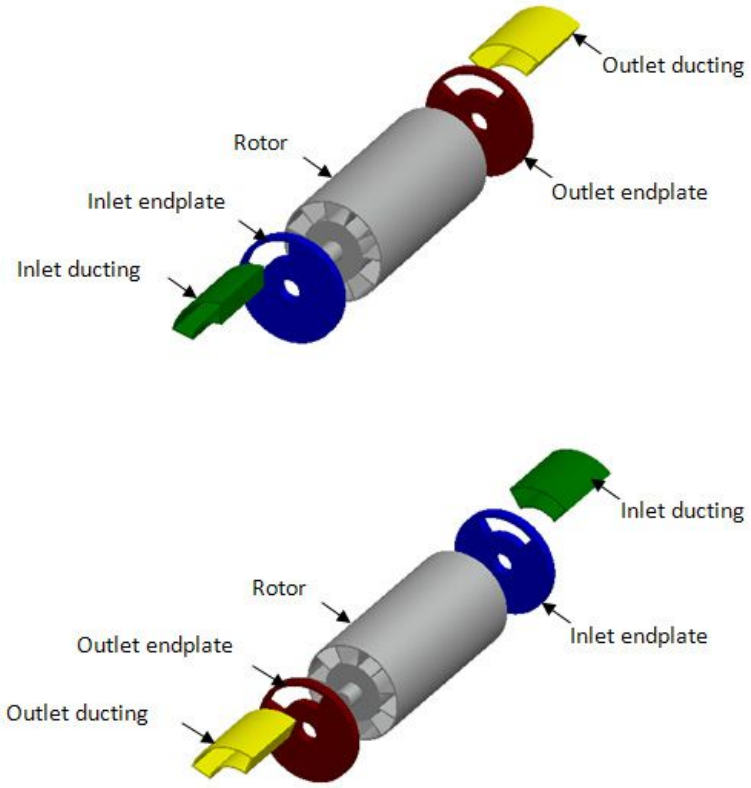

Figure 1.1. : Schematic of a wave rotor combustor. Top-orientation shown from inlet, Bottom-orientation shown from outlet. [6]

Wave rotors can be simply classified into two types based on their history of operation. The pressure exchange wave rotors and wave rotor combustors [7]. Pressure exchange wave rotors primarily exchange pressure between two different fluids [8]. Interested readers are referred to works of Akbari et al. [2] and Costiuc et al. [9].

The present study has two key features similar to wave rotor combustors, namely, the constant-volume combustion process and ignition or reignition by a hot-jet of reactive gas. Therefore, historical background on the development of wave rotors,

especially wave rotor combustors and its operating principle are discussed in the following sections.

1.1.2 Historical Background of Wave Rotor Development

The earliest known concept of a pressure wave machine was Knauff's [10] proposal of a pressure exchanger with a single cellular drum rotating between two seal plates containing timing ports to exchange pressure levels between fluids in 1906. However, this design did not used any pressure waves and Knauff [11] in 1906 in another patent, Burghard in 1913 [12] and Lebre [13] later in 1928 refined their designs and came up with simpler design that employed long narrow channel to exchange pressure between fluids known as Lebre's machine (following his patent). In 1928, Burghard [14] first proposed a concept akin to modern wave rotor concept that utilized pressure waves, known at the time as 'dynamic pressure exchanger' since it used pressure waves for both compression and expansion processes unlike prior 'static pressure exchangers'.

The first practical application of the pressure wave concept came in the early 1940s when Claude Seippel patented a wave rotor as a topping stage for a 2200 hp locomotive gas turbine, shown in Fig. 1.2, for the Brown Boveri Company (BBC), later known as Asea Brown Boveri (ABB) [15,16]. Inspired by his work, and the experience gleaned from its operation led to using wave rotor as pressure wave supercharger for diesel engines [17, 18]. ITE Circuit Breaker Company with Cornell University and U.S. Bureau of Aeronautics developed and tested first such units from 1947 to 1955. Later, collaborating with Swiss Federal Institute of Technology (ETH Zurich) BBC continued development of the pressure wave supercharger. Successful installation of the pressure wave supercharger first in a truck in 1971 and in diesel engines of passenger cars in 1978 led to the most successful commercialization of a waver rotor device, the COMPREX, till now. COMPREX (shown in Fig. 1.3) is the trade name given to the pressure wave supercharger. Rapid response to load change, compact size and light weight made the device suitable for use in small engines. The technology was

further developed and applied to passenger cars in 1987. Mazda 626 Capella was the first of such passenger cars along with Mercedes-Benz, Ferrari and Peugeot. Approximately, 150,000 units were produced for Mazda diesel engine passenger cars. Till now, this is still the most successful implementation of a wave rotor device in commercial applications. Not only BBC established a reliable mass fabrication technique for a wave rotor supercharger for passenger cars, more importantly, key developmental challenges were addressed such as sealing against leakages, noise and thermal stress. Recently, Swissauto WENKO AG in Switzerland developed HYPREX, an advanced pressure wave supercharger for small petrol engines and demonstrated its control features and higher pressure ratio operations in a modified Renault Twingo.

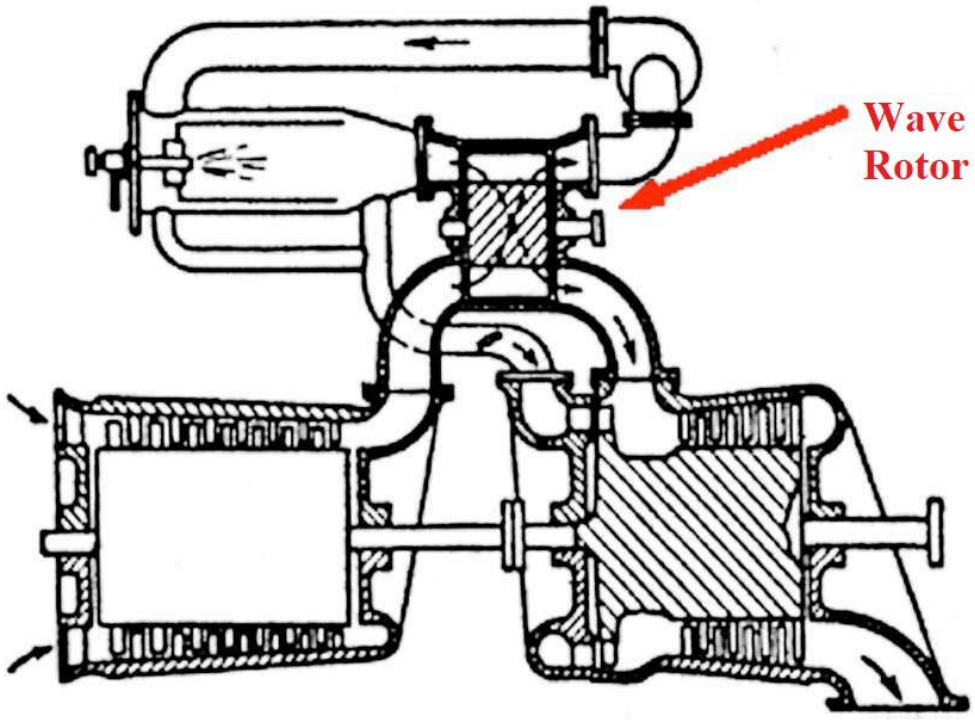

Figure 1.2. : Wave rotor topping stage for a locomotive gas turbine. [19]

Other notable applications of the wave rotor concept are the Wave Superheater built in 1958 and operated till 1969 at Cornell Aeronautical Laboratory (CAL), Jendrassik's work to deploy wave rotor machines as a high pressure topping stage for

aircraft engines developed in 1950s [20] and Pearson's unique wave rotor with helical channels that changed the direction of the flow and produced shaft work in mid-1950s [21]. Pearson called his design wave turbine engine or simply wave engine because of its similarity to produce shaft work like a conventional gas turbine. Notable achievement of Pearson's rotor was that its rapid development time of less than a year, wide range of operating conditions (3000-18000 RPM), absence of variable porting and production of significant power (26KW/35 hp) with a cycle peak temperature of 1070 K.

A completely new concept was initiated by General Electric Company (GE) taking inspiration of earlier works by Kantrowitz and Huber where combustion takes place inside the wave rotor channels in late 1950s. It was called internal combustion wave rotors. Although poor leakage control and sealing along with thermal expansion problems hindered the GE efforts, it still achieved a respectable pressure ratio of 1.3 [24]. In mid-1960s, Rolls-Royce began numerical and experimental investigation in to wave rotors as a topping spool in gas turbine applications. They invested considerable time and resources to design a small helicopter engine (Allison Model 250) with a wave rotor as topping stage [25]. Their efforts were thwarted by start-up, bearing durability, fuel system complications and control issues. Meanwhile, General Power Corporation (GPC) with initial support by Ford Motor Company and later by U.S. Department of Energy (DOE) and U.S. Defense Advanced Research Projects Agency (DARPA) aimed to design a wave rotor with curved bladed channels for application in gas turbines and automotive transportation from the 1960s to 1980s [26]. Their design lacked efficiency due to excessive blade curvature. In late 1970s, Mathematical Science Northwest Inc., later known as Spectra Technologies, spent considerable time and effort to built a laboratory wave rotor with support from DOE and DARPA [27]. Their work led to good agreement between experiment and numerical prediction, verification of scaling laws and performance optimization using unsteady computer code. They ultimately produced designs for a small turbofan engine capable of delivering 600 lb of thrust. In early 1980s, the Office of Naval Research (ONR), in a joint DARPA/ONR

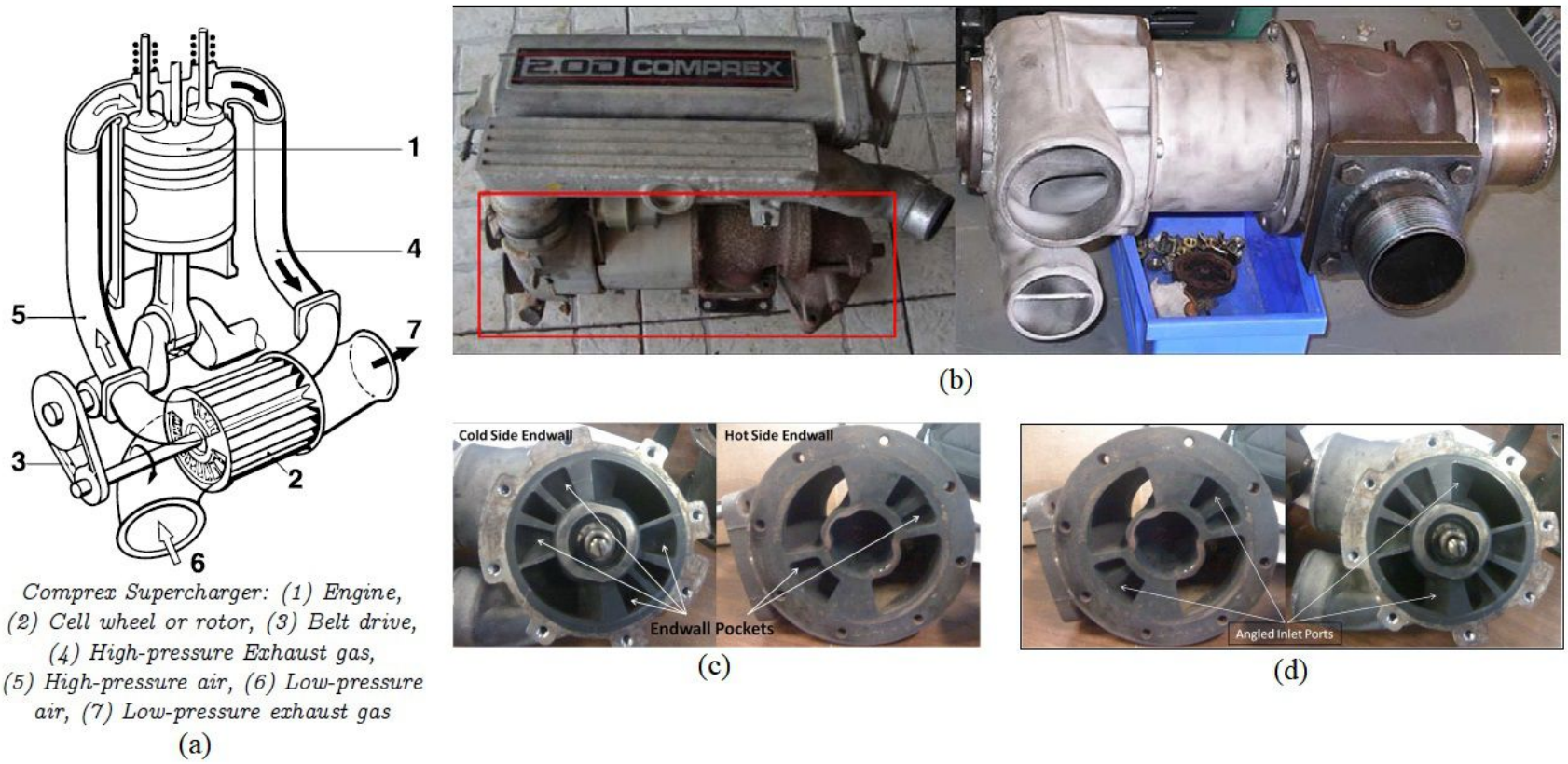

Figure 1.3. : (a) Schematic of Comprex supercharger [22], (b) Comprex CX 93 on and off the Mazda 2.0L diesel engine, (c) Endwall pockets and (d) Angled inlet ports. [23]

program, started an extensive numerical and analytical study of wave rotors. The GE rig was transferred to Turbopropulsion Laboratory (TPL) at Naval Postgraduate School (NPS). Preliminary tests revealed shaft work was produced when the rotor was running at approximately 5000 to 6000 RPM.

Notable analytical, numerical and computational efforts during this period are Resler's research at Cornell in 1980s that led to development of new wave rotor concepts and analytical methods for 3-port wave diffusers, double wave rotor cycles, five port wave rotors and supersonic wave-rotor combustors for aircraft engines. NO_x reduction potential in gas turbine applications were also modeled numerically [28]. Pioneering numerical work by Spalding at Imperial college in 1960s taking heat transfer and friction effects into consideration and using manual characteristic calculation led to the development of a computer model by Jonsson that was successfully applied to pressure exchangers [2]. Researchers at working on the ONR/NPS effort developed a 2D code to analyze flow in wave rotor channels, with effects of gradual opening and closing of channels and effect of curved channels.

From 1980s to present day, NASA Glenn Research Center (GRC), Rolls-Royce at Indianapolis has worked on application of wave rotors in aircraft propulsion. Paxson and Nalim's quasi 1D code estimated wave rotor combustor performance and validated with experiment. Nalim, in 1990s at NASA, did a feasibility study of assessment of combustion in wave rotor channels for use as a pressure gain combustor and with Paxson added combustion prediction capabilities to wave rotor code. It was also shown that deflagrative combustion with longitudinal fuel stratification could be accomplished in a short time in wave rotor channels [29–31].

ABB in 1989 started a three phase research project to employ wave rotor concept for gas turbine engines. In the first phase, a demonstrator engine was built integrating pressure wave rotor with external combustion. The engine showed improvement in efficiency and specific power compared to baseline engine [32]. Later, a rotary-valved single channel wave rotor was built and tested to investigate effects of fundamental parameters on such a constant-volume combustion device. Successes in these ventures

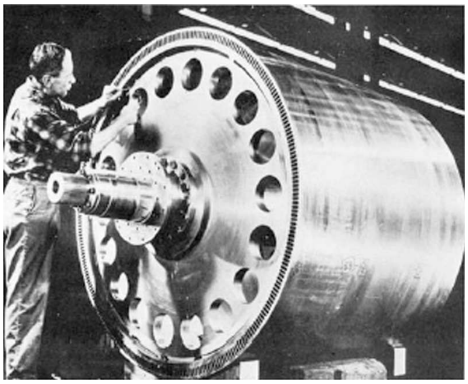

(a) CAL Wavesuperheater [2].

(b) The Pearson rotor [2].

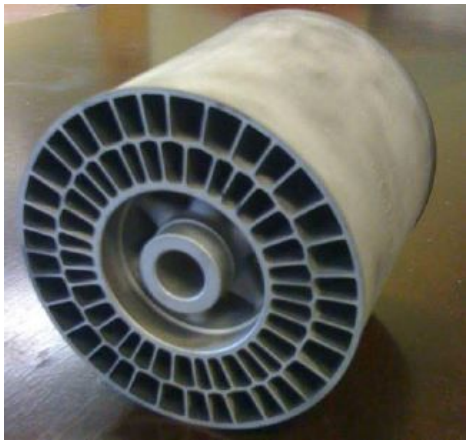

(c) Comprex PWS rotor [23].

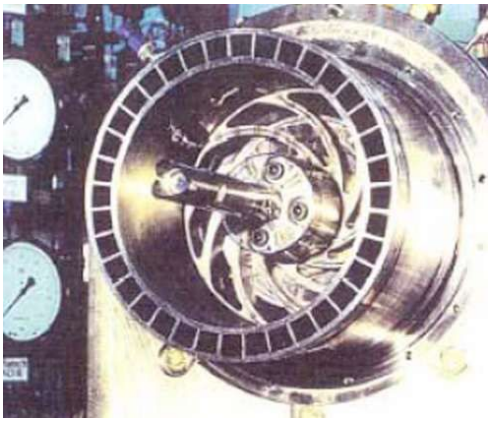

(d) 36 Channel ABB rotor [4].

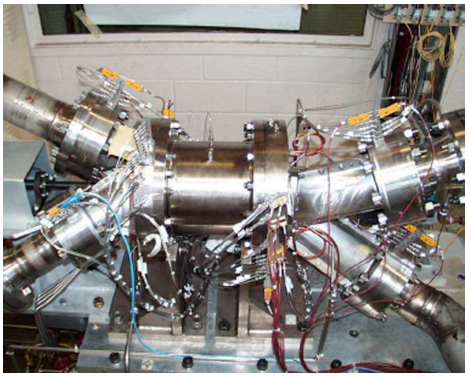

(e) Four-port NASA wave rotor [2].

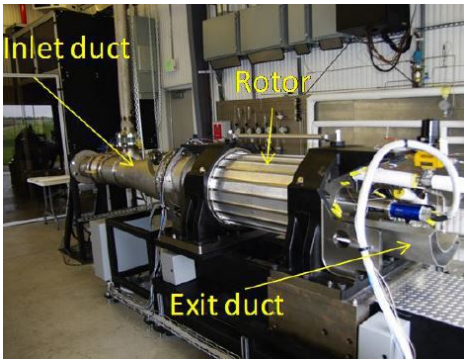

(f) IUPUI-Rolls-Royce WRCVC rig [4].

Figure 1.4. : Wave rotor examples.

led ABB to green light the design of a wave rotor combustor with 36 channels. The rotor was 20 cm in diameter and each channel measured 16.5cm (6.5 inch) in length and $15 \times 15mm$ (0.59×0.59) in cross-section and driven by an electric motor up to 5000 rpm. Both spark ignition and hot-gas injection self-sustaining gas ignition were employed in the single channel rig and the 36-channel rig. The self-sustaining ignition method uses already burnt gas from one channel to be injected to another neighboring channel to continue ignition inside the wave rotor. Bilgin and Keller showed that the self-sustaining ignition method enhances ignition reliability and burning rate and can lead essentially continuous combustion process without the need for pulsed methods that suffer from long ignition delays [33]. Also in 1990s, Snyder and Fish's study at Rolls-Royce Allison (formerly Allison Engine Company) [34] estiamted 18-20% increase in specific power and a 15-22% decrease in specific fuel consumption of a Allison 250 turboshaft engine. Lear [35] at University of Florida also developed analytical and numerical methods to analyze flow in wave rotor and their adjoining ducts, preliminary design method for selecting wave engine inflow and outflow blade angles and an analytical method to predict thermal efficiency and specific power output. Since 2000, Nagashima et al. at University of Tokyo , developed 1D and 2D numerical codes to simulate flow field inside through-flow four-port wave rotors considering passage to passage leakage with experimental validation using a single-channel wave rotor experiment rig [36]. Michigan State University wave rotor group [2] also looked into several application of wave technology in thermal cycles. Some of them worth mentioning are microturbines with wave rotor topping cycles, wave rotor enhanced R718 refrigeration cycles and radial wave rotor based wave disk engine. Interested authors are highly encouraged to read the excellent review paper by Akbari et al. [2] that traced the evolution of the wave rotor technology and summarized the aforementioned studies.

The research efforts at Indiana University Purdue University Indianapolis since early 2000 is discussed in subsection 1.3.

1.1.3 Principle of Operation

In this section, operation of a wave rotor combustor integrated with a gas turbine is briefly discussed. The wave rotor combustor replaces the constant-pressure-combustion process in a typical gas turbine cycle, i.e., Brayton cycle with a constant-volume-combustion process. In Fig. 1.5, both cycles are shown in a T-S diagram. For constant inlet temperature and outlet pressure, the Brayton cycle is represented by 1-2-3b-4b and the Humphrey cycle is represented by 1-2-3-4. The difference between the cycles lie in the heat addition process. For Brayton cycle, a constant-pressure heat addition line (2-3b) exists. Whereas, in the Humphrey cycle, a constant-volume heat addition line (2-3) replaces the constant-pressure heat addition line of the Brayton cycle. This results in pressure gain and reduction of entropy generation compared to ideal Brayton cycle. Concomitantly, for a constant input energy, output power and cycle efficiency are increased, which offers a thermodynamic benefit and is a significant advantage over other pressure-gain combustion approaches. Akbari [8] reported as much as 25% reduction in entropy generation under similar thermal conditions compared to Brayton cycle.

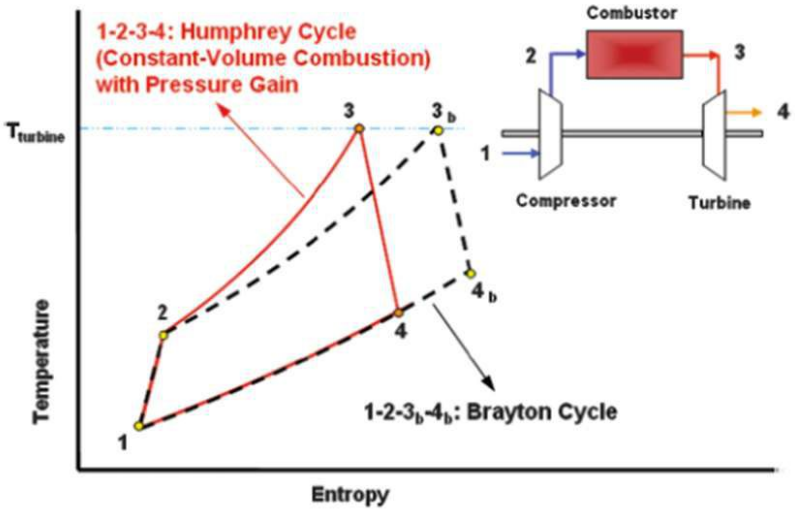

Figure 1.5. : T-S diagram of Brayton cycle and Humphrey cycle [6].

A series of channels arranged circumferentially around the axis of a cylindrical drum sandwiched between two stationary sealplates/endplates with an igniter on either/both plate constitutes a wave rotor combustor as illustrated in Fig 1.6.

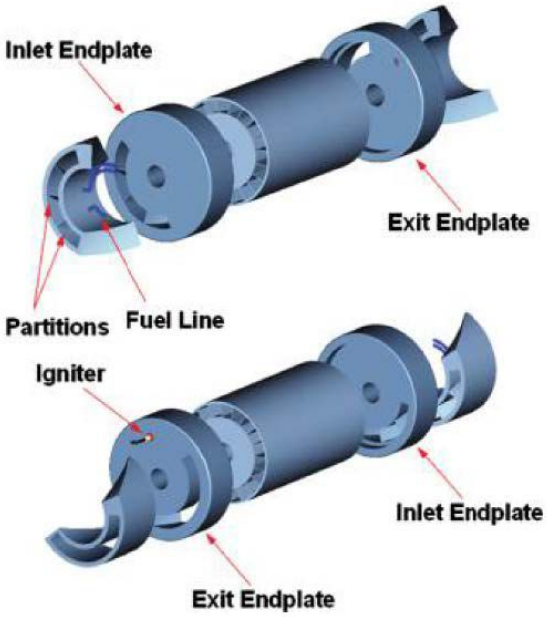

Figure 1.6. : Schematic of Wave rotor combustor with igniter on endplate [8].

Pressure waves are carefully coordinated to execute shockwave pre-compression, fast constant-volume-combustion and rapid expansion of burnt gases in channels. The drum is rotated using an electrical motor or by other mechanical means between the endplates. The endplates have partial-annular inlet and outlet ports flow control thorough the wave rotor. The channels are fueled when they come into alignment with the port itself sequentially. When the exit port is suddenly closed a shockwave propagates (know as hammer shock) in a channel that compresses the mixture inside the channel (illustrated in Fig. 1.7). After a combustion event takes place inside a channel, burnt gases are expanded and expelled through exit port due to the sudden pressure drop when a channel is suddenly exposed to a open exit port that generates an expansion wave. The combustion event can be achieved by a torch igniter mounted

on either/both endplates or by taking combusted gas with chemically active radicals from another channel that gas undergone combustion previously.

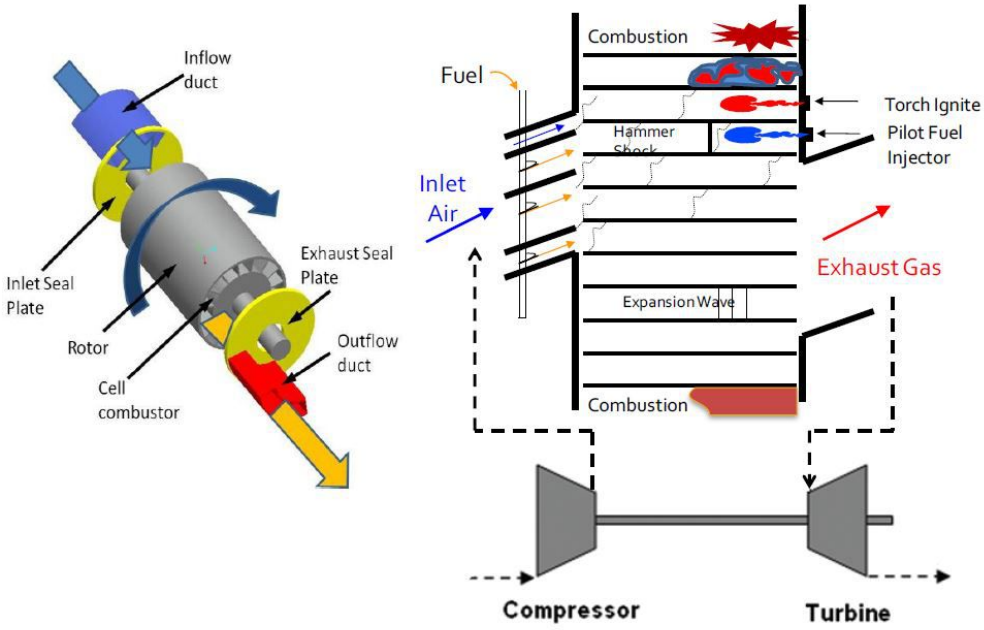

Figure 1.7. : Schematic of Wave rotor combustor (left) and combustion process inside a channel (right). Igniter is located on exit endplate [4].

Due to rotation, channels are periodically fueled, combusted, purged as they pass the inlet and exit port giving rise to compression and expansion wave inside the channels. Combustion event can be achieved in deflagration(flame) mode or detonation mode [4,29].Deflagration is the preferred mode of combustion in the channels and has been demonstrated [37]. Given the success of rotating detonation engines, detonation in wave rotor channels are unlikely to be demonstrated.

The ports are precisely designed to considering the timescales of the gas dynamic processes, rapid ignition and combustion inside the channels.Moreover, the location of the ports ensure that pressure drop inside the channel due to expansion waves allow fresh fuel or premixed fuel-air mixture to sweep the entire length of the channel. These

fast expansion and rapid combustion reduces the residence time and consequently reduces nitrogen oxide (NO_x) emissions [31].

1.2 Hot-Jet Ignition

A pre-chamber issued turbulent hot-jet, due to the presence of chemically active radicals and fast turbulent mixing can effectively ignite premixed combustible mixture rapidly. For a combustion process to take place, fuel and oxidizer must react when energy is supplied in the form of heat from any source exceeds the activation energy of the fuel-oxidizer mixture within their flammability limit. The heat source could be spark as in spark ignition engines, temperature rise in a compression process such as in a diesel engine, plasma, laser targeted points inside the chamber [38]. In a wave rotor, with very fast rotating speed of the elongated channels, the fuel-air mixture must be ignited rapidly and the flame must propagate through the entire length to completely the burn the fuel-air mixture.

The fast turbulent mixing coupled with active radicals rapidly develops a ignitable mixture when a jet is introduced in quiescent fuel-air mixture. Sadanandan et al. [39] reported the high shear stresses in shear layer on the lateral side of the jet has high rate of mixing however, the jet tip, subjected to low rate of mixing has a higher probability of ignition. However, Elhsnawi [40] concluded that ignition is likely to occur on jet edge by introducing heated inert gas into $H_2 - O_2$ mixtures. Ignition is also dependent on reactant diffusivity variation compared to jet Reynolds number and for very diffusive fuels such as hydrogen (Lewis number less than unity) ignition occurs at jet tip but for less diffusive fuels (Lewis number much greater than unity) ignition occurs on shear layer or lateral side of the jet [41].

Biswas experimented with lean hydrogen-air mixture using a small pre-chamber (about 1% of main chamber volume) and several nozzles and found a reduction in ignition delay and lean flammability limit, particularly with a supersonic nozzle [42]. The shock behind the supersonic jet increases the static temperature behind the

shock and contributes to the increased likelihood of ignition compared to straight nozzle geometries. Unlike converging and converging-diverging nozzles that produce such high temperature regions ahead of the shock. Therefore, nozzle geometry and fuel type are two key parameters to control ignition initiation.

Wrmel et al. discussed diluent effects on chemical auotignition delay times measured in rapid compression machines (RCM) and shock tubes. In rapid compression machines, argon increased the ignition delay but in shock tubes ignition delay times decreased (Fig. 1.8). In RCM, the postcompression heat loss is much higher for cases when a diluent gases that contributed to the increase in ignition delay over the longer timescale of ignition in RCM, about 1-200ms. Although argon does not take part in the combustion reaction, due to the lower heat capacity and the adiabatic reaction in shock tubes, iso-octane diluted by argon mixtures were expected to ignite earlier from computational predictions. However, when the fuel was methane and diluent argon proportion was much lower (at 74%), the overall heat capacity of the system (fuel, oxygen and diluent) was not reduced significantly and there was not any significant variation among the predicted and measured autoignition delay times for concentrated mixtures and diluted mixture. The effect of heat capacity of diluent argon diminishes further at higher temperatures which was due to the chemistry of the reactive system being different at higher temperatures [43].

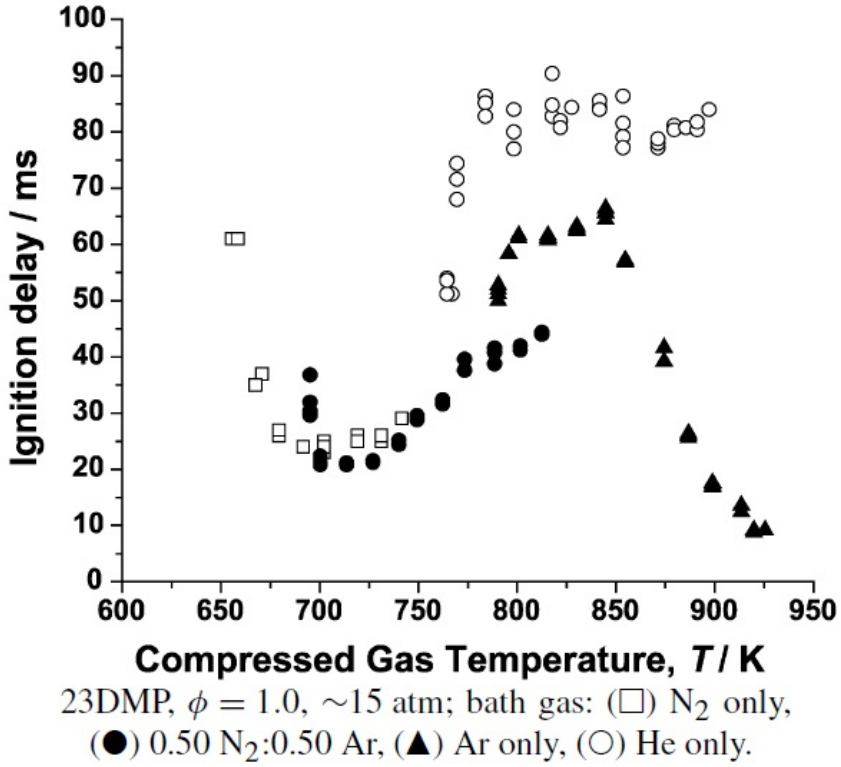

Figure 1.8. : Autoignition delay times as a function of compressed gas temperature for a stoichiometric 2,3-dimethylpentane mixture in air using N2-only diluent, 0.50 N2:0.50 Ar, Ar only, and He only [43]. Tests are conducted in rapid compression or shock-tubes.

In contrast to rapid compression machines and pure autoignition phenomenon, chemically active radicals in the hot-jet can minimize ignition delay and energy required for ignition compared to spark ignition, if rapidly mixed with combustible mixture. Campbell et al. [44] described two key benefits of radical ignition. One being reduction in ignition delay by several order of magnitude (less than 200 nanoseconds at 300K, 5 order of magnitude less than typical 10 ms for autoignition of methane-air mixtures) by greatly accelerating the ignition process. The other being the supply of external energy due to exothermic reactions between undecomposed fuel and oxydizer that liberate energy. The second process reduces the energy required for the fuel to be decomposed into radicals. Also this liberated energy makes the radical ignition

process energy requirement to be lesser than the thermal energy required for spark ignition which is entirely supplied by the electric arc.

1.2.1 Application of Hot-Jet Ignition

The hot-jet ignition process offers several benefits suited to implementation in wave rotor combustors. Fast turbulent mixing, higher ignition energy and radical aided ignition are some of these benefits. Hot-jet ignition, especially, stationary hot-jet ignition, has been applied in internal combustion engines. Honda have developed an engine called compound vortex controlled combustion or CVCC that has a pre-chamber [45,46]. However, in strict sense it is not a complete jet ignition system since the flame is not quenched when coming out of the pre-chamber, unlike conventional pre-chamber based jet ignition system where the flame is quenched by chamber and nozzle geometries. Volkswagen [47], Ford [48] , GM [49], Porsche [50] and Mahle powertrain [51] all experimented or created different torch ignited engines turbulent jet ignition (TJI) systems that employed pre-chamber jet ignition technology. Interested readers are referred to the excellent review by Toulson et al [52]. The applicability of traversing hot-jet ignition is almost exclusively suitable for wave rotor combustors since conventional engine design do not incorporate jet traversing capabilities.

1.2.2 Definition of Hot-Jet Ignition Delay Time

The definition of ignition delay time is dependent on two time events. How these two time events are identified varies among different researchers due to constraints imposed by the ignition phenomena they are studying and also due to available equipments and instrumentation [6]. Ignition delay is typically defined in diesel engines as the time interval from the moment of end of fuel injection to onset of ignition inside a combustion chamber. In SI engines, the time difference from the application of spark in the engine and the first point of noticeable pressure rise in the engine is characterized as ignition delay. For shock tube studies, ignition delay time is defined

as the time interval from the moment of arrival of the reflected shock and the moment characterizing the onset of ignition shown in Fig. 1.9.

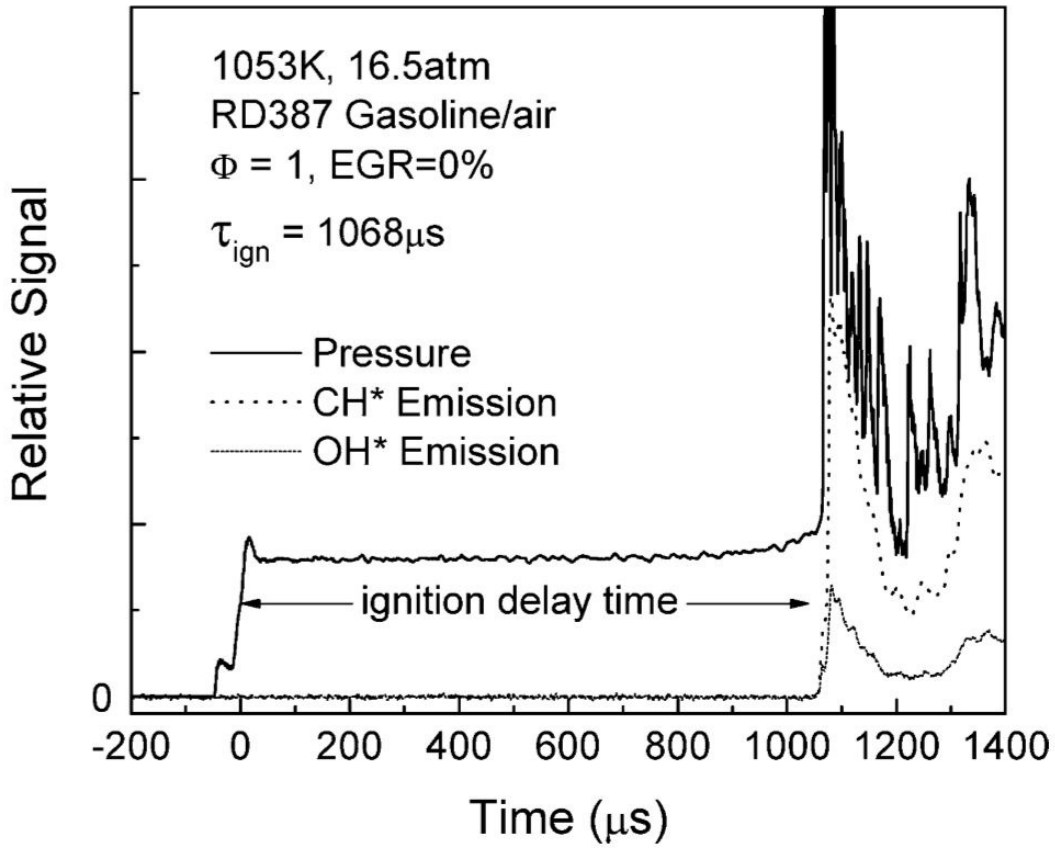

Figure 1.9. : Ignition delay time measurement in a shock tube. [53].

In this study, ignition delay is defined from the pre-chamber nozzle diaphragm rupture moment to the moment of onset of ignition. The estimation of ignition delay is discussed in subsection 4.4.1.

1.3 Prior Research at IUPUI CPRL Test Rig

Prior works at IUPUI have revealed key insights and enhanced understanding of design, construction, operation, control and other functional aspects of wave rotor technology. A wave-rotor constant-volume combustor was collaboratively built and tested at Purdue University Zucrow Laboratories by IUPUI, Rolls Royce North America and Purdue University. Details on this WRCVC can be found in [37]. The WRCVE operated with ethylene fuel ignited by a propane torch igniter. It had 20 channels, with 15 circumferential fuel injectors and equipped with pressure transducer, thermocouples and ion probes. Initial tests with the WRCVC at different operating characteristics such as fuel-air equivalence ratio, mixture stratification etc were conducted and it was operated up to 2100 RPM. Wijeyakulasuriya conducted detailed numerical and modeling studies [4] on traversing and translating gas jet mixing process in a confined volume and useful insights were gleaned about jet dynamics which are directly applicable to wave rotor combustion and fluid flow. His efforts revealed that at the center of the entrance of the confined volume, when the jet is centered, the penetration length for a translating or traversing jet is similar to a stationary jet. However, a stationary jet lacks lateral penetration while the traversing motion enhances lateral penetration significantly and enhance mixing. Fig. 1.10 shows the main vortices that are generated by the feeding stream of non-reacting jet. Two counter rotating vortices V1 and V2 are fed by the traversing jet that are developed throughout the entire traversing period while also developing and shedding small scale vortices along the process (such as one in the upper corner in the second image from the top). In the present investigation, the schlieren images reveal such vortex formation and interaction in the flow field. It is understood that these vortices influence formation of ignition kernel in the flow field by bringing unburned fuel-air mixture to their core and increasing the local temperature. This vortex evolution was not captured in any previous experimental study due to the unavailability of the required optical arrangement at the time. Wijeyakulasuriya also identified that the

mixing dynamics is greatly influenced by geometry, particularly, by the width of the nozzle with respect to channel dimension, but not as much by the injection pressure. However, nozzle geometry, position, injection pressure and channel geometry (also number of channels for an actual wave rotor) greatly influence the development of the vortices.

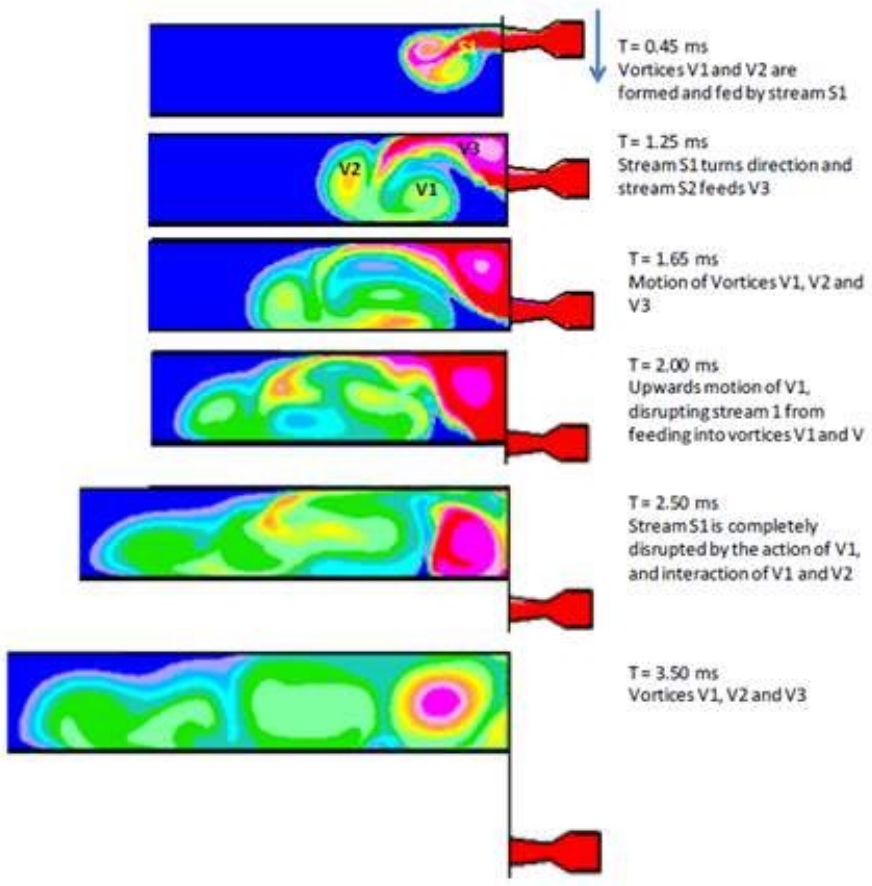

Figure 1.10. : CFD simulations showing vortices evolving in a confined volume by a two dimensional non-reacting jet. Time is from start of the translating or traversing injector [4].

The jet ignition process was experimentally studied by Bilgin [54] in 1998 at University of Washington by developing an experimental rig with two pre-chambers and a single premixed main combustion chamber. Both stationary and traversing hot

jet ignition process and their limitation were studied and ignition success estimated based on a suitably defined Damkoehler number. Although the use of relatively slower high speed camera made it difficult for him to report details on the jet traverse time or ignition to be observed and key conclusions were drawn by observing the combustion process after initial ignition. Later, Bilgin's experimental rig was operated by Perera [6] at IUPUI with a faster high speed camera and data acquisition system. He tested various fuels and introduced a methodology to estimate the rupture moment by measuring the pre-chamber pressure. Chinnathambi conducted traversing hot-jet ignition experiments [55] and revealed the dependency of ignition delay on the jet traverse time. However, since pre-chamber pressure measurement under rotating operation was not possible, Chinnathambi assumed a constant 0.2ms delay between the rupture moment and the first appearance of the jet in his recorded high speed camera flame luminosity images. The present investigation revealed that the diaphragm rupture process can be gradual and can create vortex rings, which are discussed in subsection 3.2. Paik [7] installed an optical arrangement to conduct schlieren photography and introduced a new methodology to estimate ignition delay time by calculating the shock travel time from pressure traces of two pressure transducers to estimate the rupture moment. The methodology was validated for stationary tests with the high speed camera. Ignition delay times of methane hydrogen blends were estimated for two set of compositions for a range of equivalence ratios and rupture pressures. One is a 50%-50% methane hydrogen blend and the other is a 30%-70% methane hydrogen blend. Paik also experimented on heating the main combustion chamber air, however, due to the then main chamber being made of aluminum, which has a high thermal conductivity, the design prove to be inadequate. A new combustion chamber was built by Kojok [38] with upgraded instrumentation and automated main chamber fuel delivery. This made conducting high temperature experiment in the main combustion chamber possible. Preheated air was supplied to the chamber and experiments were conducted at temperatures up to 500K with methane, hydrogen and 50%-50% methane hydrogen blend. Paik's methodology was not applicable to

the hydrogen cases and they were not analyzed. However, the other two fuels, under different equivalence ratios and pre-chamber initial pressures (jet momentum) were tested. Ignition delay was found to be increasing with increase in equivalence ratio, pre-chamber initial pressure and decrease fuel hydrogen content or reactivity. These findings were in agreement with Paik's conclusions. The effect of temperature was not found to be strong and was in agreement with findings of Khan [56].

Other numerical and computational studies, include Baronia's [57] effort to simulate Bigin's experimental work (discussed in next paragraph) using temperature based hybrid combustion model and understand jet mixing, flame propagation and shock-flame interaction. Karimi [58] took into account the modifications of the single chamber ignition test rig of Bilgin by Perera and Chinnathambi and used a 2D RANS coupled with a hybrid eddy breakup model and finite rate chemistry based combustion model to gain insights about the effects of chemical kinetics on the ignition process by both stationary and traversing hot-jets. Khan [56] sped up the chemical kinetics by using adaptive mesh refinement (AMR) based on velocity, temperature and multi-zone reaction and investigated ignition delay using 21 species and 84 elementary reactions (DRM19) in his three dimensional numerical study. Feyz is presently developing an analytical model supported by 3D simulations of the hot-jet ignition process [59].

1.4 Objectives

The objectives of this research investigation are

1. Upgrade the spark trigger control system for a traversing jet and integrate it with the existing data acquisition and controls system of the rig .

2. Design and build a seal plate that allows constant rubbing contact between a rotating pre-chamber and main combustion chamber face with minimal leakage of fuel-air mixture.

3. Conduct traversing and stationary hot-jet ignition experiments to gain insight into suitability of various fuels for wave-rotor combustor and pre-chamber based turbulent jet ignition systems.

4. Investigate the influence of jet traverse time, equivalence ratio of fuel-air mixtures and fuel reactivity on the traversing hot-jet ignition process.

5. Investigate the level of stratification of flammable fuel-air mixture inside the main combustion chamber by using a spark to ignite and propagate laminar flames in fuels of various molecular weight mixed with air.

6. Compare the hot-jet ignition process and the spark ignition process in the laminar flame propagation experiments in terms of pressure rise in the chamber.

1.5 Scope of Present Research

The current research concentrates on investigating and understanding the effects of traverse time, equivalence ratio and fuel reactivity on the ignition delay of various hydrocarbon fuels . It is a continuation of previous experimental investigations undertaken by Pererra, Chinnathambi, Paik and Kojok. While Perera, Paik and Kojok [6, 7, 38] worked on stationary jet ignition and Chinnathambi [55] worked on traversing jet ignition. In order to vary the traverse time, the pre-chamber is rotated at different RPMs. In this study, only the main chamber is stationary and the pre-chamber is rotated when a test is being referred to traversing hot-jet ignition experiment. Ignition delay of various hydrocarbon fuels were investigated such as methane, hydrogen, propane, 50%-50% blend of methane and hydrogen, 50%-50% blend of methane and propane and a special fuel blend of methane and argon consisting of 46.4% methane and 53.6% argon by volume. The hydrogen volume fraction in the methane-hydrogen fuel blend was kept to be 50% to have consistency with experimental results of Paik and Kojok and computational work of Khan [56] which is available at this hydrogen volume fractions. Preliminary results indicated possi-

bility of mixture stratification and inadequate mixing of the fuel and air in the main chamber. Therefore, further experimentation in the main chamber was performed in the main chamber where the fuel-air mixture air was ignited by a spark instead of a hot-jet to generate a laminar flame. These laminar flame propagation tests revealed buoyancy effects and vertical as well as longitudinal stratification of the fuel-air mixture in the main chamber. Moreover, the maximum pressures achieved in the main chamber for hot-jet ignition cases and spark ignition cases were compared and the mixing of the fuel and air inside the main chamber was explored in terms of mixing time, i.e., the time difference between end of fuel injection and triggering of the spark plug. Qualitatively, the mixing of the fuel and air was characterized from schlieren images for methane, 50%-50% methane and hydrogen blend, 50%-50% methane and propane blend, propane, hydrogen and gas blend that has equal density of air. A gas blend consisting of 46.4% methane and 53.6% were chosen to fulfill this requirement since methane kinetics is well known and previous researchers at CPRL have used methane for their experiments. This gas blend, having the same density as that of air minimizes stratification issues and further investigated for ignition by a stationary and traversing hot-jet.

Another fuel blend, namely a 30% methane and 70% hydrogen blend by volume was tested using a stationary hot-jet. However, the chosen methodology for estimation of ignition delay cannot be applied to investigate the pressure trace of such experiments. The fuel-air mixture ignites as soon as the diaphragm ruptures and the ignition moment cannot be identified from the schlieren images.

Unless otherwise specified, the main chamber fuel-air mixture is at atmospheric pressure (P = 1 atm) and temperature (T = 296 K) and the pre-chamber is initially filled with a 50%-50% methane-hydrogen blend and air at an equivalence ratio of 1.1 and pressure of 1 atm for stationary and traversing hot-jet ignition tests. However, a number of tests are reported where the equivalence ratio of both pre-chamber and main chamber were kept the same. Three pre-chamber RPM were chosen to investigate the effect of traverse time, namely, 400 RPM, 800 RPM and 1200 RPM that

correspond to traverse times of 16.9ms, 8.4ms and 5.6 ms. For traversing hot-jet ignition tests, the equivalence ratio of the fuel-air mixture in the main chamber was 0.4, 0.7, 1 and 1.3. For stationary tests, the equivalence ratio was varied in steps of 0.1 from 0.4 to 1.3. For spark-ignited laminar flame propagation experiments, the equivalence ratios were varied similar to traversing hot-jet ignition test and the mixing time was varied from 0 seconds, 10 seconds and 30 seconds. The exception being hydrogen where the equivalence ratio was varied up to 1 only and the mixing times are 3s, 13s and 33s. The wide range of data reported here can be useful for design and operation of pre-chamber based turbulent jet ignition system. Moreover, any ignition delay model would benefit from taking into account the wide range of equivalence ratio data points over various range of reactivity of the fuels tested.

The pressure traces of all ignition tests are analyzed and matched with the captured schlieren images to report the estimated ignition delay. Flame propagation characteristics were visually investigated using another camera.

1.6 Chapter Contents

Chapter 1 introduces the concept of pressure-gain combustion, discusses relevant studies found in literature and presents the scope of the research. Detailed description of the experimental setup is presented in chapter 2. Chapter 3 discusses preliminary experiments and some hot-jet ignition experiments that illuminates effect of some distinct parameters or specific experimental conditions. Chapter 4 consists of presentation of experimental data and discussion relevant to traversing and stationary hot-jet ignition delay. Chapter 5 discusses laminar flame propagation experiments in the main combustion chamber to understand mixture stratification in the chamber. Chapter 6 summarizes the finding of this investigation and recommends improvements that can be implemented for future investigations.

2. EXPERIMENTAL SETUP

The experimental apparatus is located at the Combustion and Propulsion Research Laboratory facility at Indiana University-Purdue University Indianapolis (IUPUI). The apparatus, originally designed by the late Jakob J. Keller (formerly VP Research and Development of Asea Brown Boveri Corporate Research and Boeing Professor at the University of Washington) and constructed by Bilgin [54] at the University of Washington with support from NASA Lewis Research Center, has gone through substantial improvement and redesign since it arrived at IUPUI.

The present combustion chamber is the third generation combustion chamber designed and constructed by Kojok [38]. Each generation of chambers had their strengths and weaknesses. Some of the critical issues that hindered experimentation with previous generation chambers are leakage of the fuel-air mixture, excessive heat loss, cracking of chamber glass and obscuring of the view of the high speed camera for schlieren videography. The 3rd generation chamber was constructed specifically to minimize chamber heat loss, improved sealing and ease of opening and cleaning the chamber. The sealing improvements resulted in greatly reducing leakage from the combustion chamber when stationary hot-jet experiments were conducted. However, for traversing jet experiments a new seal plate was machined and implemented. The high friction of the O-ring seals and their subsequent ejection due to stretching or melting due to generated heat, as reported by Chinnathambi [55] was the primary cause of concern with older seal plates. Moreover, using any sort of additional diaphragm to seal the main chamber resulted in burning of the debris of the diaphragm in the ignition region and affecting the outcomes of the experiments. Another seal plate with spark plug mounted at the center was also machined to conduct spark ignition experiments in the main combustion chamber. A voltage data acquisition module was added to the existing instrumentation and control system to read the

magnetic pickup voltage and subsequently time the trigger of spark plug inside the pre-chamber for traversing hot-jet ignition experiment. In order to obtain a unobstructed view of the the chamber using schlieren imaging, a plate was installed next to main combustion chamber, on top of the XY mounting plate that prevents the jet from coming into view of the schlieren images when it is not traversing the chamber, but is flowing into the surrounding atmosphere. A meshgrid-type cage was also installed loosely that prevents the magnet, mounted on the rotating shaft from flying away if it were to come loose from the mounting. The mass flow controller was also moved closer to fuel storing tank, reducing piping length upstream. A number of new fuels were installed and calibrated with the mass flow controller. Pipe and tube fittings were used to create new fuel delivery lines and vacuum port in the main combustion chamber.

2.1 Overview and Experimental Facility

The experimental facility is currently located in the first floor of the engineering and technology building at IUPUI in room ET 109. The facility is equipped with compressed air line, 3-phase high voltage motor controller, gas cylinders, storage of maintenance and supply, several computers and the experimental apparatus itself. Fig. 2.1 depicts the pre-chamber, main combustion chamber and some of the associated instrumentations schematically.

Fig. 2.2 depicts the experimental facility with all instrumentation and systems. All the systems shown in the schematic diagram are located in ET 109A except the remote control panel. The following subsections describe each component of the hot-jet ignition experiment and the facility in detail.

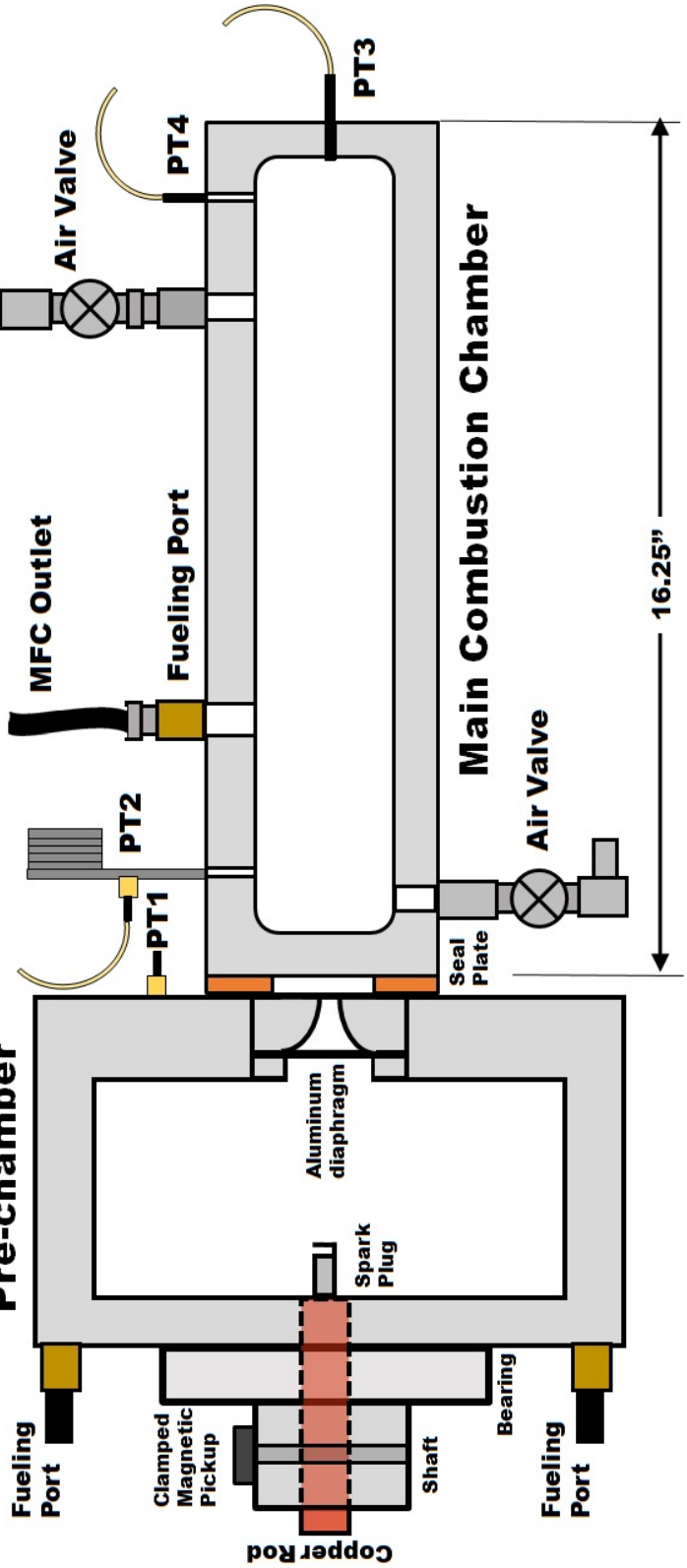

Figure 2.1. : Schematic diagram of the main combustion chamber for hot-jet ignition experiments.

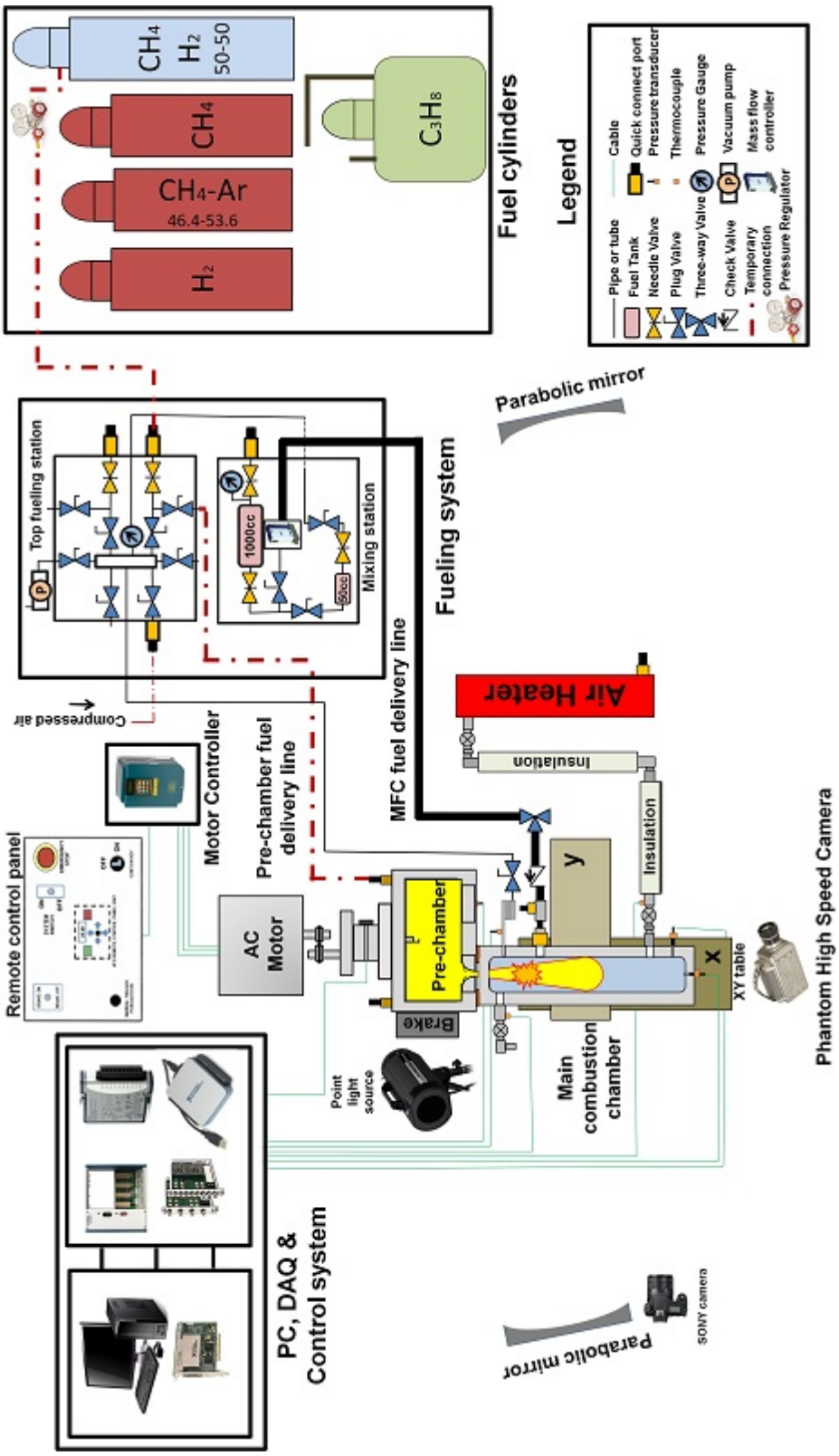

Figure 2.2. : Schematic diagram of the experimental facility located at Combustion and Propulsion Research Laboratory. Path of light rays for the schlieren optical arrangement is shown in Fig. 2.26

2.2 Main Combustion Chamber

The main combustion chamber is made of SS304 steel and consists of 3 rectangular blocks that holds two rectangular glass blocks for optical access. The blocks are sealed by two Buna-N/Aramide gaskets and four o-rings serve as sealing contact between the metal surface and glass surface on both side of the chamber. The main combustion chamber also holds a seal plate in the front (the side of the pre-chamber) and spreader bars on the rear end by eight screw holes. The chamber was originally designed to minimized heat loss for heated air experiments and also reduce the leakage of fuel-air mixtures. The rectangular glass blocks are made of TSC-3 clear fused quartz glass.

The chamber has six ports for measurement and instrumentation. Three ports are used for mounting pressure transducers (PT2, PT3 and PT4) and two ports are used for air inlet and outlet. The air inlet and outlet ports can also be used for purging the chamber with compressed air, especially for laminar flame propagation experiment in main combustion chamber experiments. The remaining port is the fueling port. A quick connect stem is also installed with a tee fitting at the fueling port. This stem can be directly connected to a vacuum pump to vacuum the main combustion chamber.

The chamber dimensions are chosen such that it represents a single channel of a wave rotor combustor and can be found in Table 2.1. The pre-chamber and main combustion chamber and some of the instrumentation are schematically shown in Fig. 2.1. Combustion inside the chamber is observed during an experiment shown in Fig. 2.3. The chamber is sealed with different seal plates. The images (Figs. 2.12-2.11 and drawings (Figs. 2.12 and 2.13) of the seal plates are given in section 2.6.

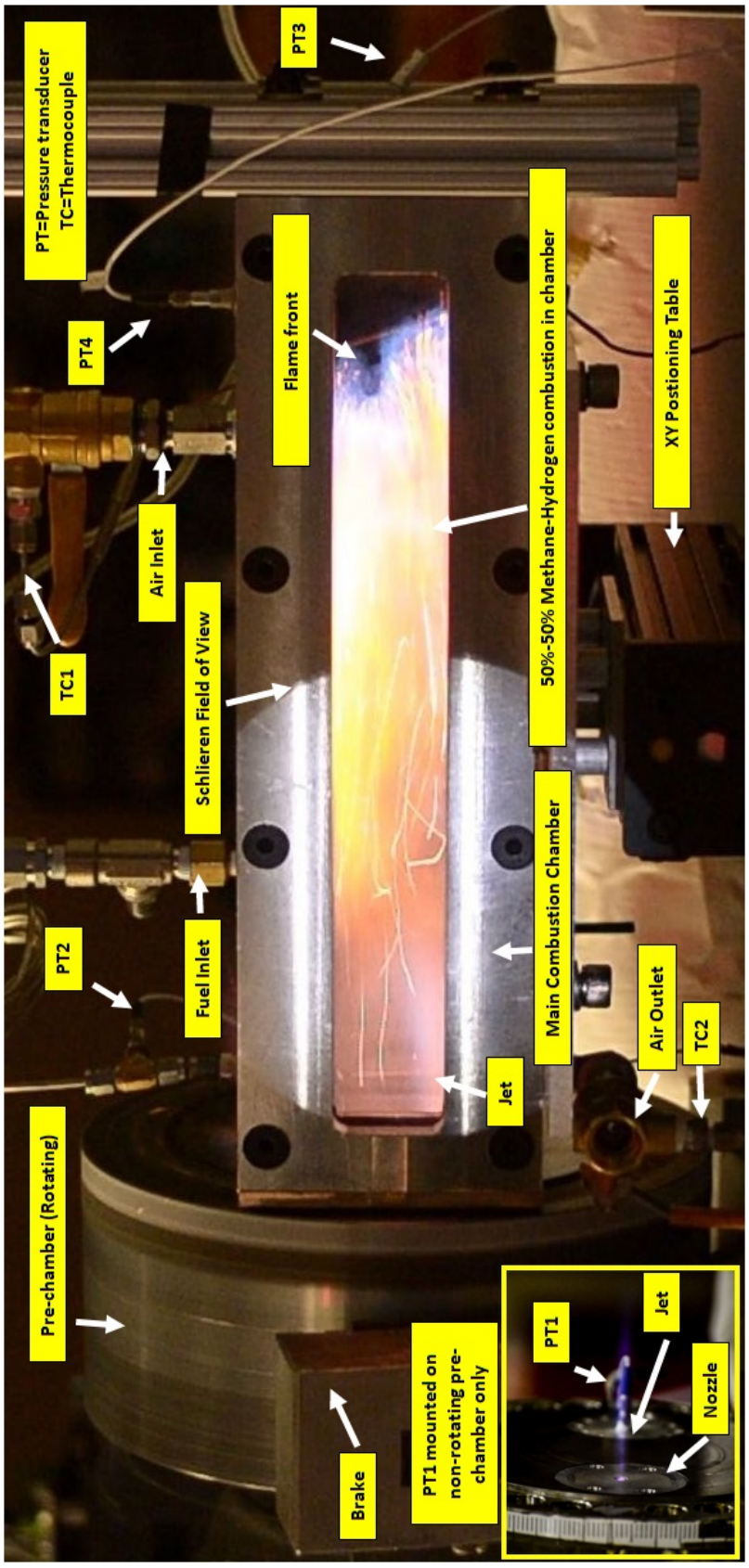

Figure 2.3. : A photograph from test no. 126 of hot-jet ignition demonstrating a snapshot of luminescence of combustion (ignition and flame propagation). The inset (test 204) is showing hot-jet with main chamber removed.

Table 2.1. : Pre-chamer and main chamber dimensions.

Name	Value
Main Chamber	
Length × Width × Height	$16.25 \times 4.43 \times 4.99\ in^3$
Channel cross-sectional area	$1.43 \times 1.84\ in^2$
Aspect ratio	0.77
Length to hydraulic diameter	8.69 inches
Combustion volume	$43.1\ in^3$
Optical Window	$15 \times 2.77 \times 1\ in^3$
XY Table linear resolution	2 mm/rev
Viewing area	$14 \times 1.85\ in^2$
PT2 distance (from chamber front edge)	1.50 inches
PT3 distance (from PT2)	10.22 inches
PT4 distance (from chamber rear edge)	1.75 inches
Air inlet distance (from chamber rear edge)	4 inches
Air outlet distance (from chamber front edge)	1.5 inches
Fueling port distance (from chamber front edge)	5 inches
Wear plate (A2 tool steel) thickness	0.5 inch
Seal plate (Steel/Bronze) thickness	0.25 inch
Pre-chamber	
Internal diameter	6.52 inches
Width (without wear plate)	1.54 inches
Converging nozzle throat diameter	0.27 inch
Diaphragm thickness	0.003 inches
Diaphragm to nozzle outlet	1 inch
Nozzle L/D ratio	3.73
Combustion volume	$49.3 in^3$
Combustion volume ratio	1.14

2.2.1 XY Table

The main combustion chamber is mounted on a Velmex XY positioning table (Model MN10-0100-M02-13). The table has two lead screw slides served by two stepper motors. The table enables the coupling of main combustion chamber with the pre-chamber face. After completing an ignition test, both chambers can be quickly separated by the XY table. For spark ignition main combustion chamber tests the table also allows the chamber to be positioned carefully for performing schlieren visualization at different regions of the chamber.

2.2.2 Laminar Flame Propagation Experiments

The main combustion chamber is sealed with an aluminum seal plate with a spark plate mounted in it. The spark plug is triggered to propagate a laminar flame in the chamber. The schematic diagram of this setup is shown in Fig. 2.4.

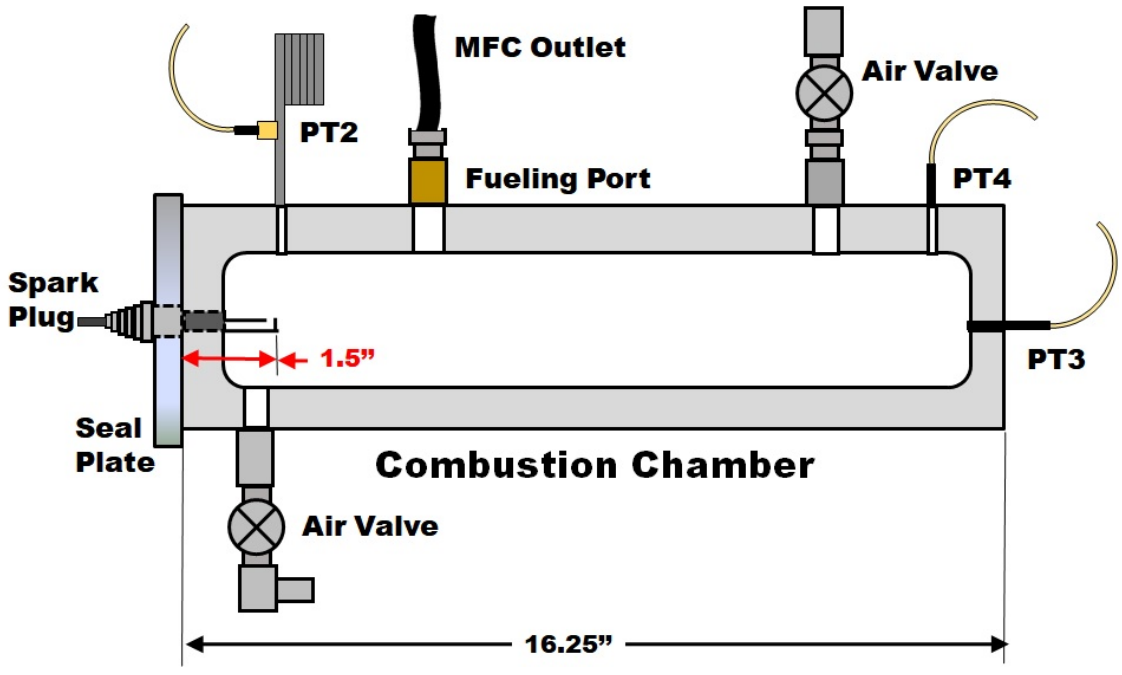

Figure 2.4. : Schematic diagram of the main combustion chamber for laminar flame propagation experiments to study fuel-air stratification.

2.3 Pre-chamber

The pre-chamber is a cylindrical combustion chamber machined from stainless steel. It serves as the igniter for the main combustion chamber by issuing a hot-jet through a converging nozzle mounted on it which is discussed in the following subsection. The pre-chamber has four parts. A wear plate, a front plate, a rear plate and an intermediate ring. The wear plate is mounted on the front plate and machined from A2 tool steel and surface finished to 16 microns average surface roughness [38]. This smooth surface finishing ensures good sealing with the oil-impregnated bronze seal plate for traversing hot-jet ignition experiments when the pre-chamber is rotating. There are two fueling ports in the rear plate of the pre-chamber. One of the fueling ports could potentially be used for mounting a pressure transducer for traversing hot-jet experiments. The rear plate connects the pre-chamber to the drive-shaft and hosts a spark plug at its center discussed in subsection 2.3.3. A quick-connect line from the top fueling station can be connected to any one of the available fueling ports to fuel the pre-chamber. The nominal volume of the pre-chamber was estimated to be 51.27 cubic inches by Paik [7]. A more accurate estimation of the internal volume can be made by taking into account space occupied by fasteners such as bolt heads that connect the different parts of the pre-chamber together internally. Kojok estimated the internal volume in the pre-chamber available for combustion to be 49.3 cubic inches [38] since the bolts connecting the wear plate and the rear plate reduces combustion volume. The pre-chamber also houses two inserts in two machined cavities in the form of cylindrical cut-outs. The location of the cavities are symmetrical to assure static and dynamic balancing when the pre-chamber is rotated to perform traversing hot-jet experiments. The pressure measured by PT1 subjected to influences of pre-chamber flame propagation and pressure rise. It is assumed the pressure measured at fueling port is equal to the pressure at nozzle inlet. An analytical model of the flame propagation and fuel consumption inside the pre-chamber and measurement of pre-chamber pressure using two pressure transducers,

one at fueling port and one at solid insert center can be performed to justify the validity of the assumption. Readers are referred to [6] for a detailed discussion on the importance of the symmetry of the cavities. The nozzle insert assembly, discussed in the following subsection, is mounted in one of these cavities. The other cavity hosts two types of inserts depending on the requirement of the ignition experiment to be performed. For stationary hot-jet ignition experiments, an insert containing the pre-chamber pressure transducer (PT1) is mounted in the other cavity to measure the pre-chamber pressure.Besides, due to the symmetry of the location of the inserts, the pressure measured by the pressure transducer PT1 is assumed to be the same at nozzle inlet. However, for traversing hot-jet ignition experiments, a solid insert without any pressure transducers is mounted on the cavity. The pressure transducer (PT1) can not be mounted in the cavity on a solid insert since the rotating motion will damage PT1 due to high speed impact with the main combustion chamber walls or tear the connection of the coaxial cable connecting the pressure transducer to the data acquisition system. A teared coaxial cable will not conduct the pressure signal through a slip ring interface.

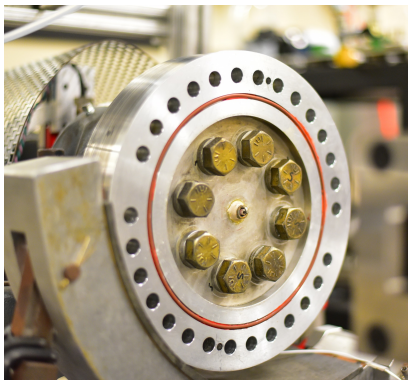

(a) The pre-chamber rear plate showing the spark plug inside.

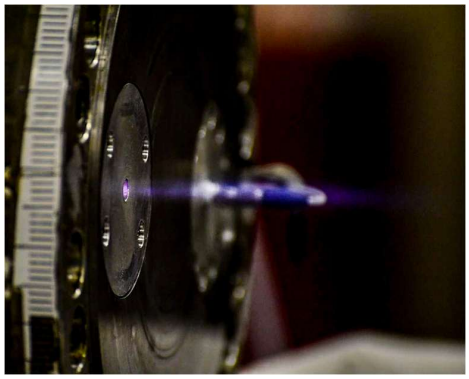

(b) Close up of the nozzle whilst issuing a hot-jet (test 205).

Figure 2.5. : Inside of the pre-chamber and hot-jet issued by the pre-chmaber.

2.3.1 Nozzle

Several nozzle geometries are available in the CPRL lab facility for testing. Bilgin and Perera constructed several nozzles to for their respective studies. Due to the addition of the wear plate for traversing hot-jet ignition cases, a new nozzle design was required to reduce the distance between the nozzle insert outer surface and the wear plate surface so that the nozzle face will flushed against the oil-impregnated bronze seal plate. The convergent nozzle used in the study has exit diameter of 0.27 inches, and 10 degree taper and the distance between the diaphragm and nozzle exit is 1 inch. This is a slightly upgraded design compared to the nozzle used by Paik and Perera. However, among the nozzles tested by Perera, such as convergent, convergent-divergent, straight-cone, hemispherical convergent etc., this particular nozzle design resulted in the minimum prechamber ignition delay [6]. The nozzle insert assembly has a nozzle insert, a diaphragm and a circular nozzle plate.

2.3.2 Diaphragm

A 0.003 inch thick 1010 aluminum diaphragm is scored using an ScoreOne 50050 glass cutter. The scoring is performed in the shape of a '+' sign. The scoring assists with the controlled rupture of the diaphragm once pressure inside pre-chamber rises due to spark ignition. Moreover, the diaphragm isolates the pre-chamber and the main combustion chamber. This enables filling of either chamber independently. Therefore, different equivalence ratios can be maintained in both chambers during ignition experiments. The diaphragm is sandwiched between the nozzle insert rear face and the circular nozzle plate. Perera tested thicker nozzles that did not rupture even at maximum pressure due to combustion pressure rise inside the pre-chamber. Moreover, diaphragms made of Mylar polyester film was melted during the rapid heat release accompanying the combustion inside the pre-chamber during [6]. Consequently the diaphragm rupture time was increased and consumption of the diaphragm due to melting introduces undesired chemical species in the jet. The diaphragm rup-

ture process should leave four symmetric petals to ensure there is no asymmetric variations in the flow field and chemical properties of the issued jet.

Perera and Paik also discussed diaphragm debris [6, 7]. Solid particles coming out of the nozzle outlet cases were discarded by Perera. However, due to the rich fuel-air mixture condition of the pre-chamber, soot formation conditions were satisfied and both Paik and Kojok considered this phenomena to be a concomitant natural phenomena that accompanies fuel rich premixed combustion and test cases involving this phenomena were included in their investigation [7, 38]. This author reports an interesting rupture phenomena where vortex rings are produced. They are discussed in section 3.2.

Fig. 2.6 shows some instances of the diaphragm rupture and subsequent paths of travel of visible particles/debris. The debris, traversing the entire chamber strikes the end-wall of the main combustion chamber and settles at the bottom of the chamber. None of the recorded schlieren images show any ignition event from the particles or debris.

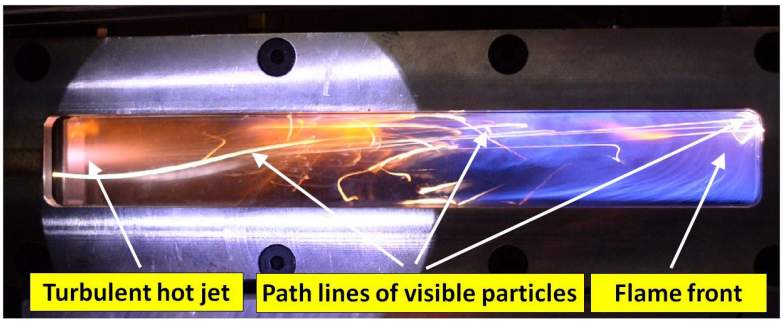

(a) Stationary hot-jet ignition test 67.

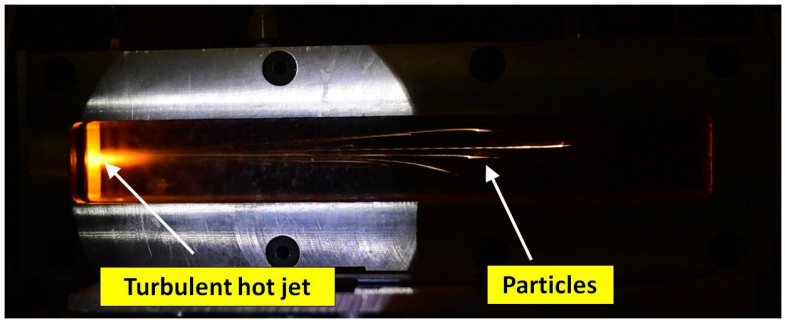

(b) Stationary hot-jet ignition test 229.

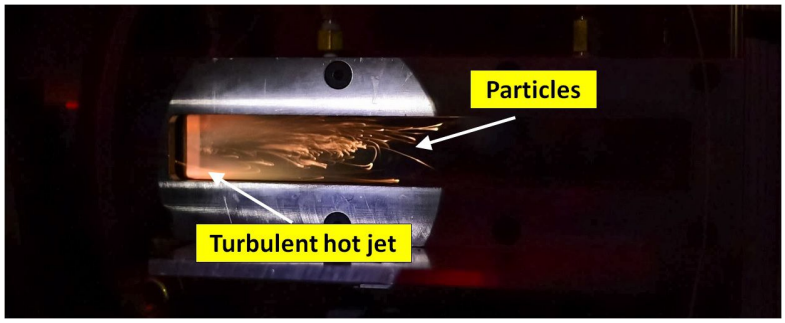

(c) Traversing hot-jet ignition test 304.

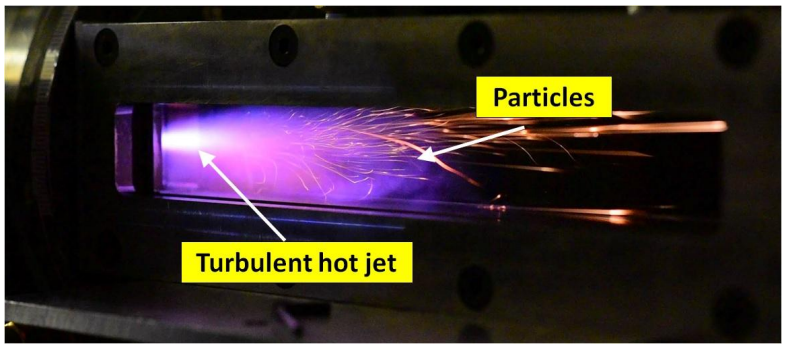

(d) Traversing hot-jet ignition test 450.

Figure 2.6. : Visible particles originating from diaphragm rupture.

2.3.3 Spark Plugs

A Champion spark plug model RC11ZYC4 with a single side electrode and 1 mm spark gap is housed inside the pre-chamber and is positioned at the center of the rear plate. The current of electrons surging across the spark gap is used to trigger the high speed camera and synchronize thepressure data acquisition system.

In a separate series of experiments designed to investigate the mixture in the main chamber, a special cover plate with a different spark plug is installed, on the front side of the main combustion chamber. This spark plug, a Champion spark plug model FI21501 (manufacturer part no. 220, shown in Fig. 2.10(a)) was used because it has a long electrode (1.5mm from seal plate surface to plug tip) and same spark plug gap of 1 mm. Therefore, the emergence and growth of the flame kernel can be visually seen in the schlieren images.

2.4 Leakage Gap

The leakage gap is needed to be closely monitored when conducting traversing hot-jet ignition experiments. If it is too large, the leakage from main chamber increases, as well as the active radical of the jet can escape to the atmosphere instead of entering the desired combustion zone. If the gap is too small, due to friction, the speed of rotation of the pre-chamber cannot be maintained, given the range of motor power available. Moreover, the heat energy, dissipated due to friction, transmits to the fuel-air mixture in the entrance zone. Since, measuring the leakage or the gap is quite difficult, pre-chamber speed was monitored when pressing the chambers together. Before each experiment was conducted the speed was adjusted and noted by rotating the wheel manually by hand on the X-slide of the XY positioning table. Moreover, unlike the stationary hot-jet ignition experiments where a C-clamp was used to tighten and seal the chambers, a flexible rope clamp was used to provide a finely adjustable contact force between sliding surfaces during the traversing hot jet ignition experiments.

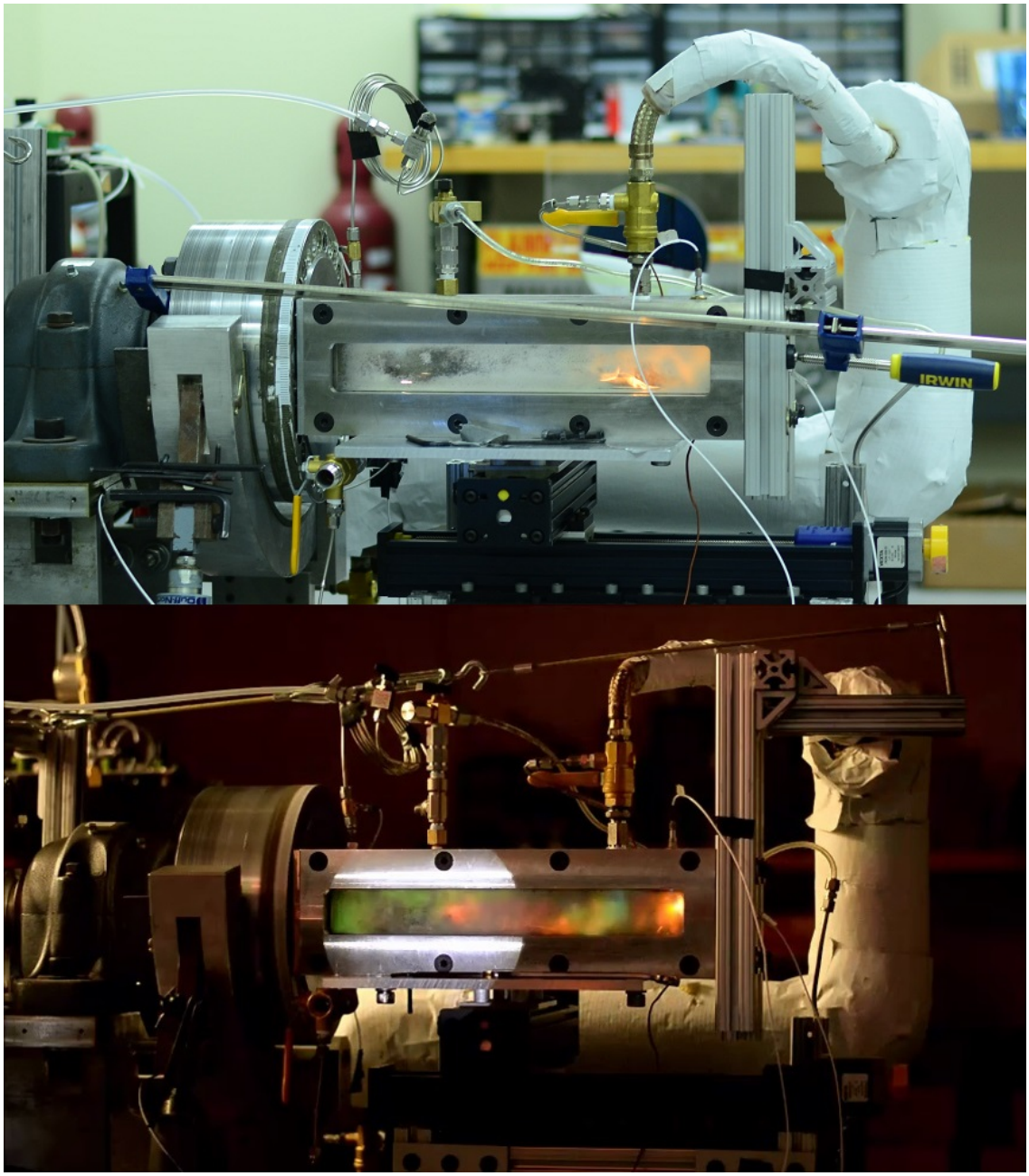

Figure 2.7. : C-clamp used in stationary hot-jet ignition experiment (top) and flexible rope clamp used in traversing hot-jet ignition experiment (bottom) to maintain chamber coupling.

2.5 Ignition Process

2.5.1 Stationary Hot-Jet Ignition Process

Ignition event by a hot-jet issued from a stationary pre-chamber coupled with the main combustion chamber is referred to as stationary hot-jet ignition process. The spark plug inside the pre-chamber, when triggered, initiates ignition of the pre-chamber fuel-air mixture. Pressure inside the pre-chamber increases due to flame propagation inside the pre-chamber. The increased pressure causes the diaphragm to rupture and issues a radical equipped hot-jet, carrying combustion products, to the main combustion chamber and subsequently ignite the fuel-air mixture inside the main combustion chamber. A rupture shock, due to diaphragm rupture and the disturbance created by sudden pressure change, precedes the ignition event and propagates back and forth inside main combustion chamber. It returns as a reflected shock from the end-wall. The pressure continues to rise as the chamber mass increases, with local oscillations caused by the back and forth motion of waves. The pressure transducers pick up these pressure variations.

As the pre-chamber, continue to deposit more radical mass along with jet inside the main combustion chamber, the fuel-air mixture ignites. This is different from ignition in shock tubes and rapid compression machines, which is autoignition starting from stable fuel and oxidant species, without any introduction of reactive species. The ignition point can be visually identified from schlieren images. The flame kernel grows and propagates toward the end wall of the main combustion chamber. The reflected shocks interacts with the propagating flame while refracting from density interfaces. The residual gas is thus subjected to numerous waves that give rise to longitudinal back and forth bulk motion of the gas. The flame propagation is superimposed on this bulk motion of the gas.

2.5.2 Traversing Hot-Jet Ignition Process

The traversing hot-jet ignition process, as shown schematically in Fig. 2.8, is very similar to stationary hot-jet ignition process except for two events. The rotation of the pre-chamber and the traverse motion of the hot-jet preceding ignition event in the main combustion chamber. The pre-chamber, once fueled, is rotated and then precisely triggered. Without precision, depending on the trigger moment, the hot-jet will be issued earlier causing less amount of hot-jet to be deposited in the main chamber or will be issued somewhere in between the chamber entrance top edge and bottom edge leading to shorter traverse time or will be issued later without initiating the traverse motion of the jet. Based on the position of the magnet on the pre-chamber mounting shaft, the spark plug inside the pre-chamber is triggered as soon as the main combustion chamber is fueled by the mass flow controller.

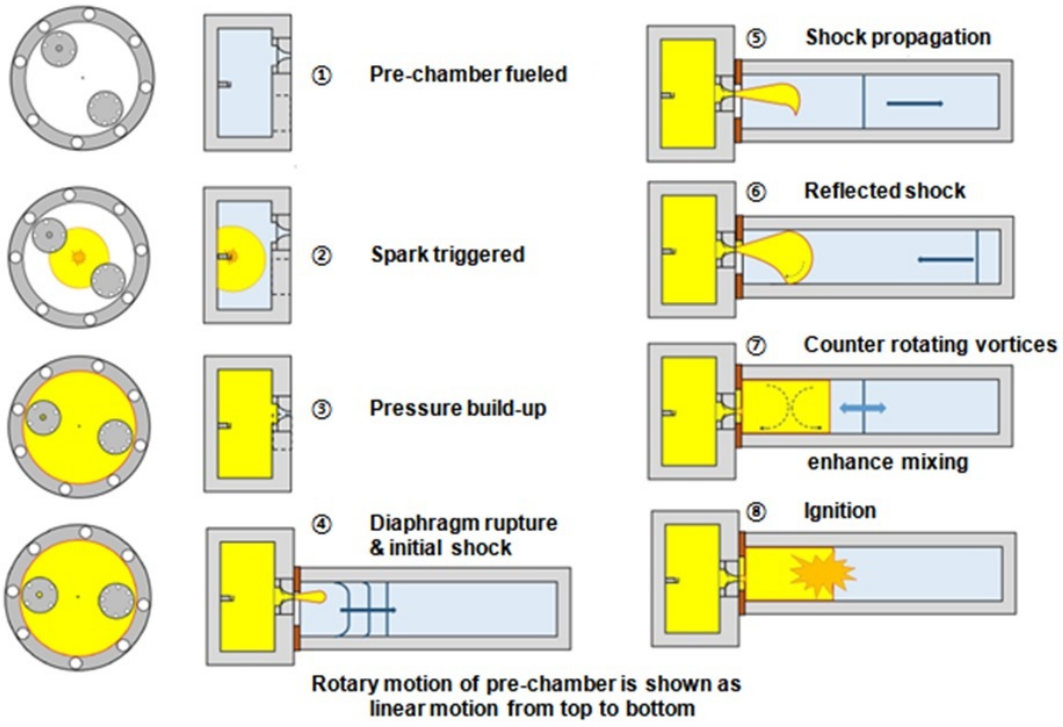

Figure 2.8. : Schematic representation of the traversing hot-jet ignition process.

Initiation of ignition inside the pre-chamber, much like the stationary hot-jet ignition process, causes the pressure to rise as the flame kernel inside the pre-chamber grows. Once the pre-chamber pressure, reaches beyond the yield point of the scored diaphragm, the diaphragm ruptures and issues a hot-jet. Due to the rotation of the pre-chamber, the issued hot-jet traverses across the entrance of the main combustion chamber. The timing of the spark plug firing ensures the hot-jet starts traversing from the entrance of the main combustion chamber. The rupture causes a shock wave to propagate and reflect back inside the main combustion chamber similar to stationary hot-jet ignition process. However, the shock has more curvature compared to stationary hot-jet ignition process. While the bulk motion of the hot-jet in to the residual gas of main combustion chamber enhances mixing, counter rotating vortices due to traverse motion emerge and further enhance mixing compared to stationary hot-jet ignition process before ignition occurs inside the main combustion chamber. The ignition kernel is affected by the vortex motion of the eddies present in the the gas motion and the flame propagation is superimposed on the bulk motion of the gas and these eddies.

2.5.3 Spark Ignition in Laminar Flame Propagation Experiments

The main combustion chamber fuel-air mixture is ignited by a spark plug. A small ignition kernel develops between the spark gap and causes a spherical flame to propagate. The flame kernel gradually grows and the fills the width of the main combustion chamber and propagates longitudinally. Due to fuel stratification and buoyancy effects the propagating flame front curvature is greatly affected. The flame front travels the main combustion chamber, interacts with pressure and shock waves and ultimately extinguishes. In the absence of the jet induced motion, the flame front propagation to the chamber end-wall timescale is of the order of 100ms.

2.6 Seal Plates

2.6.1 Oil-impregnated Bronze Seal Plate

A new seal plate made of oil-impregnated bronze, with O-ring seal on the main chamber side was machined. Bronze has lower coefficient of friction and is widely used for manufacturing bearing sleeves. Frictional coefficient of bronze alloys against steel range from 0.08 to 0.14 with lubricant and without any lubricant from 0.12 to 0.30. In comparison, friction coefficient of aluminum on steel is 0.32 and steel on steel is 1.00. The wear plate of the pre-chamber and the front side of this seal plate has no O-ring. The rotating contact surface between pre-chamber wear plate and the seal plate reach elevated temperatures causing the impregnated oil to emerge and form a sealing surface and function as lubricant. This design improved upon previous experimental difficulties such as melting of the O-ring due to higher amount of heat generation and subsequent replacement of the O-ring in the seal plate for each experiment. Leakage rate of fuel-air mixture from the main combustion chamber is much higher with this seal plate. Consequently, the hot-jet is issued as soon as the main chamber fueling is over.

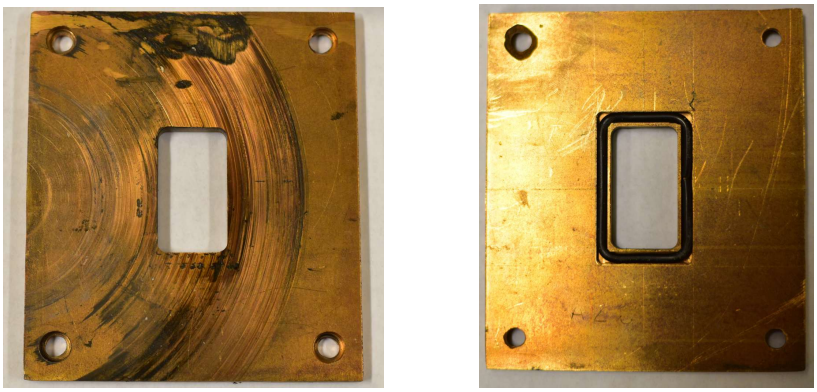

(a) Front side. (b) Rear side.

Figure 2.9. : Oil-impregnated bronze seal plate after 150 hot-jet ignition experiments.

2.6.2 Spark Plug Mounted Seal Plate

A 0.375 inch thick aluminum seal plate was machined to seal the main combustion chamber in order to conduct spark ignition experiments. The spark plug was installed using 250 Nm of torque.

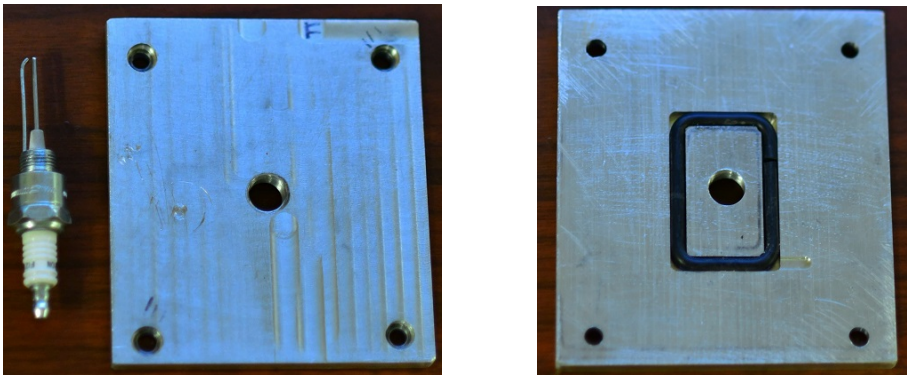

(a) Front side. (b) Rear side.

Figure 2.10. : Champion spark plug model FI21501 mounted seal plate after 285 spark ignition experiments.

2.6.3 Conventional Seal Plate

Fig. 2.11 shows a conventional seal plate with O-rings on both sides.

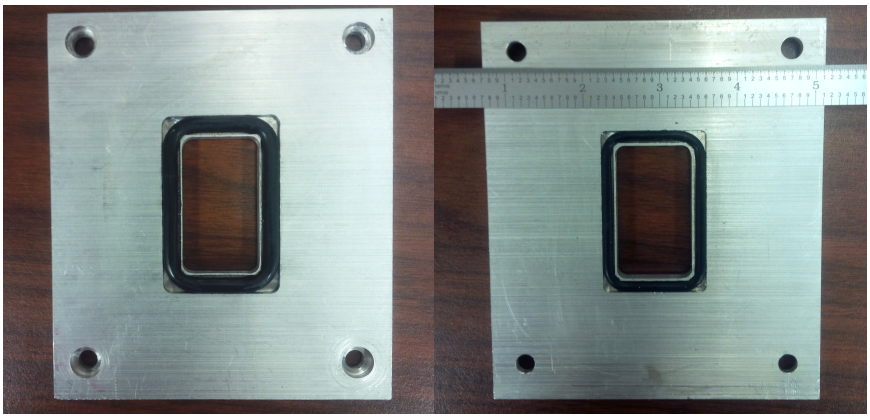

Figure 2.11. : Seal plate used in stationary hot-jet ignition experiments [38].

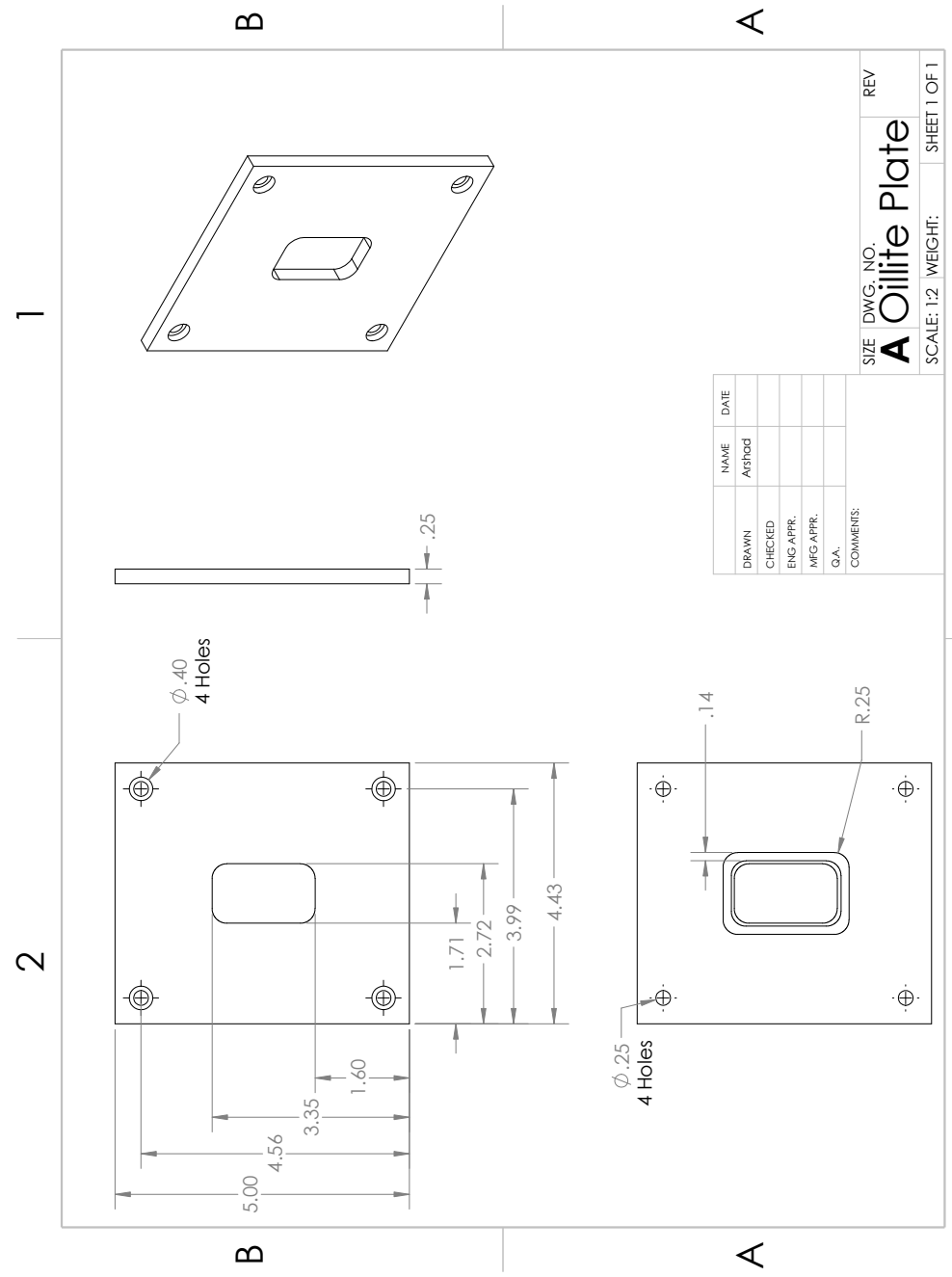

Figure 2.12. : Drawings of oil-impregnated bronze seal plate.

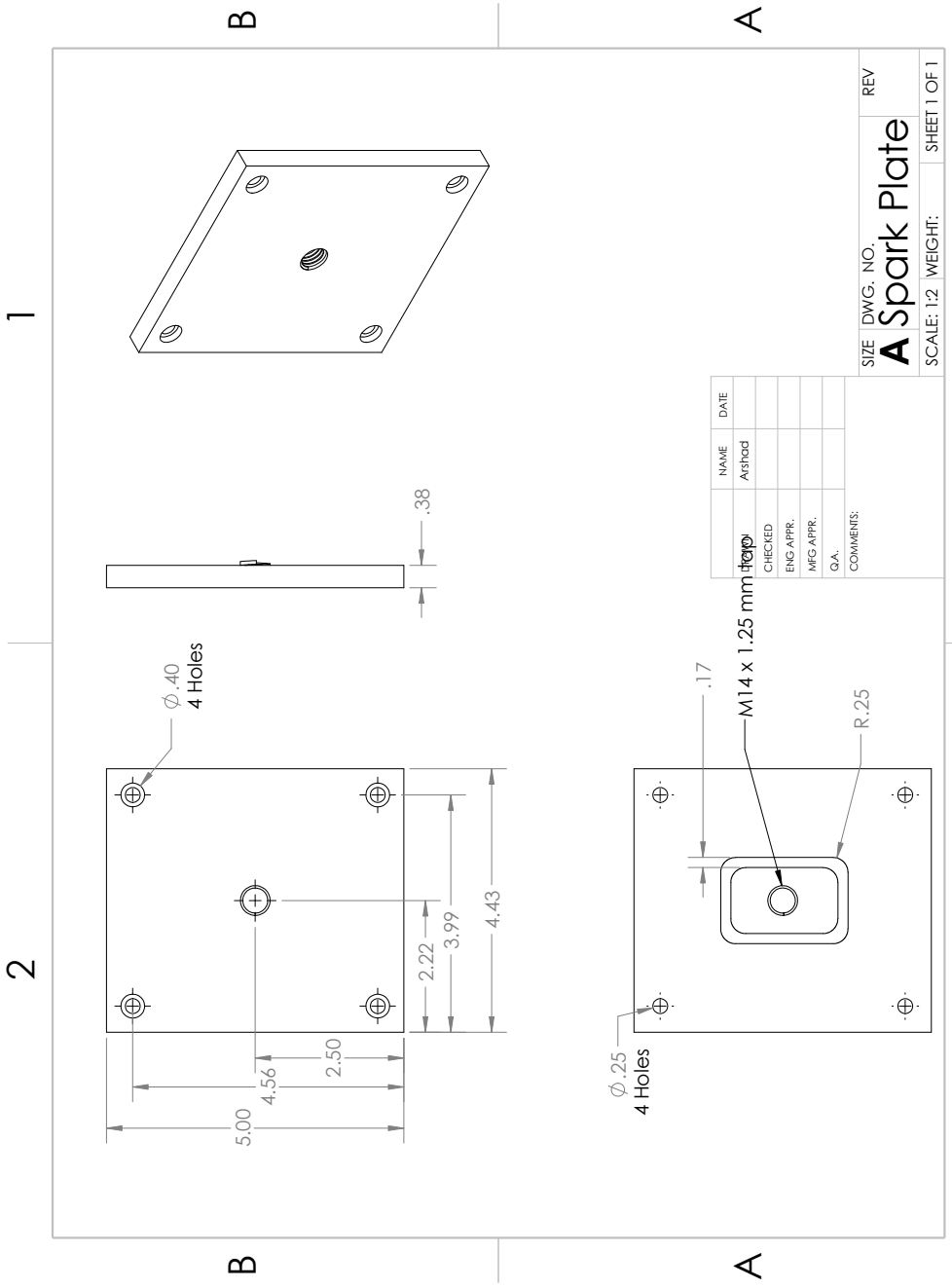

Figure 2.13. : Drawing of spark plug mounting seal plate.

2.7 Fueling System

The fueling of the pre-chamber was done based on partial-pressure method and the main chamber was fueled using a mass flow controller. Kojok, Paik, Chinnathambi and Perera also used partial pressure method to fuel the pre-chamber [6,7,38,55]. Minor differences exist in the fueling strategies employed by these investigators. Mostly in terms of using make-up air to enhance mixing or not and delivering methane and hydrogen separately or together from a premixed bath. This author did not use make-up air to enhance mixing and neither prepared methane-hydrogen batches to deliver to the pre-chamber. A premixed gas cylinder filled with 50%-50% methane and hydrogen was used instead to deliver fuel to the pre-chamber.

Pure methane, $50\% - 50\%$ methane-hydrogen blend, pure hydrogen, $50\% - 50\%$ methane-hydrogen blend, pure propane and a $46.4\% - 53.6\%$ methane-argon blend fuel were used in this study. The fuel cylinders are filled by Praxair with 99.97% purity for methane and 99.999% purity for hydrogen. The $50\% - 50\%$ methane-hydrogen blend was produced by Prax-air on request to reduce uncertainty in the pre-chamber equivalence ratio fuel composition. Previously, the pre-chamber was fueled by Kojok and Paik by creating the $50\% - 50\%$ methane-hydrogen blend fuel by mixing the two pure fuel first. The certified concentration of hydrogen in the blend fuel cylinder is 49.8% with purity of 99.999% and the balance is pure methane of 99.97% purity. The blend fuel was used to fuel the pre-chamber. It was also used as fuel in the main chamber along with pure methane and propane. The pure hydrogen fuel was used to make $30\% - 70\%$ methane-hydrogen blend for some special experiments. The propane tank was filled by Blue Rhino. Batches of $50\% - 50\%$ methane-propane blend were made using fuel from the methane cylinder and the propane cylinder

The fueling system consistently delivers the same amount of fuel to the pre-chamber and the main chamber. For fueling the main chamber, the mass flow con-

troller needs to be calibrated. The author calibrated $30\% - 70\%$ methane-hydrogen blend fuel, $50\% - 50\%$ methane-propane blend, propane and $46.4\% - 53.6\%$ methane-hydrogen blend. Calibration curves for pure methane, pure hydrogen and $50\% - 50\%$ methane-hydrogen blend fuel are previously reported by Kojok [38].

Fuel specifications are presented in Table 2.2.

Table 2.2. : Manufacturer fuel specifications

Fuel/ Blend	Quality Assay	Grade /Manufacturer
Methane	CH_4 99.97% O_2 <15 ppm H_2O <5 ppm N_2 <100 ppm $CO + CO_2$ <10 ppm H_2 <10 ppm C_nH_m <100 ppm	3.7 Ultra high purity (Praxair)
Hydrogen	H_2 99.999% O_2 <1 ppm H_2O <3 ppm THC <0.5 ppm	5.0 Ultra high purity (Praxair)
Methane-hydrogen (50% − 50%)	CH_4 50.2% H_2 49.8%	Ultra high purity (Praxair) 2% Analytical uncertainty
Methane-argon (46.4% − 53.6%)	CH_4 46.4% Ar 53.6%	Ultra high purity (Praxair) 1% Analytical uncertainty
Propane	C_3H_8 85 − 100% C_3H_6 0 − 10% C_2H_6 0 − 5% C_4H_{10} and heavier 0 − 2.5% C_2H_6S 0 − 0.0025%	Blue Rhino

2.7.1 Pre-chamber Fueling

The pre-chamber has two identical fueling ports. A quick connect fuel delivery line can connect to either of the fueling ports (shown by dotted red line in Fig. 2.2). For all hot-jet ignition experiments, the fueling port located further from the nozzle insert was used to fuel the pre-chamber. The pre-chamber leakage must be minimized for the partial-pressure method based fueling to be employed. The $50\% - 50\%$ methane-hydrogen blend cylinder pressure regulator outlet is connected to the top fueling station and and a quick connect of the top fueling station is then connected to the pre-chamber port to create a fuel line. Using a needle valve and an ASHCROFT VAC 30psig pressure gauge the fuel is delivered to the pre-chamber. The pre-chamber pressure can be monitored continuously using the pressure gauge. If the pre-chamber needs to be vacuumed to deliver the exact amount of fuel to reach equivalence ratio of 1.1 at 1 atm absolute pressure, the vacuum pump (a Thermo Science Model 420-1901) is operated first to reach the desired pressure below atmospheric pressure first and then the fuel is delivered in the aforementioned method. The pre-chamber can be pressurized opening a valve in the top station that connects the pre-chamber fueling port to a branch of the compressed air supply. The pre-chamber leakage at -10psig is estimated to be about 0.0001 psi/min.

Since the pre-chamber contains some air inside it before fueling is conducted, we can write the following, considering Dalton's law of partial pressure of gases, the ideal gas law and the chemical reaction between equimolar methane-hydrogen blend and air we can write,

$$P_{total} \quad = \quad P_{initial} \quad + \quad \frac{2\phi}{2\phi + 4.76 \times 2.5} P_{total} \tag{2.1}$$

Where P_{total} is the target pressure (for example , 1 atm) and $P_{ambient}$ is the ambient pressure in the room. $P_{initial}$ is the pre-chamber air pressure that must be attained by vacuuming or pressurizing the pre-chamber to reach the target pressure. Unless the pre-chamber needs to be at pressures greater than atmospheric, $P_{total} = P_{ambient}$

The pre-chamber is fueled by connecting it indirectly with 50%-50% methane-hydrogen cylinder and the amount of residual air in the pre-chamber is assumed to be at the same pressure as the ambient. Makeup air was not used in the pre-chamber for any experiment. Except for some supplemental experiments the equivalence ratio in the pre-chamber is 1.1.

2.7.2 Main Chamber Fueling

A mass flow controller, model PFC-60, made by MKS instruments delivers fuel to the main combustion chamber. The fuel delivery line is shown by a thick black line in Fig. 2.2. The maximum mass flow rate through the MFC is 1000 SCCM. Downstream of the MFC, a 3-way valve connects the MFC outlet to a check valve that prevents back flow of the fuel. The check valve is connected to a tee where a quick connect stem is connected to one branch of the tee for vacuuming the main chamber and the other branch connects check valve outlet to main chamber. The stem, check valve and the tee are made by Swagelok. The stem is self-sealing and prevents fuel from leaking as well as create another fueling line or vacuum line for other experiments similar to the 3-way valve which can also add another fuel line if required. However, the check valve has 1/3 psia pressure drop.

For stationary hot-jet ignition experiments, the chambers are well sealed and leakage of fuel-air mixture during fueling from the main chamber is very low and the main chamber can be fueled using partial pressure method. However, for traversing hot-jet ignition experiments the leakage rate is much higher even with the dynamic sealing provided by the oil-impregnated bronze seal plate against the rotating wear plate surface of the pre-chamber. Therefore, similar to high temperature ignition experiments of Kojok there is a requirement of fueling to be over as fast as possible and as accurately as possible. Moreover, partial pressure method cannot be employed to fuel the main combustion chamber for traversing hot-jet ignition cases. The mass flow controller also makes the fueling process more repeatable compared to manual

filling by partial pressure method. Furthermore, the mass flow controller is pressure insensitive, i.e., it maintains a constant fuel flow rate even if upstream pressure drops.

For details on the mass flow controller construction and operation interested readers are referred to Kojok [38]. Briefly, the mass flow controller consists of a flow measuring sensor and a flow control solenoid valve working as a closed loop feedback system. The sensor measures the mass flow rate through the MFC by continuously measuring the temperature of the flow in the upstream and the downstream. The sensing element is a resistive heated winding and the mass flow rate through the MFC is proportional the temperature difference. The operator of the valve can send voltage pulses to keep the solenoid valve opened for a desired time to deliver the required amount of fuel. The MFC monitors its internal flow rate using the sensor and make adjustments to keep the flow rate constant even if the pressure upstream drops. Since the mass flow controller is located downstream of the 1000 cm^3 mixing tank, (which is also used to store pure fuels other than prepared batches) as more tests are conducted the pressure in the tank drops and this necessitates a pressure insensitive fuel delivery system. Otherwise, after each test the MFC would have to be adjusted.

Since the fueling process is unsteady and requires delivery of a certain quantity of fuel, the unsteady operating characteristics of the MFC must be validated to ensure the steady operation of the MFC and delivery of the fuel. Therefore, the MFC is calibrated using volume displacement method the details of which is also discussed by Kojok [38]. Briefly, the gas coming out of MFC is passed through water in a acrylic container which is immersed in a burette. The gas is trapped inside the burette and displaces water. The difference in water level before and after fuel gas delivery can be used to estimate the mass delivered by the gas using ideal gas equation at local atmospheric pressure and temperature. Since the MFC reports a voltage in the range of 0V to 5V corresponding to the mass flow rate and the full scale output settings in software, for each fuel the flow rate per unit voltage, i.e., a calibration factor has to be estimated and validated using the volume displacement method. Factory

constants or calibration factor value are available for pure methane (144 SCCM/V) and pure hydrogen (200 SCCM/V). However, Kojok found an unexplained difference between factory calibration and lab calibrated values for methane. For all fuels except pure methane, pure hydrogen and 50%-50% methane-hydrogen blend, the MFC is recalibrated using the volume displacement method to estimate their flow rate vs voltage relation. These three fuels were calibrated by Kojok previously. To determine the calibration curves for the rest of the fuels a 5V single pulse square signal (DC voltage) acted as the set point signal. The rise time of the signal is about 1.5s and the signal has about 2-3s of settling time. Therefore, during experimentation any on time selected must be above this rise time to avoid large errors in the amount of fuel delivered. This author used the reported SCCM value instead of the nominal SCCM value for each fuel required to calculate equivalence ratio unlike Kojok. Therefore, the variation in equivalence ratio, i.e., the error is apparent in the plotted results.

For each fuel, a calibration test was performed and the resulting SCCM/V value and calibration curves are presented here. For all the fuels, the internal setting of the MFC was kept at methane setting. Table 2.3 enumerates lab measured constants and the slope of the zero intercept linear fit of mass delivered and time MFC open plots. For continuity, Kojok's calibration curves are also shown here in Figs. 2.14-2.16 . The other calibration curves are given in Figs. 2.17-2.20.

The calibration curves consist of mass of fuel delivered vs time MFC is on and also a comparison of the mass of fuel delivered by the MFC and the mass of fuel estimated by the volume displacement method. A common trend in all the calibration curves is that during the operation for the first 2s of MFC on time, there is a large error in the mass delivered by MFC and mass estimated by volume displacement method. This is because the MFC has a rise time of 2s approximately [38].

To deliver fuel to the main chamber the following equation is used to calculate the mass of fuel required and create a fueling chart in MS Excel

$$m_{fuel} = \frac{P_{air} V_{main} M_{air} \phi}{R T_{air} (A/F)_{stoichiometric}} \tag{2.2}$$

From the linear fit of mass of fuel delivered (m_{fuel}) against MFC on time (t) is related as follows

$$t = \frac{m_{fuel}}{k} \tag{2.3}$$

The value of the calibration constant/slope is given in all the linear fit calibration curves and also in Table 2.3.

The duty cycle is calculated by dividing the MFC on time (t) by the set point signal on time (t_{set}) and entered in the LABVIEW VI.

Table 2.3. : Mass flow controller calibration factors for various fuels .

Fuel	Factory constants (SCCM/V)	Lab measured constants (SCCM/V)	Slope,k (mg/s)
CH_4	144	115	6.423
50%-50% $CH_4 - H_2$	NA	131	3.928
30%-70% $CH_4 - H_2$	N/A	135	1.446
H_2	200	200	1.338
C_3H_8	N/A	56	8.674
50%-50% $CH_4 - C_3H_8$	N/A	69	7.276
46.4%-53.6% $CH_4 - Ar$	N/A	154	14.775

Values for CH_4, 50%-50% $CH_4 - H_2$ and H_2 are taken from [38]

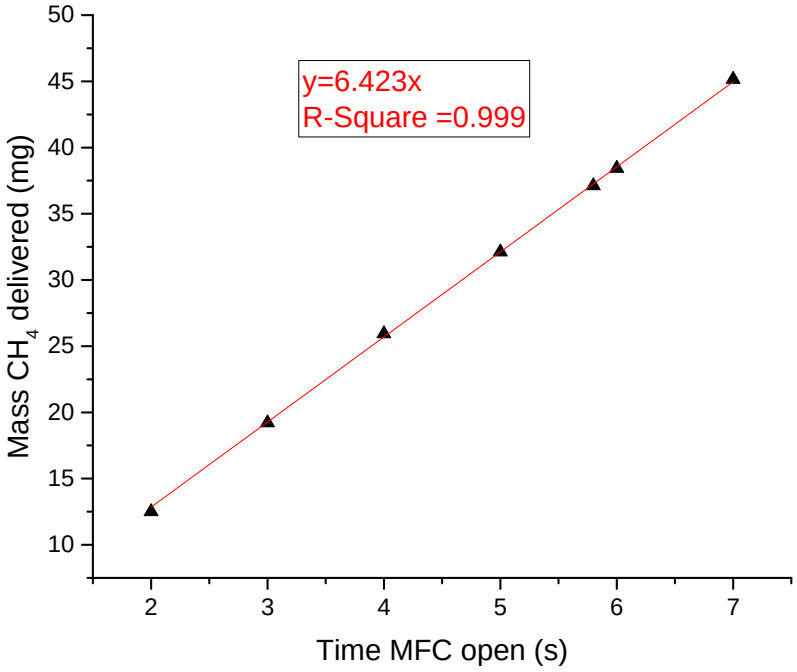

(a) CH_4.

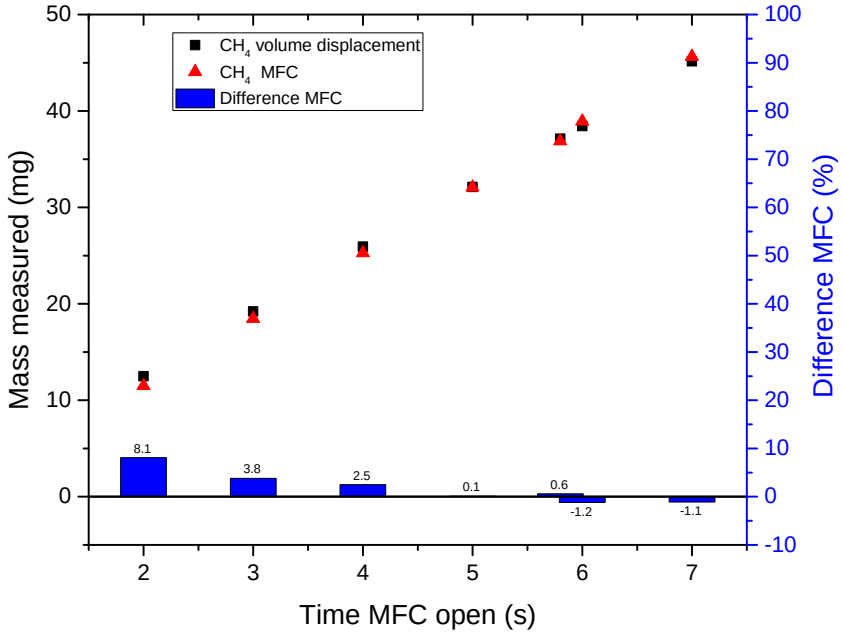

(b) Percentage error in CH_4 mass delivered.

Figure 2.14. : CH_4 Calibration curves and error comparison in terms of mass delivered between MFC and volume displacement method [38].

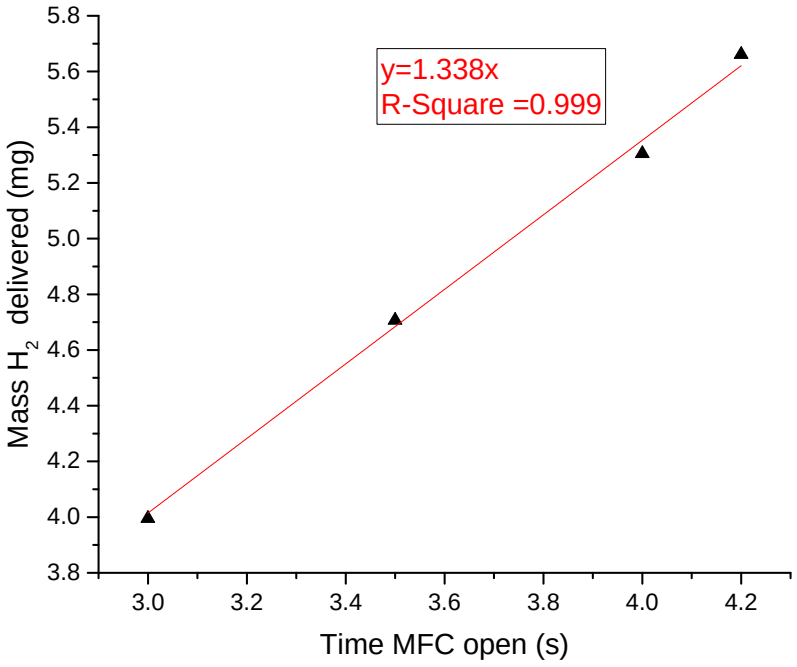

(a) H_2.

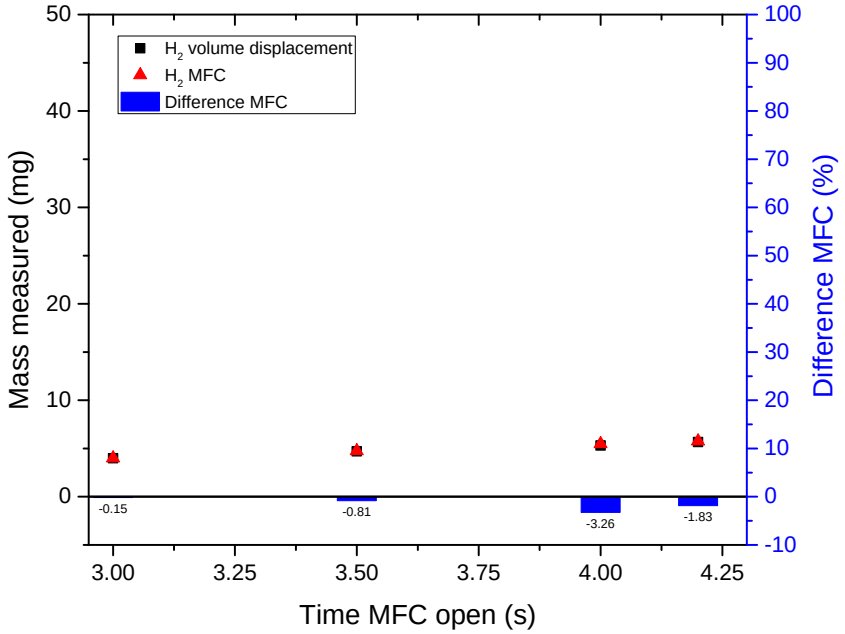

(b) Percentage error in H_2 mass delivered.

Figure 2.15. : H_2 Calibration curves and error comparison in terms of mass delivered between MFC and volume displacement method [38].

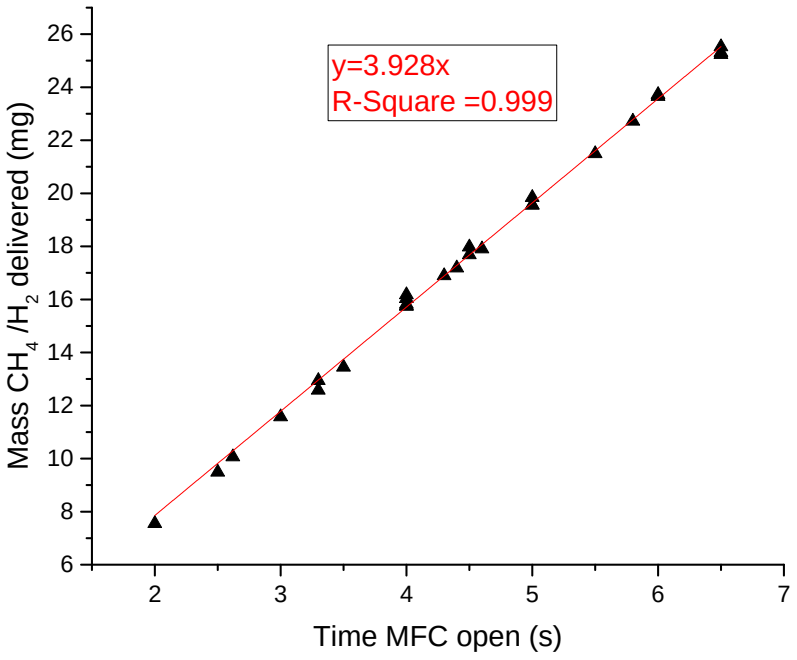

(a) 50%-50% $CH_4 - H_2$.

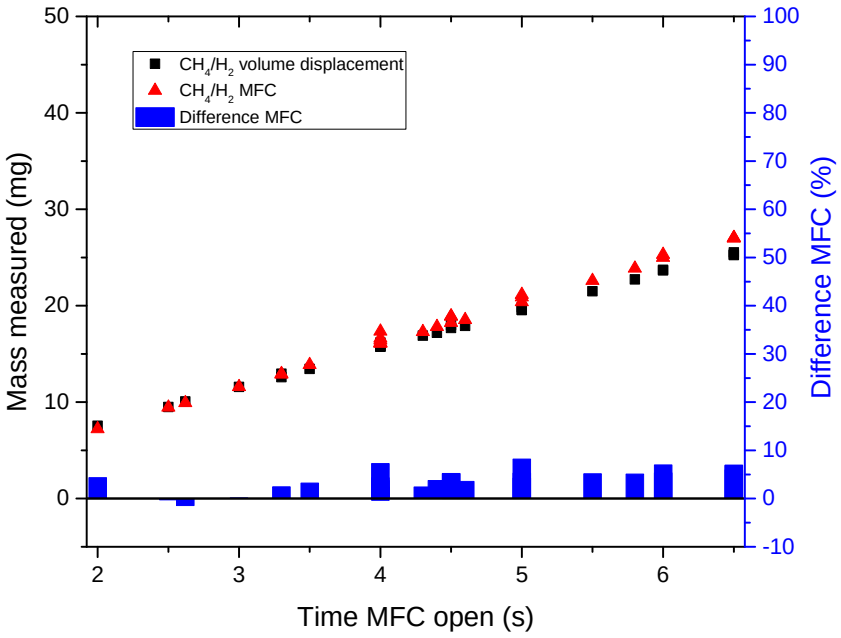

(b) Percentage error in 50%-50% $CH_4 - H_2$ mass delivered.

Figure 2.16. : 50%-50% $CH_4 - H_2$ Calibration curves and error comparison in terms of mass delivered between MFC and volume displacement method [38].

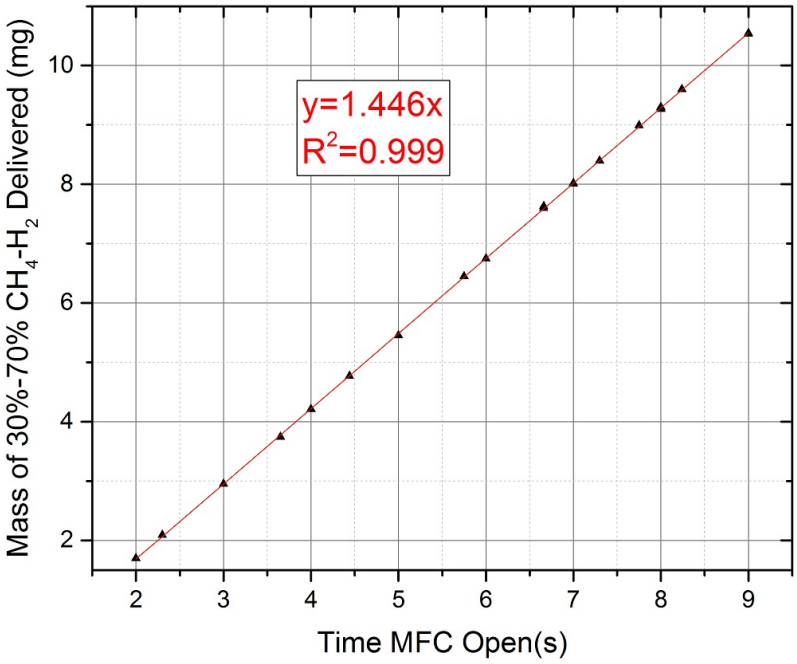

(a) 30%-70% $CH_4 - H_2$.

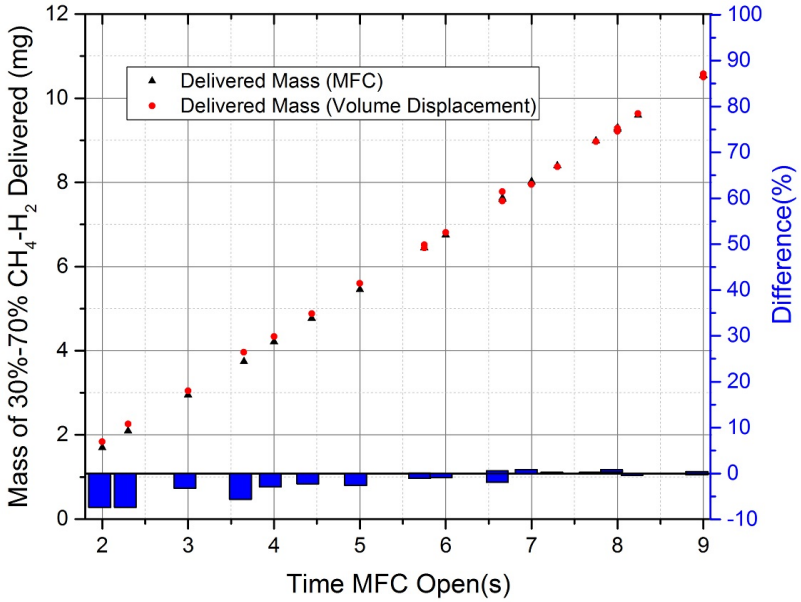

(b) Percentage error in 30%-70% $CH_4 - H_2$ mass delivered.

Figure 2.17. : 30%-70% $CH_4 - H_2$ Calibration curves and error comparison in terms of mass delivered between MFC and volume displacement method.

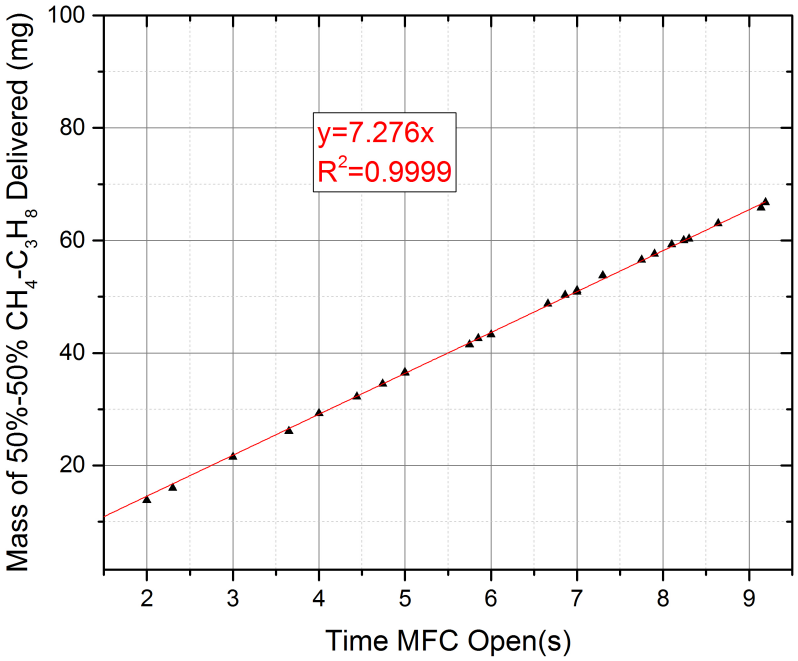

(a) 50%-50% $CH_4 - C_3H_8$.

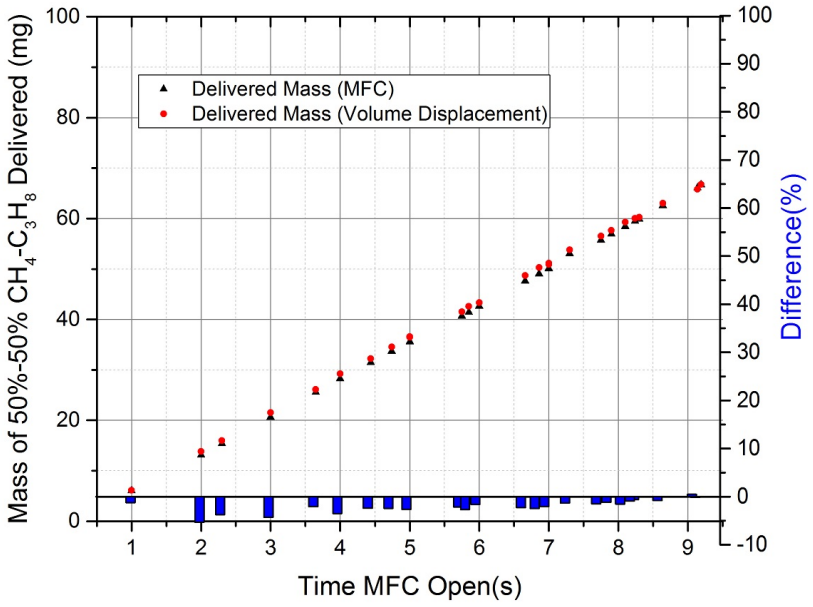

(b) Percentage error in 50%-50% $CH_4 - C_3H_8$ mass delivered.

Figure 2.18. : 50%-50% $CH_4 - C_3H_8$ Calibration curves and error comparison in terms of mass delivered between MFC and volume displacement method.

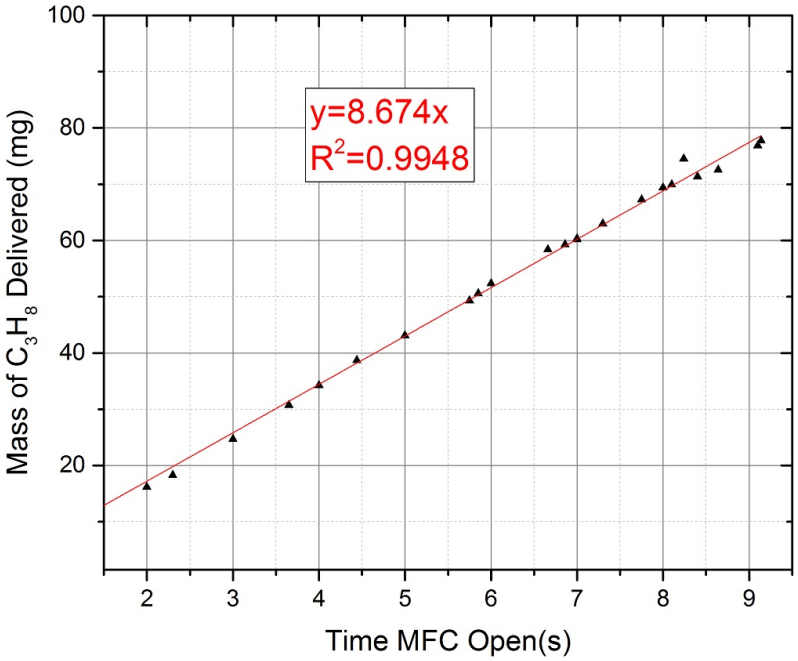

(a) C_3H_8.

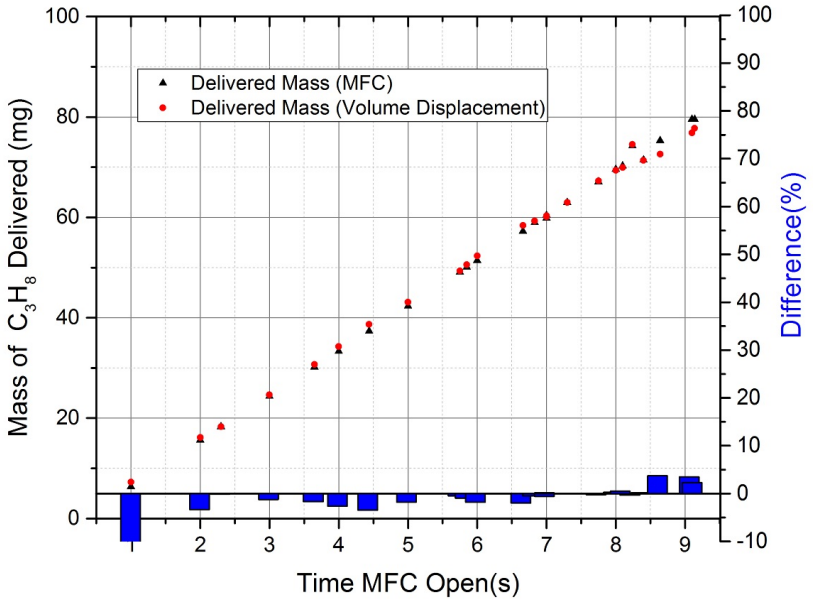

(b) Percentage error in C_3H_8 mass delivered.

Figure 2.19. : C_3H_8 Calibration curves and error comparison in terms of mass delivered between MFC and volume displacement method.

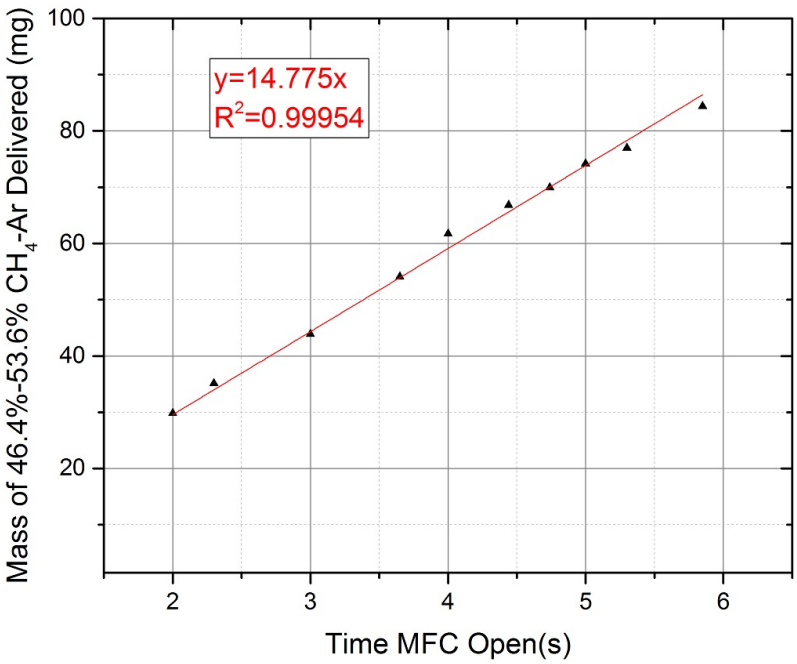

(a) 46.4%-53.6% $CH_4 - Ar$.

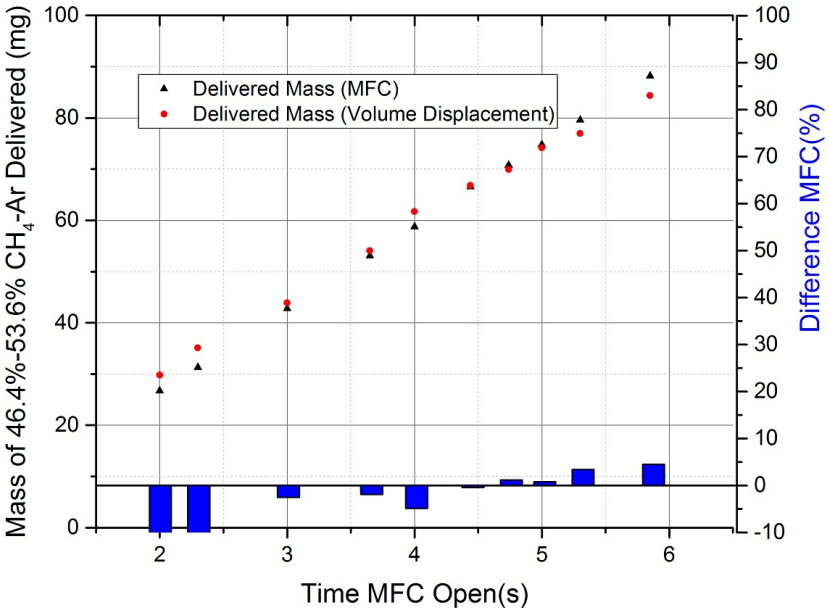

(b) Percentage error in 46.4%-53.6% $CH_4 - Ar$ mass delivered.

Figure 2.20. : 46.4%-53.6% $CH_4 - Ar$ Calibration curves and error comparison in terms of mass delivered between MFC and volume displacement method.

2.7.3 Batch Preparation

Two types of batches were prepared for delivery to the main combustion chamber. 30%-70% methane and hydrogen and 50%-50% methane and propane fuel. All the batches were made in the large 1000 cm^3 tank in the mixing station. To minimize the presence of air in the batches, air is first vacuumed from the tank using top station quick connect and then vacuumed using the vacuum pump. As more batches are made over time, the proportion of air in the batch decreases provided the gases in the mixture creates a homogeneous mixture after 2 hours of mixing time. For safety reasons, during batch preparation, caution should be exercised to avoid flammable mixture. The flammability limits of pure fuels and air at 1 atm are shown in Table 2.4.

Table 2.4. : Flammability limits of methane, propane and hydrogen.

Fuel	Flammability limit (%vol in air at 1 atm)
CH_4	5-15
C_3H_8	2.1-9.5
H_2	4-75

Flammability data referred from Zabetakis et al [60].

Composition of the created batches are presented in Table 2.5 and Table 2.6.

Table 2.5. : 30%-70% methane-hydrogen batches.

Batch no.	$\%CH_4$	$\%H_2$	Purpose
1	31.1	68.9	MFC calibration
2	29.0	71.0	MFC calibration
3	30.0	70.0	MFC calibration
			and hot-jet ignition test 38
4	29.5	70.5	Hot-jet ignition test 39-40
5	30.1	69.9	Hot-jet ignition test 41-44
6	30.7	69.3	Hot-jet ignition test 45-47
7	30.6	69.4	Hot-jet ignition test 48
8	30.4	69.6	Hot-jet ignition test 49-50
9	29.2	70.8	Hot-jet ignition test 51-57
10	31.2	68.8	Hot-jet ignition test 58-69

Table 2.6. : 50%-50% methane-propane batches.

Batch no.	$\%CH_4$	$\%C_3H_8$	Purpose
1	50.0	50.0	MFC calibration
2	50.0	50.0	MFC calibration
3	49.5	50.5	MFC calibration
4	49.6	50.4	MFC calibration
5	49.7	50.3	Hot-jet ignition test 389-408
6	49.6	50.4	Hot-jet ignition test 409-411
7	49.7	50.3	Hot-jet ignition test 422-431
			and flame propagation test 193-204
8	50.0	50.0	Flame propagation test 205-226
9	50.0	50.0	Flame propagation test 227

2.8 Instrumentation, Data Acquisition and Control System

Fig. 2.21 represents path of acquired voltage data from the sensors (PTs, thermocouples, MFC voltage output and magnetic pickup voltage) to flow back and report to the data acquisition system as well as the control system to send signals to operate various actuators (spark plug, MFC and the Phantom high speed camera).

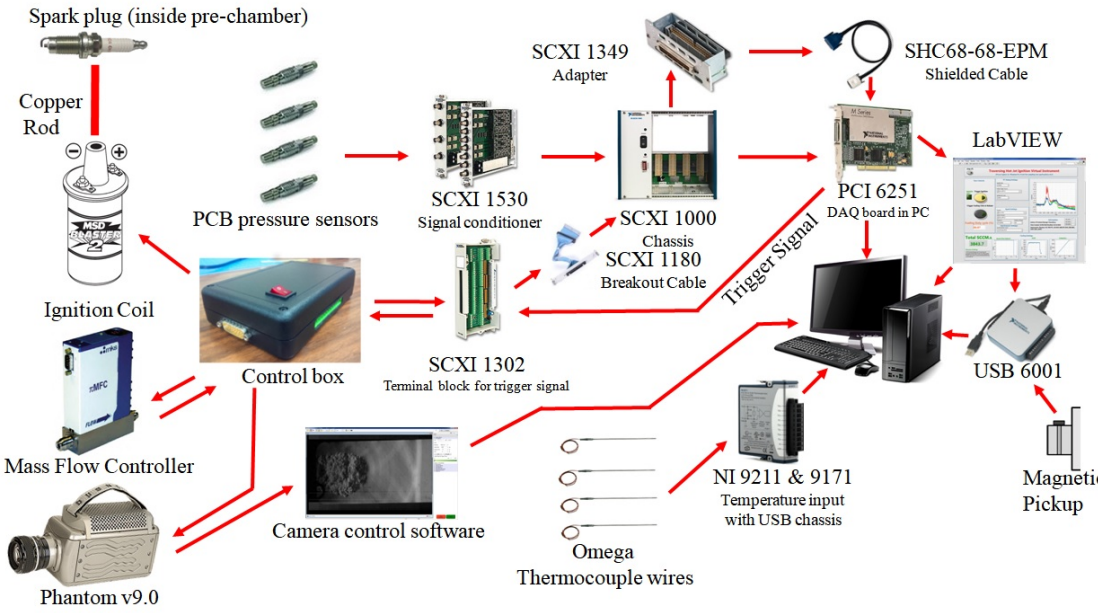

Figure 2.21. : Flow of data and signals through the instruments and the data acquisition system.

The pressure data acquired by the PCB pressure sensors are conditioned by a National Instruments (NI) pressure signal conditioner NI SCXI-1530 and sent back to the NI SCXI-1000 chassis. The chassis is connected to the data acquisition board NI PCI-6521 inside the CPRL-PC by means of an SCXI-1349 adapter and a SHC68-68-EPM shielded cable. A NI SCXI-1302 terminal breakout board is connected to the SCXI-1000 chassis by a SCXI 1180 breakout cable and is used to generate trigger signal (discussed later) to the spark plug through a in-house made control box and receive mass flow controller output voltage signal. The trigger signal to the spark plug also triggers the camera through trigger circuitry inside the control box. The Phantom

camera is also connected to the PC by an Ethernet connection and the proprietary Phantom camera control software (PCC) controls the triggering of the camera by waiting for the trigger signal from the spark plug to arrive. The magnetic pickup voltage is acquired by an independent DAQ, NI USB 6001. Similarly, thermocouple voltages are acquired by NI 9211 temperature input module in a NI 9171 USB chassis which also operates independently from the other DAQs.

2.8.1 Electrical System

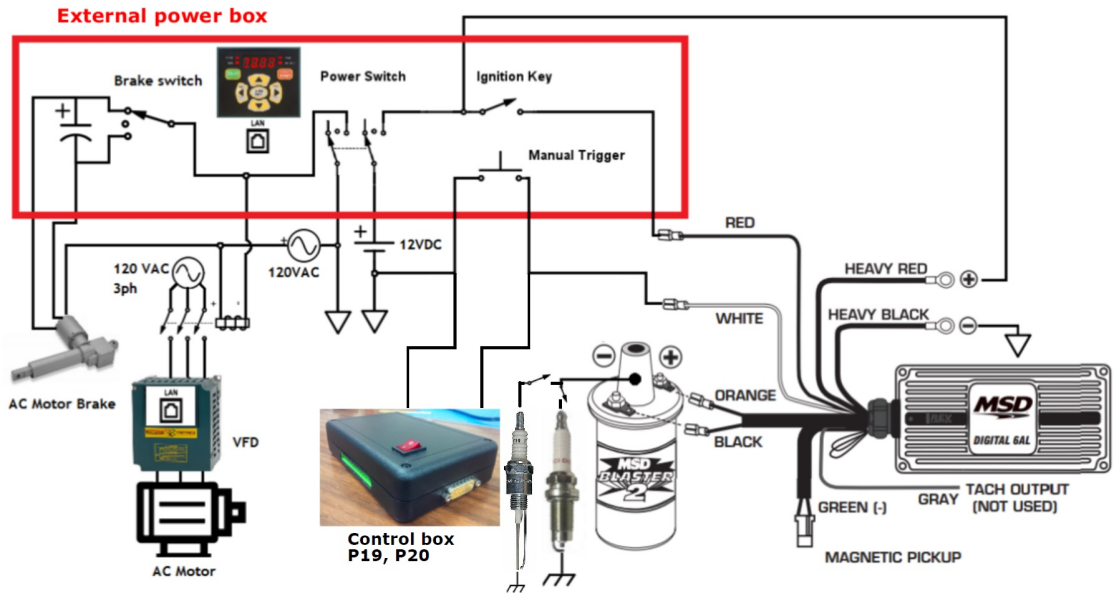

Figure 2.22. : Rig electrical system and internal circuitry of the remote control panel.

The electrical system of the rig is shown in Fig. 2.22. The brake is operated by an AC motor. The geared motor pushes and pulls the brake pad. The variable frequency drive (VFD) remote control panel is connected by LAN to the VFD control box next to the rig. The MSD 6AL ignition module is either closed by a push button switch or receives a trigger voltage pulse from the NI SCXI modules and outputs 500V which is passed through the ignition coil to generate 10KV and the subsequent spark

breakdown. Depending on the type of experiment the spark plug wire is connected to the different spark plugs.

2.8.2 Ignition and Control System

The ignition system triggers a spark plug (inside pre-chamber or inside main combustion chamber). The triggering signal is a 5V square pulse generated from the DAQ board PCI-6251 through NI SCXI-1000 chassis and the NI SCXI 1302 breakout board. The circuit is shown in Fig. 2.23. A pulse width modulated 5V square signal is divided to 1.2V signal through a voltage divider and sent to energize the push button switch and trigger the spark. The triggering circuit has a NPN-2222A common emitter transistor. The pulse width modulated signal is input to the transistor base and the camera's internal trigger circuit voltage is collected at the collector side which is 5V. The arrival of the pulse width modulated trigger signal raises the base current and lowers the camera's internal trigger voltage to 2V. This falling edge of the voltage triggers the camera. Since the analog programmable function input APFI0 is wired with the collector circuit, this sends a trigger signal back to the DAQ which then triggers the pressure transducers. For traversing hot-jet ignition experiments, the PFI12 port which is internally shorted with CTR0 is used to trigger the pressure transducers instead of APFI0. This is necessary since the noise in the magnetic pick up sensor voltage and the rotation of the copper rod connected to the spark plug creates excessive noise in the APFI0 line and triggers the PT randomly. For details on the effectiveness of a counter signal as trigger, readers are referred to spark timing test conducted by Kojok [38]. The timing of the spark for a traversing jet is discussed in section 3.1.

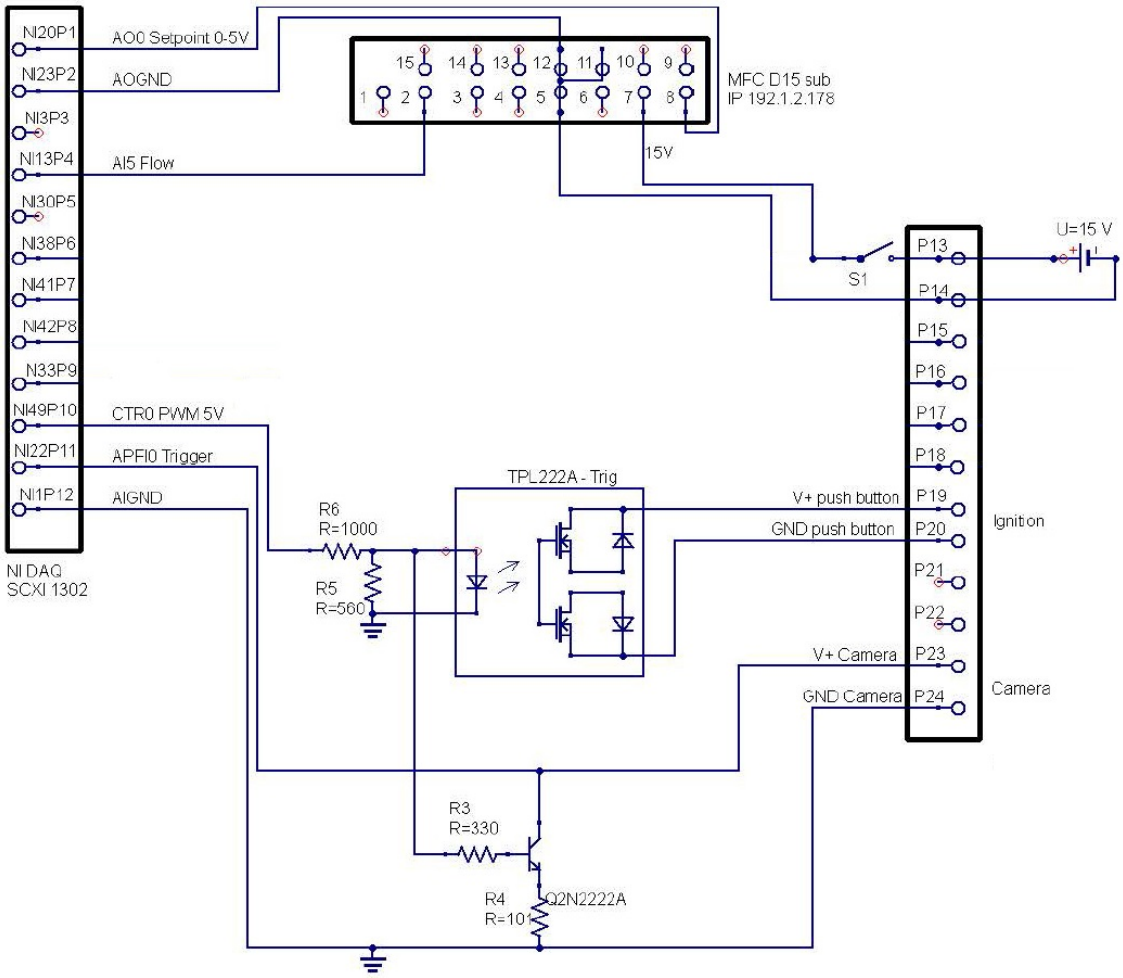

Figure 2.23. : MFC control, spark triggering and synchronization circuit.

A 15V adapter powers the MFC which connected by a DB15 plug. An analog 5V signal is sent to the MFC to control the mass flow. The MFC reports back a voltage corresponding to mass of fuel delivered through to port 13 of the breakout board which is read by the PCI-6251 board and then converted to a SCCM value. Internal fuel setting of the MFC can be varied by plugging the MFC to the PC with a network cable.

2.8.3 Magnetic Pickup Sensor

A magnetic pick up sensor assembly (Fig. 2.24, was originally installed as part of the development of the rig that could operate with MSD magnetic pick up input to the MSD 6AL ignition box [61]. The position of the magnet was not continuously tracked during the experiments. Therefore, this author installed a NI USB 6001 DAQ that reads the magnetic pickup voltage and use the LABVIEW code to trigger ignition when a threshold value of the magnetic pickup voltage is reached. The threshold voltage represents the moment when the magnet approaches the pickup sensor.

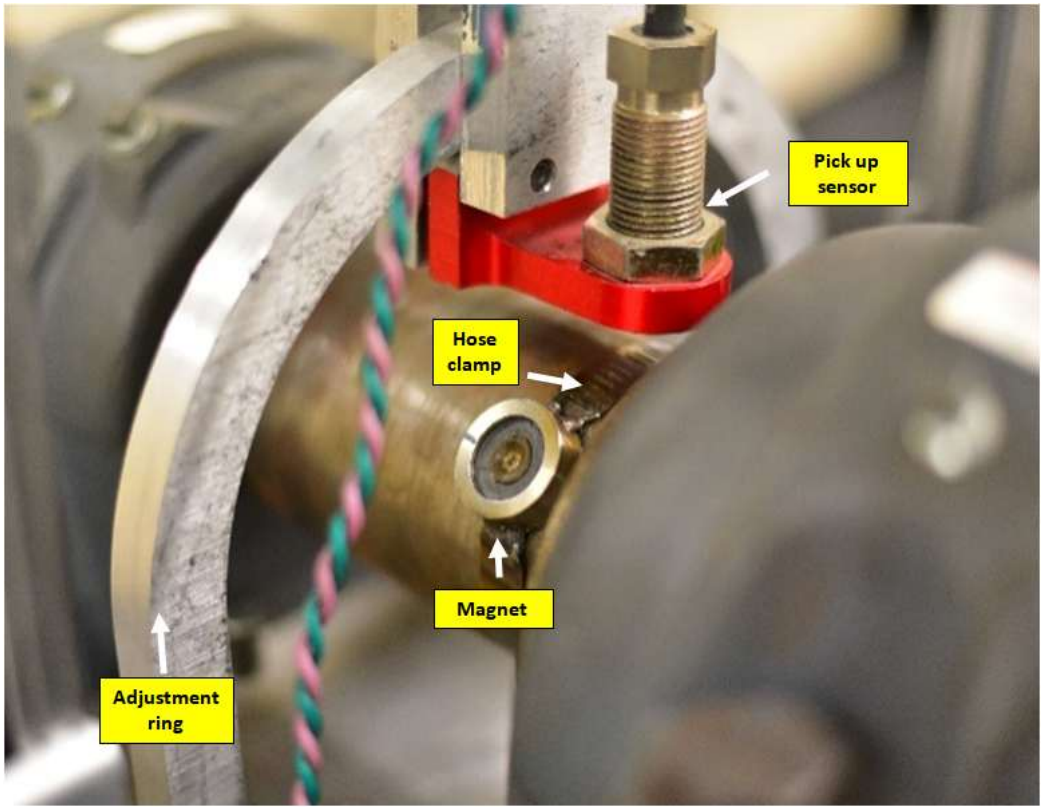

Figure 2.24. : Magnetic pick up sensor assembly

The sensor assembly consists of a adjustment ring on which the pick up sensor is mounted and can be adjusted, a magnet and a hose clamp that clamps the magnet to the pre-chamber shaft. In this investigation the pick-up sensor position was never

adjusted and all magnet position correspond to the vertical position (90°) of the pick up sensor.

2.8.4 Pressure Transducers

Four PCB Piezoelectric pressure transducers are used in this experimental investigation. The model, serial number and calibration are tabulated in Table 2.7. In order to identify the ignition moment, rupture moment and capture the pressure oscillation due to shock propagation and reflection, the pressure transducers must operate at a high sampling rate. This will also allow the pressure transducer to response to very fast rise time of the pressure change due to onset of ignition. From the rise in pressure trace, a passing shockwave can be detected and from two pressure transducer peaks, the velocity of the shock can be measured. In this experimental investigation shock speeds were measured in the range from 300 m/s to 450 m/s. The pressure transducers were operated at 250 KHz under all operating conditions for all stationary hot-jet, traversing hot-jet and flame propagation test cases. However, for flame propagation test cases, up to 0.8s of pressure data were collected whereas for hot-jet ignition experiment 0.2s of pressure data were collected for all cases. The slower flame velocity and occasional delayed spark ignition required a larger time-frame to capture the pressure rise due to ignition.

Table 2.7. : Pressure sensor calibration and installation information.

Pressure Transducer	Model	Serial no.	Conversion factor (mv/psig)	Installation
PT1	111A26	14462	9.906	Cylindrical cavity
PT2	113B26	28580	9.861	Infinite probe
PT3	113B26	28466	9.725	Flush
PT4	113B26	28465	9.992	Chamber cavity

The 4 pressure transducers are labeled in various figures as pre-chamber PT, near PT, far PT and end-wall PT. They refer to PT1, PT2, PT4 and PT3 respectively and are identified in Fig. 2.3. PT1 is installed in a cylindrical hole flushed into the pre-chamber on a mounting insert. Paik's design was implemented in installing PT2. PT4 was installed in a cavity similar to a Hemholtz resonator. PT3 is installed flushed at the end wall of the main combustion chamber [38]. For more information on the installation of the pressure transducers, readers are referred to [7].

The measurement of the pressure rise inside the pre-chamber when the pre-chamber is rotating was attempted to be measured by an on-board Arduino. Due to the small size of the Arduino it could be easily mounted on a rotating pre-chamber. The idea was that the pressure transducer PT1 will be replacing one of the fueling ports of the pre-chamber when this measurement was attempted. Any type of Arduino (Uno, Mega or Nano) could be used. PT1 (PCB 111A26) were directly connected by means of a coaxial cable with a BNC female jack to a Arduino analog input port as shown in Fig. 2.25. From MATLAB, the analog input signal (voltage data of the PCB) can be recorded. However, the very small voltage output of PCB transducer was not captured by the Arduino and the attempt was unsuccessful. A suitable signal conditioner may be used to amplify the signal.

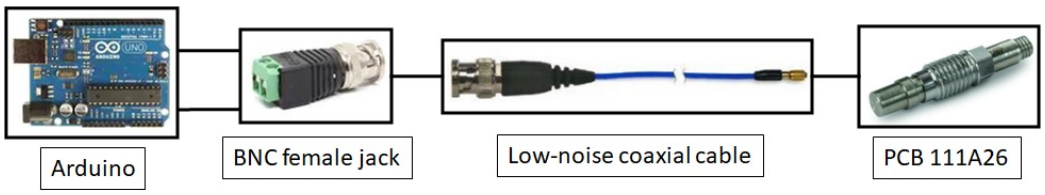

Figure 2.25. : Schematic diagram of the Arduino data acquisition system.

2.8.5 Schlieren Image Acquisition

Schlieren images are acquired using the existing optical arrangement consisting of two parabolic mirrors, a point light source, a knife edge and a Phantom V9 high speed

monochrome camera. A schematic of the optical arrangement is shown in Fig. 2.26. Schlieren images are used primarily for identifying ignition moment, start and end of traverse motion of the jet, vortices and eddies present in the flow field, shock-flame interaction and growth and propagation of the flame kernel when the main chamber fuel-air mixture is ignited by a spark plug.

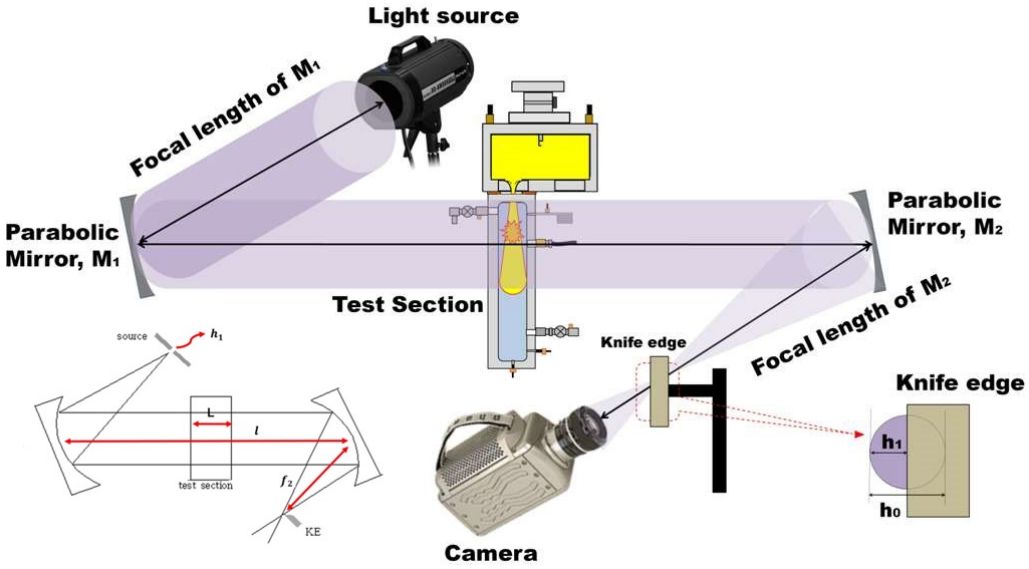

Figure 2.26. : Schematic diagram of the schlieren optical arrangement.

The entire optical window of the main combustion chamber cannot be viewed when recording schlieren images since the diameter of the mirror only covers approximately 7 inches of the chamber optical window. Therefore, each data point is at least repeated once when the schlieren is looking at rear side of the chamber, measuring 7 inches from the end-wall of the optical window to the left of the chamber. The front side of the chamber is typically viewed through the recorded schlieren images. To observe the flame propagation at the rear end of the chamber and to observe shock-flame interaction the schlieren system is focused on the rear end of the chamber.FPS, resolution and pixel per inch information are summarized in Table 2.8 for each schlieren setup used in this investigation.

For details on the construction and operating principle of schlieren photography, readers are referred to Paik [7] and Settles [62].

Table 2.8. : Schlieren setup information.

Setup	Resolution	Frames-per-second	Pixel-per-inch
F1	528×160	18691	72.00
F2	528×160	18691	70.40
F3	528×144	18691	77.48
F4	528×144	18691	75.64
F5	528×144	18691	75.51
F6	528×144	18691	75.51
F7	528×144	18691	75.51
F8	528×144	18691	73.50
F9	528×144	18691	73.50
F10	528×144	18691	71.59
F11	528×144	18691	71.17
F12	528×144	18691	74.52
R1	528×160	18691	73.40
R2	528×144	18691	72.28
R3	528×144	18691	71.72
R4	528×144	18691	71.86
R5	528×144	18691	73.54
R6	528×144	18691	73.54
R7	528×144	18691	74.19

2.8.6 High Speed Flame Luminosity Image Acquisition

Images were recorded at 960 frames per second using a SONY DSC-RX10 IV high speed digital camera. This camera was primarily used to observe the laminar

flame propagation. In the absence of a triggering port, the camera offers a digital end trigger option. When the digital end trigger is executed, the camera records the preceding 7s of video. The digital end trigger was used to record flame luminosity images that were visually time resolved with the recorded schlieren images. The first appearance of ignition kernel in the spark plug electrode gap is matched in the flame luminosity images and the schlieren images.

2.8.7 Motor and Drive Control System

A Baldor electric motor (Catalog no. M3218T, 5 HP, 60Hz) is driven by VS1MD25 variable frequency drive (VFD) controller. This AC motor drive controller modulates the speed of the motor by varying the frequency of input AC voltage from the 3-phrase supply line. The supply voltage, due to time-varying nature of AC supply creates a magnetic field inside the motor and rotates the rotor inside. The controller changes the frequency of AC current depending on the speed requirement. Therefore, to drive the pre-chamber at a certain speed, the frequency of the controller should be known. The motor is operated at different controller frequencies and a correlation has been developed to predict the pre-chamber speed from the VFD controller frequency. Figs 2.27, 2.28 and 2.29 refer to peak voltage, measured pre-chamber RPM, motor output RPM, and speed ratio against VFD frequency. In Fig. 2.28, motor speed refers to motor output shaft is speed reported by the controller. Pre-chamber rotation speed is measured by a tachometer. A linear fit with zero intercept (equation 2.4) was developed to predict the pre-chamber speed in RPM from the VFD frequency. The linear fit is given by

$$N = 39.11x \tag{2.4}$$

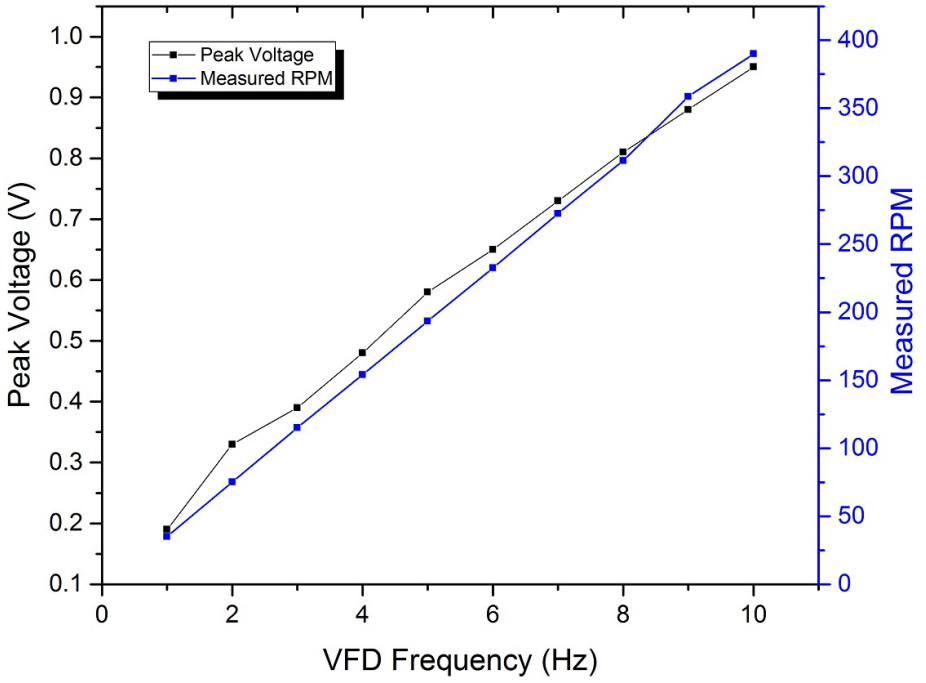

Figure 2.27. : Peak voltage and measured pre-chamber speed against VFD frequency.

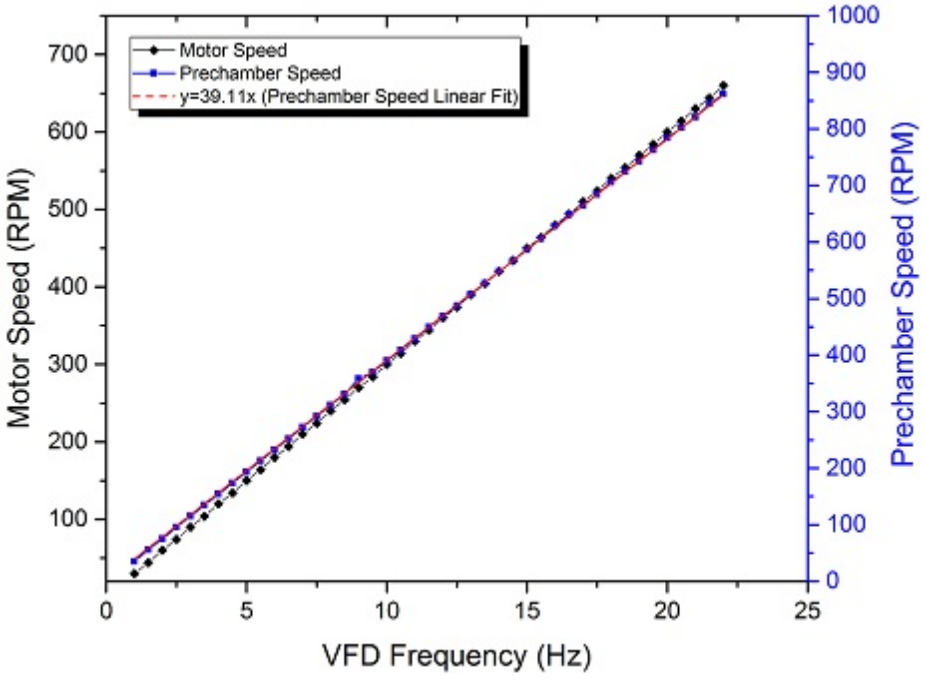

Figure 2.28. : Pre-chamber rotation speed against VFD frequency.

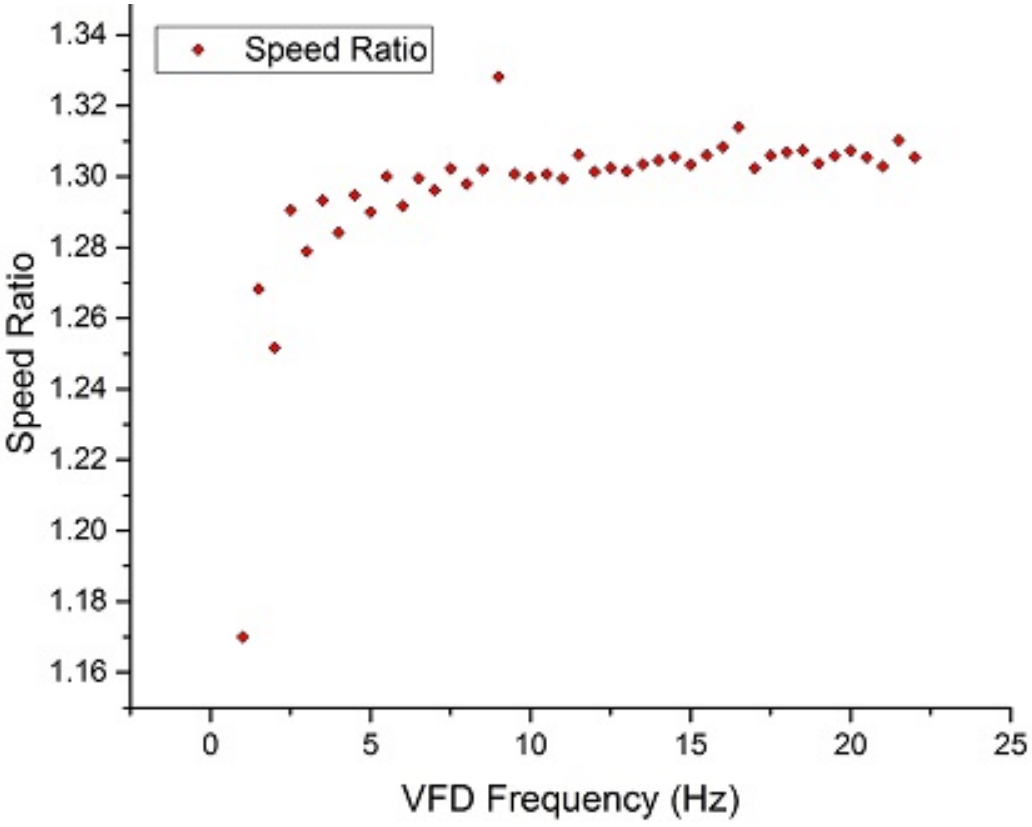

Figure 2.29. : Variation of drive speed ratio against VFD frequency.

2.8.8 Remote Control Panel

Fig. 2.30 depicts the remote control panel which is located in the room (ET109) next to the experimental facility (ET109A). It has an ignition key, push button ignition switch, two toggle switches (one for powering the control panel and the other for engaging/disengaging the brake), a red emergency stop button and the VFD control panel. The manual ignition switch is never used for any hot-jet ignition experiments except for testing the spark plug connection since the spark plug is triggered by a signal generated from the DAQ and control system.

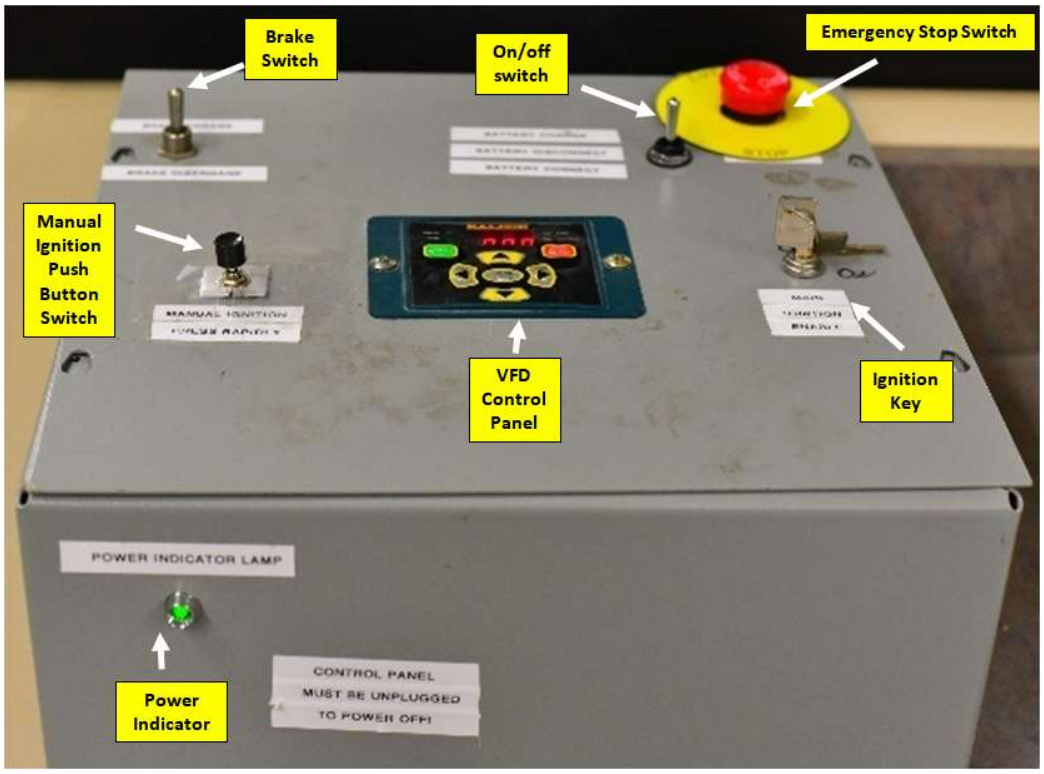

Figure 2.30. : Remote control panel.

Safety features includes a pre-chamber brake, emergency stop and an ignition key. The brake is engaged only for stationary hot-jet ignition experiments but not for other experiments. The brake is never used for bringing a rotating pre-chamber to stop since it produces excessive heat and repeated such operation would wear the brake pad quickly. The start button in the VFD control panel is used to start the rotation of the pre-chamber and the stop button in the VFD control panel stops the rotation of the pre-chamber. Depending on the rotating speed of the pre-chamber it take up to 20s for the rotation to be stopped. In case of emergency or gross blunders, the emergency stop button is pressed. This action immediately cuts all power to the electrical system and stops the rotation of the pre-chamber by engaging the break. The ignition key must be turned to ON position for performing any ignition experiments.

2.8.9 VFD Control Panel

The VFD control panel provides access to the setting of motor speed control settings. The operating frequency, motor power output, current, torque, acceleration and deceleration time etc. can be set in the panel. There are actually two panels, one located near the wall mounted control box near the motor and the other one is mounted on the remote control panel by a network cable. However, only one can be operated at any time. Plugging in the network cable results in activating the remote control mounted VFD control panel to be activated and the other one is disabled. The motor speed and consequently the pre-chamber RPM and the jet traverse time is varied by inputting different operating frequency of the motor in the control panel. The pre-chamber RPM is measured by an Extech tachometer. The VFD control panel can be used to read the motor speed, torque, current and other parameters in real time. The pre-chamber RPM was measured with main chamber being flushed against it to account for the speed loss. By measuring the pre-chamber RPM during its free rotation, a 2% variation was found. This 2% speed loss is expected when conducting traversing hot-jet ignition experiments. Any speed loss greater than this results in early rupture of the diaphragm during traversing hot-jet experiments.

To initiate pre-chamber rotation the green start switch in the VFD control panel is pressed. Within a few seconds, the pre-chamber accelerates up to the desired speed based on the set frequency. To stop the rotation of the pre-chamber, the red stop button the VFD is pressed and the pre-chamber decelerates to a complete stop withing a few seconds. The pre-chamber RPM measured at different VFD operating frequencies are shown in Fig. 2.28 and Table 3.1.

2.8.10 Heating System and Thermocouples

A Watlow heater (model CFMN720J12S) with a Novus N1020 temperature PID controller is mounted alongside the apparatus carrying the pre-chamber and main combustion chamber to deliver preheated air to the main combustion chamber. Two

K-type thermocouples made by Omega (model TJ250-CXIN) are mounted on the air inlet and outlet port to monitor inlet air and oulet air temperatures. A NI 9211 thermocouple input module in a NI 9171 USB chassis acquires temperature data. Details on the heating system and thermocouples can be found in [38]. For the current study the heater was not used.

2.8.11 LABVIEW VI

LABVIEW virtual instrument or VI's provide user interface to conduct ignition experiments. This author used different VI's for performing stationary hot-jet, traversing hot-jet and spark-ignited laminar flame propagation experiments. The user interfaces and block diagrams are shown in figures below.

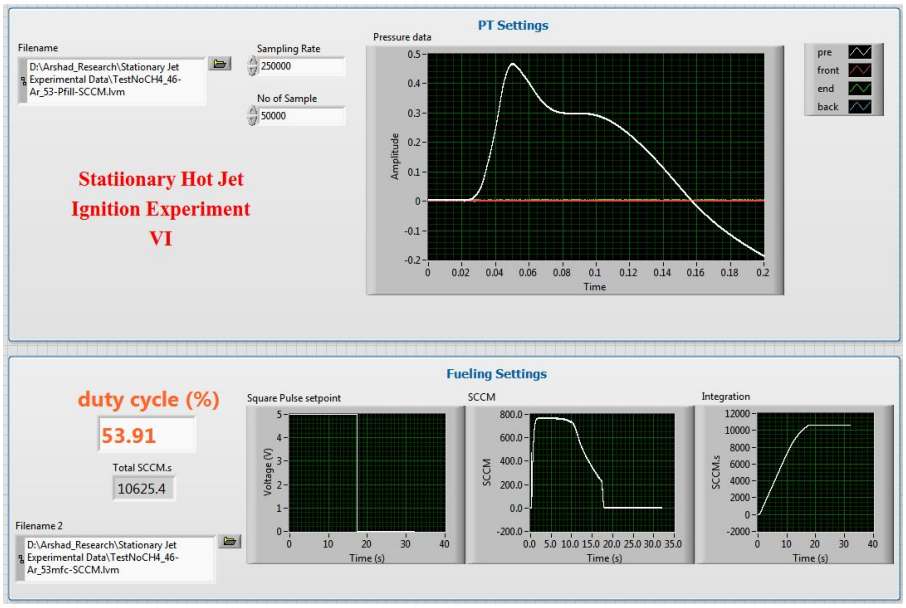

Figure 2.31. : Stationary hot-jet ignition VI.

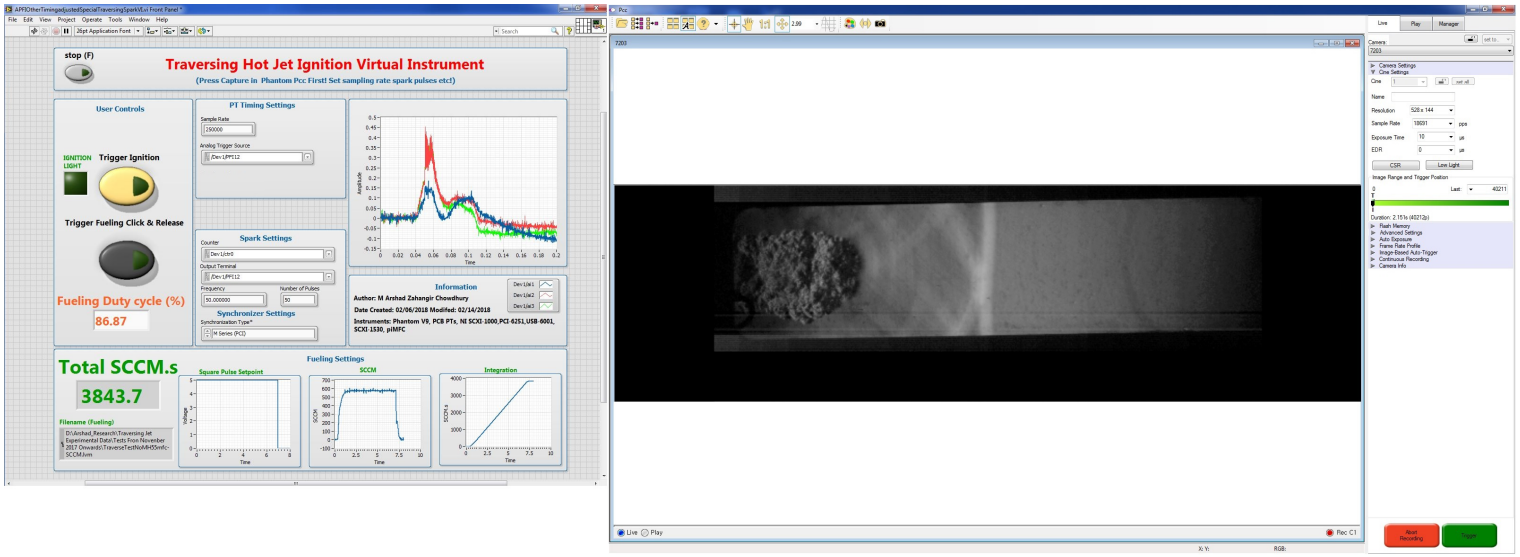

Figure 2.32. : Traversing hot-jet ignition VI and Phantom camera control software.

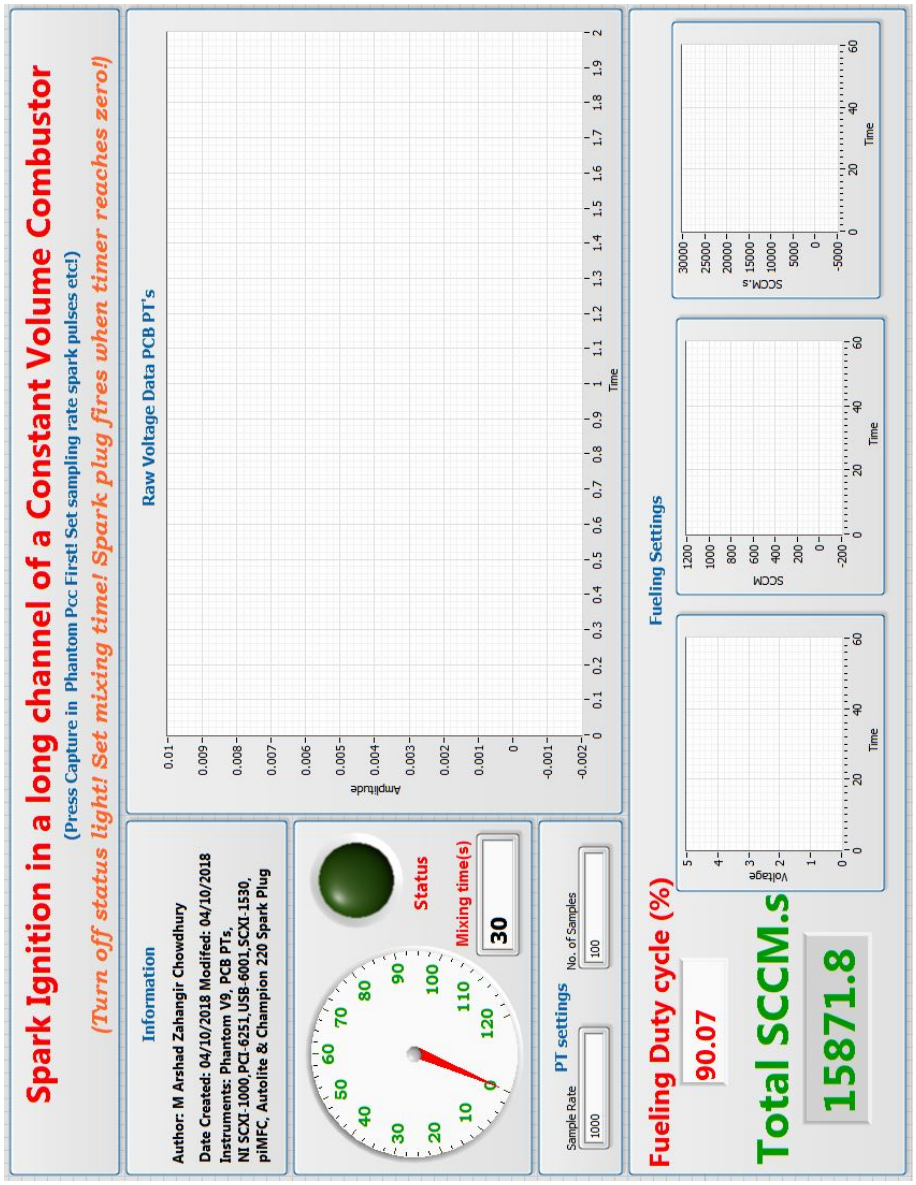

Figure 2.33. : Spark-ignited laminar flame propagation experiment VI.

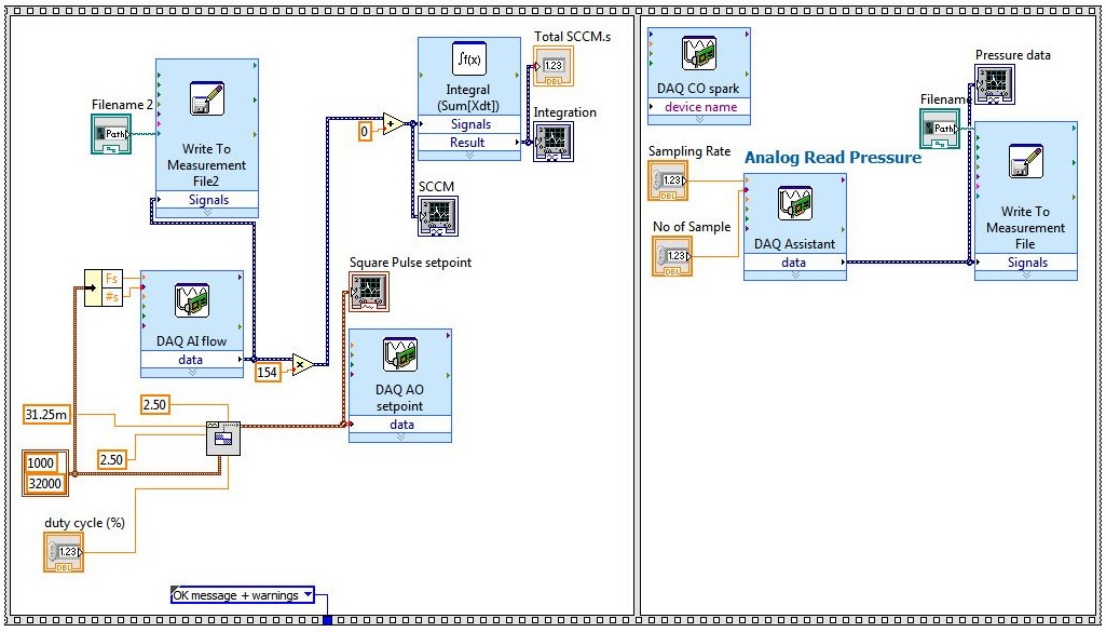

Figure 2.34. : LABVIEW block diagram of stationary hot jet ignition virtual instrument.

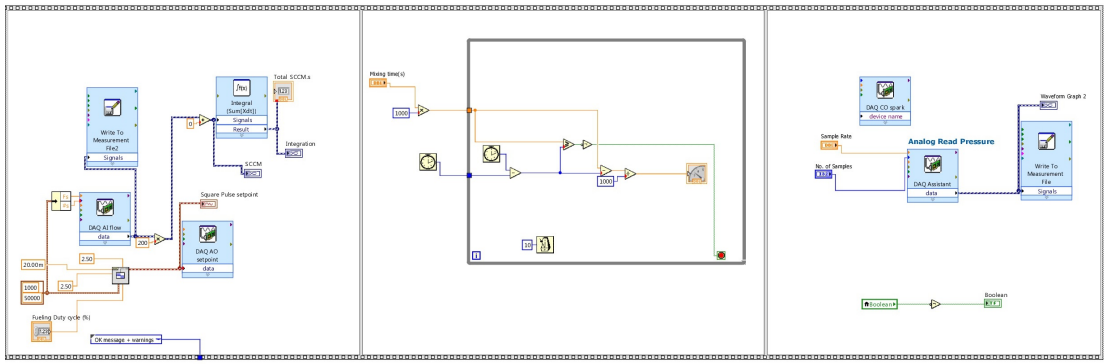

Figure 2.35. : LABVIEW block diagram of laminar flame propagation experiment virtual instrument.

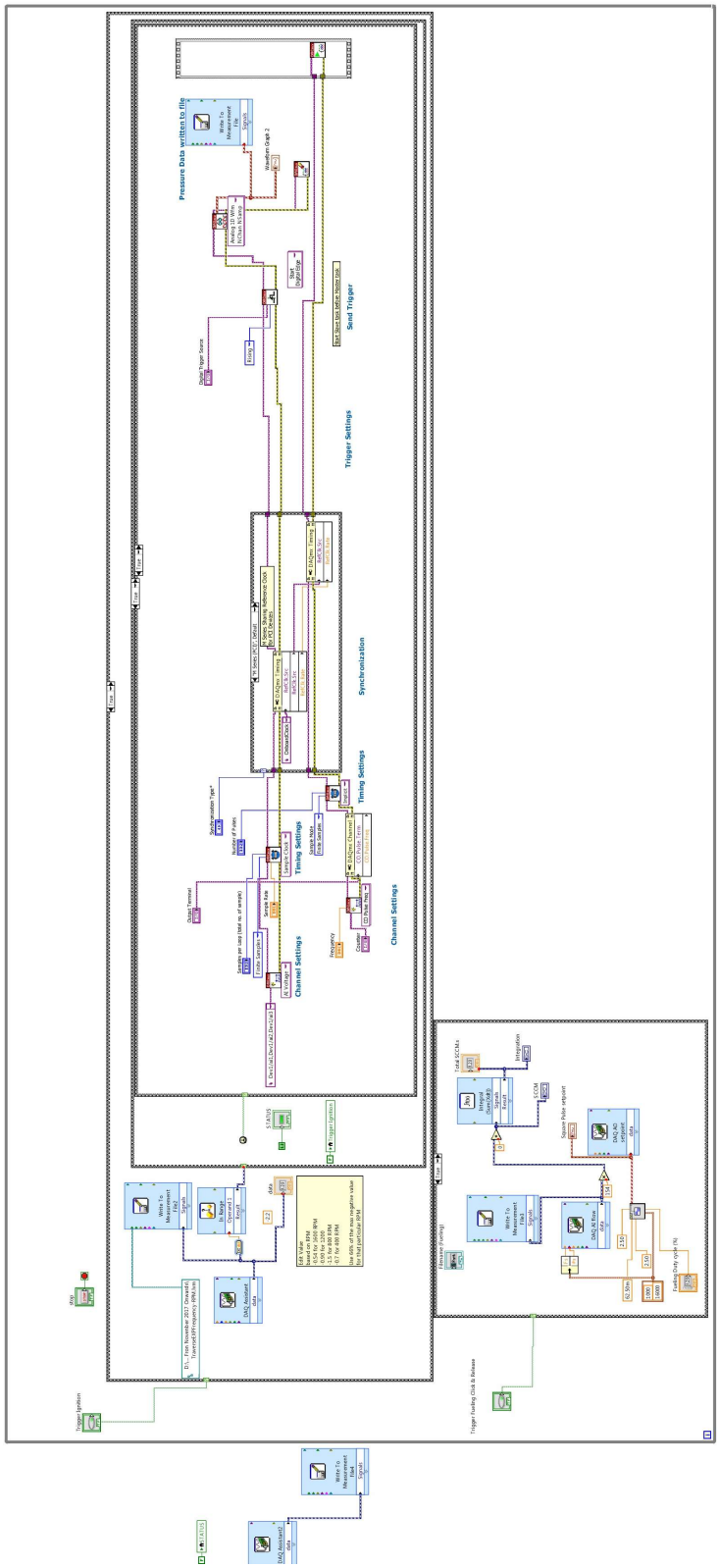

Figure 2.36. : LABVIEW block diagram of traversing hot jet ignition virtual instrument.

2.9 Experimental Procedure

All the experiments performed in the rig are broadly classified in the following three categories. Stationary hot-jet experiments refer to ignition experiments performed where the pre-chamber is kept stationary by applying the brake and the pre-chamber pressure transducer is mounted on a nozzle insert. Traversing hot-jet experiments refer to ignition experiments where the pre-chamber is rotated at different speeds in order to issue chemically reactive hot-jets with different traverse times. The pre-chamber pressure transducer insert is replaced by a solid insert for these experiments. Laminar flame propagation experiments refer to ignition performed in the main combustion chamber with the help of a spark plug instead of a hot-jet issued from the pre-chamber. Before proceeding with any experiment the high speed schlieren image acquisition system is set up first. The following preparatory steps are than carried out.

2.9.1 Preparatory Steps

1. All fuel lines and chambers are purged with compressed air at 60 psig or higher.
2. The large tank in mixing station is fueled with the desired fuel.
3. One-by-one, all fuel valves are opened for purging all fuel lines with fuel. The mass flow controller is used to purge the fuel delivery line immediately before the main chamber check valve.
4. Main combustion chamber and pre-chamber are purged again with compressed air.
5. Once 1-4 are done, a number of experiments can be performed as long as the large mixing chamber contains fuel.
6. It is recommended that once in a month all lines in the mixing station are leak tested.

7. NI SCXI-1000 chassis, SCXI-1530, mass flow controller, Phantom Camera are turned on. A few seconds must be passed to initialize these devices. The heater and NI 9211 module are turned off unless preheated air is need for an experiment.

8. NI MAX software is launched in PC and is used to reset, self calibrate and test all NI devices.

To conduct any type of ignition experiment the following steps are take which are described in the following subsections.

2.9.2 Traversing Hot-Jet Experiments

The steps for traversing hot-jet ignition experiments are described below.

1. Pre-chamber and main combustion chamber are purged with 60 psig compressed air.

2. The magnet of the magnetic pickup coil is set at the desired degree location marked on the pre-chamber. The magnet position for a particular pre-chamber rotation speed is tabulated in Table 3.1.

3. An aluminum diaphragm is scored and inserted in the nozzle assembly.

4. The nozzle insert is mounted in pre-chamber cavity. The pre-chamber is positioned such that the 70^o degree mark is aligned with an imaginary straight line along the shaft's vertical axis.

5. The two chambers are coupled together using the XY table. The nozzle exit should be at the center of the main chamber entrance.

6. The chambers are clamped with flexible rope. The pre-chamber is hand rotated to make sure clamp is not too tight. The nozzle exit is positioned at the center of the main chamber entrance again.

7. The pre-chamber is fueled either from mixing station manual fueling line or the top station fueling line (directly from fuel cylinder). For the later path, the cylinder valve and pressure regulator valve must be closed and the regulator outlet fuel delivery line must be completely detached once pre-chamber fueling is done.

8. Pre-chamber fueling line and quick connect is disconnected and moved away from the immediate vicinity of the pre-chamber.

9. The pre-chamber and its surroundings are carefully examined to make sure nothing is blocking the pre-chamber rotation path. The following checks are performed. Check for engaged brake, any pressure transducer lines (pre-chamber or main chamber).

10. The VFD is turned on by plugging its power cable and the control panel in the next room is turned on. This gives the VFD enough time to warm up. Remote access to the DAQ computer from a laptop or a PC is activated. The ignition key is turned to ON position.

11. The capture button on PCC software is pressed. The experiment should be complete in a minute before it will reset.

12. Frequency of the VFD controller is set and start button is pressed to initiate pre-chamber rotation. The pre-chamber takes 2-4 seconds to reach desired speed. The pre-chamber rotation speed is measured with a tachometer (Extech, model 461920) to ensure adequate clamping force is applied. The speed loss of the pre-chamber due to clamp should not be more than 2% of the pre-chamber RPM.

13. To initiate fueling from LABVIEW the estimated duty cycle necessary needs to be entered.

14. From live schlieren view in PCC and auto updated LABVIEW plots fueling is monitored.

15. Spark trigger is pressed in the LABVIEW VI as soon as fueling is over (indicated by registering an SCCM value in the VI). Based on the continuous magnet position data, spark will be triggered when the position value reaches voltage threshold (say, lower than -1.5V for 800 RPM). The triggered spark would ignite the pre-chamber combustible fuel-air mixture, build up pressure and rupture the diaphragm once the pressure exceeds the yield point of the diaphragm. Combustion products will exit the pre-chamber and traverse across the main chamber entrance. Once inside the main chamber, the traversing jet mixes with the fuel-air mixture inside the main chamber and ignites it.

16. The LABVIEW VI is stopped. The ignition key is turned to OFF position and the stop button is pressed in the VFD controller to stop rotation of the pre-chamber.

17. The flexible rope clamp is released to decouple the two chambers.The nozzle insert is removed from the pre-chamber and the combustion products and water vapor are purged with compressed air from both chambers.

18. This concludes a single experiment. All data and video files are saved in PC for further analysis.

19. The control panel, VFD, MFC, Phantom Camera and NI DAQs are turned off if no further experiment is to be performed.

2.9.3 Stationary Hot-Jet Experiments

Paik and Kojok [7, 38] have described the stationary hot-jet ignition experiment process in detail, hence, it is not repeated here. Without rotating the pre-chamber, all the other steps from a traversing hot-jet ignition experiment may be followed to

conduct a stationary hot-jet ignition experiment. The pre-chamber pressure transducer (PT1) must be installed and the chambers must be sealed using a conventional seal plate with o-rings on sealing surfaces on both sides.

2.9.4 Laminar Flame Propagation Experiments

Before proceeding with laminar flame propagation experiments, the seal plate designed for mounting a spark plate is installed in front of the main combustion chamber. Moreover, the spark plug wire is removed from the pre-chamber spark plug and is rerouted to the main chamber spark plug. To perform an experiment the following procedure was followed:

1. The chamber is thoroughly purged by opening the air valves and connecting the compressed air line heater air inlet.
2. Both air valves are shut off.
3. The data acquisition system, mass flow controller, Phantom high speed camera and flame propagation camera is turned on. The control box outside the room is also turned on and the ignition key is turned to ON position.
4. The chamber is fueled using the mass flow controller from Labview VI.
5. A delay time is set in the VI to allow the fuel-air mixture inside the main chamber to mix.
6. The spark plug is fired by the VI and flame propagation is observed.
7. The air valves are opened and the chamber is purged with compressed air.

2.9.5 Design of Experiments

Experiments were designed to understand the effects of equivalence ratio, traverse time and pressure on hot-jet ignition delay. To obtain validation quality data over

a wide range of operating conditions, factorial based design of experiment were implemented. Unless otherwise specified, the pre-chamber is filled with a $50\% - 50\%$ $CH_4 - H_2$ blend at equivalence ratio of 1.1 and all test points are repeated at least 3 times.

Traversing Hot-Jet Ignition Experiments

Traverse time, equivalence ratio of the fuel air mixture were varied for traversing hot-jet ignition experiments for three different fuels. Table 2.9 lists these values.

Table 2.9. : Traversing hot-jet ignition experiment parameters.

Fuel	Traverse Time(ms)	ϕ
CH_4		
$CH_4 - H_2$ Blend	5.6, 8.4, 16.9	0.4,0.7,1,1.3
$(50\% - 50\%)$		
$CH\_Ar(46.4\% - 53.6\%)$		

Stationary hot-jet ignition experiments

Primarily the effect of equivalence ratio and fuel reactivity on ignition delay at atmospheric pressure were studied in detail for stationary hot-jet ignition experiments. Table 2.10 lists these values.

Table 2.10. : Stationary hot-jet ignition experiment parameters.

Fuel	ϕ
CH_4	0.4-1.3
$CH_4 - H_2$ $(50\% - 50\%)$	0.4-1.5
$CH_4 - C_3H_8$ $(50\% - 50\%)$	0.4-1.3
$CH_4 - Ar$ $(46.4\% - 53.6\%)$	0.3-1.3
C_3H_8	0.4-1.3
$CH_4 - H_2$ $(30\% - 70\%)$	0.4-1.3

ϕ is increased in steps of 0.1 for all fuels except $CH_4 - H_2$ $(30\% - 70\%)$

Unless specified otherwise, for $CH_4 - Ar$ blend fuel, Ar is considered in calculation of ϕ.

For $CH_4 - H_2$ $(30\% - 70\%)$ blend fuel only 10 cases were conducted.

Laminar Flame Propagation experiments

Table 2.11 lists experimental parameters for laminar flame propagation experiments. Since mixing of the fuel-air in the main combustion chamber was of interest a mixing time parameter was added along with equivalence ratio of six different fuel-air mixtures.

Table 2.11. : Laminar flame propagation experiment parameters.

Fuel	MW_{fuel}	ϕ	Mixing time, τ_{mix}(s)
H_2	2.01	0.4-1	3,13,33
$CH_4 - H_2$ $(50\% - 50\%)$	9.03	0.4-1.3	0,10,30
CH_4	16.04	0.4-1.3	0,10,30
$CH_4 - C_3H_8$ $(50\% - 50\%)$	30.07	0.4-1.3	0,10,30
$CH_4 - Ar$ $(46.4\% - 53.6\%)$	28.85	0.4-1.3	0,10,30,60
C_3H_8	44.10	0.4-1.3	0,10,30

ϕ is increased in steps of 0.3

3. PRELIMINARY AND SUPPLEMENTAL EXPERIMENTS

This chapter reports essential preliminary experiments to determine timing of the spark such that the traverse motion of the jet can take place from chamber entrance top edge to bottom edge. The chapter also includes discussion on vortex rings observed from some of the hot-jet ignition experiments. Supplemental hot-jet ignition experiments are also discussed. The estimated ignition delay of these cases are presented here.

3.1 Calibration of Spark Trigger for Traversing Jet

Preliminary experiments are conducted by firing the pre-chamber at different pre-chamber rotating speeds and position of the magnet. The purpose of these experiments were to estimate the position of the magnet on the pre-chamber shaft such that the triggering of the spark plug inside the pre-chamber can be performed precisely and the diaphragm would rupture and the jet traverse the chamber entrance from its top edge to the bottom edge.

3.1.1 Estimation of Rupture Moment

In order to time the spark inside the pre-chamber to occur at a moment that would result in the jet being issued at the top edge of the seal plate or chamber entrance, the rupture time of the aluminum diaphragm separating both chambers must be known. The rupture time is defined as the moment of spark trigger to actual rupture of the diaphragm. From experiments of Kojok [38], for a 50%-50% methane hydrogen blend fuel mixed with air at equivalence ratio 1.1, the average rupture time was estimated. The rupture moment was estimated by using two pressure transducers. The diaphragm rupture shock registers pressure rise in the transducers and by

knowing the distance between the pressure transducers the rupture moment can be estimated. The average rupture time for methane-hydrogen-air mixtures at 1.1 equivalence ratio and atmospheric pressure was estimated to be 41.6 ms. Fig. 3.1 shows a scatter plot of the rupture time and rupture pressure under various pre-chamber initial filling pressures.

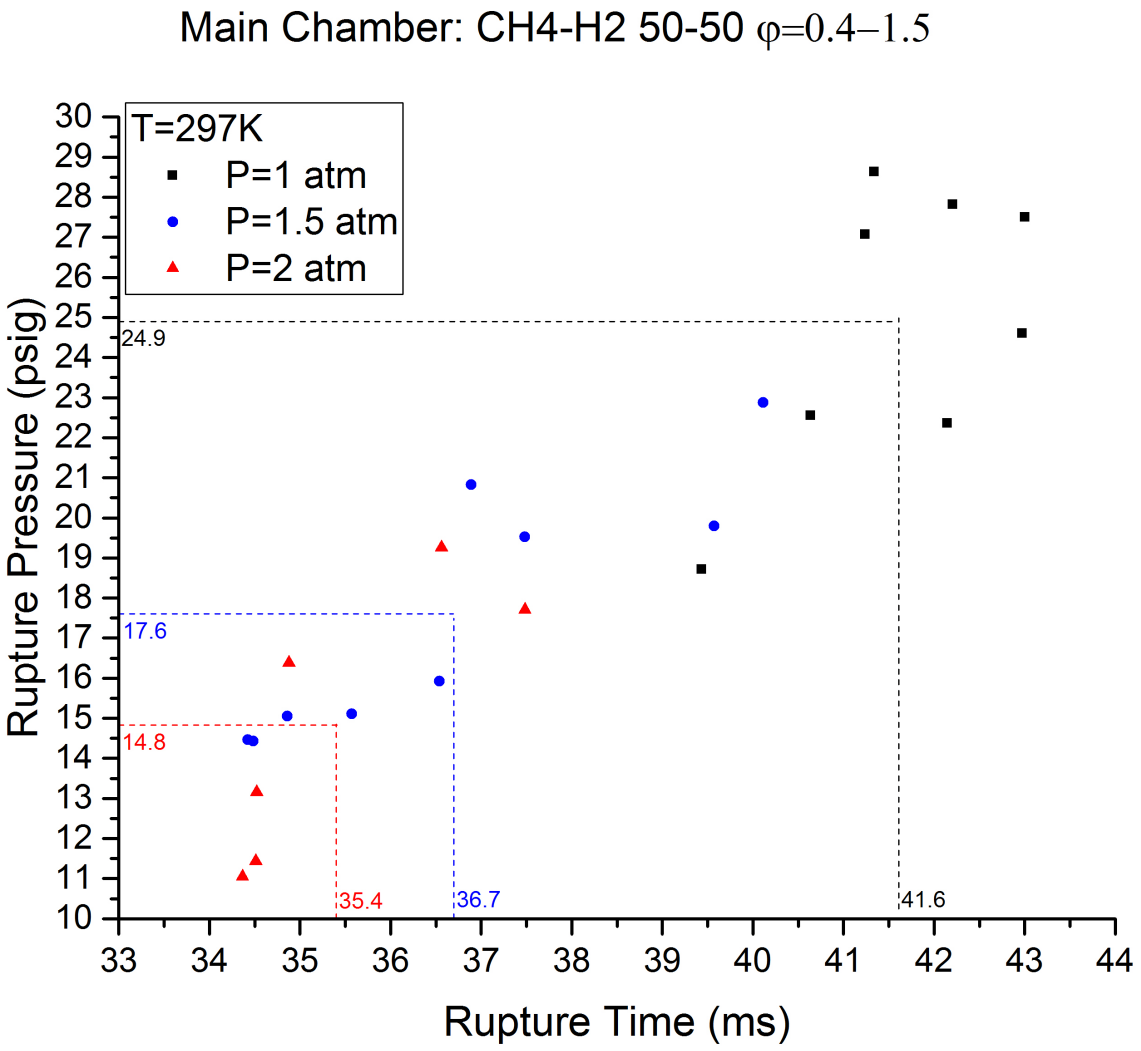

Figure 3.1. : Estimation of average rupture time of the diaphragm from Kojok's [38] tests.

Since PT1 measures differential pressure, the absolute rupture pressure is equal to the sum measured pressure data from PT1 and the absolute pre-chamber initial

filling pressure. At higher initial filling pressure, the diaphragm is already stressed and only needs slight more stress to be developed compared to a lower initial filling pressure to reach the yield stress point of the diaphragm material. Therefore, the rupture pressure decreases with an increase in pre-chamber initial filling pressure.

3.1.2 Spark Timing and Magnet Position

As shown in Fig. 3.2, the spark plug is triggered during pre-chamber rotation at an angular position before the nozzle exit reaches the top edge of the chamber entrance.

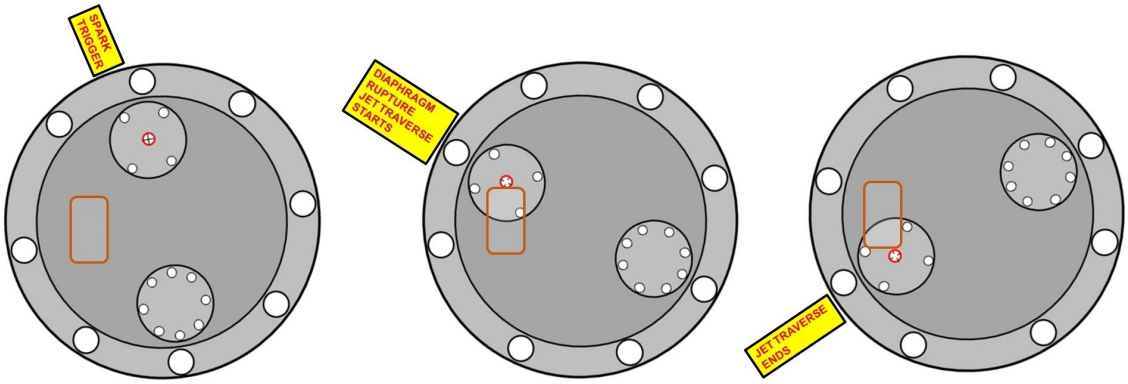

Figure 3.2. : Schematic representation of triggering of spark (left), rupture moment and onset (center) conclusion of jet traverse motion (right).

Fig. 3.3 shows the trajectory of the nozzle during the rotation of the pre-chamber. The nozzle exit must travel this distance withing the rupture moment to issue a traversing jet. The pre-chamber circumference is marked with degree positions with the nozzle center being marked 0 degree and the center of the nozzle insert is at 180 degrees apart with increment in angle values in the clockwise direction. The angular distance between the magnetic pickup and the position where the diaphragm ruptures is approximately 70 degrees. Depending on the pre-chamber RPM, the rupture position is reached at different moment. Therefore, the following equation

was used to take into account the pre-chamber RPM and calculate the initial magnet position.

$$\theta = 360^o - (\theta_{rup} - \theta_{rp}) \tag{3.1}$$

where,

Angular position of magnet (degrees) = θ

Rupture angle = θ_{rup} = Rupture time × Nozzle travel per unit time

Angular distance between magnetic pickup and rupture position = $\theta_{rp} = 70^o$

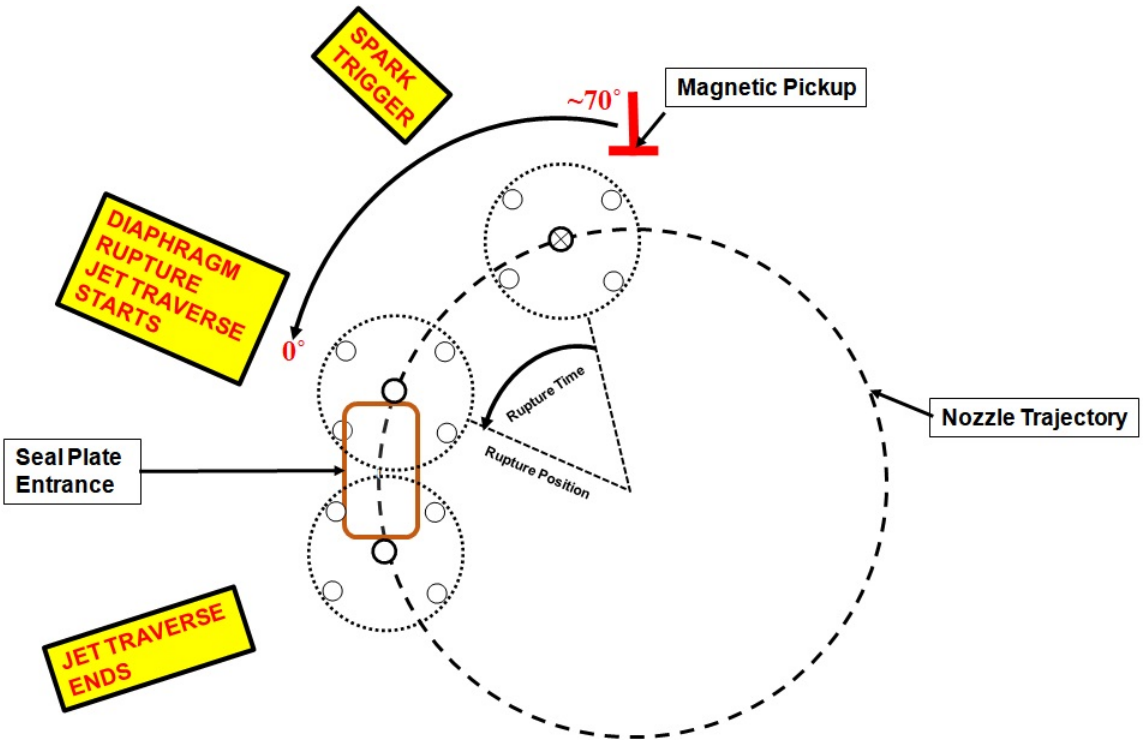

Figure 3.3. : Schematic representation of nozzle trajectory during pre-chamber rotation.

Different pre-chamber rotation speeds were achieved by using the variable frequency drive controller. An empirical correlation (equation 3.2) was formulated by

measuring the pre-chamber rotation speeds for different VFD frequencies. The correlation relates the the pre-chamber rotation speed with the VFD frequency.

$$N = 39.11x \tag{3.2}$$

The pre-chamber speed is reduced when both chambers are coupled together. The reduced pre-chamber speed is measured using the tachometer and tabulated for all experiments. This RPM value is used to calculate initial magnet position from equation 3.2. The adjusted magnet position values for different pre-chamber speeds are tabulated in Table 3.1.

Table 3.1. : Position of magnet on rotating shaft for traversing jet experiments.

Nominal Pre-chamber RPM	VFD frequency (Hz)	Pre-chamber RPM *(eqn. 3.2)*	Pre-chamber RPM *(measured)*	Traverse time (ms)	Magnet position degrees	Threshold Voltage (V)
400	10.45	408.7	401.9	16.9	295	-0.7
800	20.85	815.4	802.1	8.4	147	-1.5
1200	30.87	1207.3	1199	5.6	118	-2.2
1600	41.07	1605.5	1600	4.2	264	-0.54

3.1.3 Jet Alignment

A few pre-chamber ignition tests are conducted and the schlieren images and color flame luminosity images are observed. If the jet emerges let or there is early rupture the magnet position is updated. The iteration is continued until the jet consistently enters the chamber entrance at the top edge. Fig. 3.4(a) shows a traversing hot-jet experiment where the main chamber is not in contact with the pre-chamber and the jet is issued approximately an inch above the top edge of the chamber entrance. Therefore, the magnet position is decreased (the magnet is moved towards the nozzle) and tests were conducted till the jet entered the chamber exactly at the top edge

of the chamber entrance. An example of an aligned jet is shown in Fig. 3.4(b). If the jet is issued earlier than the rupture shock is weak and cannot be seen in the schlieren images and the shock speed cannot be estimated from the pressure transducers. Therefore, anytime the pre-chamber RPM is adjusted the traversing hot-jet is aligned by performing a few additional tests.

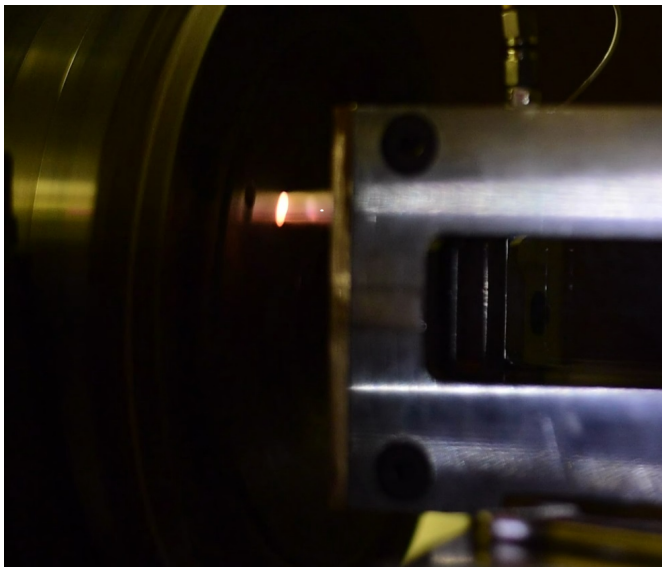

(a) Early rupture of diaphragm and issuance of traversing hot-jet from test 236. The main chamber is decoupled from the pre-chamber to make the traversing jet visible during early rupture.

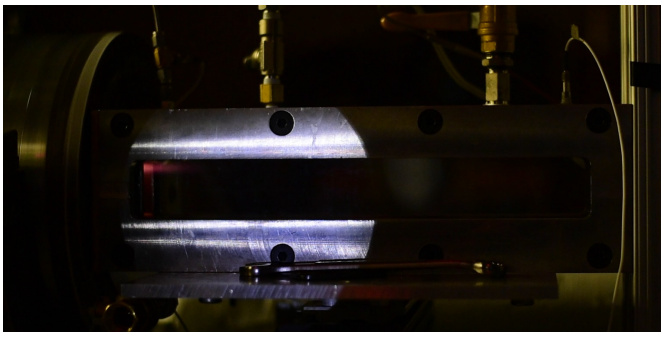

(b) Aligned jet issued at top edge of the chamber entrance from test 256.

Figure 3.4. : Traversing hot-jet alignment.

3.1.4 Spark Trigger from LABVIEW

The spark trigger is issued from LABVIEW VI once the magnetic pickup voltage output exceeds a set threshold voltage. An example of the magnetic pickup voltage output trace is given in Fig. 3.5 with the spark trigger point marked. The threshold voltage is typically chosen as half the peak voltage output of the magnetic pickup sensor. If the issued jet is not aligned for a particular threshold voltage value, the threshold voltage value is varied until the issued jet is aligned. The process of jet alignment is the same as described in the previous subsection.

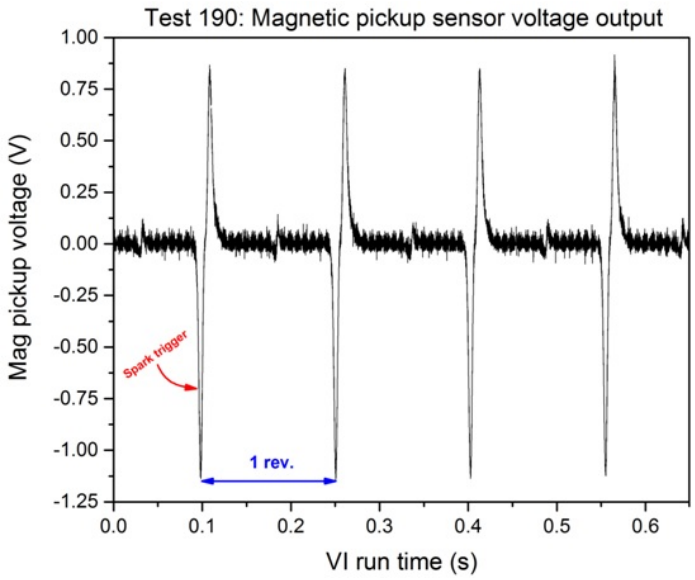

Figure 3.5. : Magnetic pickup voltage output from test 190.

3.2 Vortex Rings

This section reports the observed vortex ring in some hot-jet ignition experiments. These experiments were not performed specifically to generate the vortex rings. The schlieren images of some of the hot-jet ignition experiments demonstrated these rings. This section reports, summarizes and discusses these experiments.

Vortex rings preceding the jet itself were observed in the schlieren images in substantial number of test cases. The rings were seen mostly when the pre-chamber was stationary. Vortex rings were observed in only four traversing jet test cases and thirty-six stationary hot-jet ignition test cases. Test cases in which a vortex ring were observed are tabulated in Table 3.2 along with experimental conditions in main chamber. Unless specified otherwise, the pre-chamber is filled with 50%-50% methane-hydrogen and air mixture at 1.1 equivalence ratio. From Tables 3.2 and 3.3, it is seen that the ring is generated for a wide range of fuels and fuel-air equivalence ratio. Trapped fuel-air mixture residing between the diaphragm and nozzle outlet was thought to be pushed out during rupture of the diaphragm and form the vortex ring. However, tests were conducted without any fuel in the main chamber and firing the pre-chamber with diaphragms scored in '+' pattern and no vortex rings were produced. When tests were conducted with diaphragm's scored in the form of '—' pattern which is essentially half-scored, vortex rings were consistently observed. Therefore, it can be inferred that the vortex ring is a consequence of gradual diaphragm rupture, especially, if the strokes on the diaphragm during scoring is not same then the diaphragm, when ruptured, opens gradually, mimicking the rupture of a half-scored diaphragm. This sort of rupture consequently, expels a tiny amount of unburned fuel-air mixture from the pre-chamber during the pressure rise inside the pre-chamber due to spark ignition. However, once the pressure inside the pre-chamber exceeds beyond the yield point of both scoring lines of the diaphragm, the jet is issued and the vortex head of the jet pushes the unburned fuel-air mixture expelled previously and residing in the trapped space between the diaphragm and nozzle exit into the chamber thus forming the vortex ring. Therefore, appearance of the vortex ring can be an indicator of uneven scoring of the diaphragm. For a traversing jet, since the traversing motion starts from the top of the main chamber entrance, the vortex ring, provided it is generated, would strike the chamber or inner top surface and expand. Moreover, the rapid mixing induced by the traversing jet and accompanying vortices make it very difficult to observe the vortex ring in the schlieren images.

Table 3.2. : Summary of test cases with observed vortex rings.

Experiment no.	Main chamber fuel and equiv. ratio, Φ	Experiment no.	Main chamber fuel and equiv. ratio, Φ
'+' Scoring			
72	$CH_4 - H_2$ (50%-50%), 0.5	229	CH_4, 1.3
80	$CH_4 - H_2$ (50%-50%), 1.3	230	CH_4, 1.2
83	$CH_4 - H_2$ (50%-50%), 0.6	233	CH_4, 1.0
84	$CH_4 - H_2$ (50%-50%), 0.6	234	CH_4, 0.9
85	$CH_4 - H_2$ (50%-50%), 0.6	331^T	CH_4, 1.0
87	$CH_4 - H_2$ (50%-50%), 1.2	333^T	CH_4, 1.0
88	$CH_4 - H_2$ (50%-50%), 1.2	344^T	Air only, 0
89	$CH_4 - H_2$ (50%-50%), 1.1	355	CH_4, 1.0
120^S	$CH_4 - H_2$ (50%-50%), 1.2	372	C_3H_4,1.0
124^S	$CH_4 - H_2$ (50%-50%), 0.9	383	C_3H_4,1.0
155^T	$CH_4 - H_2$ (50%-50%), 1.0	397	$CH_4 - C_3H_8$ (50%-50%), 0.4
206	CH_4, 1.1	398	$CH_4 - C_3H_8$ (50%-50%), 0.4
207	CH_4, 1.3	408	$CH_4 - C_3H_8$ (50%-50%), 0.9
209	CH_4, 0.4	420^a	C_3H_8, 0.9
210	CH_4, 0.9	447	$CH_4 - Ar$ (46.4%-53.6%), 0.9
217	CH_4, 0.7	453	$CH_4 - Ar$ (46.4%-53.6%), 0.4
221	CH_4, 1.1	454	$CH_4 - Ar$ (46.4%-53.6%), 0.4
226	CH_4, 0.6	458	$CH_4 - Ar$ (46.4%-53.6%), 0.8
227	CH_4, 0.5	460	$CH_4 - Ar$ (46.4%-53.6%), 1.0
228	CH_4, 0.4	469	$CH_4 - Ar$ (46.4%-53.6%), 1.3
^{T} Traversing jet	^{S} $\phi_{pre} = \phi$		^{a} Fueling port vortex ring

Table 3.3. : Summary of specific test cases conducted to generate vortex rings.

Experiment no.	Pre-chamber fuel-air and equiv. ratio, Φ_{pre}	Experiment condition	Main chamber fuel-air and equiv. ratio, Φ
'| ' Scoring (ring observed)			
200	1.10	no-fuel	0
202	1.10	open-air	0
203	1.10	open-air	0
No Scoring (No ring observed)			
58	1.10	no-fuel	0
59	1.10	open-air	0
60	1.10	open-air	0
70	1.10	open-air	0

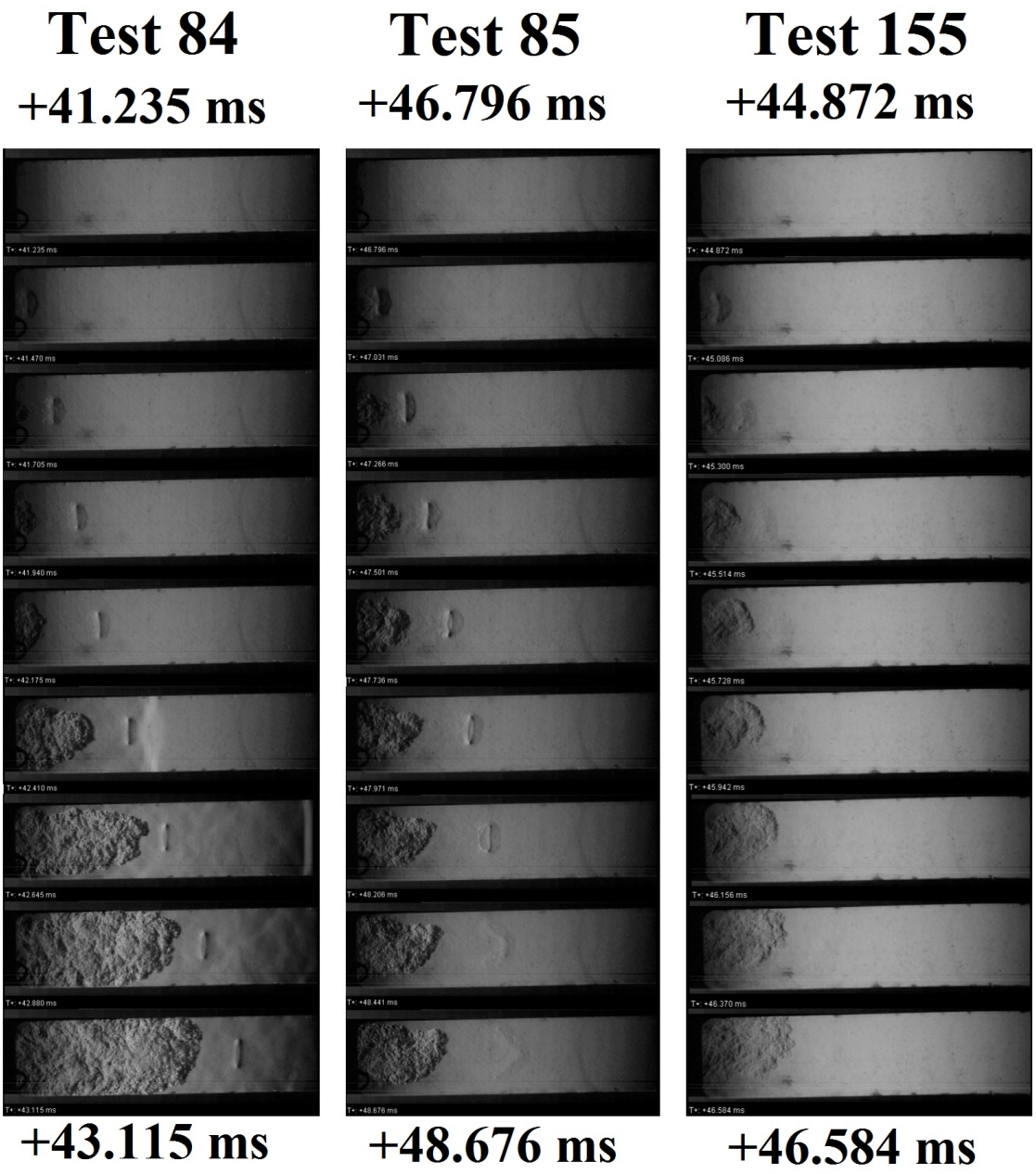

Figure 3.6. : Comparison of schlieren images for 3 test cases.From left, a fast moving vortex ring, a slow moving vortex ring and vortex ring from a traversing hot-jet ignition test. Fuel: $CH_4 - H_2$ (50%-50%).

The observed vortex rings, once inside the main chamber mostly travel in the longitudinal direction. They can be very broadly classified in mainly two types.

1. Relatively slow traveling vortex rings: These vortex rings move slowly relative to the hot-jet and once the diaphragm ruptures completely and issues a hot-jet in the main chamber, the jet catches up with the ring and the vortex head of the jet consumes the vortex ring. An example is shown in Fig. 3.6 test 85. In some cases the vortex ring distorts or spreads out before it is consumed and mixes with the unburned fuel-air mixture first and eventually consumed by jet vortex head. Exception to these cases is test 155 where a vortex ring was observed for a traversing hot-jet. Such rings are typically consumed by vortices produce by the jet itself or near the walls.

2. Relatively fast traveling vortex rings: These vortex rings move fast compared to the velocity of the jet and travels across the visible region of the schlieren images and the jet never catches up with ring in this region. An example, test 84, is shown in Fig. 3.6. These rings during their travel, keeps their ring structure and rarely spreads out or consumed entirely in the aforementioned visible region.

Since the vortex rings are mostly limited within the region close to the near pressure transducer (PT2), its traces of test 84, test 85 and a test (test no. 111) subjected to similar experimental conditions that did not produce a vortex ring are compared in Fig. 3.7. Although PT2 pressure signal is attenuated, it is evident that maximum pressure developed during combustion is highest for the slow traveling vortex ring of test 85. For cases with observed vortex ring the ignition delay, for some cases, were longer.

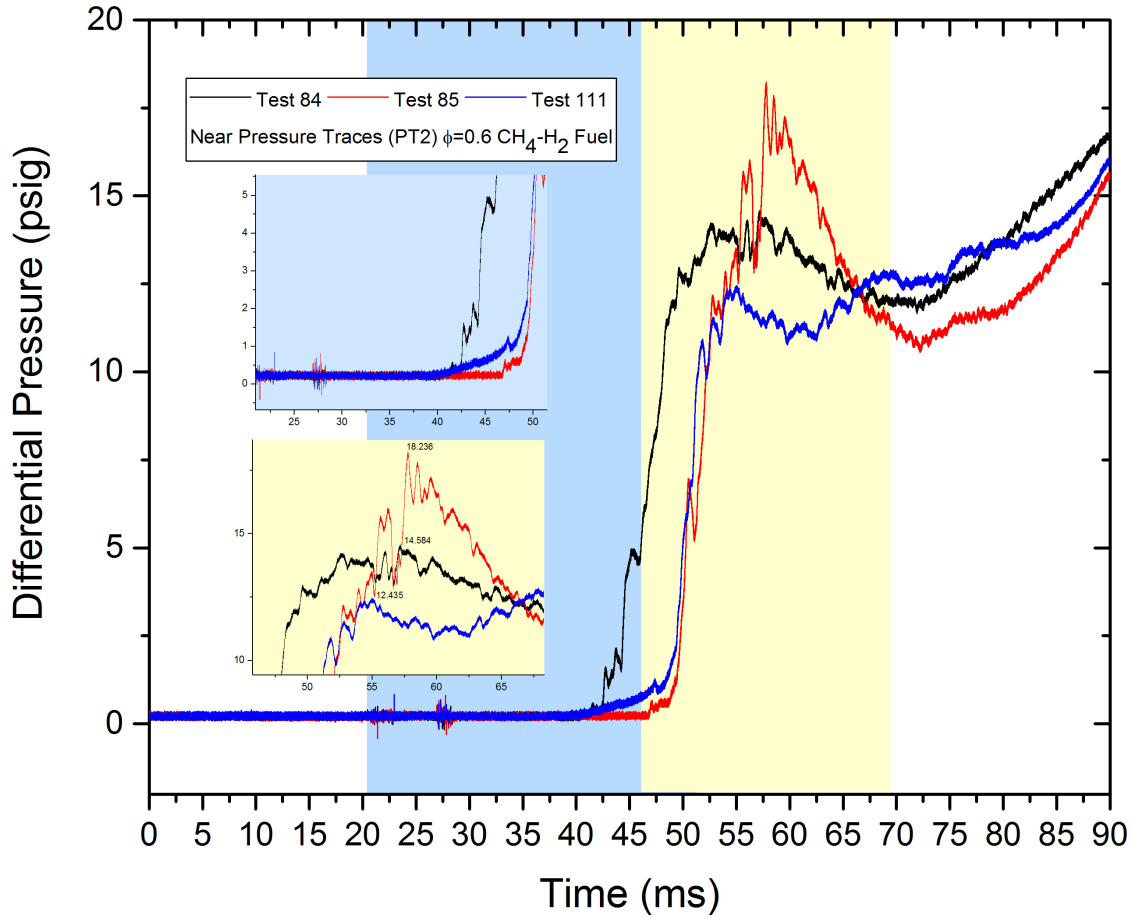

Figure 3.7. : Comparison of near pressure traces (PT2) for 3 test cases. Fuel: $CH_4 - H_2$ (50%-50%) $\phi = 0.6$.

3.3 Composite Chamber Ignition Experiment

Experiments were conducted where pre-chamber and main combustion chamber were coupled together without the aluminum diaphragm isolating the chambers. This effectively forms a composite chamber consisting of the entire pre-chamber volume and the main combustion chamber volume (combined volume of approximately 92.3 cubic inches). The purpose of conducting these experiments were to observe the flame propagation in the entire combustion volume and glean useful insights about the difference in combustion process compared to a typical hot-jet ignition experiment.

The composite chamber was fueled with 50%-50% methane-hydrogen blend fuel-air mixtures with an overall equivalence ratio of 1.1 from one fueling port, either on the pre-chamber or the main combustion chamber. When fueled from the pre-chamber fueling port, it is assumed that the mixture is too rich near the spark plug location and thus it did not ignite.Also, the fuel-air mixture is deemed too lean when the main combustion chamber fueling port is used. For either fueling strategies, the fuel has to travel through the 0.27 inch diameter hole of the nozzle. The allowed mixing time, which was less than a minute for all the trials may not have been enough for molecular diffusion to sufficiently mix the fuel with air alone resulting in highly stratified fuel-air mixture in the entire combustion volume.

A better fueling strategy would be to fuel both chambers separately. During fueling of the pre-chamber, some amount of air will be expelled to the main chamber through the nozzle. The amount of air can be calculated to deliver the correct amount of fuel in the pre-chamber. Similar adjustments can be made to the main chamber fueling. This strategy will result in the fuel-air mixture being relatively less stratified compared to the aforementioned fueling strategy.

However, a fuel with higher binary coefficient of diffusion with respect to air, such as hydrogen, would be much effectively diffused across the composite chamber. The test was repeated with hydrogen at equivalence ratio of 1 and fueling was performed from the fueling port in the main chamber. The mixing time, defined as moment of end of fuel injection to firing of spark plug, was 13s. The test was repeated once at the same mixing time. When the mixing time was increased to 33s, ignition didn't take place. The pressure test of one of the cases, test 470 is discussed here.

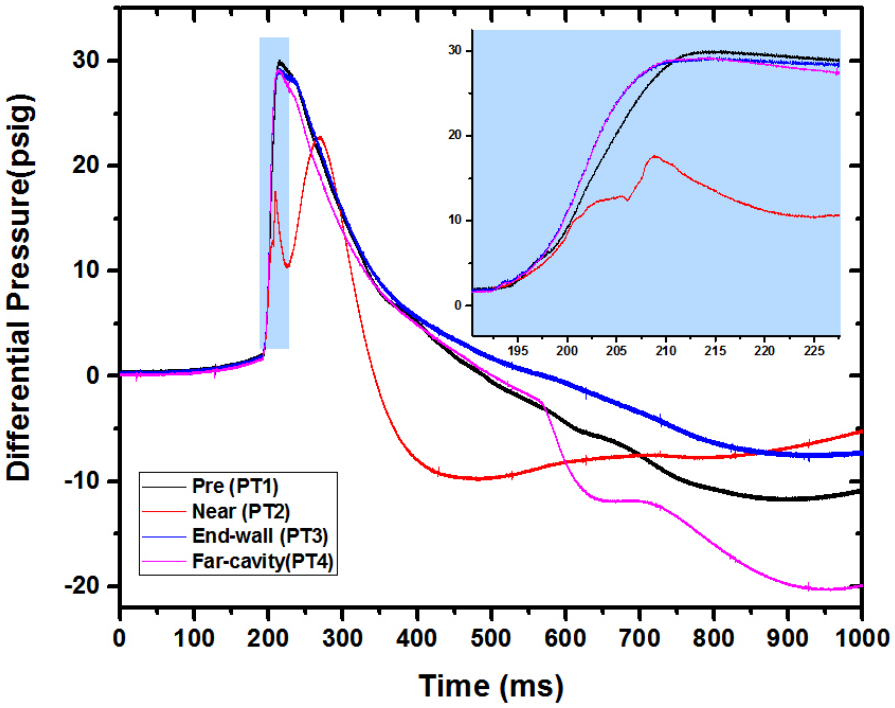

Figure 3.8. : Pressure trace of test 470 composite chamber experiment. Fuel-hydrogen, $\tau_{mix} = 13s$ and $\phi = 1$.

From Fig. 3.8, a gradual rise in all pressure transducer signals can be observed till approximately 192 ms after spark trigger in pre-chamber. This rise pushes out unburned fuel-air mixture from the pre-chamber volume through the nozzle to the main chamber which is observed from schlieren images (Fig. 3.9) and at about 192.8 ms after trigger a sudden burst of combustion products enter the main chamber and traverse the entire length of the chamber. The entrance event is characterized by the sharp rise in all the pressure traces. The near pressure trace, unlike the other three pressure traces, records a delayed second rise in pressure sometime between 205 ms and 210 ms after trigger, which may indicate possibility of autoignition of the fuel-air mixture due to compression and consequent temperature increase of the unburned fuel-air mixture at the rear end of the chamber. However, this rise in pressure is not picked up by the other transducers which also indicate that the second rise in

the pressure trace may be a delayed response to the ignition event and the first rise recorded by PT2 is due to the expulsion of pre-chamber unburned fuel-air mixture.

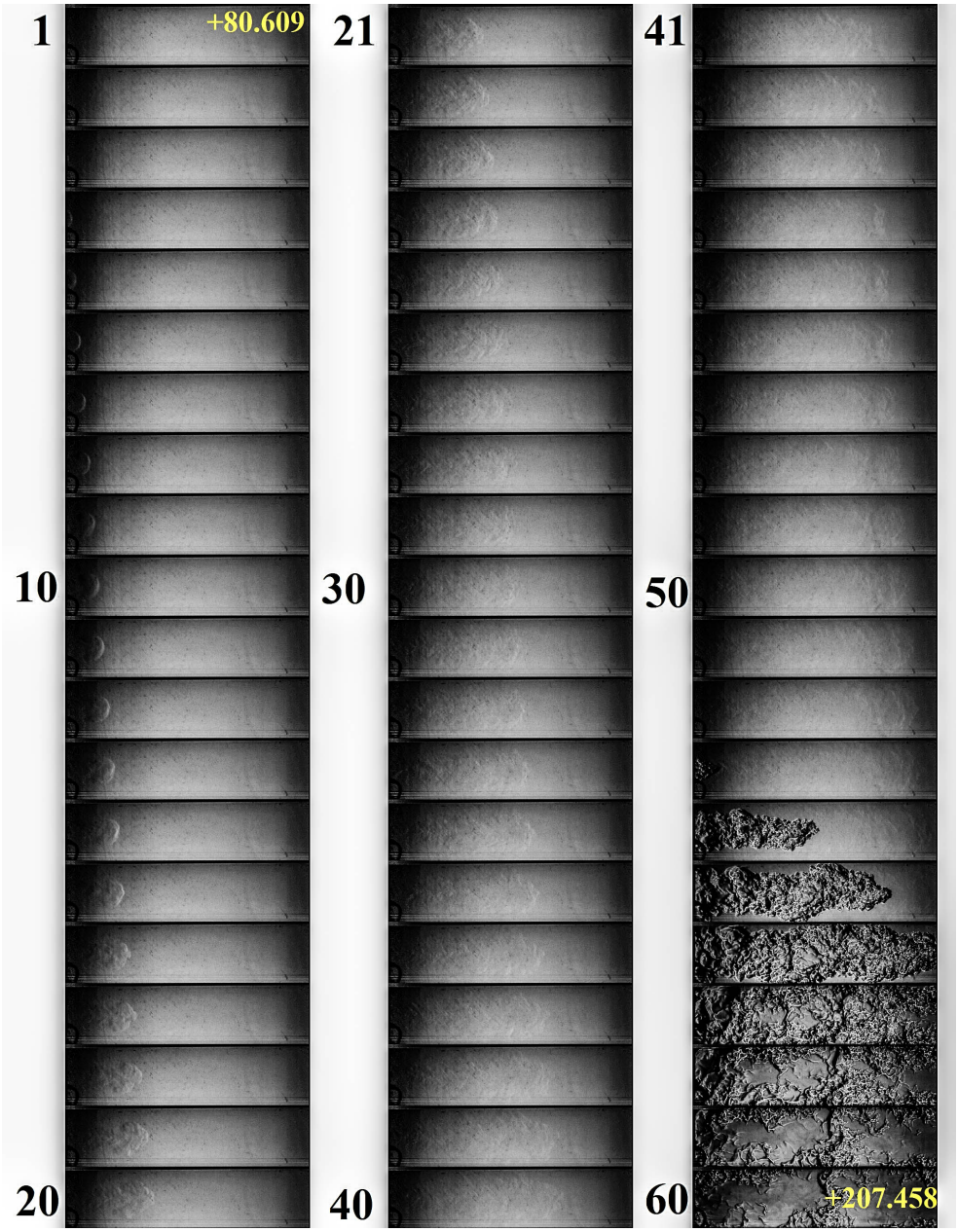

Figure 3.9. : Schlieren images of test 470 composite chamber experiment from the onset of combustion products coming inside the chamber. Fuel-hydrogen, $\tau_{mix} = 13s$ and $\phi = 1$. Images are darkened for better visualization of density gradients.

3.4 Supplemental Main Chamber Hot-Jet Ignition Experiments

In this section, a few specific hot-jet ignition cases are discussed which are different from the hot-jet ignition tests conducted for the design of experiments previously mentioned in section 2.9.5. In a wave rotor combustor, combusted products from one channel could be transferred from one channel through a transfer passage to another channel. The transferred products, containing reactive radicals could then act as a source of ignition and ignite the fuel-air mixture in the later channel. A simple fueling strategy of the wave rotor combustor may include fueling all the channels with the same fuel at the same equivalence ratio. Also some of the tests, discussed here, also represent conditions such that the effect of fuel reactivity and effect of addition of hydrogen can be explored.

3.4.1 Same Equivalence Ratio in Chambers Experiments

These tests are hot-jet ignition experiments where the pre-chamber is kept at the same condition in terms of fuel-air mixture and equivalence ratio in the main chamber. This represents the the aforementioned conditions of a wave rotor combustor channel that is ignited by a fuel-air mixture having the same conditions initially of the channel . These tests are different from the typical hot-jet ignition cases where the pre-chamber is filled with 50%-50% methane hydrogen blend and air mixture at equivalence ratio of 1.1. Table 3.4 shows the experimental conditions.

The pressure traces of these cases are similar to typical stationary hot-jet ignition pressure traces discussed in section 4.2 and hence not discussed here. Here, the estimated shock speeds, maximum pressure developed and ignition delay of the fuel-air mixtures for these cases are presented in Figs. 3.10-3.12. Methodology for calculation of rupture shock speed and ignition delay is discussed in section 4.4.1.

Table 3.4. : Summary of test cases with same fuel in both chambers at same equivalence ratio.

Experiment no.	Pre-chamber and Main chamber fuel and equiv. ratio, Φ
112	$CH_4 - H_2$ (50%-50%), 0.7
113	$CH_4 - H_2$ (50%-50%), 0.8
114	$CH_4 - H_2$ (50%-50%), 0.9
115	$CH_4 - H_2$ (50%-50%), 1.0
116	$CH_4 - H_2$ (50%-50%), 1.2
117	$CH_4 - H_2$ (50%-50%), 1.0
118	$CH_4 - H_2$ (50%-50%), 1.0
119	$CH_4 - H_2$ (50%-50%), 1.2
120	$CH_4 - H_2$ (50%-50%), 1.2
121	$CH_4 - H_2$ (50%-50%), 0.8
122	$CH_4 - H_2$ (50%-50%), 0.8
123	$CH_4 - H_2$ (50%-50%), 0.9
124	$CH_4 - H_2$ (50%-50%), 0.9

In Figs. 3.10-3.12, both chambers have 50%-50% methane-hydrogen and air mixtures at the same nominal equivalence ratio. Fig. 3.10 shows the increasing trend of shock speeds for these hot jet ignition tests up to equivalence ratio of 1.1 in both chambers. The maximum pressure developed (Fig. 3.11) is also highest at the same equivalence ratio of 1.1. This is expected due to higher flame temperature attained in constant-volume combustion and dissociation of combustion products at slightly rich fuel-air mixture which leaves molecular oxygen in combusted gases that can partially burn additional fuel leading to an increase in the maximum pressure developed. $\phi = 1$ and then decrease. Lean mixtures ignite relatively fast due to complete combustion, however, the ignition delay (Fig. 3.12) time of some of the rich fuel-air mixtures were also similar to ignition delay of lean fuel-air mixture cases. The amount of chemically active radical deposited by a rich jet, leading to fast reaction rates , causes this decreasing trend for rich fuel-air mixtures.

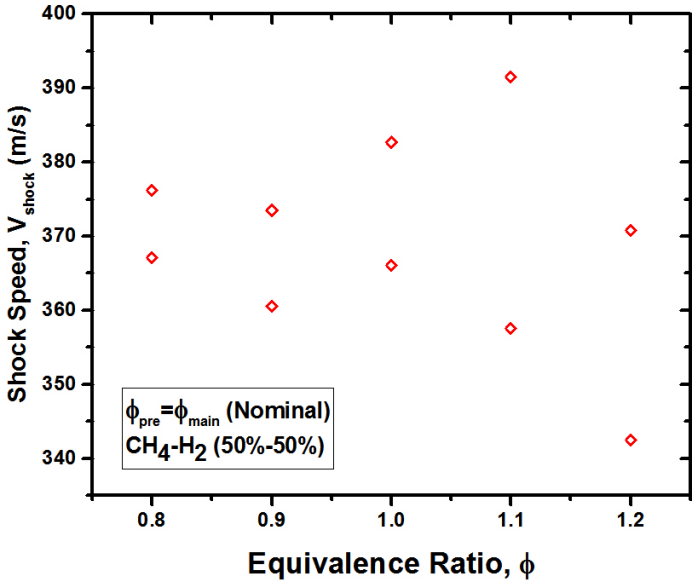

Figure 3.10. : Variation of rupture shock speed.

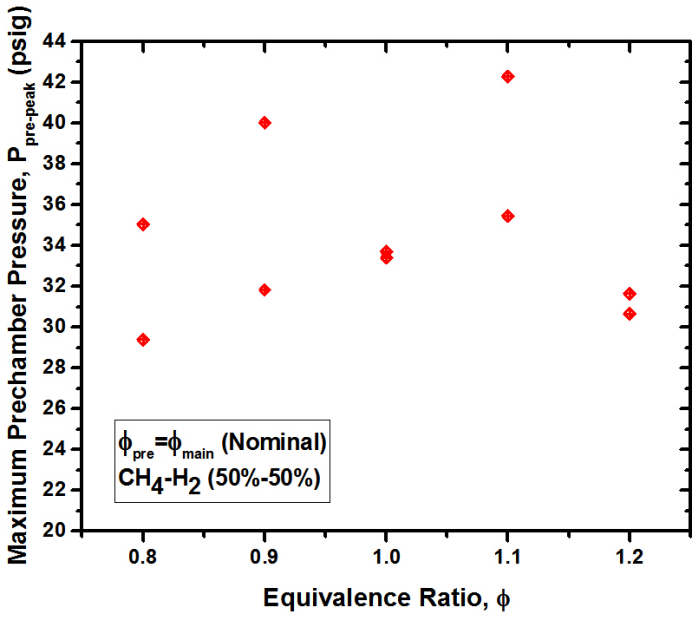

Figure 3.11. : Variation of maximum differential pressure.

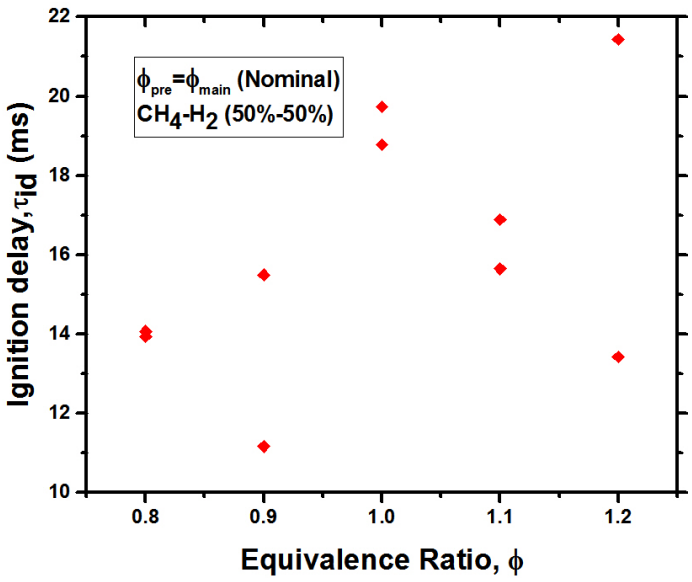

Figure 3.12. : Variation of ignition delay.

3.4.2 More Reactive Fuel in Both Chambers

Two hot-jet ignition tests (test 37 and test 45) were conducted with two different blends of methane-hydrogen. The equivalence ratio of both chambers are 1.1 and it is kept constant for both tests. The fuel in both chambers are also same for each test. The fuel for test 37 was 50%-50% methane-hydrogen and air mixture at $\phi = 1.1$. However, the fuel for test 45 was 30%-70% methane-hydrogen and air mixture at $\phi = 1.1$. The pressure traces and schlieren images of test 37 (Fig. 3.13(b)) reveal an ignition delay of 2.7 ms. For a more reactive fuel, test 45 pressure traces (Fig. 3.13(a)) and schlieren images are expect to show a shorter ignition delay. The pressure trace of test 45 apparently indicates a longer ignition delay of 4.3 ms. However, the jets for both tests when compared at the same timescale of 1 ms after diaphragm rupture (Fig. 3.14) reveal that for more reactive fuel-air mixture, the mixture ignites very fast, almost as soon as it crosses the chamber entrance and enters the chamber. The jet with higher hydrogen content shows darker gradients 1 ms after rupture which indicate presence of substantial pressure rise, a characteristic of ignition. For the 30%-70%

methane-hydrogen blend fuel ignition is often too fast to be seen in the schlieren view and also the rupture shock pressurization and pressure rise due to ignition are overlapped. Therefore, the methodology adopted in section 4.4.1 is inadequate and incapable of determining the ignition delay of such cases.

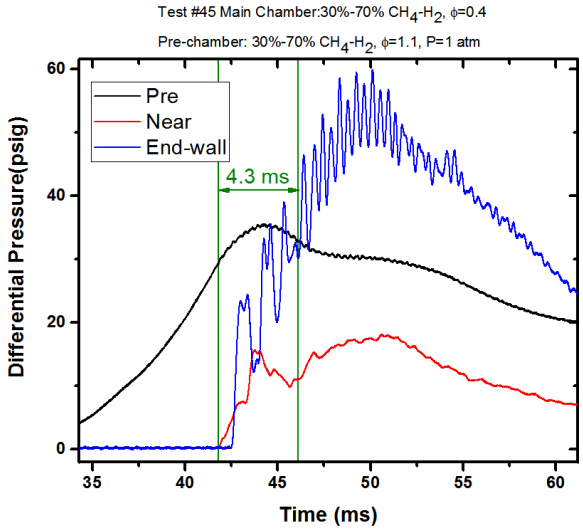

(a) Test 45. Fuel 30%-70% $CH_4 - H_2$.

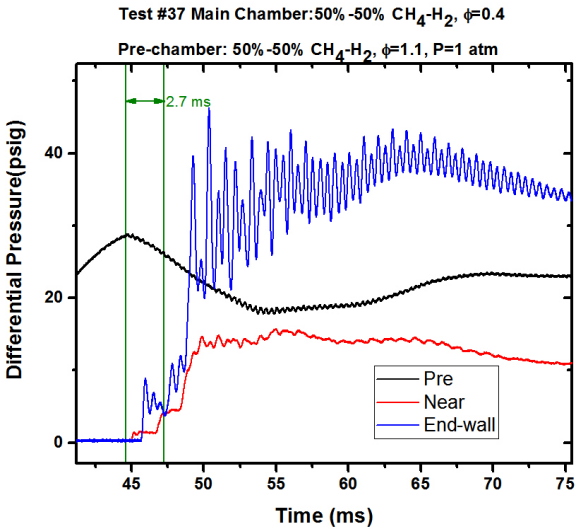

(b) Test 37. Fuel 50%-50% $CH_4 - H_2$.

Figure 3.13. : Same fuel in both chambers with increase in hydrogen content.

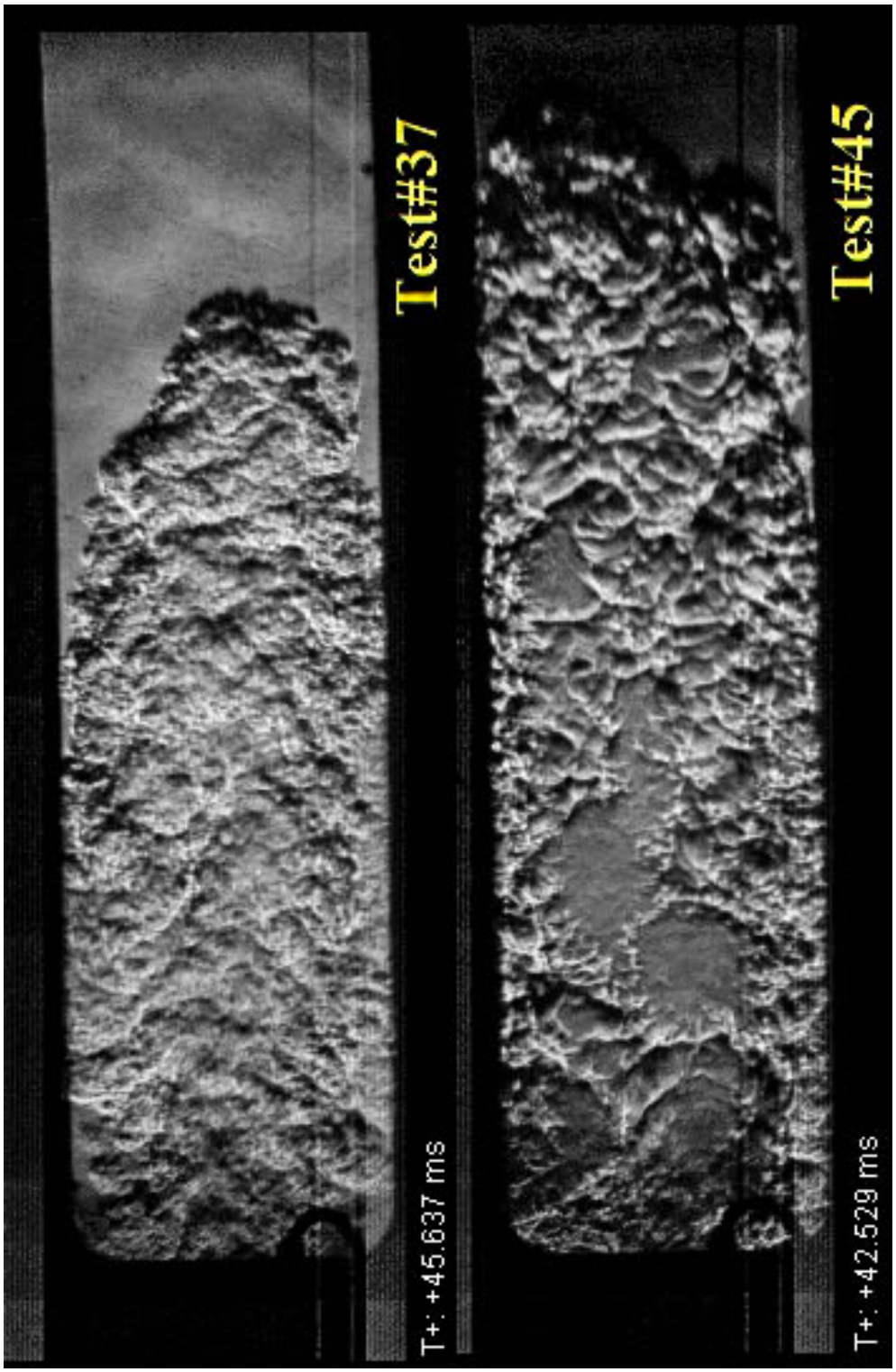

Figure 3.14. : The jets from test 37 and test 45 approximately 1 ms after diaphragm rupture.

3.4.3 Increase in Hydrogen Content

Pressure traces of three hot-jet ignition tests are compared to better understand the effect of addition of hydrogen in the fuel blend. The compositions are methane-air mixture with no hydrogen (test 214), 50%-50% methane-hydrogen and air mixture (test 29) and 30%-70% methane-hydrogen and air mixtures (test 53) pressure trace and ignition delay. Increasing trend in maximum pressure developed and decreasing trend in calculated ignition delay as more and more hydrogen is added. In Figs. 3.15-3.17 we see the onset of ignition progressively decrease with addition of hydrogen resulting in reduced ignition delay. Also hydrogen being highly flammable increases the maximum pressure developed during combustion substantially. With addition of 50% hydrogen, the max pressure increases by approximately 50%. 70% hydrogen in the mixture increase the developed pressure by nearly two and a half times. This is consistent with findings of Zhang et al. [1]. They suggested the dominance of hydrogen chemistry in the blend fuel chemistry of methane and hydrogen beyond 60% hydrogen content. The schlieren images also reveal a considerable amount of mixing is required for the less reactive fuel (pure methane) to eventually ignite. Overall, hydrogen, due its reactivity, reduces ignition delay significantly and the reduction in ignition delay due to fuel reactivity is much higher compared to the reduction in ignition delay due to fuel-air equivalence ratio.

3.5 Schlieren Images of Fueling and Initial Mixing

These tests were conducted to observe the fueling process and the initial mixing of the reactants. A set of schlieren images presented in Figs. 3.18-3.23 demonstrates the fueling of six fuels. The images show the initial mixing of the fuels with residual air. The schlieren images show a manufacturing defect in the glass as a curved black region (slightly right to the fueling port). The effect of buoyancy due to the difference in molecular weight of the fuel and air results in lighter fuels such as hydrogen, methane and their blend (Figs. 3.18, 3.19 and 3.20) being stratified to the top and

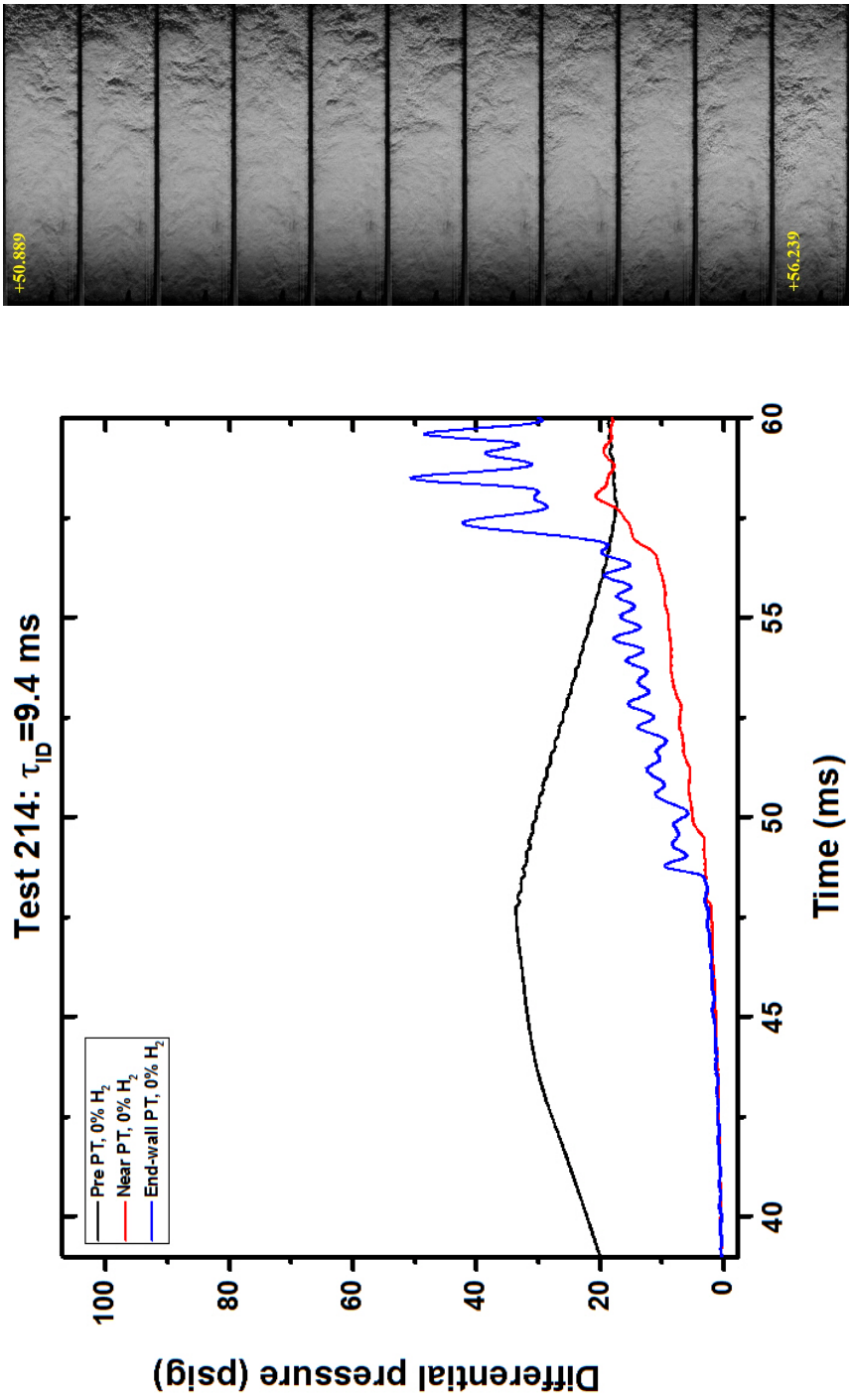

(a) Test 214: 100% methane 0% hydrogen mixed with air.

(b) Test 214: Schlieren of jet.

Figure 3.15. : H_2 addition in stoichiometric $CH_4 - H_2 - air$ mixtures (Test 214).

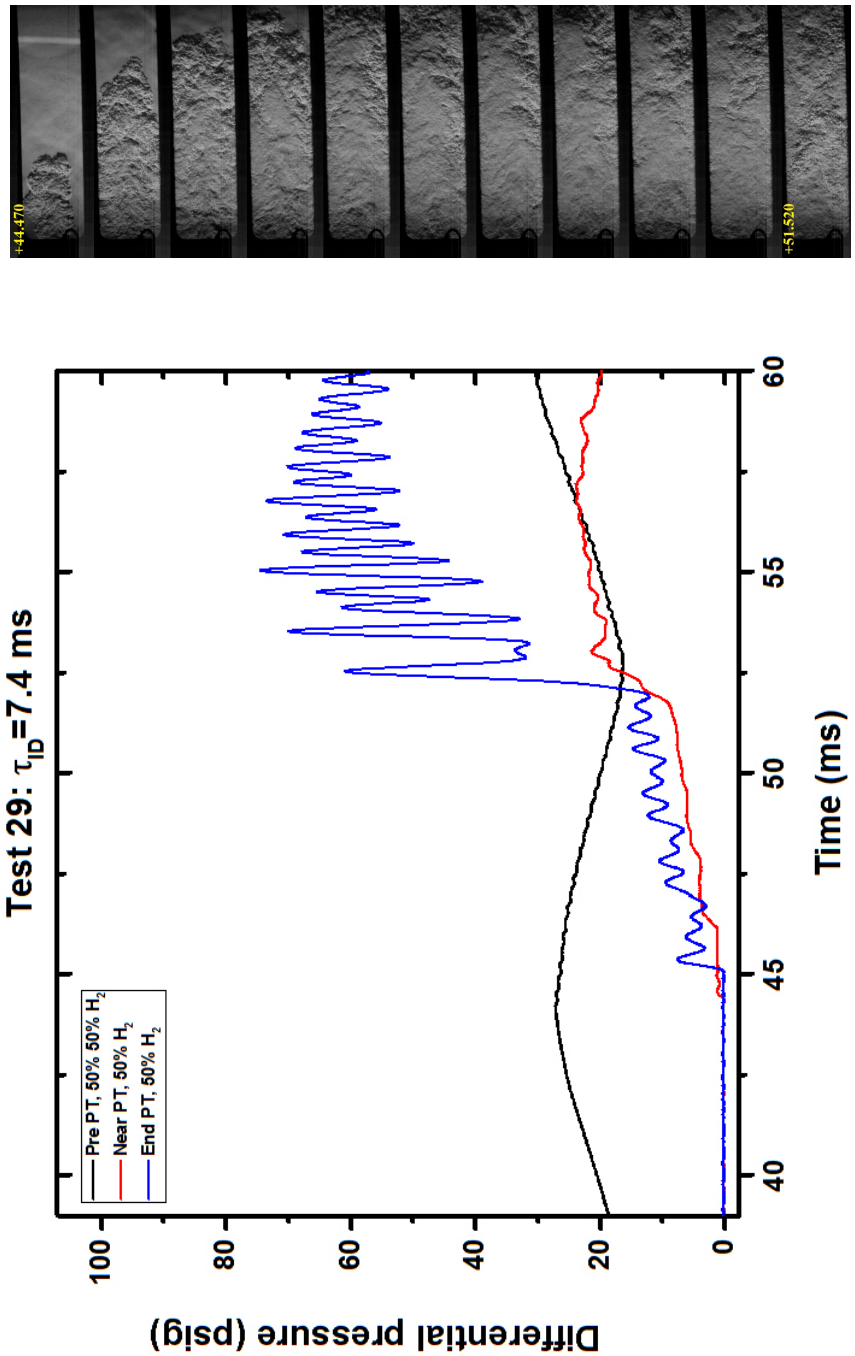

(a) Test 29: 50% methane 50% hydrogen mixed with air.

(b) Test 29: Schlieren of jet.

Figure 3.16. : H_2 addition in stoichiometric $CH_4 - H_2 - air$ mixtures. (Test 29)

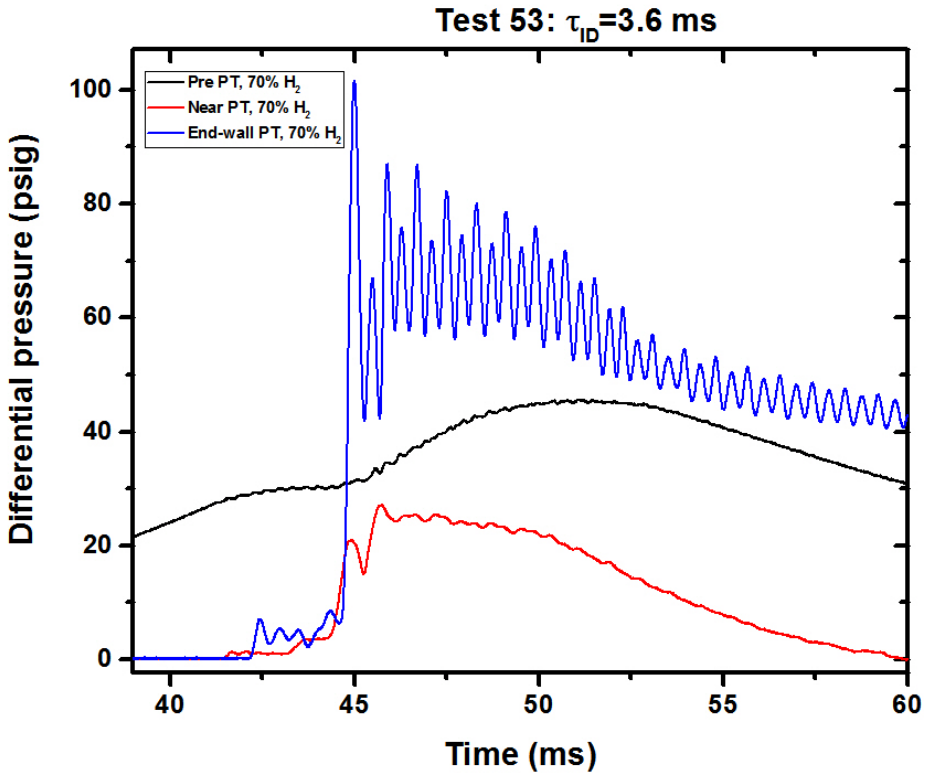

(a) Test 53: 30% methane 70% hydrogen mixed with air.

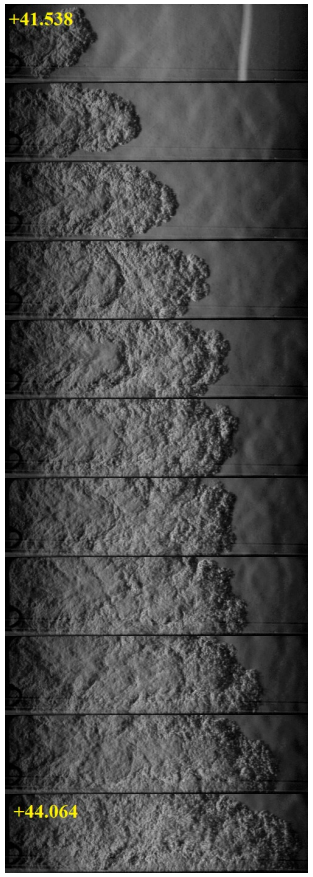

(b) Test 53: Schlieren of jet.

Figure 3.17. : H_2 addition in stoichiometric $CH_4 - H_2 - air$ mixtures (Test 53).

propane, a heavier fuel (Fig. 3.22), stratify to the bottom of the chamber. The 50%-50% methane and propane blend and 46.4%-53.6% methane and argon blend have approximately the same molecular weight as air. For this two fuels the stratification effect is minimized compared to the other four fuels. Visually, it appears that the methane-propane blend stratifies to the bottom initially since its molecular weight is slightly greater than air. The laminar flame propagation experiments conducted for the purpose of verifying fuel-air mixture stratification did not demonstrate any significant difference in stratification of the methane-propane fuel blend compared to the methane-argon fuel blend.

For the light fuels, the jet of fuel coming out the fueling port impinges on the bottom wall of the chamber and then rise upwards and bifurcate into two opposing jets to the right and left of the chamber. Depending on the lightness of the fuel the bifurcated jets stay as close to the top wall as possible. For heavier fuels, the bifurcation occurs at the bottom wall and much more distinct compared to the lighter fuels. The methane-argon blend and the methane-propane blend shows the bifurcated jets spreading over a much larger region compared to the other of fuels.

3.6 Room Pressure and Temperature

The hot-jet ignition experiments were conducted over a period of 10 months. The laminar flame propagation experiments were conducted over a period of two months. The fuel delivered by the MFC and partial pressure method requires the knowledge of the room pressure and temperature to estimate amount of residual air present in the combustion chambers. The pressure and temperatures of these tests are given here in Figs 3.24 and 3.25.

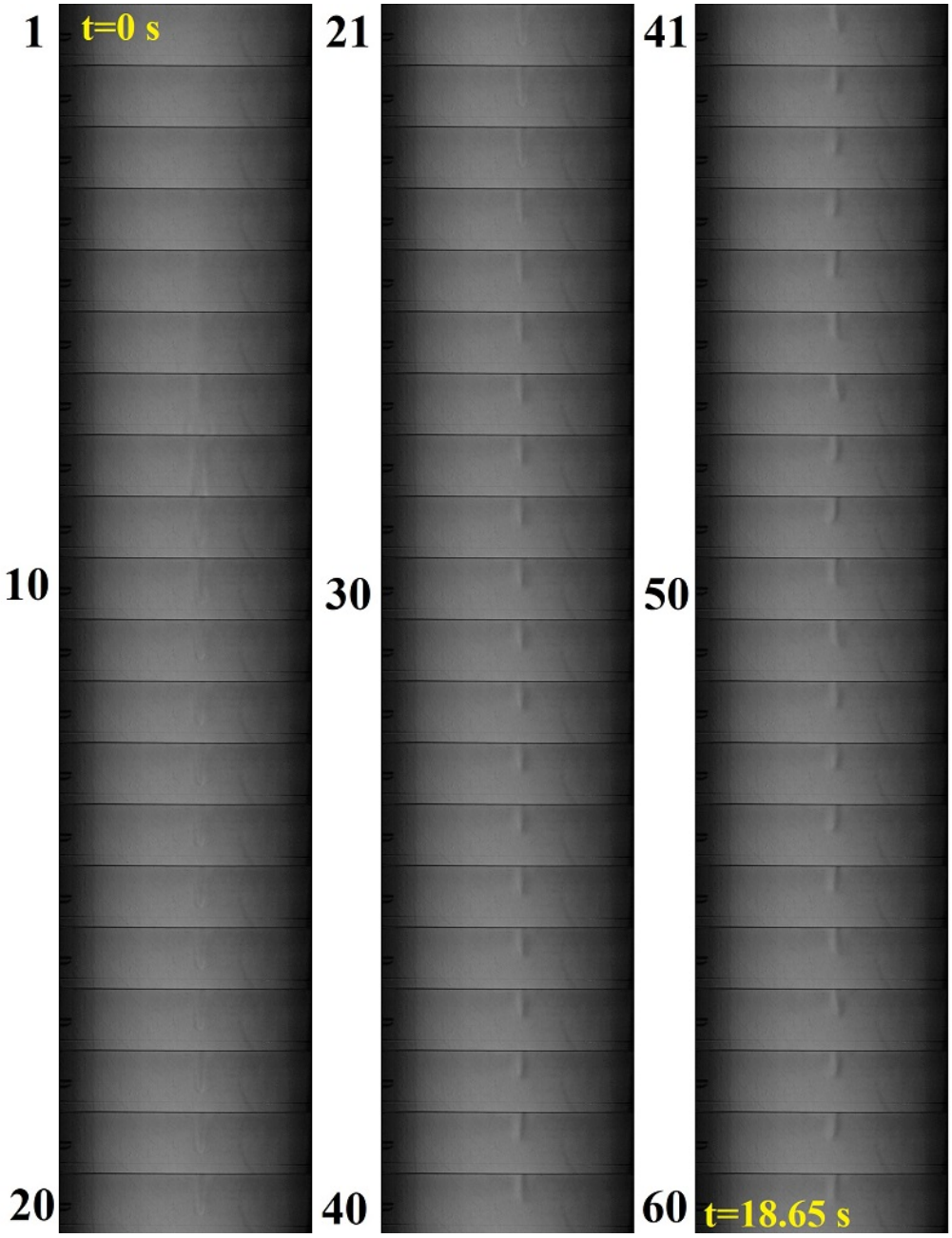

Figure 3.18. : Injection of H_2 fuel at P = 995.9 mbar, T= 295.9 K and $\phi = 1$.

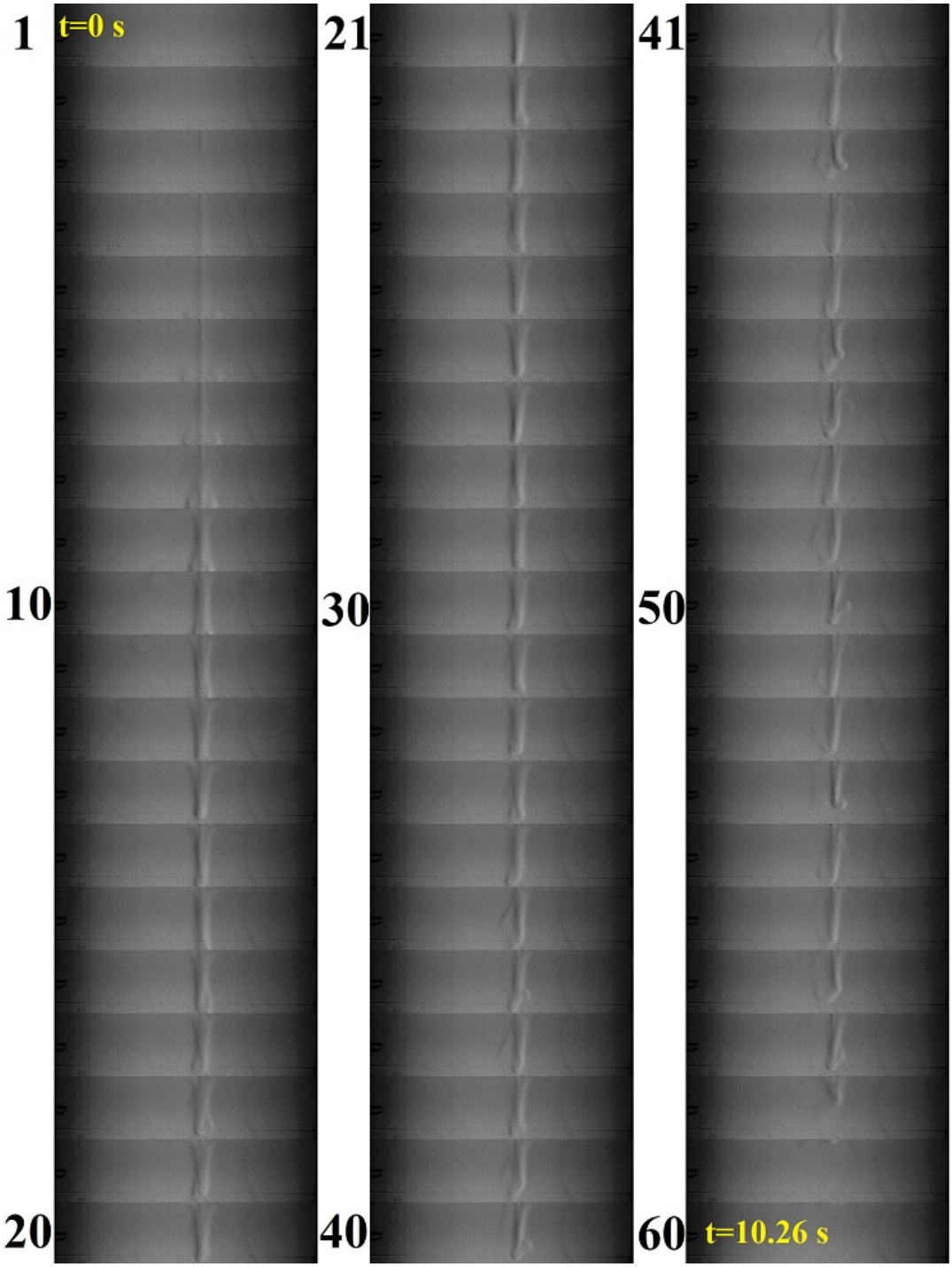

Figure 3.19. : Injection of CH_4 fuel at P = 990 mbar, T = 295.9 K and $\phi = 1.3$.

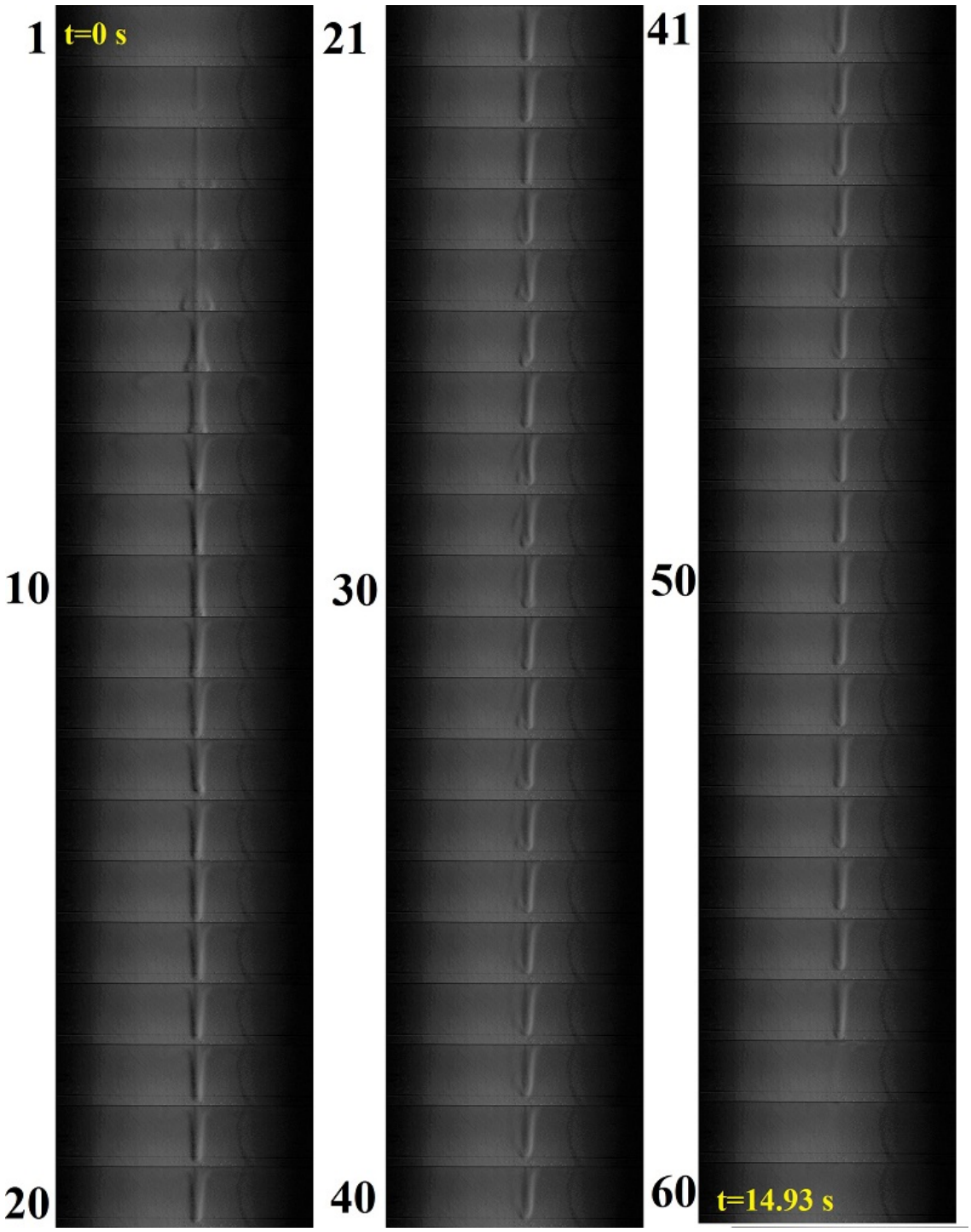

Figure 3.20. : Injection of $50\% - 50\%$ $CH_4 - H_2$ fuel at P = 990 mbar, T = 295.9 K and $\phi = 1.3$.

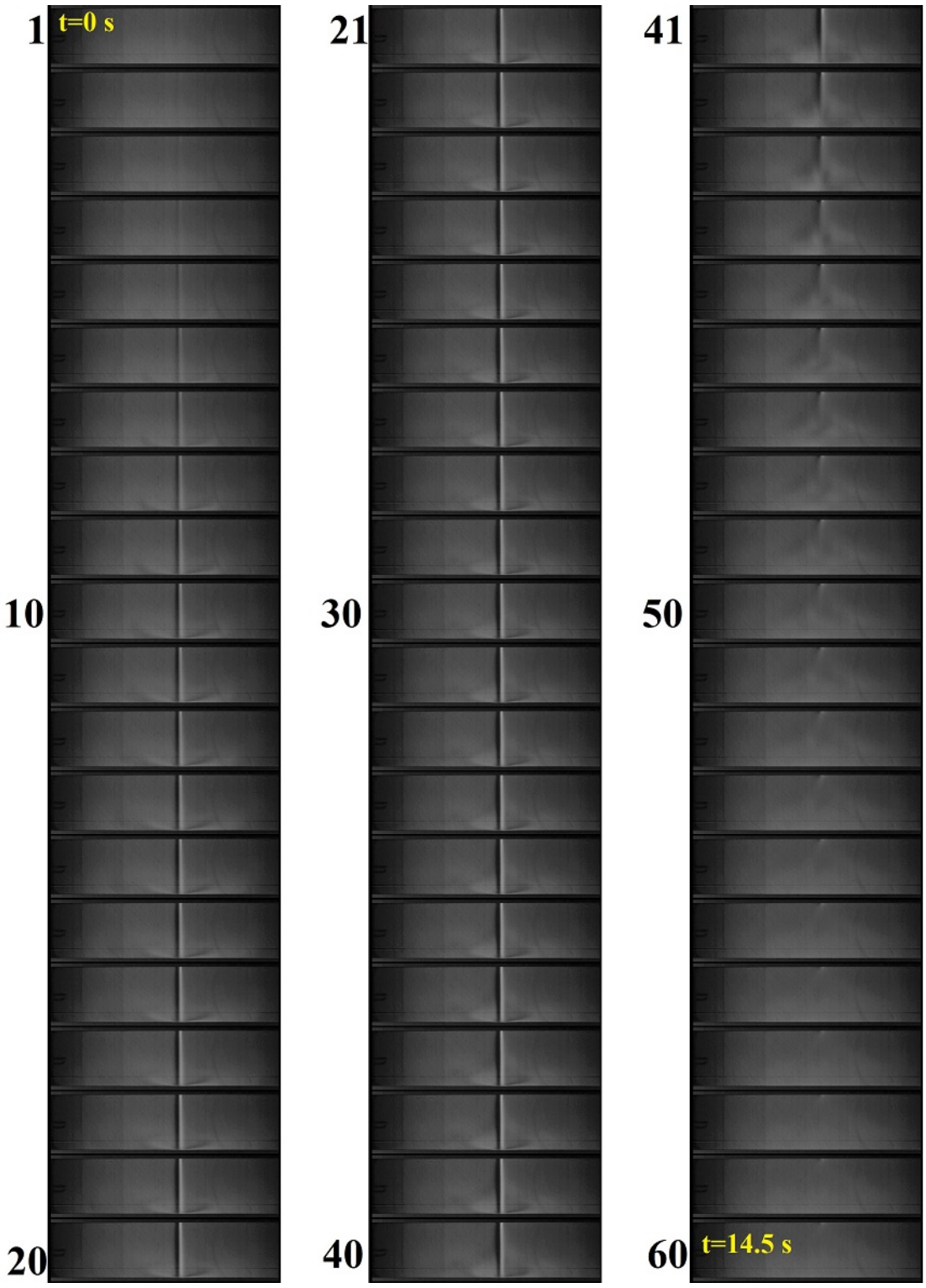

Figure 3.21. : Injection of $50\% - 50\%$ $CH_4 - C_3H_8$ fuel at P = 987 mbar, T = 296 K and $\phi = 1.3$.

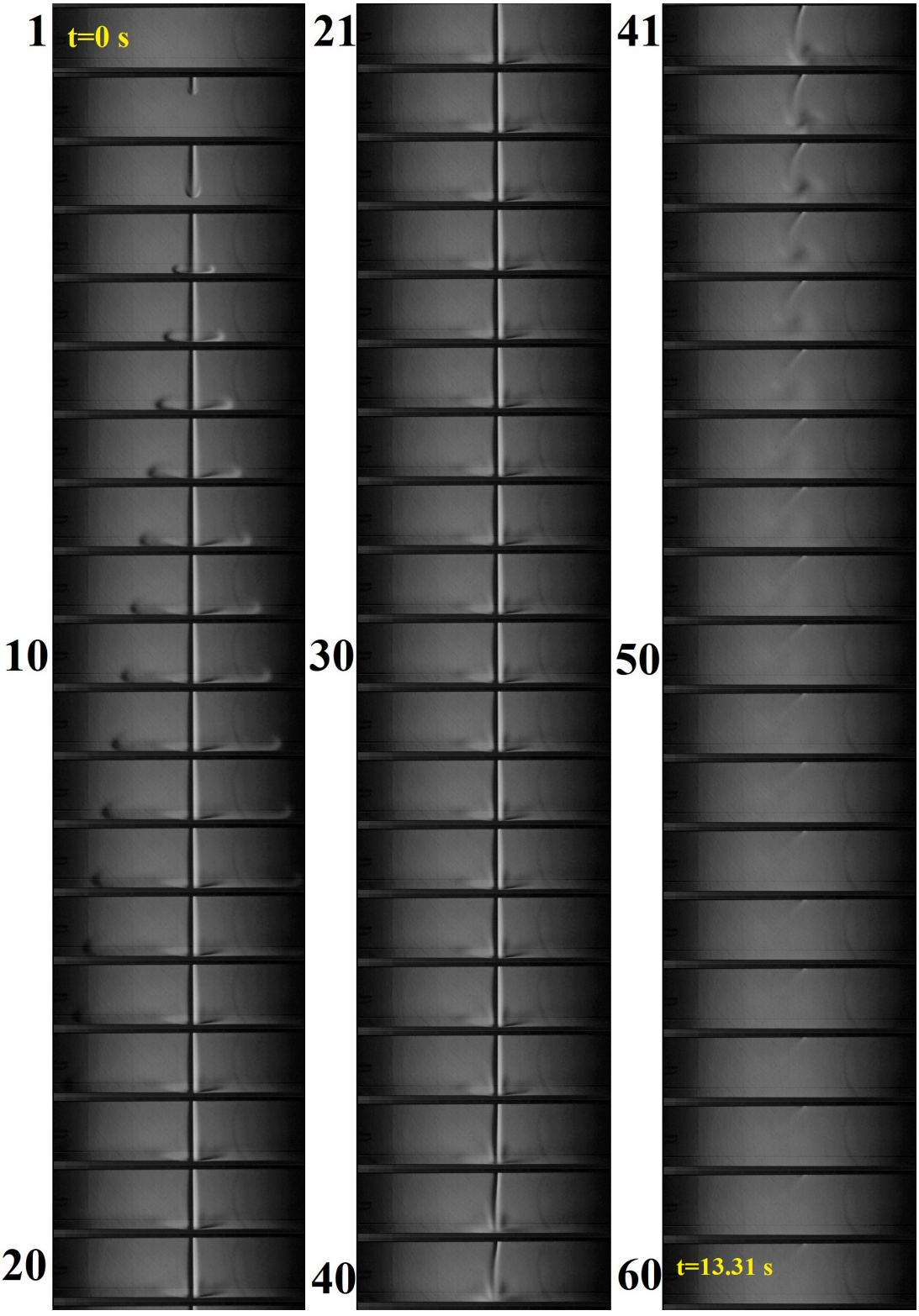

Figure 3.22. : Injection of C_3H_8 fuel at P = 983 mbar, T = 295.9 K and $\phi = 1.3$.

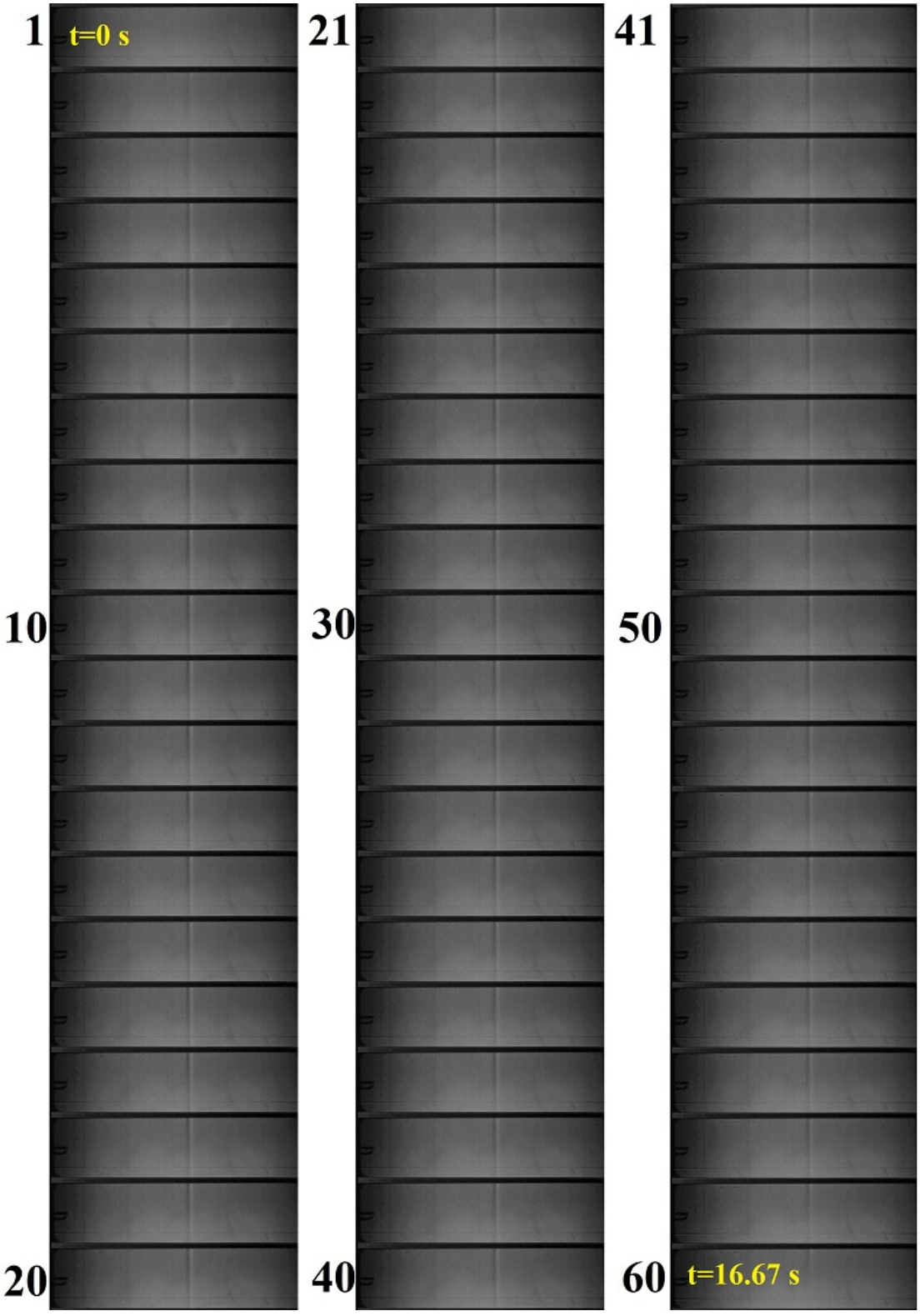

Figure 3.23. : Injection of $46.4\% - 53.6\%$ $CH_4 - Ar$ fuel at P = 986 mbar, T = 296.1 K and $\phi = 1.3$.

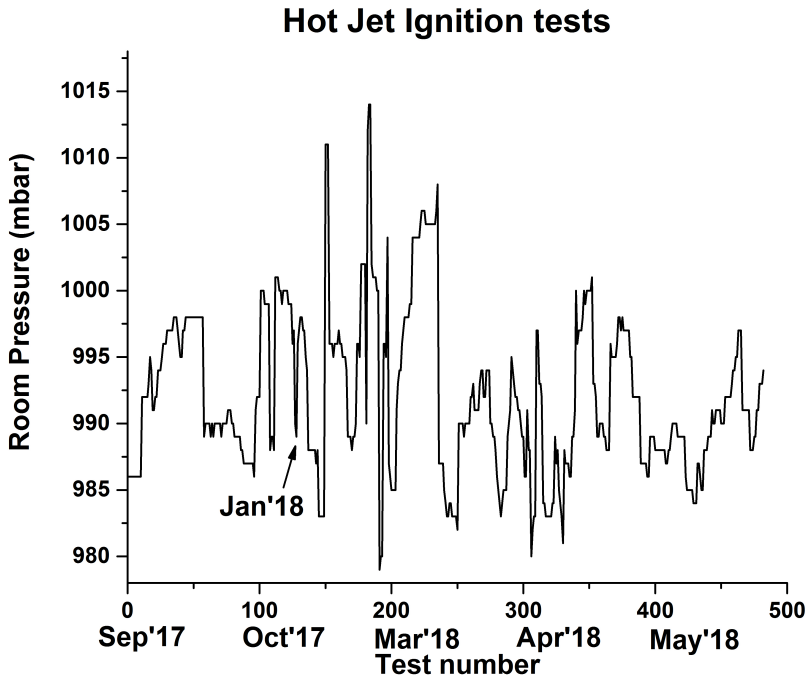

(a) Room pressures for hot-jet ignition tests.

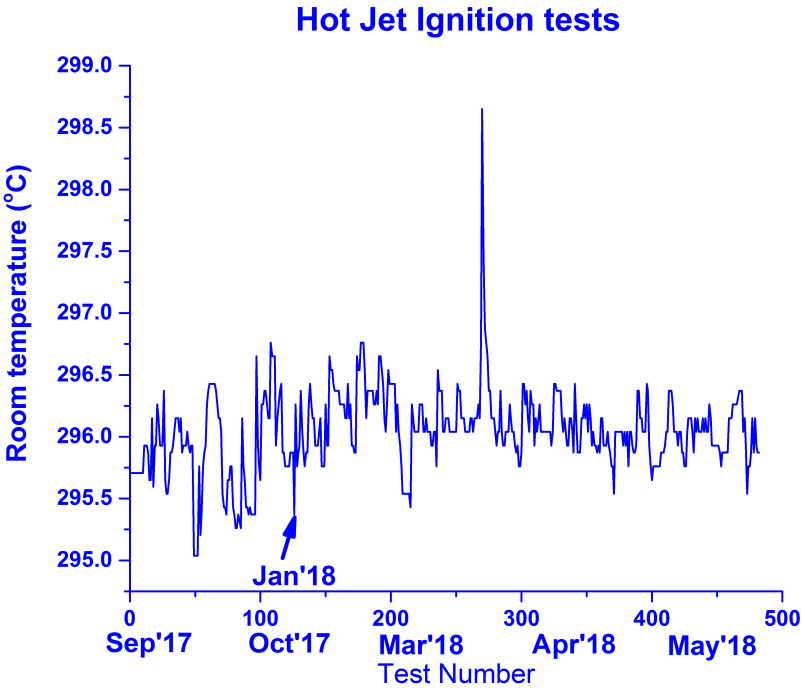

(b) Room temperatures for hot-jet ignition tests.

Figure 3.24. : Room pressures and temperatures for hot-jet ignition tests.

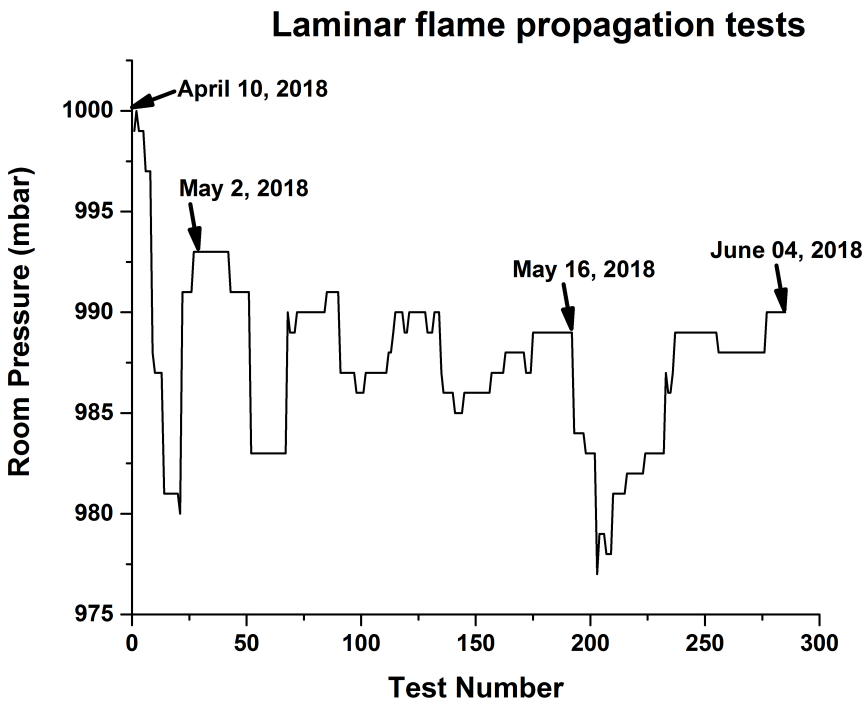

(a) Room pressures for laminar flame propagation tests.

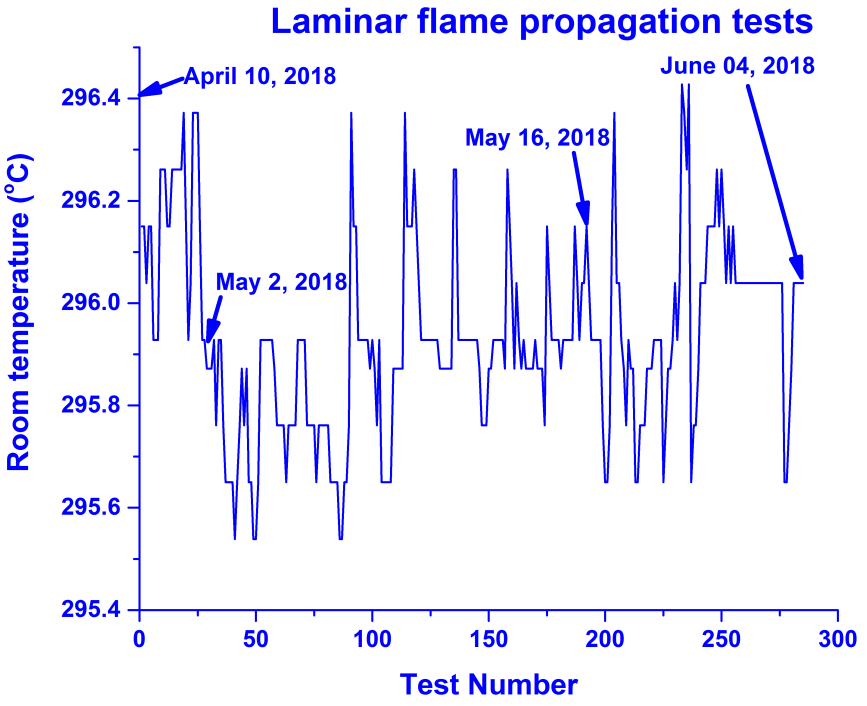

(b) Room temperatures for laminar flame propagation tests.

Figure 3.25. : Room pressures and temperatures for laminar flame propagation tests.

4. IGNITION DELAY INVESTIGATION

In this chapter, the pressure traces of the hot-jet ignition cases, both stationary and traversing hot-jet, are presented along with time resolved schlieren images. The estimated ignition delay times for different experimental conditions such as effect of jet traverse time, fuel reactivity and equivalence ratio are discussed.

4.1 Non-reacting and Reacting Jet Pressure Traces

For any hot ignition test, ignition is verified from the pressure traces by comparing it to a similar non-reacting test case pressure rise. In Fig. 4.1 pressure traces of a non-reacting stationary hot-jet (test 25, $\phi = 0$) and six reacting stationary hot jets (tests 29, 45, 218, 387, 402 and 454) are plotted. For all the cases, $\phi_{pre} = 1.1$, $\phi = 0.4$ and initial filling pressure of pre-chamber is 1 atm. In test 25, no fuel is present in the main chamber. The pressure rise for this non-reacting case is the lowest compared to the six other cases when different fuel-air mixture is ignited in the main chamber. The maximum pre-chamber pressure (Fig. 4.20(a)) is less than 25 psig for the non-reacting case, and reaches a high of approximately 37 psig during propane-air ignition test in the main chamber. In the near pressure traces (Fig. 4.20(b)), the effect of fuel reactivity is observed, keeping in mind that this transducer does not measure pressure directly in the chamber (to avoid heat damage), but measures attenuated pressure with fast response. The 30%-70% methane-hydrogen blend ignites very early and with very small delay between its rupture moment and ignition moment. All the other fuels, however, ignites much later compared to the 30%-70% methane-hydrogen blend. The maximum pressure is attained by 50%-50% methane-hydrogen blend. At this location too, the non-reacting case has the lowest maximum pressure, due to the absence of ignition. The pressure rise for the non-reacting case is essentially due to

rupture shock propagation. The same trend is continued in the end-wall pressure traces (Fig. 4.20(c)).

For traversing hot-jet ignition experiments in Fig. 4.2, for both near pressure trace and end-wall pressure traces, at the same jet traverse time higher pressure is developed for reacting cases compared to non-reacting cases. It is interesting to note that, with an increase pre-chamber rotation or decrease in jet traverse time, the maximum pressure registered by both transducers decreases.

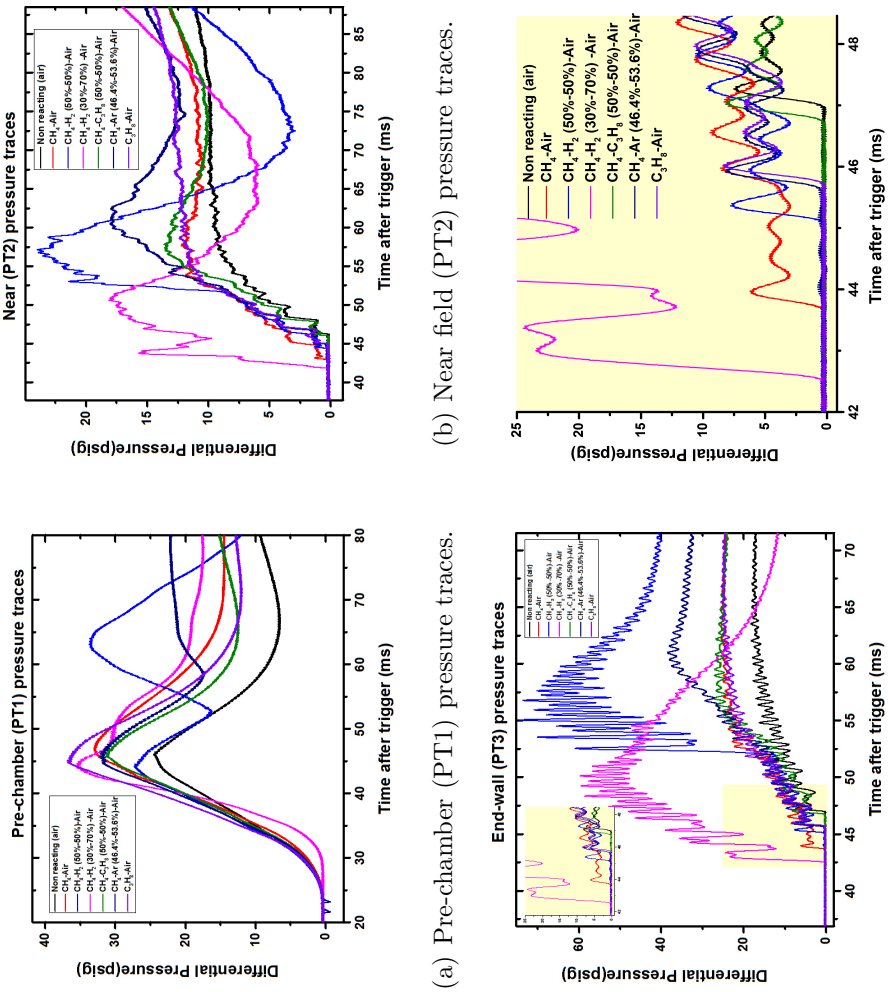

(a) Pre-chamber (PT1) pressure traces.

(b) Near field (PT2) pressure traces.

(c) Far-cavity (PT3) pressure traces.

(d) 30%-70% $CH_4 - H_2$ early ignition.

Figure 4.1. : Pressure trace comparison between a non-reacting jet and a reacting jet (stationary).

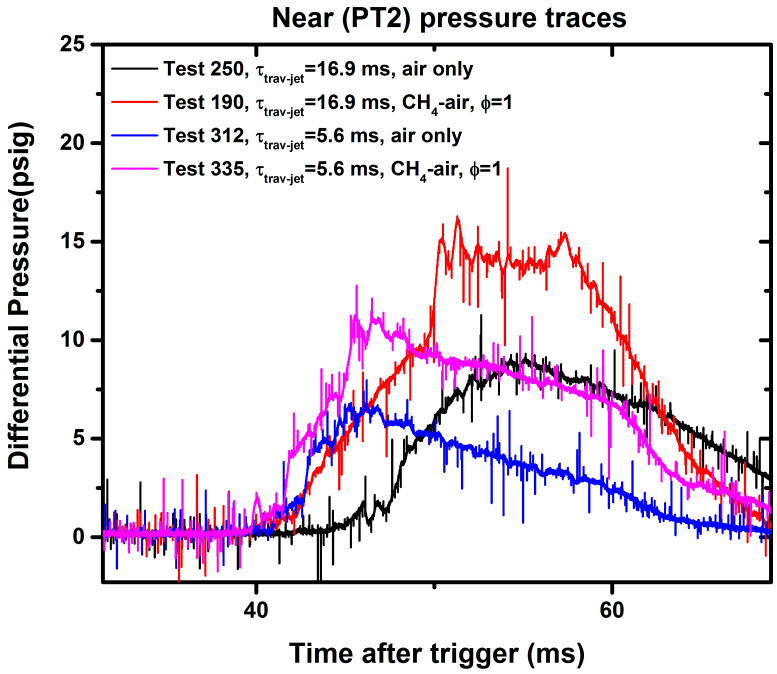

(a) Near (PT2) pressure traces.

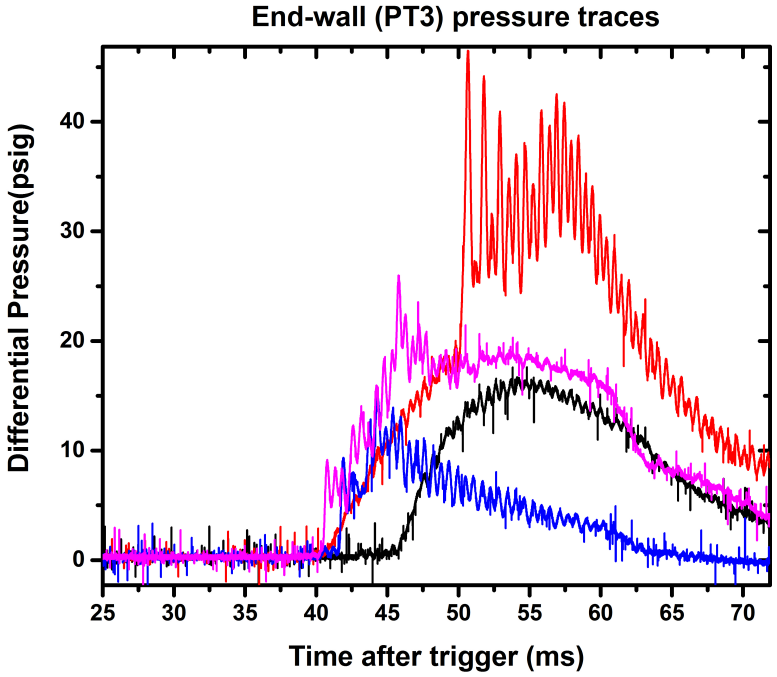

(b) End-wall (PT3) pressure traces.

Figure 4.2. : Pressure trace comparison between two non-reacting traversing hot-jet cases and two reacting traversing hot-jet ignition cases.

4.2 Pressure Trace Analysis

Pressure data from all the pressure transducers PT1, PT2, PT3 and PT4 are recorded. In this section, typical pressure traces for stationary hot-jet ignition and traversing hot-jet ignition are discussed. The pressure traces are utilized for validating the ignition moment with schlieren images from the camera and estimation of shock speed, rupture moment, ignition delay, maximum pressure and oscillation frequency of wave motion in chamber.

4.2.1 Stationary Hot-Jet

A typical pressure trace from a stationary hot-jet ignition test (no. 78) is shown in Fig. 4.3. The main chamber is fueled with methane-hydrogen (50%-50%) blend fuel and air mixture. From near and end-wall pressure trace it can be inferred that after the rupture of diaphragm at 42.31 ms two successive shock waves increases the pressure inside the main chamber by about 10 psig. Although the pressure value registered by the near PT is much less since its signal is attenuated. From the first rise in these traces the estimated shock speed is approximately 440 m/s. Using this speed, the rupture moment is estimated at 42.31 ms. The pre-chamber pressure trace also begins to show a oscillation at the same time. The end-wall pressure traces indicate onset of ignition at 46.37 ms after trigger. Schlieren images from the camera starting at 45.991 ms to 46.520 ms are examined and ignition is visually identified at 46.344 ms after trigger from the camera. The rise time of the pressure transducers causes a slight delay in registering the pressure event compared to the camera. The images also reveal the rapid expansion of the ignition kernel. This validates the pressure rise reported by the transducers to be a consequence of ignition. The ignition pressure rise also increases the pressure inside the pre-chamber Once the pressure rises due to ignition, the combustion event is characterized by rapid pressure oscillation. The flame front, which can be seen in rear schlieren images from another test, interacts with pressure waves and consequently retracts and expands again. This

event is discussed in the next subsection with schlieren images from test 98. Across all fuel-air mixtures subjected to different equivalence ratios the general trend of the pressure traces are same except for the magnitudes of the pressure rise and oscillation frequency.

4.2.2 Shock-flame Interaction

Pressure traces and schlieren images from from test 98 is given in Fig. 4.4. The rupture shock arrives at the end-wall at 48.554 ms after trigger and the end-wall pressure trace registers an increase in pressure due to the shock at 48.606 ms. The difference in time being the rise time of the PT. The reflected shock can be seen traveling backwards to the entrance of the chamber. After ignition these reflected shocks compresses and retracts the flame front (frame 25) at 50.317 ms after trigger. This increases the reaction rate of the reactant gases and volume expansion of products, which results in the production of further compression waves. These compression waves again compresses and retracts the flame front creating a feedback mechanism [7] that sustains the flame propagation until the reactants are consumed.

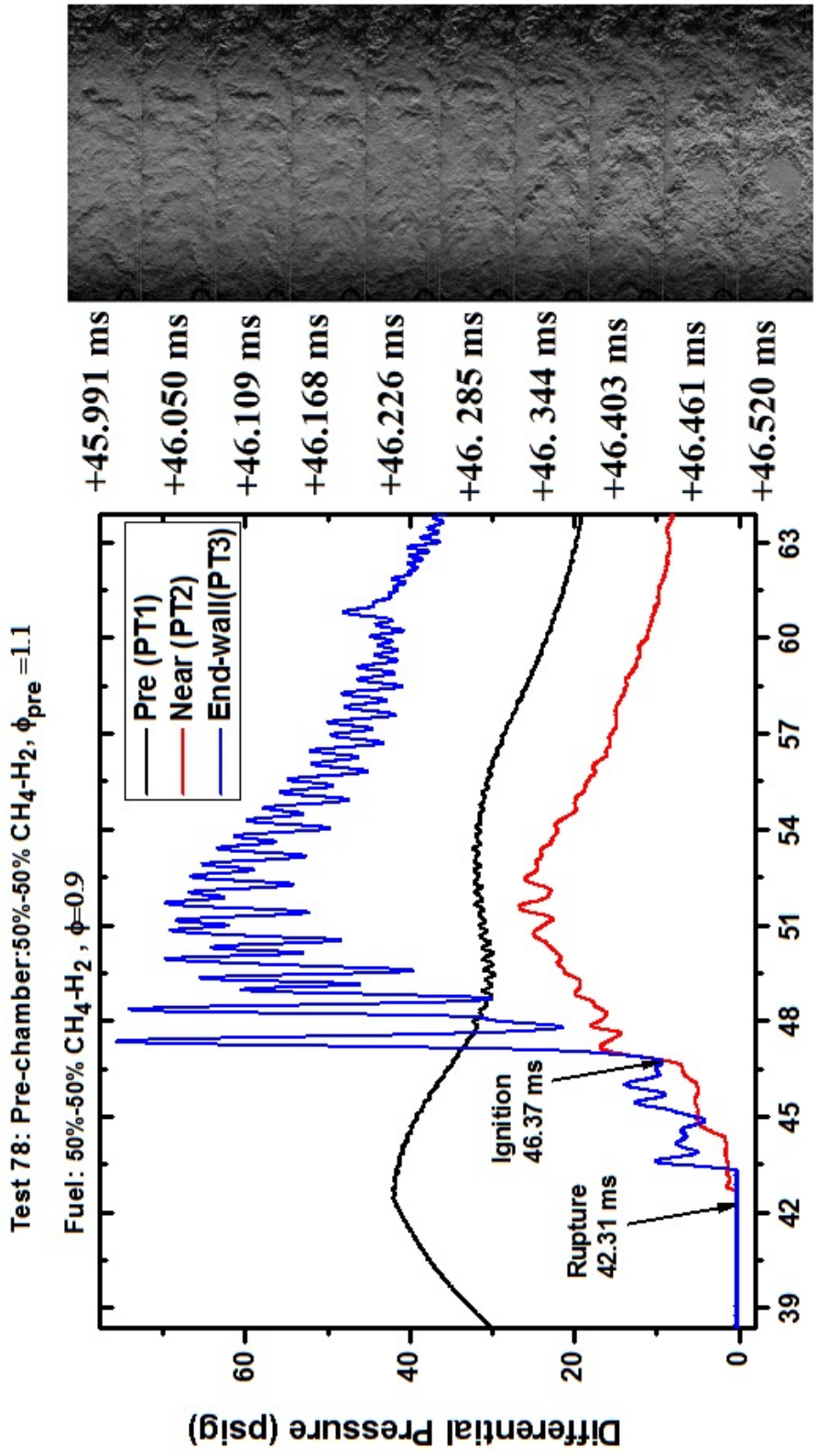

Figure 4.3. : Pressure traces associated with a stationary hot-jet ignition test 78.

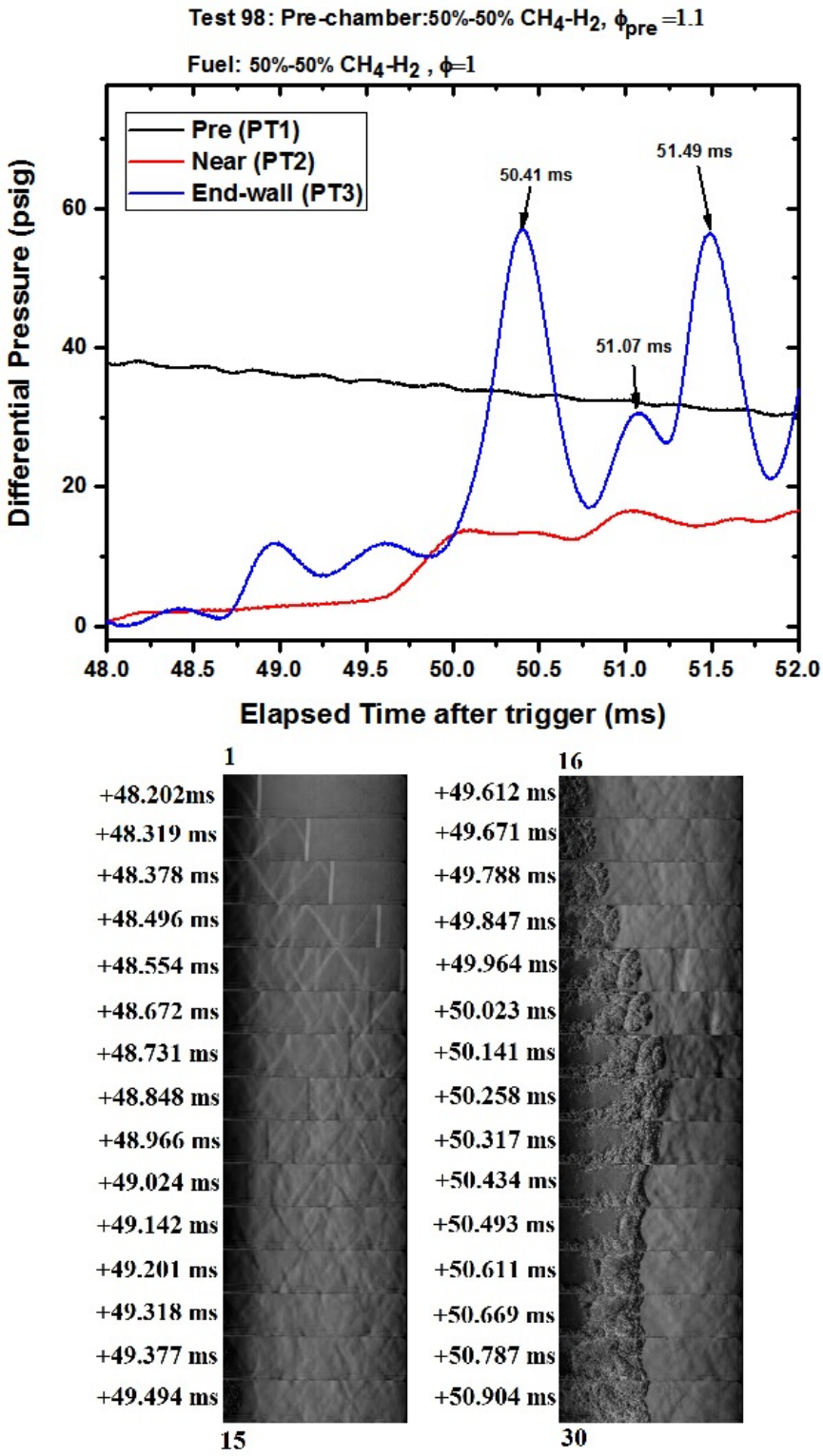

Figure 4.4. : Pressure traces associated with a stationary hot-jet ignition test 98.

4.2.3 Traversing Hot-Jet

The pressure traces from two traversing hot-jet ignition cases are discussed. Both test cases have stoichiometric methane-air mixture in the main combustion chamber. The difference between the two test cases is mainly in the variation of jet traverse time. Test 190 was conducted at 400 RPM (jet traverse time of 16.7 ms) and test 335 was conducted at 1200 RPM (jet traverse time of 5.6 ms). The pressure traces of both cases have many similarities with the stationary hot-jet typical pressure trace. Particularly, the initial shock wave pressurization, onset of ignition and oscillation due to shock-flame interaction. The noise due rotation of the pre-chamber and the resulting vibration of the copper rod carrying the spark plug is induced in the pressure traces. However, due to very fast response time of the pressure transducers and large magnitude change in pressure rise they are mostly attenuated. In test 190 (Fig. 4.5) after rupture and start of jet traverse motion an increase in pressure is seen from 40.19ms to the onset of ignition at 50.03 ms. The initial pressure rise is a consequence of both rupture shock pressurization and mass injection. Due to the relative longer jet traverse time of 16.9ms, the pressure rise after ignition essentially is a superposition of pressure rise due to combustion and pressure rise associated with mass injection. Jet traverse and mass injection ends at 57.09 ms where an increases in pressure observed. Due to the large eddies induced by a traversing jet, which grow in size with the progression of traverse, the pressure rise due to ignition is reduced. Moreover, traversing hot-jet ignition cases have significantly higher amount fuel-air mixture leakage, due to the seal plate design, that also reduces the pressure after ignition. The PT4 pressure transducer (whose pressure history is shown in Fig. 4.5) has different mounting configuration consisting of an associated volume for the combusted gas to expand and also tubing compared to the flush mounted PT3. PT4 is also spatially located ahead of PT3, therefore, it registers pressure rise earlier compared to PT3 and its pressure signal is slightly attenuated.

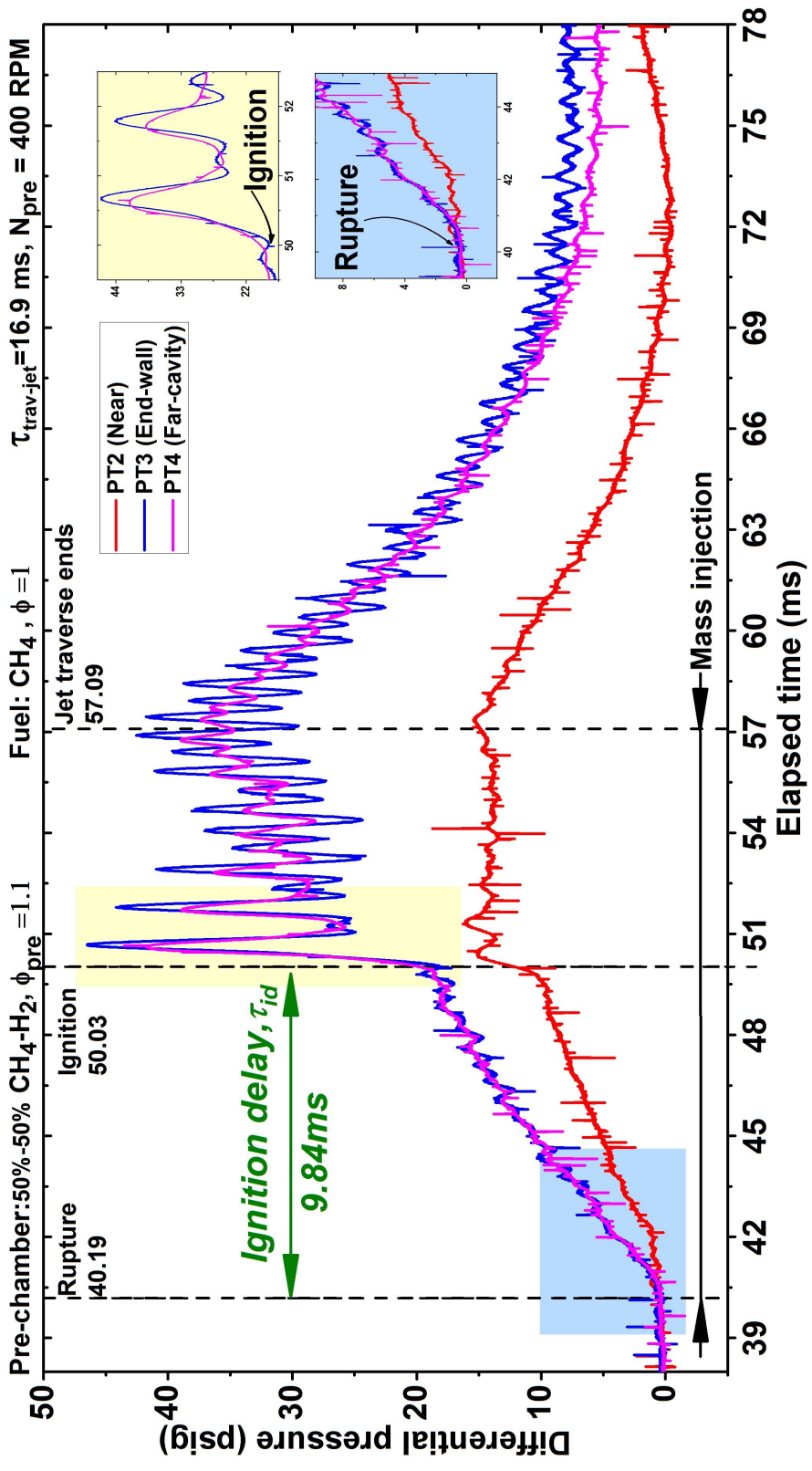

Figure 4.5. : Pressure trace of traversing hot-jet ignition test 190.Time resolved schlieren images are presented in Fig 4.6.

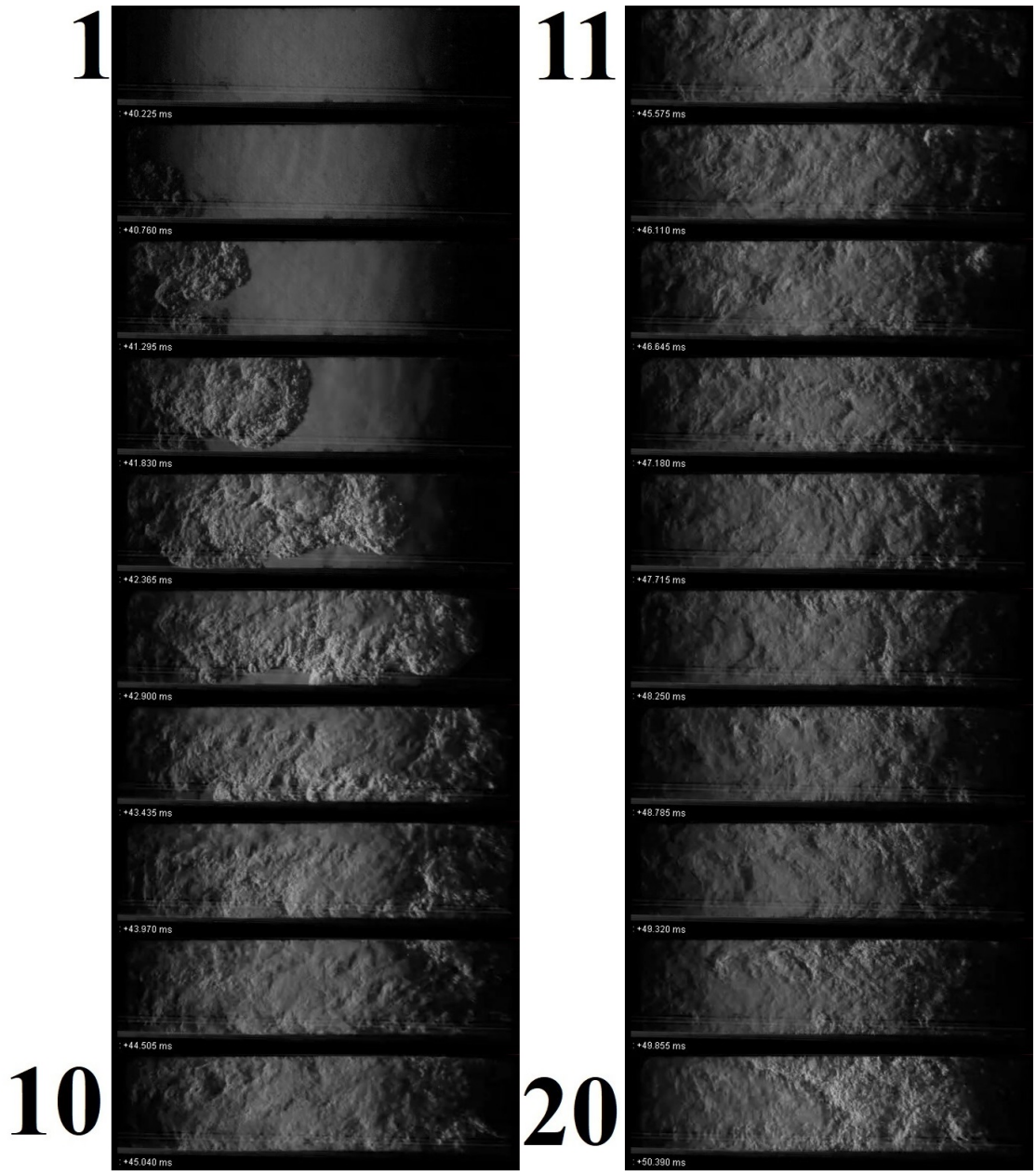

Figure 4.6. : Time-resolved schlieren images for test 190 from start of jet traverse to onset of ignition.

In test 190, ignition occurs about half-way through the traverse motion and mass injection continues to deposit chemically active radicals and combustion products in the flow field. However, in faster jet traverse time cases, the amount of deposited

radicals are much less and but the induced vortices are much stronger resulting better turbulent mixing and in particular for test 335(Fig. 4.7 reduces the ignition delay significantly. The pressure traces of test 335, which has a very short jet traverse time, is very similar to test 190. The primary difference being the magnitude of maximum pressure developed is less and oscillation after ignition is weaker. From the schlieren images, a curved bow shock initially increases the pressure inside the chamber. A major difference being the end of mass injection do not induce any change in the end-wall pressure trace, however, a sharp increase in near pressure trace is observed. This indicates complex interaction between the vortices and shock wave. The initial shock for traversing hot-jet ignition cases is much more distorted or curved compared to stationary hot-jet cases. To better understand the acoustic wave produced by shock distortion and vortex compression, the pressure traces of an isolated vortex may be compared [63]. Another key difference is that the burning of the reactants after ignition for a faster traversing jet is slower compared to a slower traversing jet. Because the magnitudes of pressure oscillations after ignition are much lower for test 335 compared to test 190.

All the traversing hot-jet ignition pressure traces exhibits these general characteristics of test 190 and test 335.

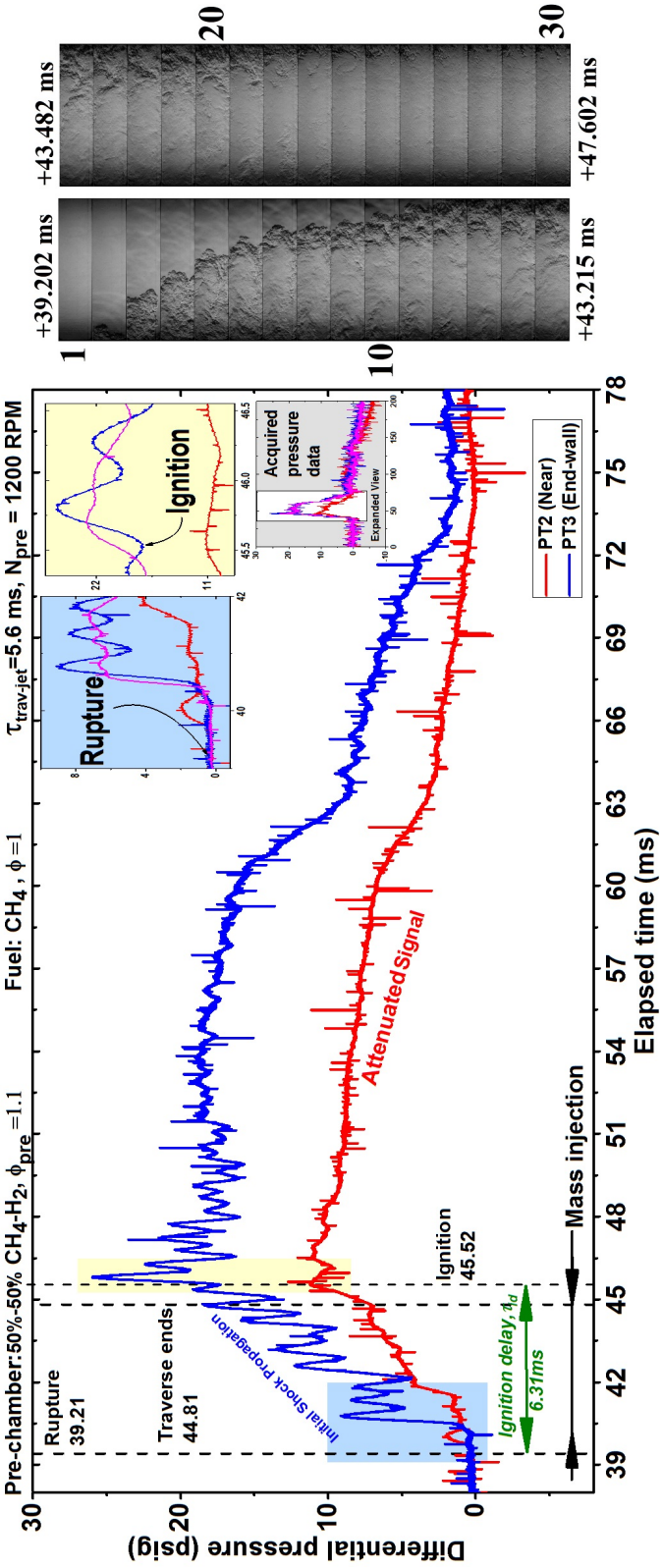

Figure 4.7. : Rise in pressure traces of test 335. In the schlieren images ignition occurs between frame 22 and 23 which are at 45.248 ms and 45.569 ms after trigger respectively.

4.2.4 Repeatability

Near and end-wall pressure traces of 9 stoichiometric propane-air mixtures ignited by a stationary hot-jet (50%-50% methane hydrogen at 1.1 equivalence ratio) are compared in Fig. 4.8. It is observed that they have the same trend for all the cases with major differences being the rupture moment, onset of ignition and maximum pressure. The variation in theses values may be a consequence of stratified mixture in the main combustion chamber and the manner and moment of diaphragm rupture. Since the stratification may not be replicated in the same manner as well as the issued hot-jet having its own mass entrainment characteristic that also varies from test to test, the variation in the pressure traces are expected. However, the pre-chamber mixture typically made 30-60s before conducting the ignition tests. The pre-chamber fuel-air mixture is likely well mixed compared to the main chamber fuel-air mixture. Later, laminar flame propagation experiments revealed, mixture stratification and buoyancy of lighter and heavier fuels inside the chamber. This suggests that during hot-jet ignition experiments, the formation of initial ignition kernel may occur at different local equivalence ratio of the fuel-air mixture inside the main combustion chamber instead of the defined global fuel-air equivalence ratio. As shown in Figs. 4.9 and 4.10, this effect is much more pronounced for traversing hot-jet ignition cases where the variations in pressure under same experimental conditions are much higher because of the possibility of the jet being issued slightly earlier than required or fuel-air mixture leakage. Examining the schlieren images in Fig. 4.10, it can be observed that the jet may be issued slightly earlier, causing weak rupture shock to propagate for test 274. Schlieren images for test 277 revealed some fuel-air mixture appearing near the bottom of the chamber entrance.

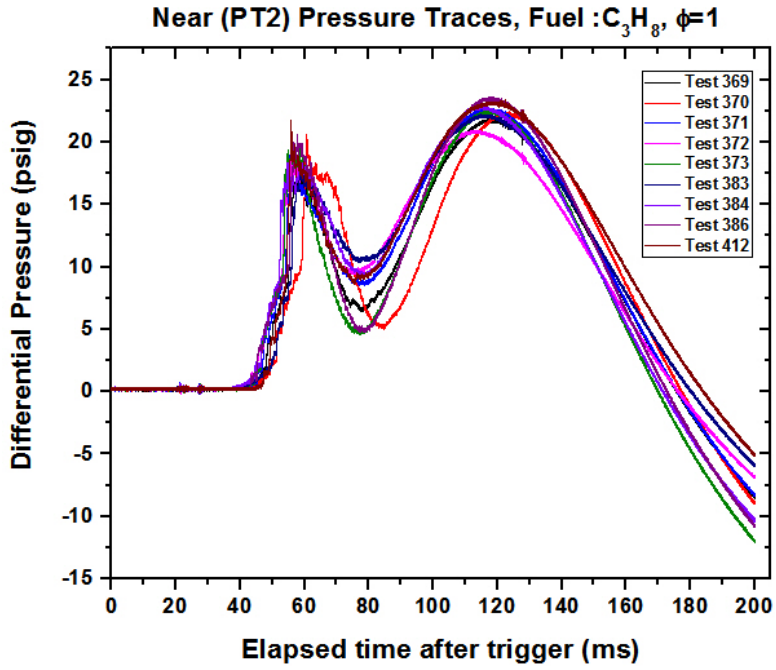

(a) Near pressure traces.

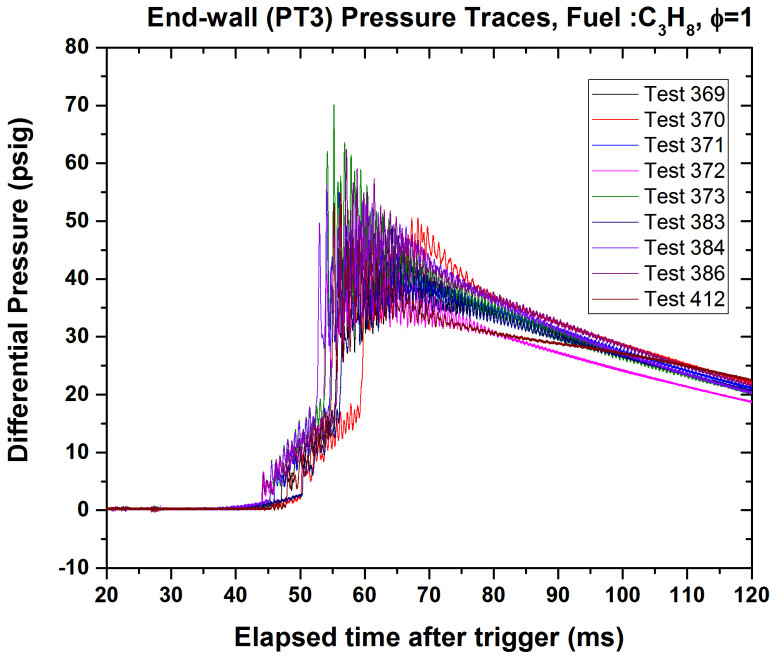

(b) End-wall pressure traces.

Figure 4.8. : Nine stoichiometric propane-air stationary hot-jet ignition near and end-wall pressure traces comparison.

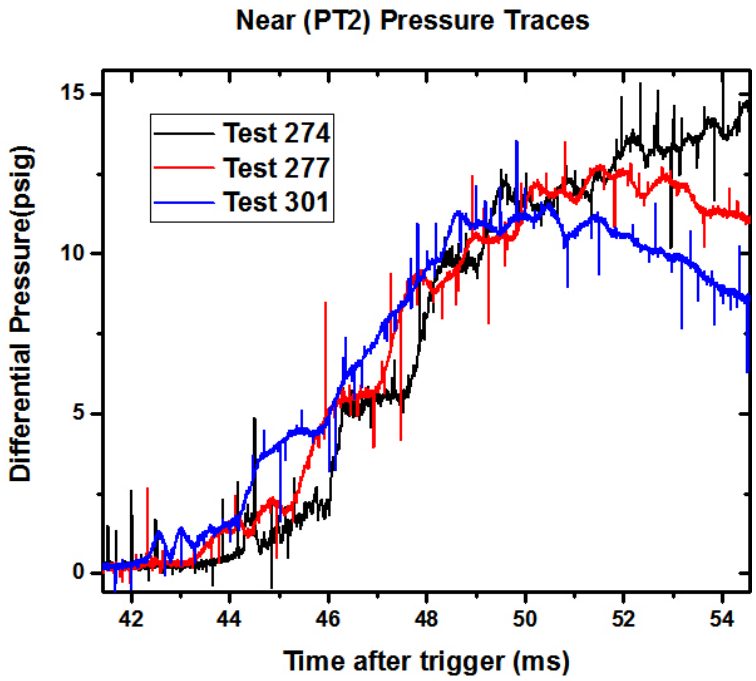

(a) Near(PT2) pressure traces.

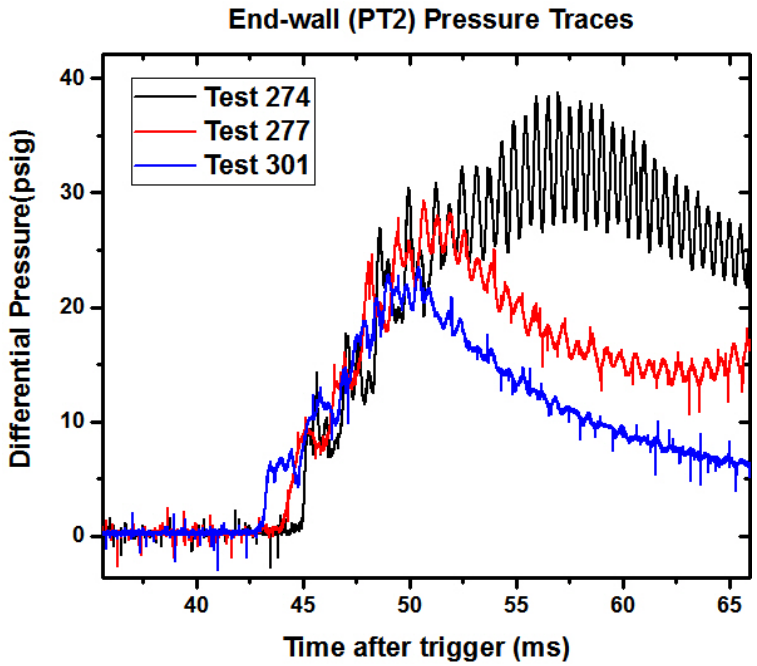

(b) End-wall(PT3) pressure traces.

Figure 4.9. : Comparison of pressure traces of three stoichiometric 50%-50% methane-hydrogen-air ($\phi = 0.7$) cases. The jet traverse time for all the cases are 8.4 ms.

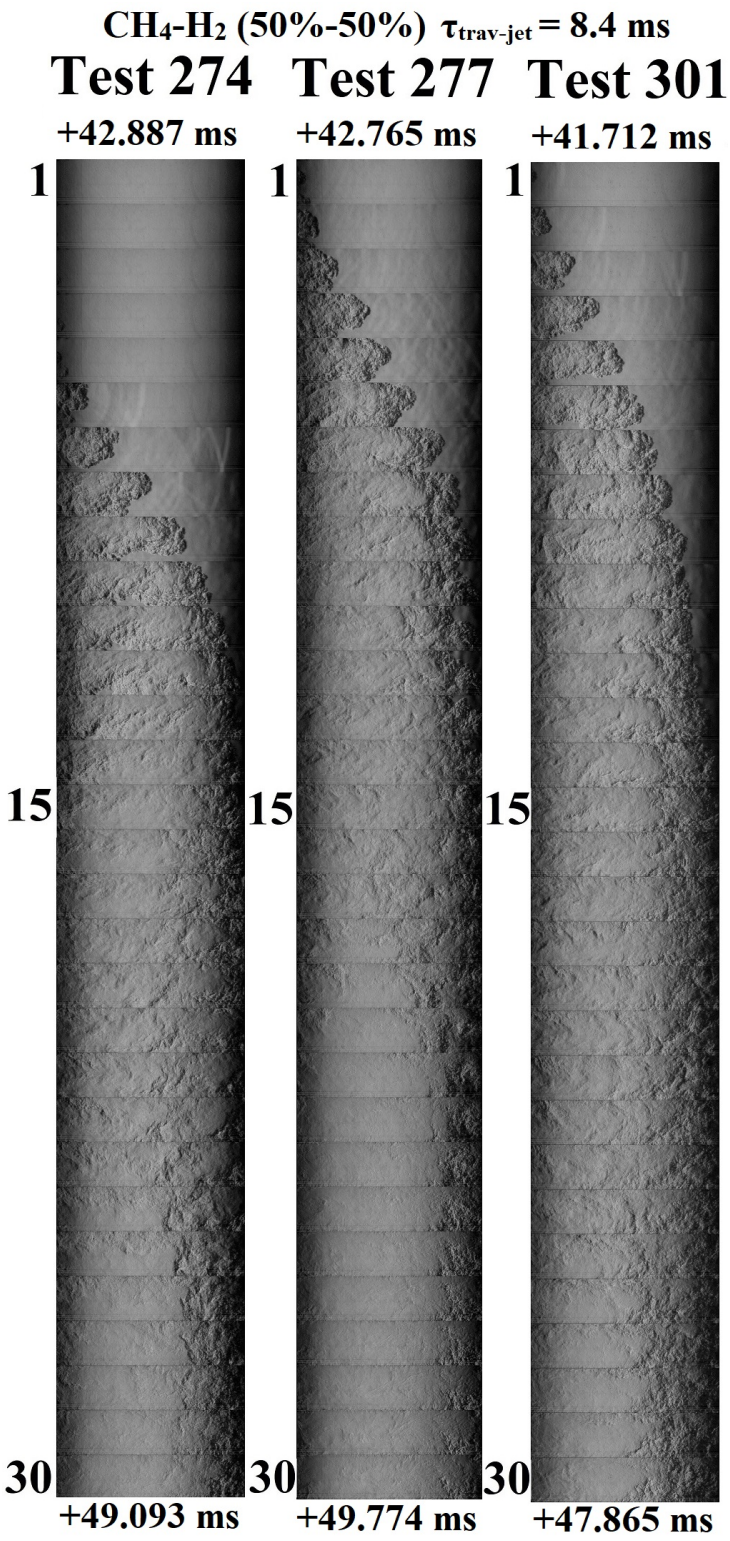

Figure 4.10. : Schlieren images of three stoichiometric 50%-50% methane-hydrogen-air ($\phi = 0.7$) traversing hot-jet ignition experiment.

4.3 Schlieren Image Sequence

4.3.1 Effect of Equivalence Ratio

Figs. 4.11 and 4.12 depict sequence of schlieren images showing ignition moments from 4 test cases with the same 50%-50% methane-hydrogen fuel-air mixture and 46.4%-53.6% methane-argon fuel-air mixture. Typically, the rupture shock propagates and reflects back from end-wall. The injection of mass gradually increases pressure inside the chamber. At the onset of ignition, a small kernel forms and progressively grows. The schlieren images reveal formation of the kernel through variation in density and relatively darker regions surrounding the kernel. With increase in equivalence ratio, the ignition moment is typically delayed. The methane-argon cases does not demonstrate any significant qualitative difference from the other fuels, although having same density as air this fuel is expected to have better mixing with the air inside the channel

4.3.2 Effect of Fuel Reactivity

Figs. 4.13 and 4.14 depicts hot-jet ignition of six stoichiometric fuel-air mixtures by a stationary hot-jet. The ignition kernel forms earlier for a reactive fuel and the initial growth of the kernel is also much faster. As discussed in chapter 3, the addition of hydrogen has much more significant effect on the ignition delay compared to saturated hydrocarbons with higher hydrogen content. Therefore, the variation of ignition delay for more reactive hydrocarbon such as propane, compared to methane is very small. The methane-propane blend, in fact have longer ignition delay time, suggesting the fuel being highly stratified in the chamber. Since ignition is typically faster at lower equivalence ratios, a highly stratified mixture near chamber entrance would a have mostly rich zones and consequently take a long time to ignite.

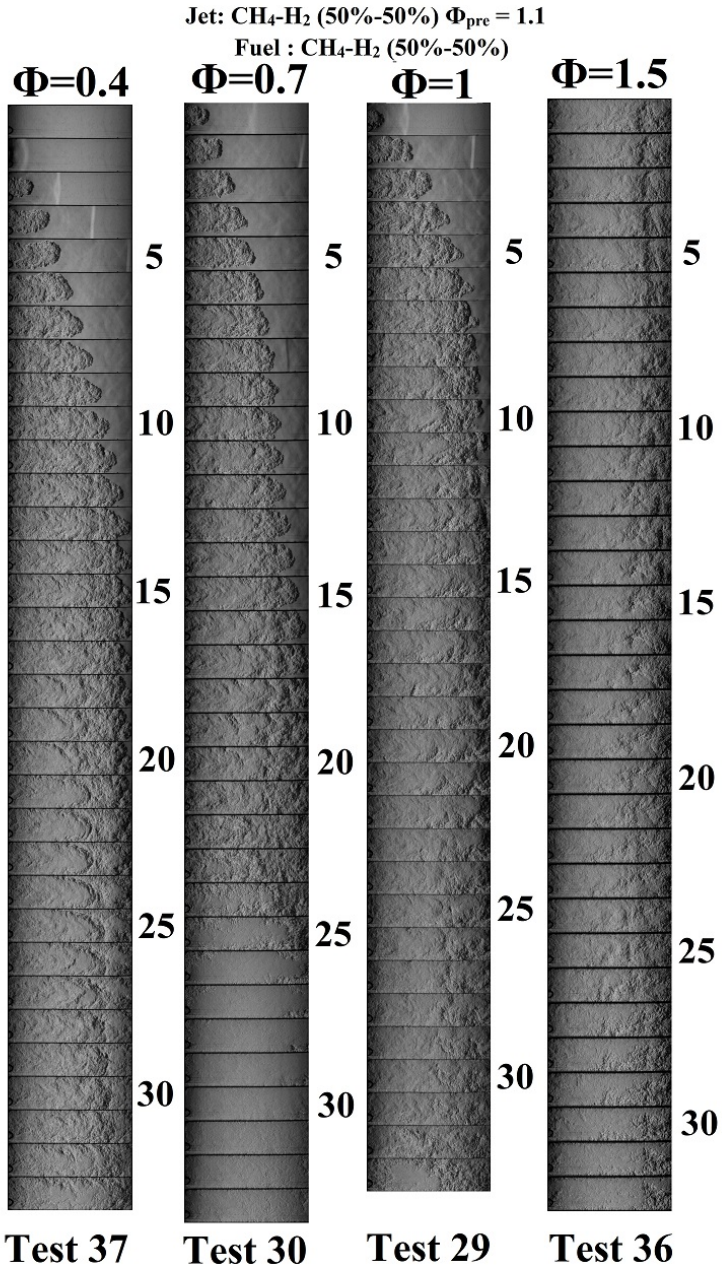

Figure 4.11. : Ignition moments at different equivalence ratios for 50%-50% $CH_4 - H_2$ fuel at P = 1 atm and T = 296 K. Beginning from left, time between each frame is 0.117, 0.176, 0.235 and 0.352 ms , total time of each image strip is 3.744, 5.632, 7.285 and 11.264 ms and absolute time at frame 1 are 44.639, 42.921, 44.235 and 52.680 ms from trigger respectively.

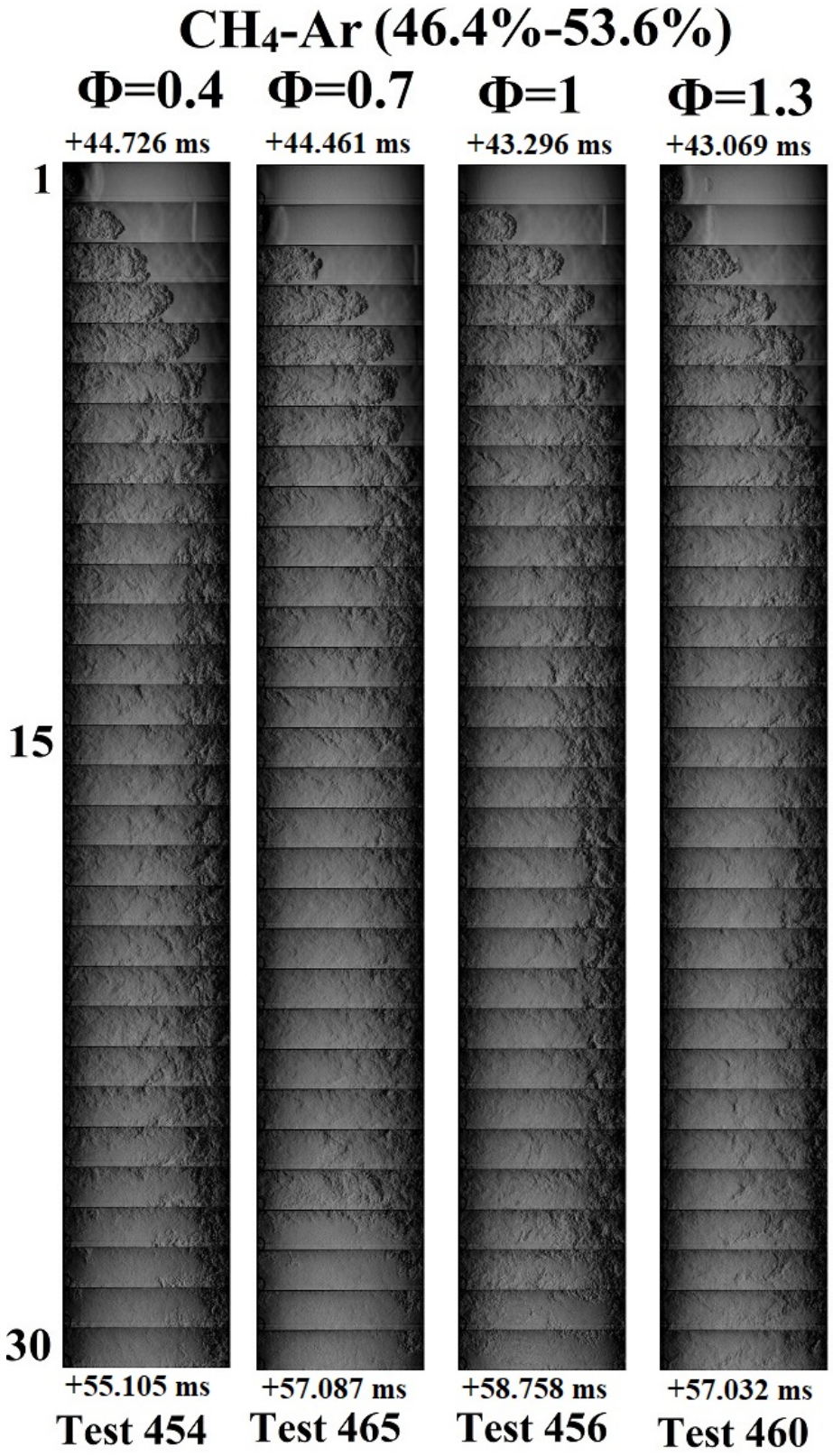

Figure 4.12. : Ignition moments at different equivalence ratios for $CH_4 - Ar$ fuel at P = 1 atm and T = 296 K.

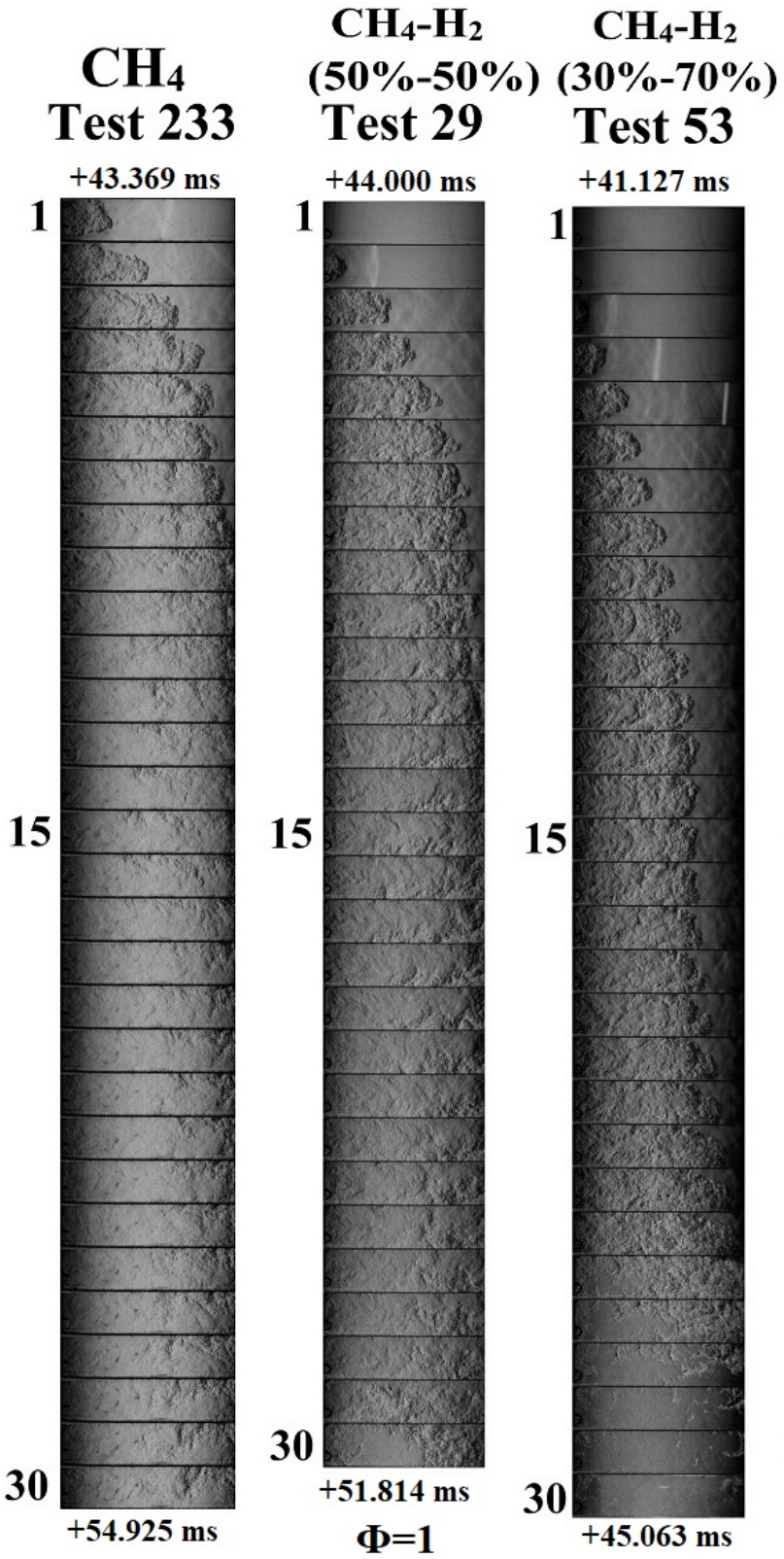

Figure 4.13. : Schlieren images of jet entrance to ignition for CH_4, $CH_4 - H_2$ (50%-50%) and $CH_4 - H_2$ (30%-70%) stoichiometric fuel-air mixtures.

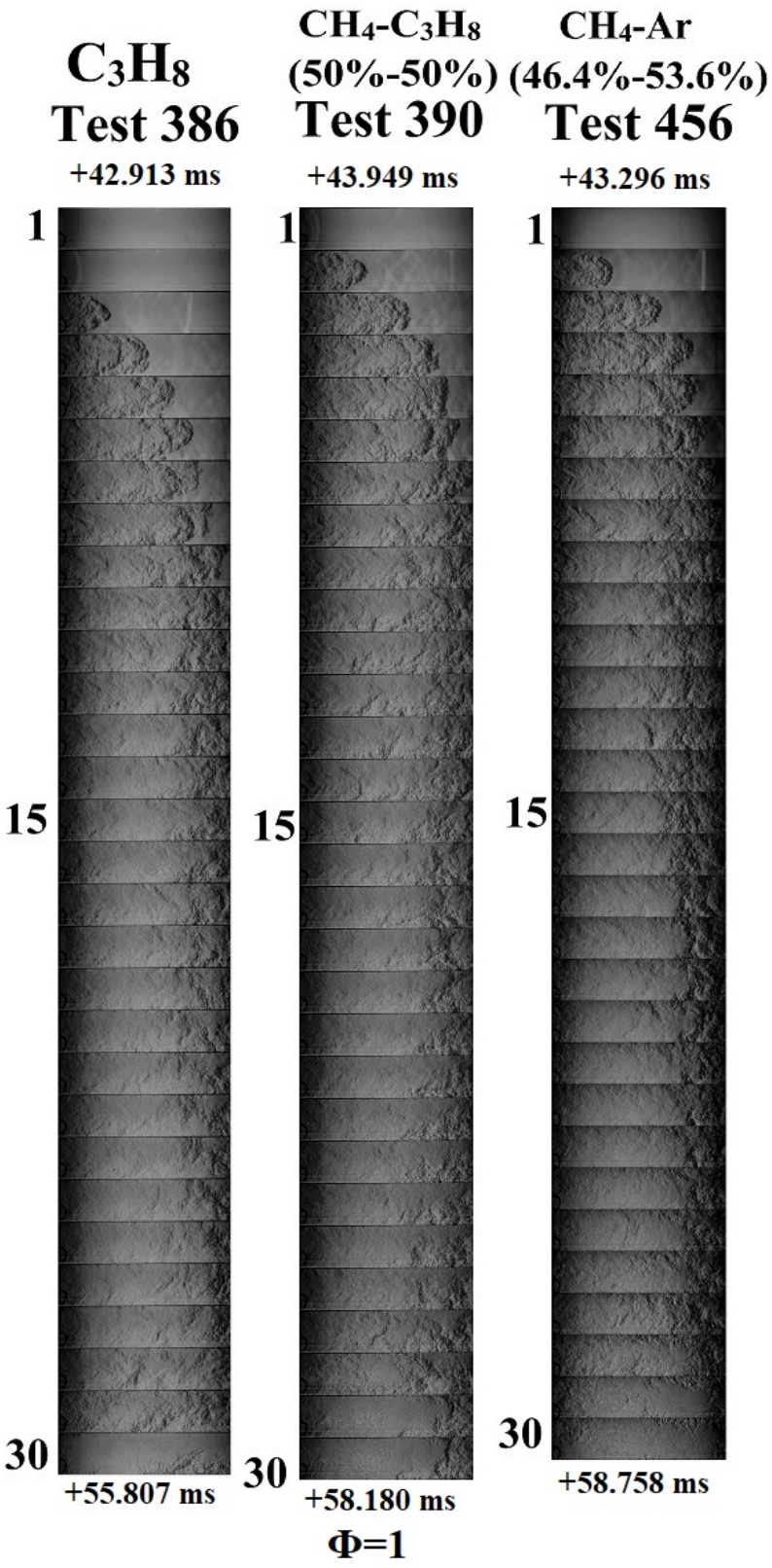

Figure 4.14. : Schlieren images of jet entrance to ignition for C_3H_8, $CH_4-C_3H_2$ (50%-50%) and $CH_4 - Ar$ (46.4%-53.6%) stoichiometric fuel-air mixtures.

4.3.3 Effect of Jet Traverse Time

With an increase in jet traverse time, pure methane exhibited shorter ignition delay and schlieren images of 3 test cases are presented in Fig. 4.15. Typically, the traversing hot-jet enters the chamber, and starts traversing from the top corner of schlieren camera view. As the the jet travels across the entrance of the chamber, vortices are induced, similar to the ones shown in Fig. 1.10. The vortices enhance mixing, and qualitatively, with faster jet traverse time they occupy larger space in the flow field reaching near the fueling port. However, longer jet traverse times produce vortices, small in size, but carrying more reactive radicals fed by the jet during the traverse motion. Ignition kernel appears near the end but before the completion of traverse motion of the jet, particularly for 16.9 ms and 8.4 ms cases. For 5.6 ms jet traverse time, typically ignition occurs after the jet traverse motion is completed. The location of the initial ignition kernel is difficult to identify for traversing jet cases, due to the presence of vortex structures.

4.3.4 Initial Shock Speed

Fig. 4.16 gives the measured shock speeds. The shock speeds are validated using the high speed camera images. Most of the shock speed for stationary hot-jet cases are within the range of 325 m/s to 450 m/s with the most reactive fuel the methane-hydrogen 50%-50% blend being the highest. It is also observed that this blend being the lightest of all the fuels tested has the highest variation in the measured shock speeds. For traversing hot-jet ignition cases, shown in Fig. 4.16(b), for three jet traverse times, the shock speeds range within 320 m/s to 380 m/s.The estimated shock speeds for most fuel and traverse time combinations are lower than the estimated shock speeds of methane-hydrogen 50%-50% blend fuel stationary cases.

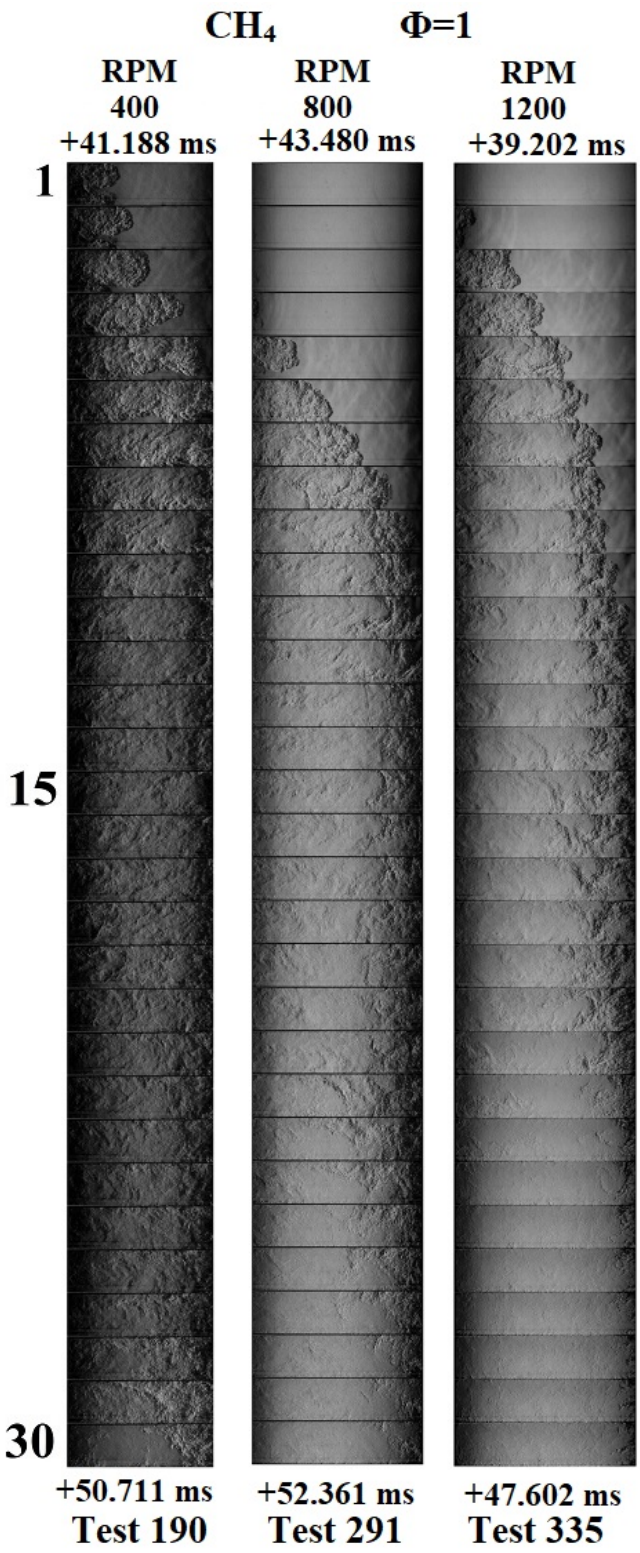

Figure 4.15. : Schlieren images of traversing jet entrance to ignition for various stoichiometric methane-air mixtures at jet traverse times of 16.9 ms, 8.4 ms and 5.6 ms from the left respectively.

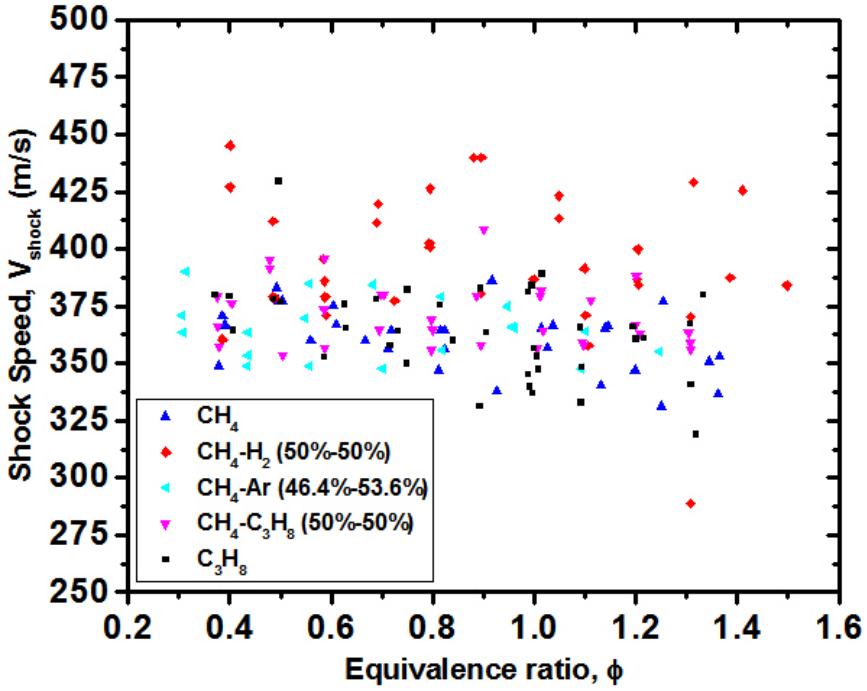

(a) Stationary hot-jet ignition tests.

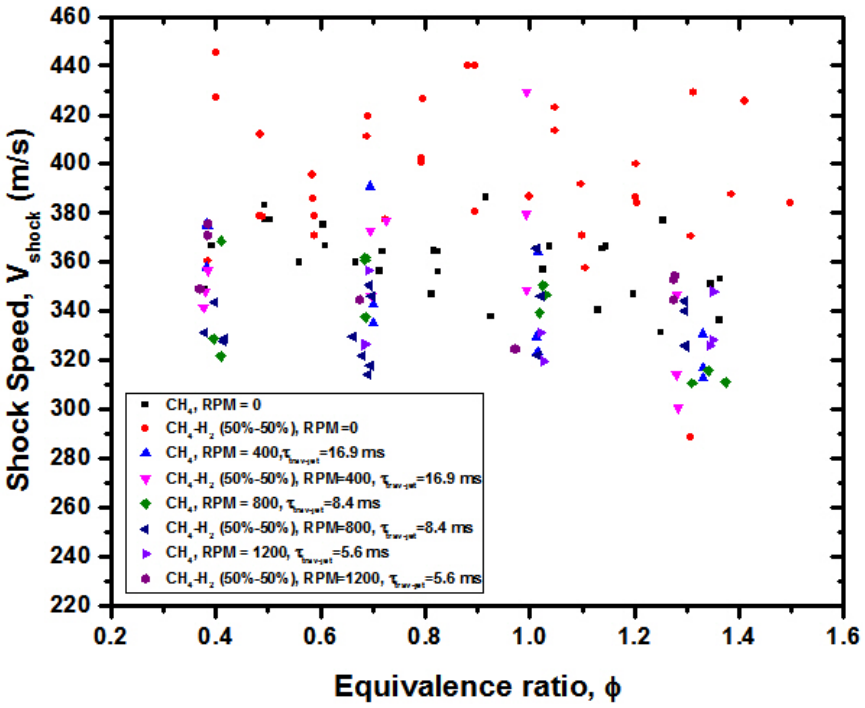

(b) Traversing hot-jet ignition tests.

Figure 4.16. : Scatter plot of measured shock speeds for hot-jet ignition cases.

4.4 Ignition Delay

4.4.1 Definition and Methodology

The definition of ignition delay time is dependent on two time events, namely the event characterizing fuel injection into the combustion chamber and the ignition event itself. How these two time events are identified varies among different researchers due to constraints imposed by the ignition phenomena they are studying and also due to available equipments and instrumentation [6]. Perera defined ignition delay time from the diaphragm rupture moment to the ignition moment observed from the high-speed Phantom camera. The ignition moment from the camera was obtained by processing the luminosity images captured from the camera and validated by matching the pressure histories from the pressure transducers located in the main chamber [6]. Chinnathambi considered the diaphragm rupture moment to occur 0.2 ms from the first instance of the jet appearing in the luminosity images captured by the high-speed Phantom camera and defined ignition delay, for a traversing jet, as the time interval from this definition of rupture moment to the ignition event which was identified from the luminosity images [55]. Paik [7] employed a methodology (similar to Perera's rupture moment estimation using pressure traces [6] to estimate the rupture moment. The diaphragm rupture shock propagates into the main combustion chamber and by tracing the pressure at two different locations, the shock velocity can be measured. Using the shock velocity and the length of the chamber, the diaphragm rupture moment can be estimated. The estimated rupture moments were validated by measuring the rupture moment from the time-resolved schlieren images captured by the high speed camera. The ignition moment was characterized by sharp rise in the pressure history of a flush mounted pressure transducer [7]. Ignition delay is then defined as the time interval between the diaphragm rupture moment and the ignition moment. Kojok [38] estimated ignition delay for fuel-air mixtures, where the air was pre-heated, by the same methodology.

In the present study, the same methodology is applied for estimation of diaphragm rupture moment for traversing and stationary jet cases. However, for the methodology to be applicable, the propagating shock must be clearly seen in the image recorded by the camera. The ignition moment can be identified if the pressure trace is highly time-resolved. To estimate the shock speed, the moment of first pressure rise due to shock from near pressure transducer(PT2) and the moment of first pressure rise due to shock from the end-wall pressure transducer(PT3) are recorded. The distance between the two transducers is 10.22 inches. For example, the shock speed for the case shown in Fig. 4.17 is $\frac{10.22in}{0.66ms} \approx 15500$ inch/s or 393 m/s. Using the shock speed and knowing the distance from the diaphragm to the end-wall pressure transducer the rupture moment is estimated. The ignition delay is defined as the time difference between the diaphragm rupture moment to the moment of onset of ignition or ignition moment.

The ignition moment is characterized by sudden rise in end-wall pressure trace. For traversing hot-jet ignition experiments this methodology is also applied, since pre-chamber pressure trace for these tests are not available.The present methodology, however, can only be applied to traversing hot-jet ignition experiments when the rupture shock can be clearly seen entering the main chamber. If the shock cannot be seen clearly in the schlieren images, diaphragm rupture could occur earlier or later than the calculated rupture moment.

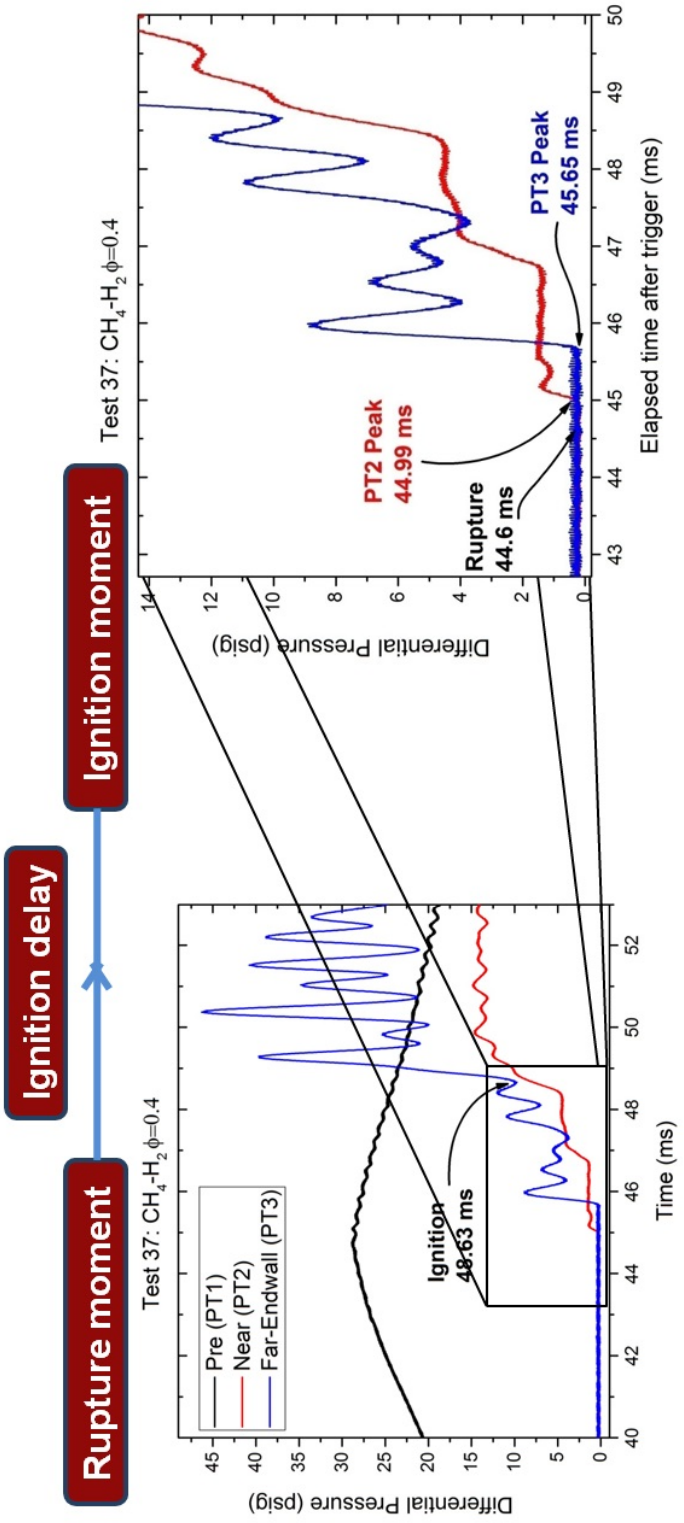

Figure 4.17. : Estimation of shock speed and ignition delay from pressure traces.

4.4.2 Ignition Delay Times

The measured ignition delay times for various fuel-air mixtures ignited by a slightly rich stationary hot-jet is plotted in Fig. 4.18. There is a global increasing trend of ignition delay with increasing equivalence ratio is present. The minimum ignition delay is expected to occur within the range of $\phi = 0.4$ to $\phi = 0.6$. Beyond this minimum the increasing trend continues till $\phi = 1$. For rich fuel-air mixtures, the blended fuels exhibit large variations in ignition delay. Whereas, pure fuels such as methane and propane, exhibits an increasing trend. The variation in ignition delay values are a consequence of the mixture being stratified. Even with the methane-argon blend fuel, which improves the stratification to some extent, these variation still remain. However, the methane-argon blend exhibits longitudinal mixture stratification, therefore, the effective local equivalence ratio is much higher then the calculated global equivalence ratio. Addition of hydrogen reduces ignition delay. The ignition delay for a more reactive fuel such as propane compared to methane is also shorter. However, addition of argon exhibited longer ignition delay times, suggesting that it may be possible that even with the addition of argon may not be enough to ensure good mixing. CFD modeling may required to validate this assumption since the fuel-air mixture stratification or longitudinal and transverse mixing effects on ignition delay are not known.

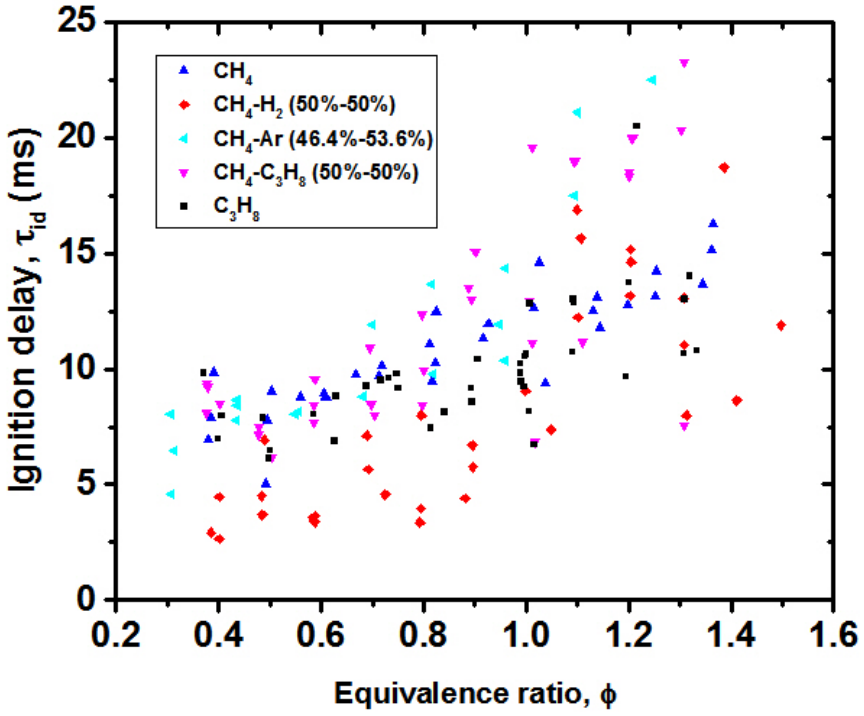

(a) Scatter plot of ignition delay of several fuels ignited by a stationary hot-jet.

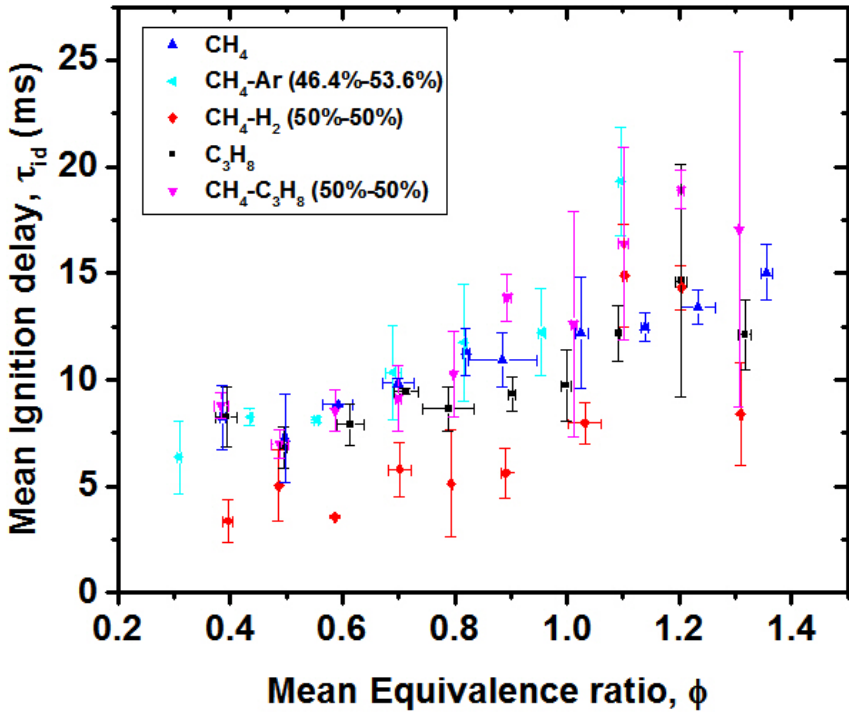

(b) Mean and standard deviation in stationary hot-jet ignition delay.

Figure 4.18. : Stationary hot-jet ignition delay for various fuels.

Fig. 4.19 gives the estimated ignition delay for methane and methane hydrogen blend fuel-air mixtures ignited by slightly rich traversing hot jets. It is important to keep in mind that the traversing hot-jet ignition cases have effectively very small to zero mixing time. Mixing time is defined as, the moment from end of fuel injection in the main chamber to the initiation of spark trigger inside the pre-chamber. Because of very small mixing time and leakage of fuel-air mixture, the local and global equivalence ratios may differ significantly. For methane-air mixtures, mean ignition delay increases with mean global equivalence ratio and with shorter jet traverse times, ignition delay is decreased. Although at 1200 RPM, the shortest jet traverse time, ignition is difficult to achieve. 0.4 mean global equivalence ratio cases did not ignite. This trends are also present in the 50%-50% methane-hydrogen fuel case. However, for this fuel, at lean global mean equivalence ratios, the jet traverse time effect is inversed. The ignition delay actually increases, even though the fuel is more reactive. At 1200 RPM, very few cases ignited and even when they ignite the ignition delay barely varies with increasing equivalence ratio. The methane-hydrogen blend fuel, having molecular weight of 9.03, is very light and for this fuel, fuel-air mixture being stratified to the top is very likely, making it very difficult to ignite. Because the local equivalence ratio is expected to be very high in the stratified region. Moreover, due to heat transfer to the walls, ignition would be difficult to achieve there.

To better understand the effect of jet traverse time on ignition delay, traversing hot-jet ignition test points in Fig. 4.19 are plotted for each nominal equivalence ratio in Fig. 4.20. With increasing jet traverse times or decreasing pre=chamber rotating speeds, ignition delay times increase for both fuels with the relatively more reactive methane and hydrogen blend fuel exhibiting shorter ignition delay times.

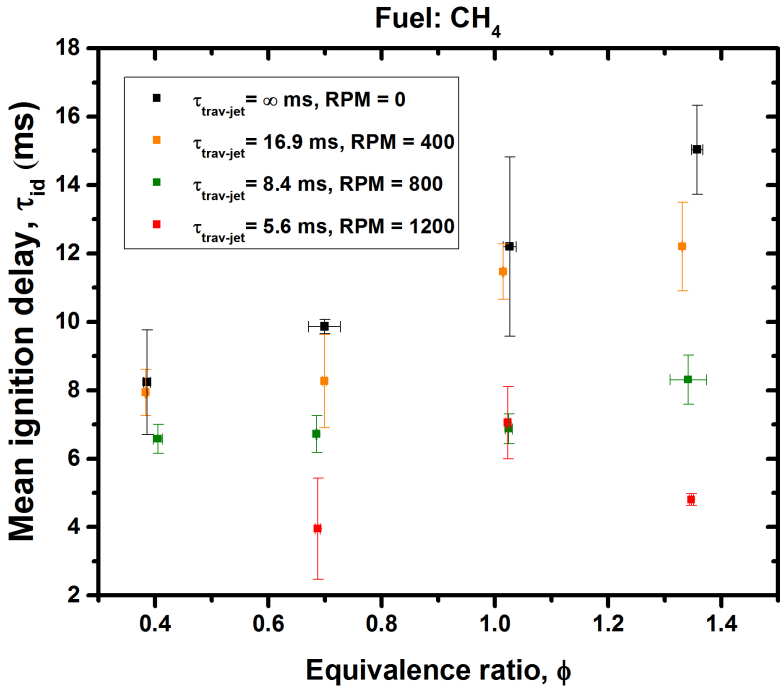

(a) Ignition delay of methane-air mixtures.

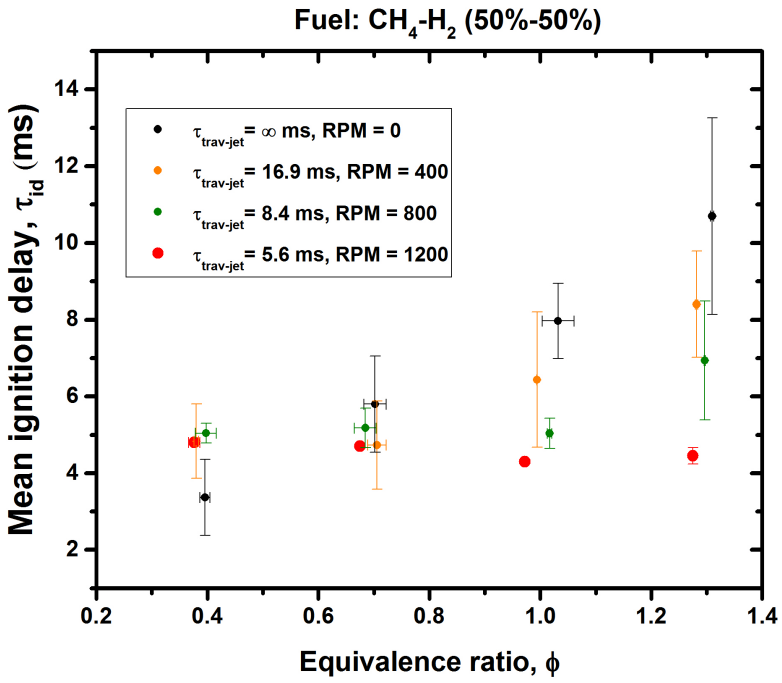

(b) Ignition delay of methane-hydrogen-air mixtures.

Figure 4.19. : Traversing hot-jet ignition delay for methane-air and methane-hydrogen-air mixtures under different equivalence ratios and jet traverse times.

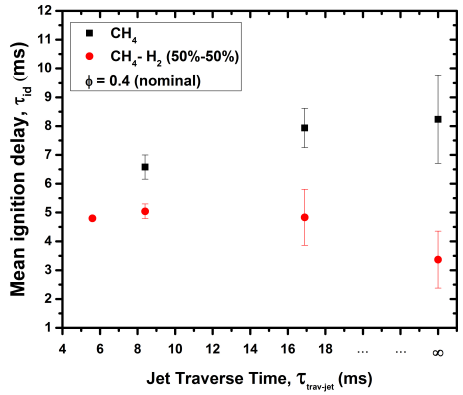

(a) Nominal equivalence ratio = 0.4.

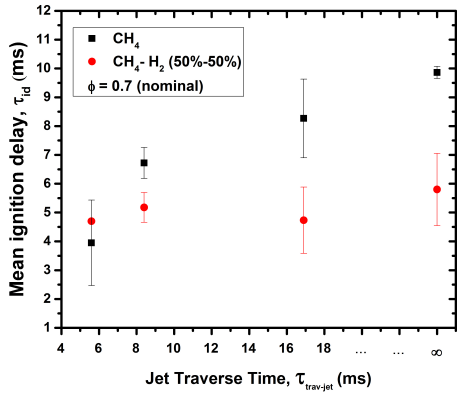

(b) Nominal equivalence ratio = 0.7.

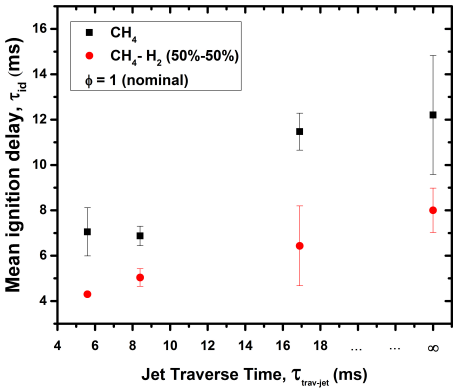

(c) Nominal equivalence ratio = 1.

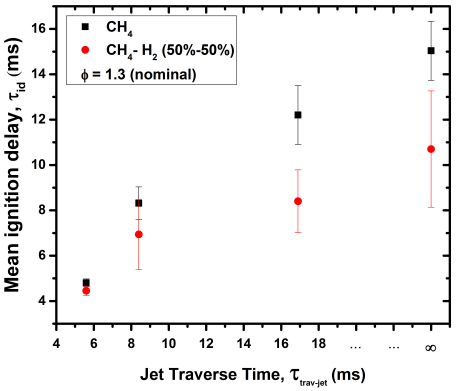

(d) Nominal equivalence ratio = 1.3.

Figure 4.20. : Effect of jet traverse time on ignition delay at different nominal equivalence ratio. $\tau_{trav-jet} = \infty$ refers to ignition by a centered stationary jet.

4.5 Maximum Pressure

The maximum pressure developed in the chamber varies with equivalence ratio. Fig. 4.21 shows the maximum pressure developed in the main combustion chamber for stationary hot-jet ignition test cases. Except for methane-air and methane-argon-air mixtures, the maximum pressure increases with increasing equivalence ratio and between $\phi = 0.8$ to $\phi = 1.1$ the peak maximum pressure in the chamber is achieved. For methane-air mixture, maximum pressure continues to increase with increasing equivalence ratios. Methane-argon-air mixture has the same general trend, similar to the other fuels, except the peak maximum pressure is achieved between $\phi = 0.5$ to $\phi = 0.8$. Typically, the maximum pressure is expected between between $\phi = 1$ to $\phi = 1.1$. Because, combustion at stoichiometric fuel-air mixture yields the maximum temperature and at such temperature due to dissociation, molecular oxygen is present in the reactants that partially combust additional fuel. The maximum pressure attained for globally lean fuel-air mixtures suggest that locally the fuel-air mixtures may be rich and dissociation is taking place and causing maximum pressure rise.

Among the traversing hot-jet cases shown in Fig. 4.22, the maximum pressure is achieved for the slowest traversing methane-hydrogen blend fuel case. For stoichiometric methane-air mixtures, faster traversing jets results reduced maximum pressure in the chamber. Comparing Fig. 4.22 and Figs. 4.21(b) and 4.21(d), it can be seen that maximum pressure achieved in traversing hot-jet ignition experiments, due to the higher leakage rate of fuel-air mixture and also due to amount of mass addition is mostly lesser than the maximum pressure developed in the similar stationary hot-jet ignition cases for similar fuels at similar equivalence ratios.

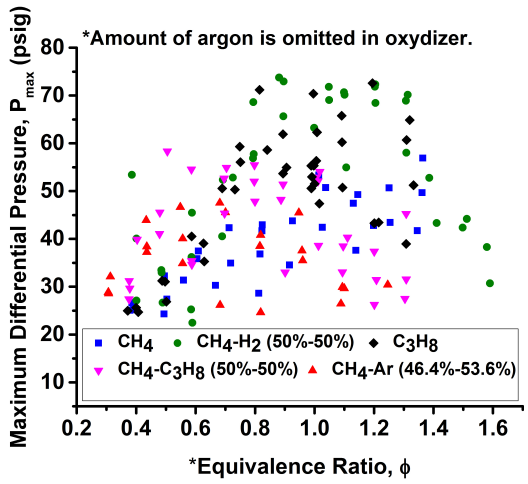

(a) All mixtures.

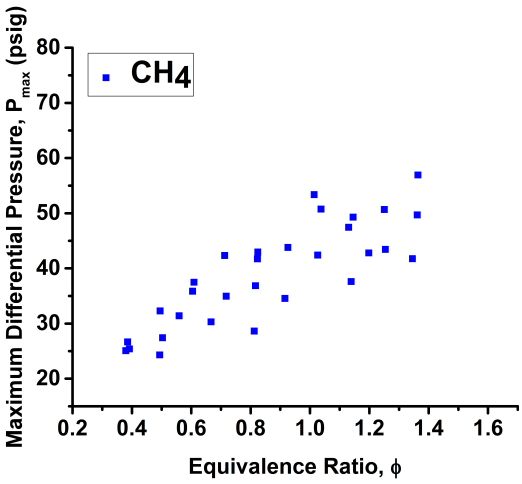

(b) Methane-Air mixtures.

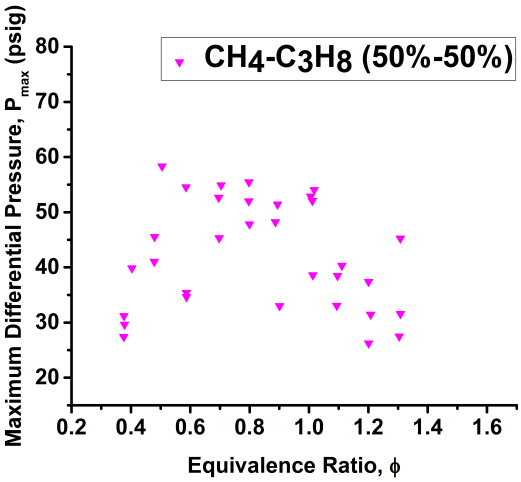

(c) Methane-Propane-Air mixtures.

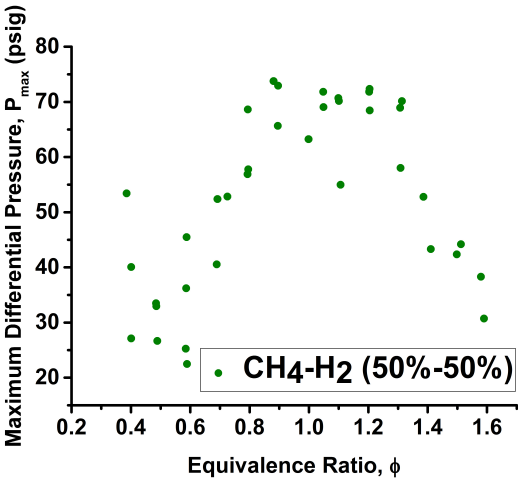

(d) Methane-Hydrogen-Air mixtures.

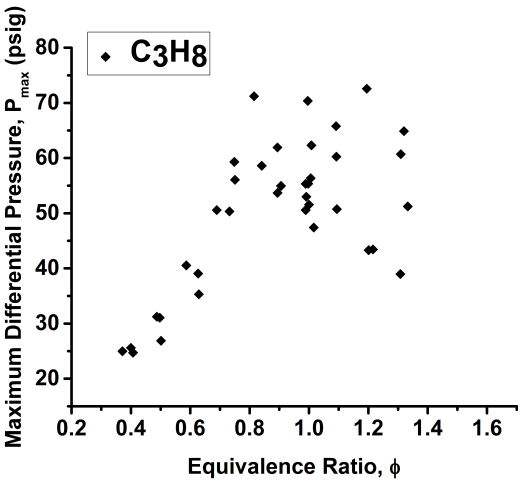

(e) Propane-Air mixtures.

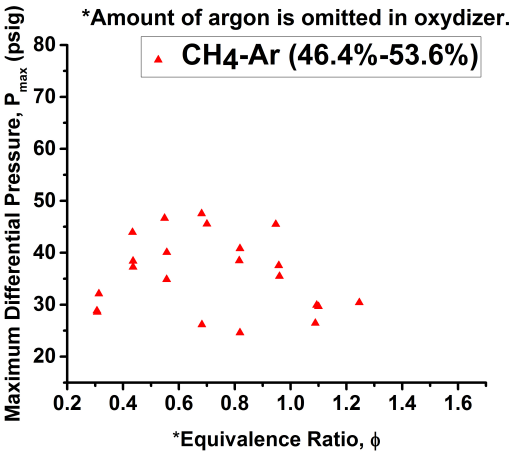

(f) Methane-Argon-Air mixtures.

Figure 4.21. : Effect of equivalence ratio on developed maximum pressure (stationary).

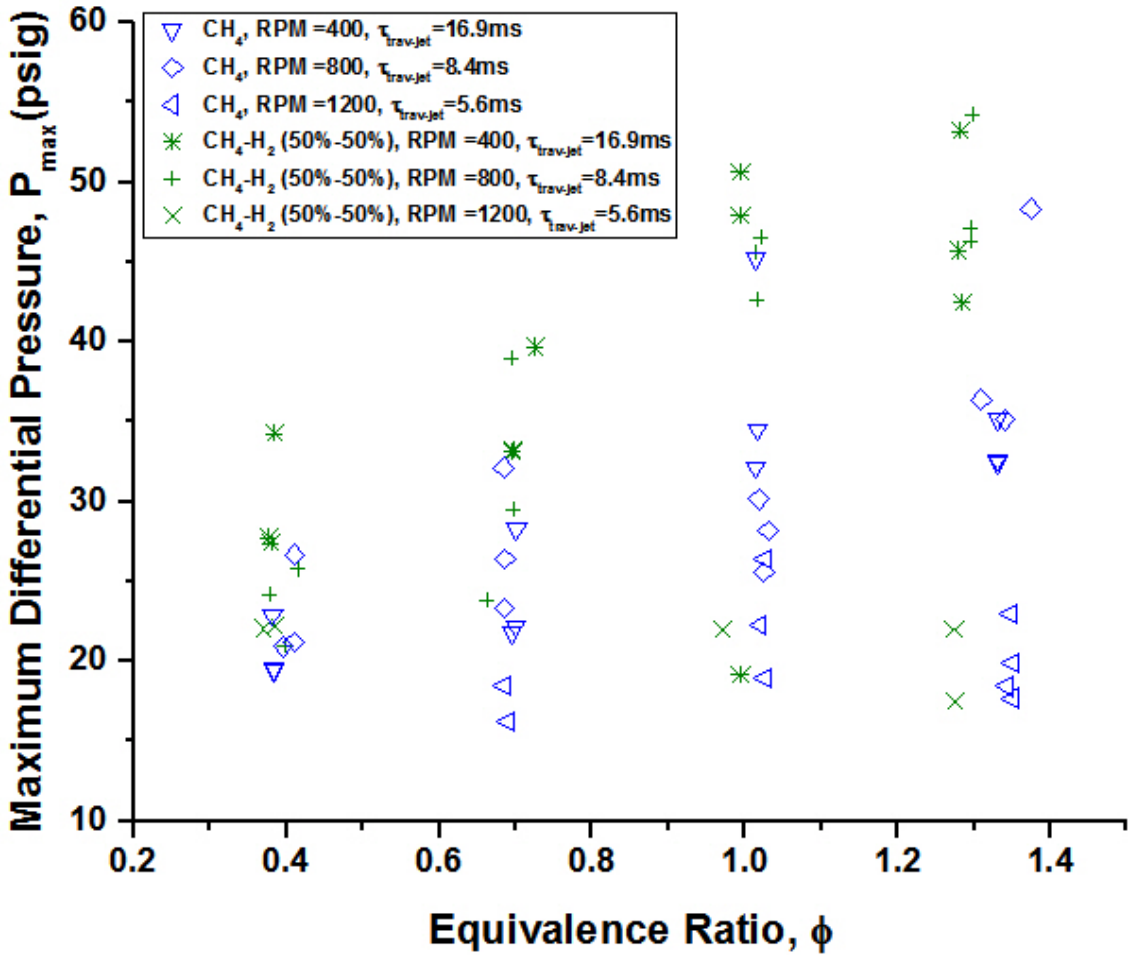

Figure 4.22. : Comparison of maximum differential pressure developed for different fuel-air mixtures during combustion initiated by traversing hot-jet ignition.

5. LAMINAR FLAME PROPAGATION EXPERIMENTS

Experiments in which the main chamber fuel-air mixture is ignited by a spark plug and a laminar flame propagates in the chamber are discussed in this chapter. These experiments were conducted base on the observation of the schlieren images of the fueling and initial mixing process and the assumption that the fuel-air mixture inside the main chamber may not be uniformly distributed which may be responsible for variations in the measured ignition delay. Useful qualitative information about fuel stratification is reported by observing the schlieren images and luminosity images from a Sony high-speed color camera. The chapter also includes comparison of maximum pressure rise developed in the chamber from all three types of experiments.

5.1 Typical Pressure Traces

Pressure traces for six different fuel-air mixtures from spark-ignited laminar flame propagation experiments are given in Fig. 5.1 and schliren images of these tests are depicted in Figs. 5.2 and 5.3. Unlike hot-jet ignition experiments, the pressure traces vary significantly from one fuel to another. In Fig. 5.1(a), for a stoichiometric methane-air mixture, we can see the gradual pressure rise in both near and end-wall PT's. As the flame consumes the unburned fuel-air mixture ahead of the flame front, pressure gradually increases. In Fig. 5.1(d), for a stoichiometric hydrogen-air mixture, the pressure traces follow similar trend as methane-air. Propane-air stoichiometric mixture pressure trace shown in Fig. 5.1(e) exhibit the same trend till weak second increase in pressure is observed in near pressure trace at approximately 72 ms after trigger. This second prominent increase in pressure is observed also for methane-propane-air mixtures Fig. 5.1(e). In schlieren images, the effect of the second rise in pressure is not observed because of the large timescale involved. For such large

timescales, the flame front is no longer seen in the front schlieren window. The second rise could be associated with autoignition of unburned fuel-air mixture ahead of the flame front. Since this unburned fuel-air mixture is compressed by the flame front, its temperature gradually increases. Fig. 5.1(d), also exhibits two large spikes in the pressure traces. From the schlieren images, (Figs. 5.2 and 5.3), the moment of the spike of the near pressure trace is related to the flame front compression by strong pressure waves propagating in the channel. In Fig. 5.1(f), we can see the relatively weak pressure increase during combustion of stoichiometric(amount of argon taken into account) methane-argon-air mixture. The schlieren images, reveal that compared to methane-hydrogen-air and hydrogen-air mixtures, where a smooth laminar flame front propagates, the methane-argon-air mixture has severe longitudinal stratification and its flame front barely propagates beyond the fueling port. Moreover, amount of soot produced during methan-argon-air combustion, observed from schlieren images are much higher compared to propane and methane-propane blend fuel. The pressure traces can be utilized to compare the effects fuel reactivity, mixing time and equivalence ratio on maximum pressure. Although the pressure traces vary significantly from one fuel to another, for the same fuel they tend to have the same general trend even at different mixing times. The variation in mixing time mostly induce changes in maximum pressure attained during combustion.

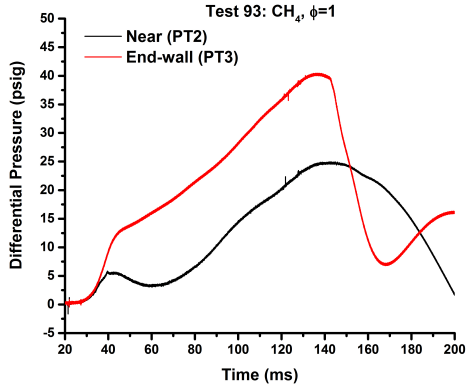

(a) Methane-Air mixtures.

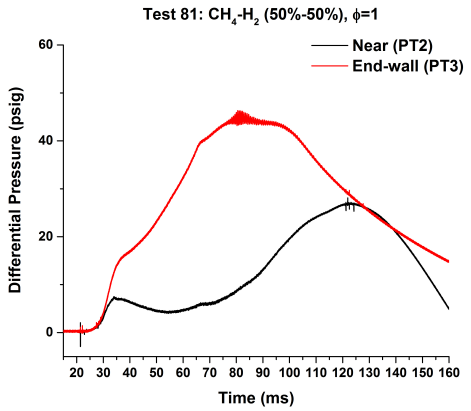

(b) Methane-Hydrogen-Air mixtures.

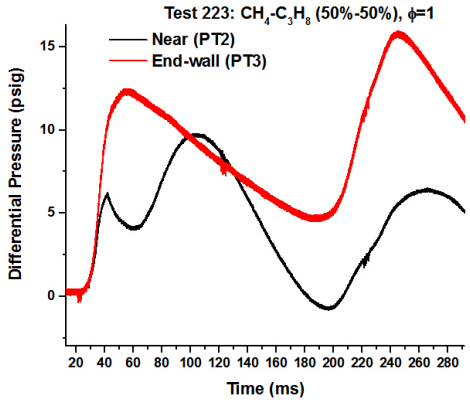

(c) Methane-Propane-Air mixtures.

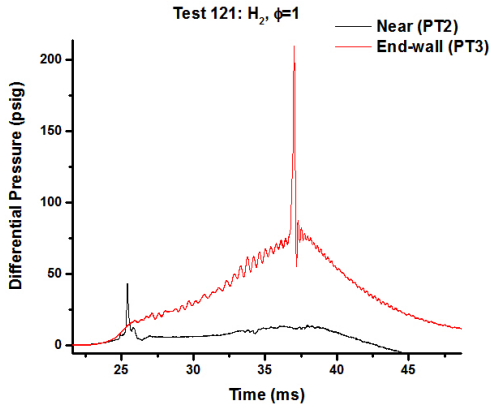

(d) Hydrogen-Air mixtures.

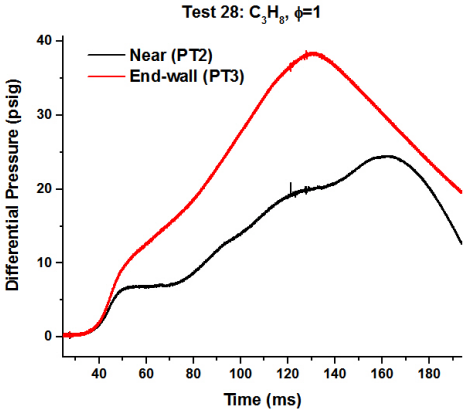

(e) Propane-Air mixtures.

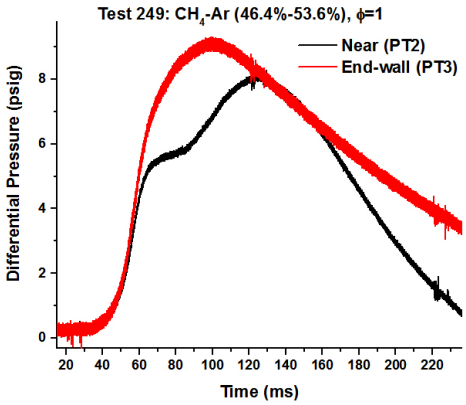

(f) Methane-Argon-Air mixtures.

Figure 5.1. : Pressure traces from various laminar flame propagation experiments. The mixing time for all the tests are 30s except for hydrogen-air case, where the mixing time is 33s.

5.2 Effect of Fuel Reactivity

From Figs. 5.1, 5.2 and 5.3, it is evident that for highly reactive fuels, such as hydrogen, methane-hydrogen blend and propane the maximum pressure developed during combustion is higher compared to the other three fuels. Methane-air mixture exhibited much higher maximum pressure compared to methane-argon blend and air mixture when compared at same equivalence ratio without taking amount of argon into account. This indicates that mixing time is a significant factor for stratification compared to buoyancy effect arising from density or molecular weight difference in fuel-air mixture.

5.3 Fuel Stratification

From the propagating laminar flames, fuel-air mixture stratification is observed visually from color images captured by the Sony high speed camera in Figs. 5.4, 5.5 and 5.6. Methane-air mixture and propane-air mixture stratifies to the chamber top wall and bottom wall respectively where as the methane and argon blend fuel-air mixture demonstrates severe longitudinal stratification and the flame for this case, occupies a very small portion near the top wall from the 5th frame presented in Figs. 5.4, 5.5 and 5.6. For zero or very short mixing time (3-10s), severe longitudinal stratification was observed in schlieren images captured at the rear end of the chamber as depicted in Figs 5.7 and 5.8. Methane-propane blend and methane-argon blend fuel didn't ignite for 0s mixing time and thus 10s mixing time cases at $\phi = 1$ are compared. Propane stratifies to the bottom and burns very brightly generating a lot of soot (Fig. 5.10) . Lighter fuel such as methane, hydrogen and methane-hydrogen blend stratifies to the top of the chamber (Fig. 5.9). Only hydrogen flame shows very negligible region in the main chamber where the flame does not propagate. The methane-argon blend, having the same density as air exhibits the worst behavior in terms of mixture stratification. It take approximately 2s for the flame front to propagate near to the end-wall and it is barely visible in the schlieren images.

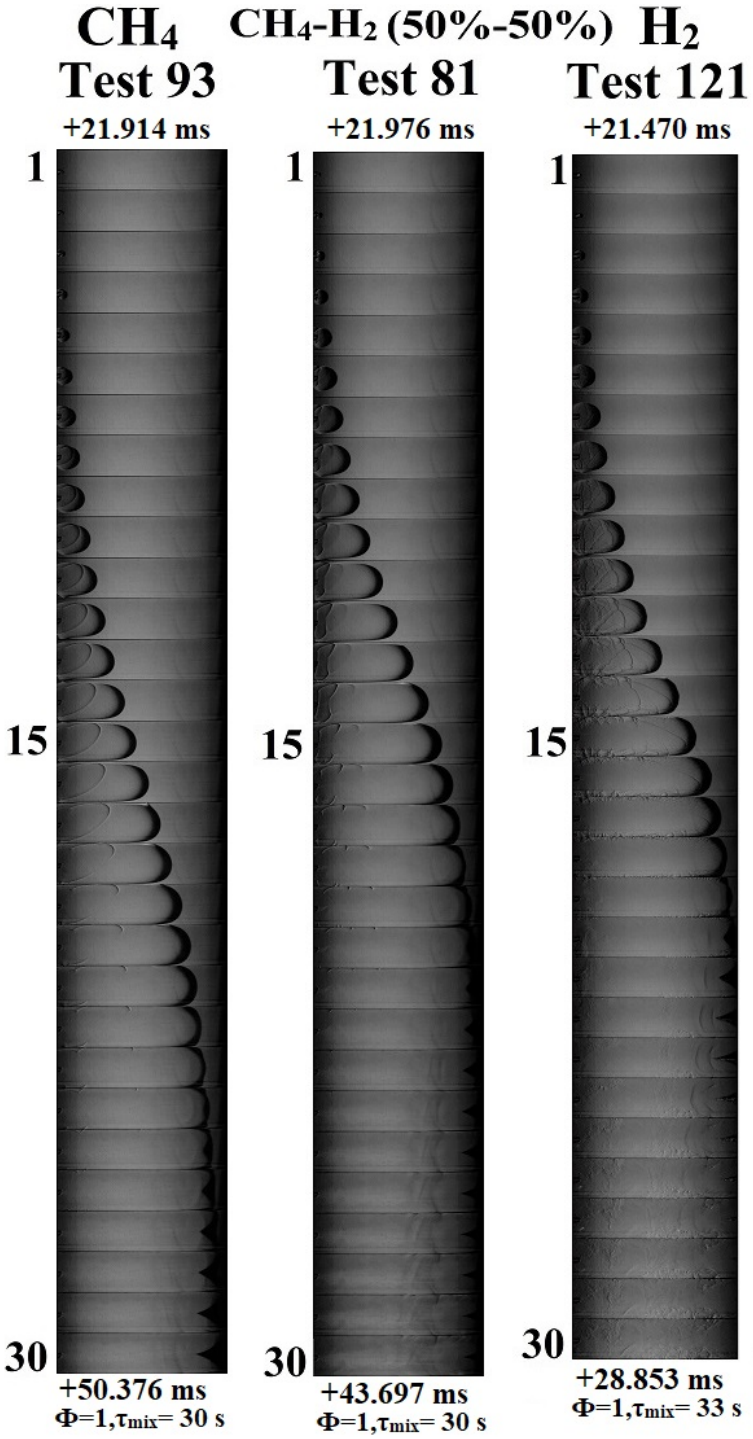

Figure 5.2. : Schlieren images of stoichiometric CH_4, $CH_4 - H_2$ (50%-50%) and H_2 laminar flame propagation experiments in air.

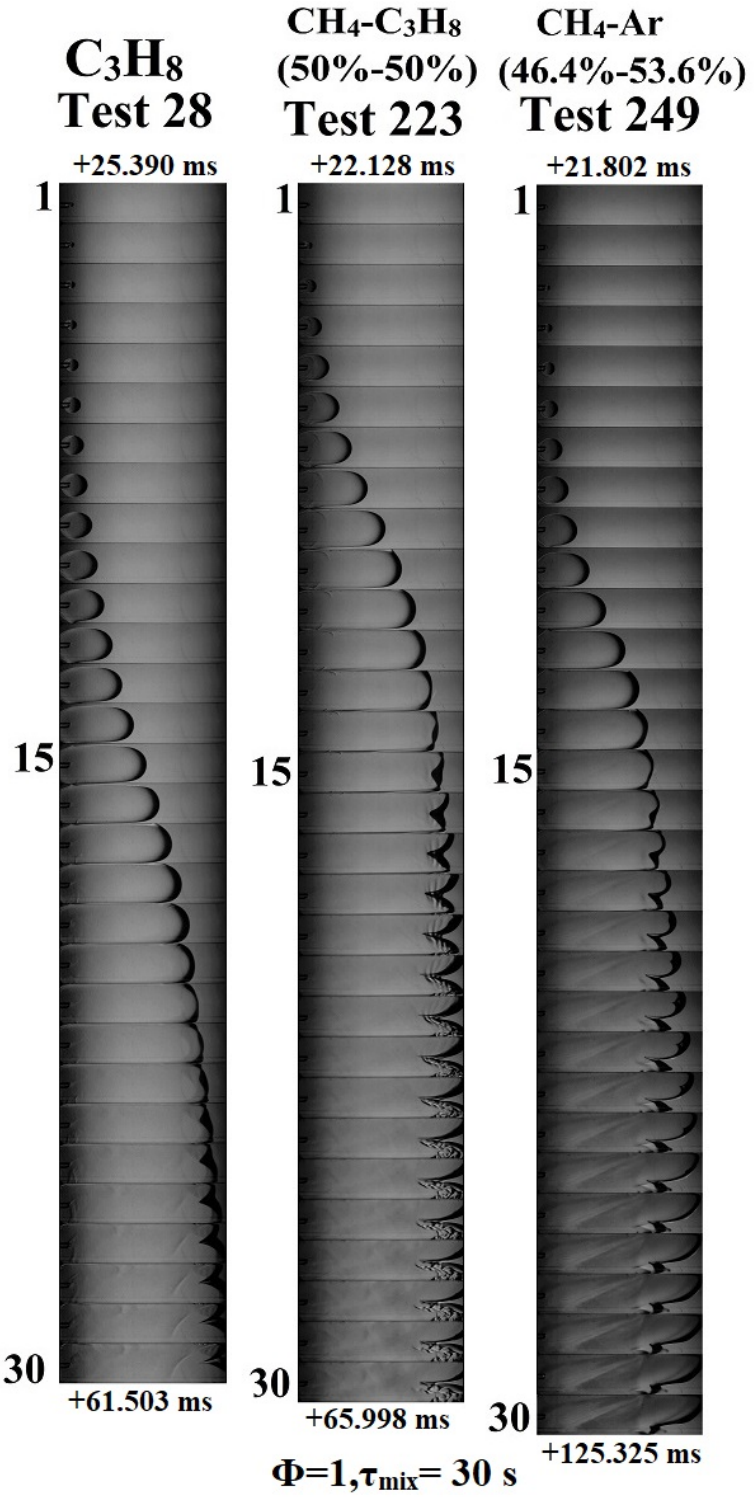

Figure 5.3. : Schlieren images of stoichiometric C_3H_8, $CH_4 - C_3H_8$ (50%-50%) and $CH_4 - Ar$ (46.4%-53.6%) laminar flame propagation experiments in air.

Figure 5.4. : Color images of methane-air mixture laminar flame propagation ($\phi = 0.7$, $\tau_{mix} = 0$). The first frame represents the triggering of the spark plug. The time difference between each frame is 0.332ms.

Figure 5.5. : Color images of propane-air mixtures laminar flame propagation ($\phi = 0.7$, $\tau_{mix} = 0$). The first frame represents the triggering of the spark plug. The time difference between each frame is 0.333 ms.

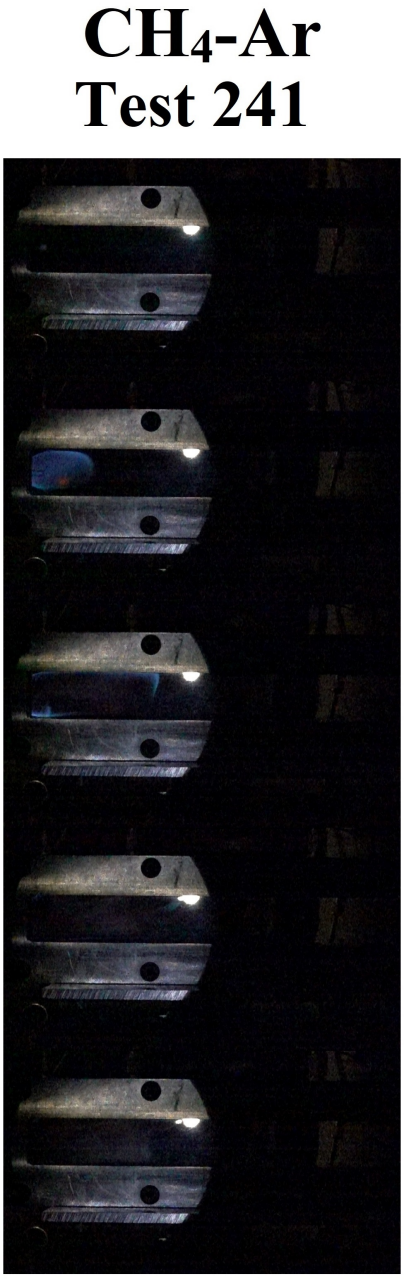

Figure 5.6. : Color images of methane-argon-air mixtures laminar flame propagation ($\phi = 1$, $\tau_{mix} = 30$). The first frame represents the triggering of the spark plug. The time difference between each frame is 0.249 ms.

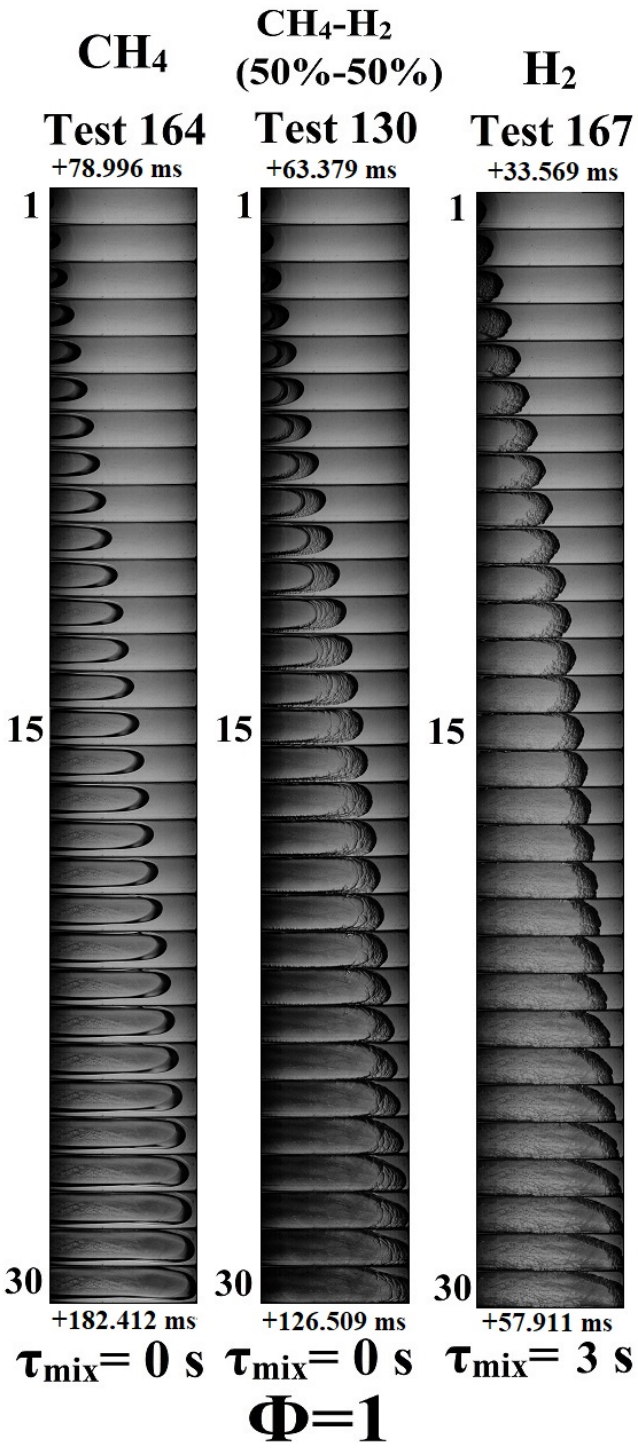

Figure 5.7. : Schlieren images for several stoichiometric mixtures of CH_4, $CH_4 - H_2$ (50%-50%) and H_2 with air showing laminar flames propagating towards rear end of chamber.

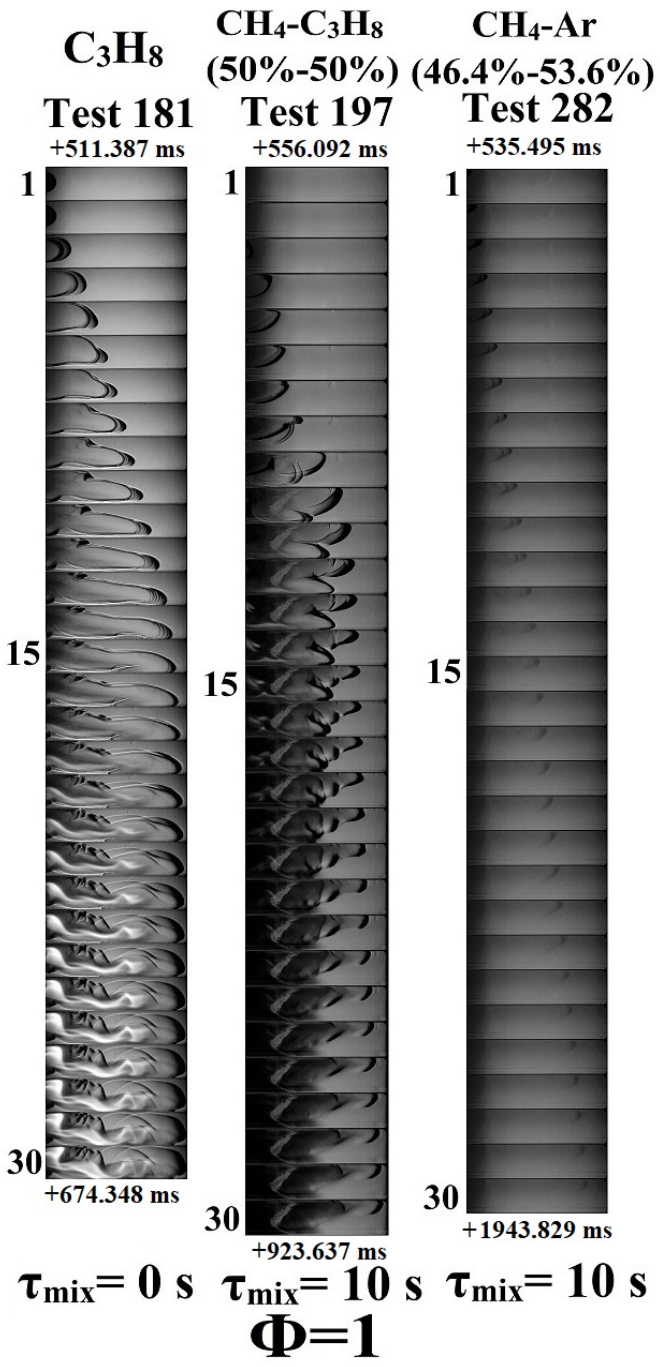

Figure 5.8. : Schlieren images for several stoichiometric mixtures of C_3H_8, $CH_4-C_3H_8$ (50%-50%) and CH_4-Ar (46.4%-53.6%) with air showing laminar flames propagating towards rear end of chamber.

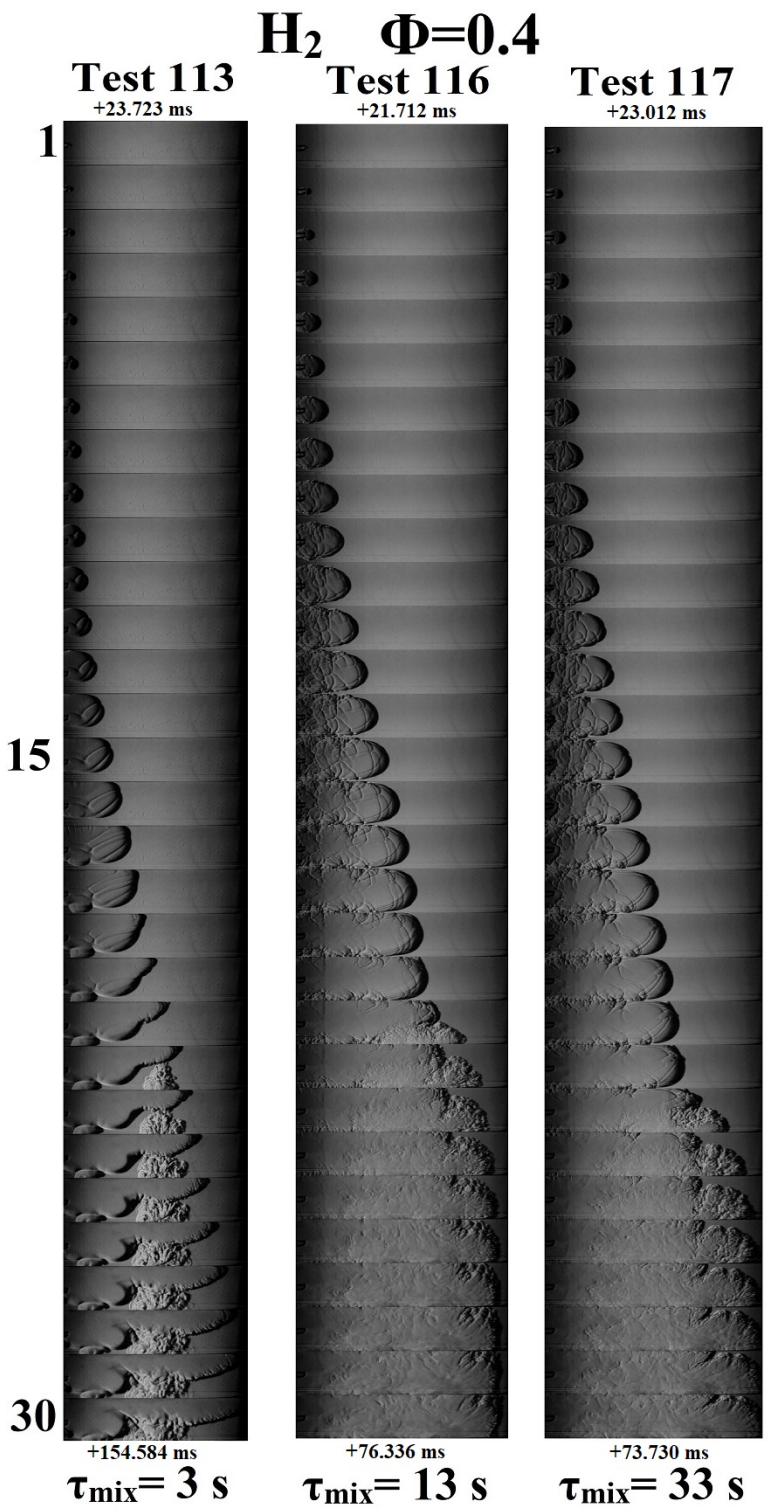

Figure 5.9. : Schlieren images of hydrogen-air mixtures at equivalence ratio of 0.4 from laminar flame propagation experiments at different mixing times.

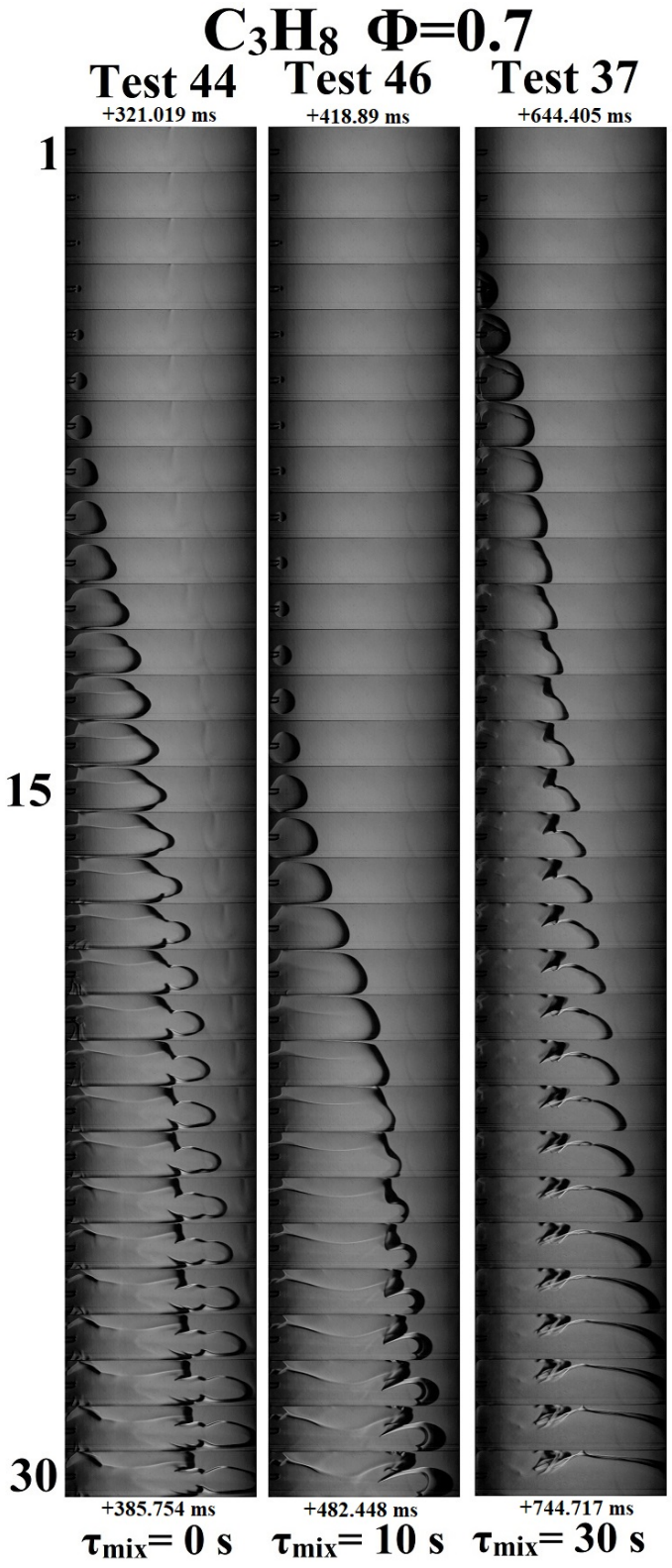

Figure 5.10. : Schlieren images of propane-air mixtures at equivalence ratio of 0.7 from laminar flame propagation experiments at different mixing times.

5.4 Maximum Pressure Inside Combustor

5.4.1 Effect of Equivalence Ratio, Buoyancy and Mixing time

Maximum pressure developed in the chamber varies with both equivalence ratio and mixing time. Fig. 5.11 depicts the variation of developed maximum pressure versus equivalence ratio for all laminar flame ignition experiments. The maximum pressure for each fuel occur at stoichiometric fuel-air ratio with hydrogen having the highest magnitude of the developed maximum pressure. Except for methane-argon blend and methane-propane blend, both of which had molecular weight approximately equal to molecular weight of air, the developed maximum pressure increases with equivalence ratio with highest maximum pressure being at stoichiometric equivalence ratio and then decreases for rich fuel-air mixtures. However, for the two fuel blends (Fig. 5.13(c) and 5.13(f) having approximately the same molecular weight of air, rate of diffusion is relatively lower according to Graham's law of diffusion in gases. Both of these two fuel exhibit a decreasing trend of maximum pressure with increasing equivalence ratio. This increases confidence in the fact that density difference or buoyancy affect the developed maximum pressure much more significantly.

Fig. 5.13 illustrates the effect of mixing time for each fuel on maximum pressure. Due to fuel stratification, some variations exist, however, comparing all fuels at the same equivalence ratio, it is observed that with increase in mixing time, the developed maximum pressure increases for all fuels, particularly for stoichiometric fuel-air mixtures as shown in Fig. 5.12.

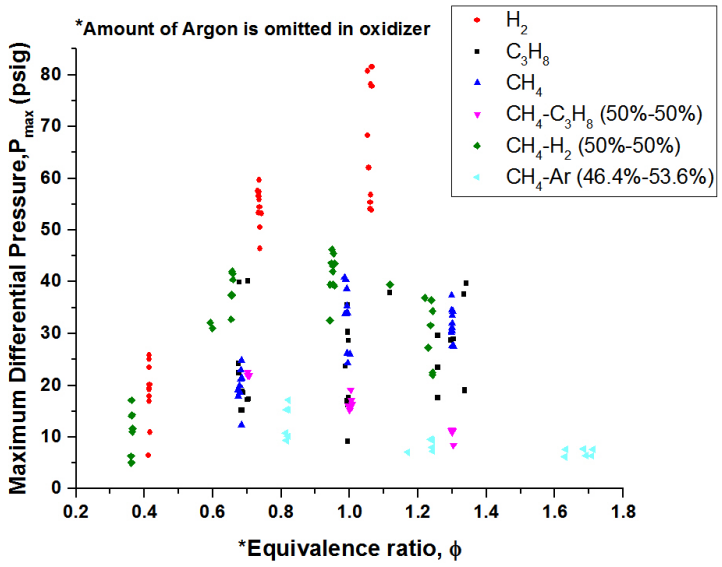

Figure 5.11. : Maximum differential pressure vs. equivalence ratio for from different laminar flame propagation experiment.

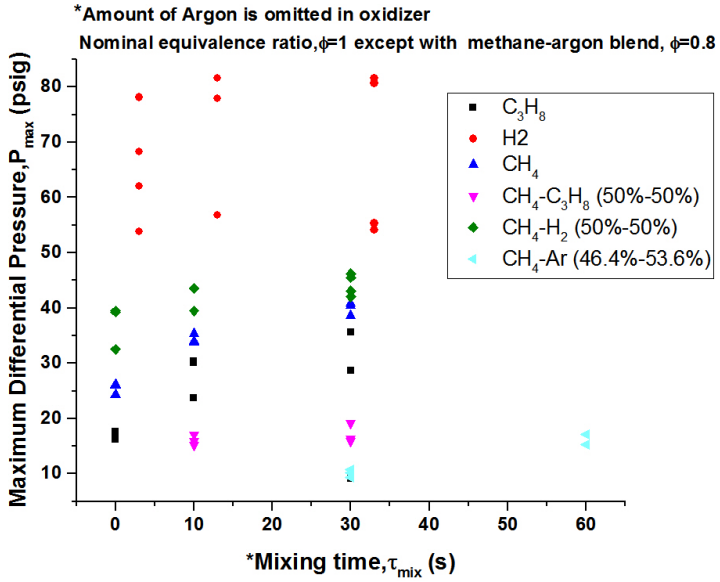

Figure 5.12. : Maximum differential pressure vs. mixing time at nominally stoichiometric fuel-air mixtures from different laminar flame propagation experiment.

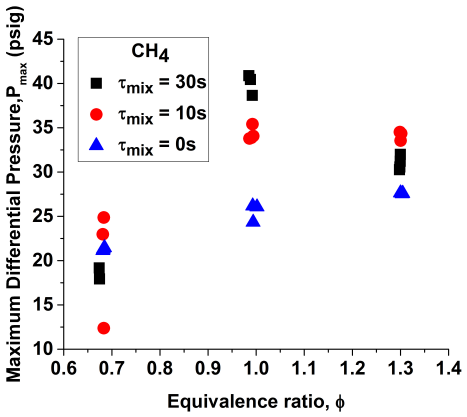

(a) Methane-Air mixtures.

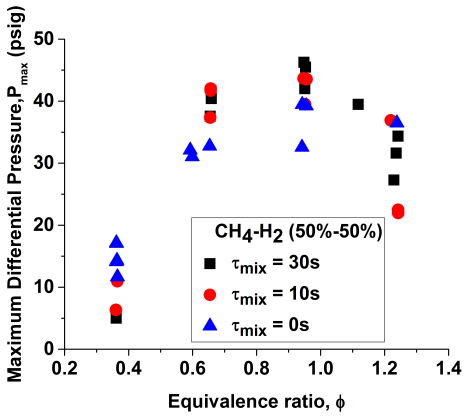

(b) Methane-Hydrogen-Air mixtures.

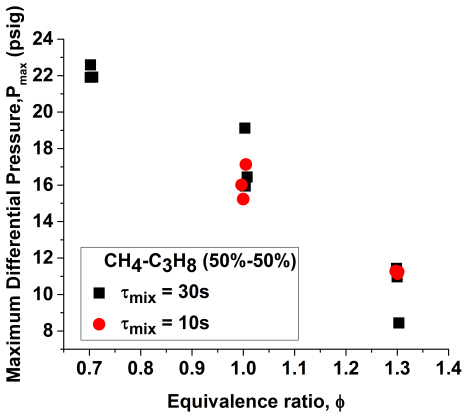

(c) Methane-Propane-Air mixtures.

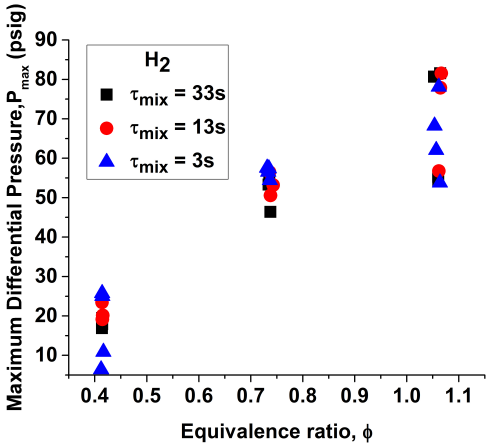

(d) Hydrogen-Air mixtures.

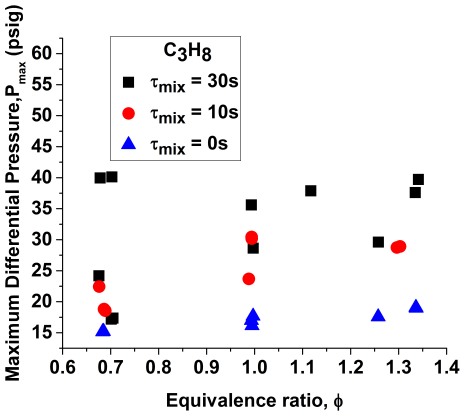

(e) Propane-Air mixtures.

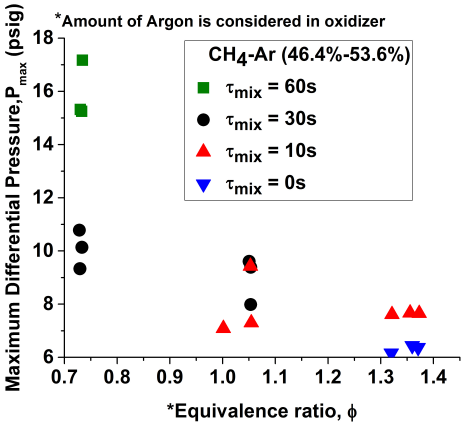

(f) Methane-Argon-Air mixtures.

Figure 5.13. : Effect of mixing time for various spark-ignited fuel-air mixtures on maximum pressure from different laminar flame propagation experiment.

5.4.2 Comparison of Maximum Pressure Rise

In Fig. 5.14, the maximum pressure developed in the chamber by various means of ignition are compared. For fuel-air mixtures containing hydrogen, the maximum pressure developed is always higher irrespective of the ignition process. Due to high leakage rate of fuel-air mixture, the maximum pressure developed with a traversing hot-jet ignition process is typically at the same if not less compared to the other two methods of ignition. Since, 400 RPM or 16.9 ms jet traverse time is the slowest traversing jet, it can be inferred that with faster traversing jets, the maximum pressure developed would be even less. Due to good sealing, stationary hot-jet ignition cases resulted in developing the highest maximum pressure. For methane-air mixtures, both stationary and traversing hot-jet ignition experiments generated higher maximum pressure in the chamber. However, the methane-hydrogen-air mixture, with increased reactivity, develops the highest maximum pressures at all equivalence ratios. Irrespective of the method of ignition, the maximum pressure developed increases from lean to stoichiometric mixtures and the decrease for rich mixtures. The pressure rise variations are due to the following effects:

1. Heat loss and leakage rate of fuel-air mixture are different for each of the different ignition method.

2. Mass addition rate varies in the hot-jet ignition experiments which is zero for the laminar flame propagation experiments.

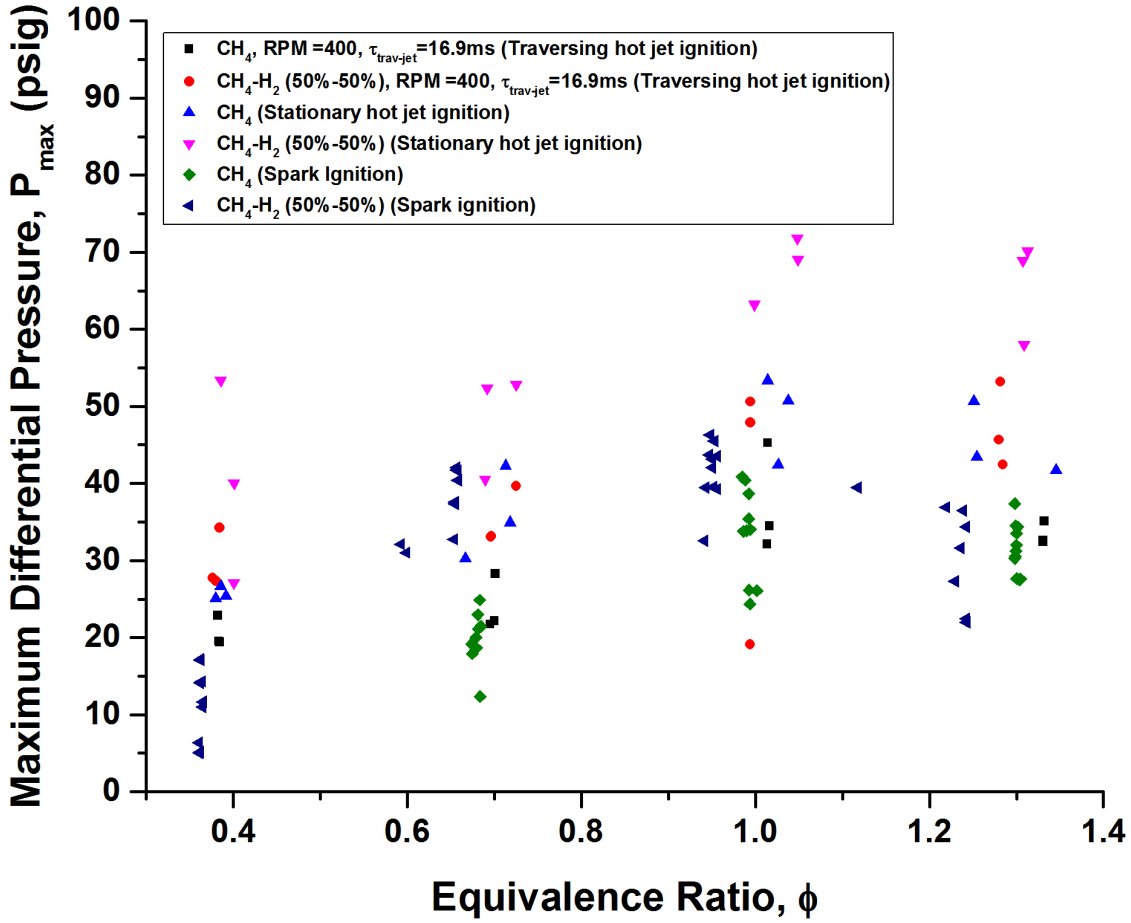

Figure 5.14. : Comparison of pressure rise for methane-air and methane-hydrogen-air mixtures ignited by stationary hot-jet, traversing hot-jet and spark plug (from laminar flame propagation experiments).

6. CONCLUSION

6.1 Conclusion

An experimental study was conducted to investigate the characteristics of transient traversing and stationary hot-jet ignition process and to measure hot-jet ignition delay in a relatively long constant-volume combustion chamber. The turbulent traversing reactive hot-jet was issued from a spark-ignited pre-chamber rotated by a motor. The issued jet traversed one end of the long chamber entrance, generated complex vortices and shock waves in the fuel-air mixture inside the main chamber and ultimately ignited it. The pre-chamber contained a slightly rich 50%-50% methane-hydrogen fuel blend and air mixture for the vast majority of hot-jet ignition experiments. The following parameters were varied. For the traversing hot-jet ignition cases, the equivalence ratios were varied in steps of 0.3 from 0.4 to 1.3. The jet traverse times were varied by rotating the pre-chamber at different speeds of 400 RPM, 800 RPM and 1200 RPM. The corresponding jet traverse times are 16.9 ms, 8.4 ms and 5.6 ms. Three fuels were tested, namely, methane, 50%-50% methane-hydrogen blend and 46.4%-53.6% methane-argon fuel blend. Although methane and methane-hydrogen fuel blend exhibited successful ignition for most of the test points the methane-argon blend exhibited ignition rare and only at equivalence ratio at 1.3. For stationary hot-jet ignition experiments propane, 50%-50% methane-propane blend and 30%-70% methane-hydrogen fuel blend were additionally tested in addition to pure methane and 50%-50% methane and hydrogen. The methane-argon blend demonstrated successful ignition by a stationary hot-jet for equivalence ratios ranging from 0.3-1.3. The equivalence ratio of the other fuel-air mixtures were varied from 0.4 to 1.3.

For a slightly rich fuel-air mixture in the pre-chamber, ignition delay generally decreased with a) increase in fuel reactivity b) decrease in equivalence ratio and c) decrease in jet traverse time, particularly for near stoichiometric fuel-air mixtures.

The addition of hydrogen greatly reduces ignition delay, due to the faster kinetics of hydrogen ignition [1]. Propane also exhibited decreased ignition delay compared to methane due to being more reactive. Due to different mixture stratification, methane-propane blend ignition delay may be longer than both pure methane and pure propane, on average. The addition of argon resulted in generally increased ignition delay compared to pure methane by a stationary hot-jet. For hot-jet ignition with a traversing jet, the 50%-50% methane-hydrogen blend exhibited shorter ignition delay at similar jet traverse times and equivalence ratios.

Hot-jet ignition delay, for both stationary and traversing hot-et cases, increase with increase in equivalence ratio. For stationary hot-jet ignition delay, the minimum ignition delay occurs for most fuel-air mixtures between $\phi = 0.4$ to $\phi = 0.6$. Traversing hot-jet ignition delay also exhibited the increasing trend. Although, fuel molecular weight compared to air, i.e., density difference affected this trend for methane-hydrogen blend fuel which is significantly lighter compared to air.

The traversing hot-jet ignition delay increased with increase in jet traverse time, particularly for stoichiometric and rich fuel-air mixture. Due to mixture stratification and buoyancy effects, the variation in the ignition delay for lean mixtures is not straightforward. This indicates possibility of mixture stratification in the main chamber.

To explain the variations in the measured hot-jet ignition delay and investigate qualitatively the effect of buoyancy on flame propagation and mixture stratification, the fuel-air mixture inside the main combustion chamber was ignited using a spark plug. The spark ignited fuel-air mixture produced a laminar flame propagating within the flammable regions of the channel in ways that sensitively reveal variations in local fuel-air mixture equivalence ratio. Flame luminosity images from a high speed camera and schlieren images revealed the fuel-air mixture, depending on the density

difference between the fuel and air (difference in molecular weight), and mixing time (0 s, 10s ,30s for most fuels) the time interval from end of fuel injection into the chamber and triggering the spark plug, being highly stratified. Propagating laminar flame for lighter fuels such as methane or methane-hydrogen blend, particularly at lean fuel-air equivalence ratios, stratifies to the top of the chamber. For propane or methane-propane blend which are heavier than air, the propagating laminar flame stratifies to the bottom of the chamber. Hydrogen, being the lightest fuel also exhibited stratification to the top of the chamber, but to a lesser extent due to is reactivity and higher binary diffusion coefficient. A blend fuel made of 46.4% methane and 53.6% argon, having the same molecular weight was chosen to minimize the buoyancy effects. The lack of buoyancy-driven spreading caused the fuel to remain in the vicinity of the fuel injector resulting in significant longitudinal stratification of the fuel-air mixture. Increasing the mixing time for the other fuels, improved the buoyancy-driven spreading and extended the flammable region as evidenced by the schlieren and flame luminosity images.

The maximum pressure developed in the combustor for the three ignition processes, namely, stationary hot-jet ignition, traversing hot-jet ignition and spark ignition process in laminar flame propagation experiments were compared. Stationary hot-jet ignition process generally exhibited the highest pressure being developed in the chamber. Variations in heat loss, fuel-air mixture leakage and mass addition mechanisms reduced the maximum pressure for spark ignition and traversing hot-jet ignition process.

6.2 Recommendations for Future Work

1. The present investigation uses an oil-impregnated seal plate to provide rubbing contact between the rotating pre-chamber face and the main chamber. The design was successful because it ensured smooth rotating operation while maintaining contact between the faces. However, due to the absence of an ad-

equate positive seal between the faces, the leakage rate of fuel-air mixture is high. Therefore, this design should be further improved. Spring loaded O-rings, use of alternative rubbing seal materials such as carbon, honeycomb flow-resistance structures, improved surface finish and surface parallel alignment, or other means could be a potential solution. To obtain better understanding of the effectiveness of sealing methods, the leakage rate needs to measured.

2. The variation in rupture moment for the same fuel-air mixture at same equivalence ratio is significant for conducting traversing hot-jet ignition experiments. Because the triggering of the spark inside the pre-chamber depends on the rupture moment. Any variation in the rupture moment offsets the starting position of the jet when it begins the traverse motion. This introduces uncertainty in the jet traverse time. The combustion process inside the pre-chamber cannot be observed visually or with a camera in the current design of the rig. The scoring of the diaphragm is an inherently poorly quantifiable, and is probably the largest source of variation of the rupture moment, which depends on the yielding of diaphragm material along the scoring marks. Although a great deal of attention and practice has been incorporated into the method, it remains somewhat an art rather than a science at this time. The fuel-air mixture in the pre-chamber, if stratified, may cause variations in the flame propagation inside the pre-chamber. Such variations and heat loss through pre-chamber walls may cause variations in the pressure that builds up during the combustion process inside the pre-chamber.

3. The laminar flame propagation experiments provided visual evidence of stratified fuel-air mixture inside the main chamber. Improved fueling strategy is required to ensure more uniform mixing of fuel and air in the main chamber. Fueling with a prepared rich (above upper flammability limit) premixed fuel-air mixture could be a solution to reduce stratification. Moreover, fueling at multiple locations (ports) and/or with angled fuel nozzles in the main chamber could

also improve mixing or reduce longitudinal stratification. A relatively low-cost approach to validation of mixture uniformity is to estimate the laminar flame propagation speed and predict the equivalence ratio of the fuel-air mixture inside the combustion chamber. Suitable image processing algorithm or software can be used to predict the flame front position and the velocity.

4. Schlieren images provide useful qualitative information regarding the combustion process. The ignition moment is also identified from the sharp change in density gradients that can be visually observed in the flow field in the images. However, the present system do not provide any quantitative information about the absolute value of density, about gas composition, or about the velocity of the flow field. Background oriented schlieren (B.O.S.) is an inexpensive novel flow visualization technique that provides quantitative information about the density present in the flow. The system does not need the mirrors, knife edge and lasers or expensive point light source of a conventional schlieren system. Only a strobe light and a high speed camera is required along with a randomly generated dot pattern. The density and refractive index of the fluid is typically correlated in this method.

5. The velocity flow field could be measured using particle-image-velocimetry (PIV) if a technique can be developed for uniformly seeding the flow regions of interest, which is not easy for transient flows. The chemical composition could be inferred by measuring luminescence of activated CH and OH radicals, by the use of filters and photomultipliers to detect weak luminosity in specific wavelengths. All of these methods may be relatively more expensive than those used in the present work.

6. Ignition delay time depends on the jet temperature, which presently has significant uncertainty due to lack of knowledge of the pre-chamber combustion process and heat loss. The jet temperature could be measured by using combustion laser diagnostics. Rayleigh scattering based temperature measurement

is suggested. A lower-cost method may be the use of BOS mentioned above, by calculating temperature from the measured density and existing pressure measurements.

7. Another method of identifying the ignition moment would be to implement measurement of specific chemical species such as CH, OH, C_2 etc. using chemiluminescence camera with spectral filters [7]. This method will also help validate the moment of ignition identified from pressure histories and from the schlieren images recored by the high speed camera.

8. Ion probes could also be used to identify deflagrative combustion and measure axial flame speed. The ion probe measurement could be correlated with pressure measurement to extract useful insights about the combustion process.

9. Inexpensive LED point light source could be used as replacement of the existing light source for the schlieren optical arrangement. LED light sources can achieve maximum power densities with minimal electricity.

REFERENCES

REFERENCES

[1] Zhang, Y., Jiang, X., Wei, L., Zhang, J., Tang, C., and Huang, Z, Experimental and modeling study on auto-ignition characteristics of methane/hydrogen blends under engine relevant pressure, *International Journal of Hydrogen Energy*, 37(24):19168–19176, 2012.

[2] Akbari, P., Nalim, R., and Mueller, N., A review of wave rotor technology and its applications, *Journal of Propulsion and Power*, 128(4):717–735, 2006.

[3] Kentfield, J. and O'Blenes, M., Methods for achieving a combustion-driven pressure-gain in gas turbines, *Journal of Propulsion and Power*, 110(4):704–711, 1988.

[4] Wijeyakulasuriya, S. D., *Transient and translating gas jet modeling for pressure gain combustion applications*, PhD thesis, Purdue University, West Lafayette, 2011.

[5] Weber, H.E., *Shock wave engine design*, John Wiley and Sons, New York, 1995.

[6] Perera, U. L. I. U., *Experimental investigation into combustion torch jet ignition of methane-air, ethylene-air, and propane-air mixtures*, Master's thesis, Indiana University Purdue University Indianapolis, 2010.

[7] Paik, Kyong-Yup, *Experimental investigation of hot-jet ignition of methane-hydrogen mixtures in a constant-volume combustor*, Master's thesis, Indiana University Purdue University Indianapolis, 2016.

[8] Akbari, P. and Nalim, M. R., Review of recent developments in wave rotor combustion technology, *Journal of Propulsion and Power*, 25(4):833–844, 2009.

[9] Costiuc, I. and Chiru, A., Evolution of the pressure wave supercharger concept, *IOP Conf. Series: Material Science and Engineering*, 252, 2017.

[10] Knauff, R., "Converting pressures of liberated gas energy into mechanical work", British Patent 2818, 1906.

[11] Knauff, R., British Patent 8273, 1906.

[12] Burghard, H., British Patent 19421, 1913.

[13] Lebre, A.F., British Patent 290669, 1913.

[14] Burghard, H., German Patent DE485386C, 1928.

[15] Seippel, C., Swiss Patent 225426, 1940.

[16] Seippel, C., Swiss Patent 229280, 1942.

[17] Seippel, C., U.S. Patent 2399394, 1946.

[18] Seippel, C., U.S. Patent 2461186, 1949.

[19] Meyer, A., Recent developments in gas turbines, *Journal of Mechanical Engineering*, 69(4):273–277, 1947.

[20] Azoury, P.H., *Engineering applications of unsteady flow*, John Wiley and Sons, New York, 1992.

[21] Pearson, R.D., A pressure exchange machine for burning Pyroil as the end user in a cheap power from biomass system, 15th International Congress of Combustion Engines, Paris, 1983.

[22] Heywood, J. B., *Internal combustion engine fundamentals*, McGraw-Hill Education, New York, 1988.

[23] Smith, B. D., *Scaling study of wave rotor turbo-normalization of a small internal combustion engine*, Master's thesis, Air Force Institute of Technology, Air University, Air Education and Training Command, Wright-Patterson Air Force Base, Ohio, 2012.

[24] Mathur, A., A brief review of the GE wave engine program, Proceedings of ONR/NAVAIR Wave Rotor Research and Technology Workshop, Report NPS-67-85-008,pp. 171-193, Naval Postgraduate School Monterey, CA, 1985.

[25] Moritz, R., Rolls-Royce study of wave rotors (1965-1970), Proceedings of ONR/NAVAIR Wave Rotor Research and Technology Workshop, Report NPS-67-85-008,pp. 116-124, Naval Postgraduate School Monterey, CA, 1985.

[26] Colman, R.R., Wave engine technology development, Final Report of GPC for AFWAL, Contract No. AFWAL-TR-83-2095, 1984.

[27] Rose, P.H., Potential application of wave machinery to energy and chemical processes, *Proceedings of the 12th International Symposium on Shock Tubes and Waves*, pages 3–30, 1979.

[28] Nalim, M. R., *Wave cycle design for wave rotor engines with limited nitrogen oxide emissions*, PhD thesis, Cornell University, Ithaca, NY, 1994.

[29] Nalim, M.R., Preliminary assessment of combustion modes for internal combustion wave rotors, *ASME J. Eng. Gas Turbines Power*, 121(2):265–271, 1999.

[30] Nalim, M.R. and Paxson, D.E., A numerical investigation of premixed combustion in wave rotors, *ASME J. Eng. Gas Turbines Power*, 119(3):668–675, 1997.

[31] Nalim, M.R., Longitudinally stratified combustion in wave rotors, *J. Propul. Power*, 16(6):1060–1068, 2000.

[32] Zauner, E., Chyou, Y.P., Walraven, F., and Althaus, R., Gas turbine topping stage based on energy exchangers: process and performance, ASME Paper 93-GT-58, 1993.

[33] Bilgin, M., Keller, J., and Breidenthal, R., Ignition and flame propagation process with rotating hot jets in a simulated wave engine test cell, *AIAA paper 98-3399*, 1998.

[34] Snyder, P.H., Wave rotor demonstrator engine assessment, NASA CR-198496, 1996.

[35] Lear, W.E. and Candler, G., Direct boundary value solution of wave rotor flow fields, AIAA Paper 93-0483, 1993.

[36] Okamoto, K., Nagashima, T., and Yamaguchi, K., Introductory investigation of micro wave rotor, ASME Paper IGTC03-FR-302, Japan, 2003.

[37] Nalim, M.R., Snyder, P.H., and Kowalkowski, M., Experimental test, model validation, and viability assessment of a wave-rotor constant-volume-combustor, *Journal of Propulsion and Power*, 33(1):163–175, 2017.

[38] Kojok, A. T., *Hot jet ignition delay characterization of methane and hydrogen at elevated temperatures*, Master's thesis, Indiana University Purdue University Indianapolis, 2017.

[39] Sadanandan, R., Markus, D., Schiel, R., U. Maas, Olofsson, J., Seyfried, H. M. Richter,, and Alden, M., Detailed investigation of ignition by hot gas jets, *Proceedings of the Combustion Institute*, 31(1):719–726, 2007.

[40] Elhsnawi, M. and Teodorczyk, A., Experimental study of hot inert gas jet ignition of hydrogen-oxygen mixture, *First International Conference on Hydrogen Safety, Pisa, Italy*, pages 8–10, 2005.

[41] Iglesias, I., Vera, M., Sanchez, A., and Linan, A., Numerical analyses of deflagration initiation by a hot jet, *Combustion Theory and MOdelling*, 16(6):994–1010, 2012.

[42] Biswas, S. and Qiao, L., Prechamber hot jet ignition of ultra-lean h2/air mixtures: Effect of dupersonic jets and combustion instability, *SAE Int. J. Engines*, 9(3), 2016.

[43] Wrmel, J., Silke, S., Curran, H.J., 'Conaire, M.S., and Simmie J.M., The effect of diluent gases on ignition delay times in the shock tube and in the rapid compression machine, *Combust. Flame.*, 151(1-2):289–302, 2007.

[44] Campbell, C.S. and Egolfopoulos, F.N., Kinetics paths to radical-induced ignition of methane-air mixtures, *Combust. Sci. and Tech.*, 10.1080/00102200500241065:2275–2298, 2005.

[45] Yagi, S, Dath, T., Ukawa, H., and Fujii, I., Research and development of the Honda CVCC engine, In paper C13/75 presented at IMechE Conference, 1976.

[46] Date, T., Yagi, S, Ishizuya, A., and Fujii, O., Research and development of the Honda CVCC engine, Technical Report, SAE Technical Paper, 1974.

[47] Brandstetter, W., The Volkswagen lean burn pre-engine concept, Technical Report, SAE Technical Paper, 1980.

[48] Adams, T.G., Torch ignition for combustion control of lean mixtures, Technical Report, SAE Technical Paper, 1979.

[49] Wyczalek, F.A., Harned, J.L., Maksymiuk, S., and Blevins, J.R., EFI prechamber torch ignition of lean mixtures, Technical Report, SAE Technical Paper, 1975.

[50] Garrett, T. K., Porsche stratified charge engine, *Environmental Science & Technology*, 9(9):826–830, 1975.

[51] Attard, W.P., Toulson, E., Huisjen, A., Chen, X., Zhu, G., and Schock, H., Spark ignition and pre-chamber turbulent jet ignition combustion visualization, Technical Report, SAE Technical Paper, 2012.

[52] Toulson, E., Schock, H., and Attard, W., A review of pre-chamber initiated jet ignition combustion systems, Technical Report, SAE Technical Paper, 2010.

[53] Gauthier, B.M., Davidson, D.F., and Hanson, R.K., Shock tube determination of ignition delay times in full-blend and surrogate fuel mixtures, *Combust. Flame.*, 139(4):300–311, 2004.

[54] Bilgin, M., *Stationary and rotating hot jet ignition and flame propagation in a premixed cell*, PhD thesis, University of Washington, Seattle, Washington, 1998.

[55] Chinnathambi, P., *Experimental investigation on traversing hot jet ignition of lean hydrocarbon-air mixtures in a constant-volume-combustor*, Master's thesis, Indiana University Purdue University Indianapolis, 2014.

[56] Khan, M. N., *Three-dimensional transient numerical study of hot-jet ignition of methane-hydrogen blends in a constant-volume combustor*, Master's thesis, Indiana University Purdue University Indianapolis, 2015.

[57] Baronia, D., *Numerical analysis of hot jet injection and premixed flame proagation in a Channel*, Master's thesis, Indiana University Purdue University Indianapolis, 2006.

[58] Karimi, A., *Numerical study of hot jet ignition of hydrocarbon-air mixtures in a constant-volume combustor*, Master's thesis, Indiana University Purdue University Indianapolis, 2014.

[59] Feyz, M.E., Nalim, M.R., Khan, M.N., Tarraf, A., and Paik, K.Y., Three-dimensional simulation of turbulent hot-jet ignition for air-ch4-h2 deflagration in a confined volume, *Flow Turbulence Combust.*, 101(1), 2018.

[60] Zabetakis, M.G., *Flammability characteristics of combustible gases and vapors: technical report*, Bulletin 627, Bureau of mines, Washington DC, 1965.

[61] Froelich, B., Development of single channel wave-rotor rig combustor rig components, CPRL Internal Project Report, 2010.

[62] Settles, G.S., *Schlieren and shadowgraph techniques: visualizing phenomena in transparent media*, Springer-Verlag, Berlin Heidelberg, 2001.

[63] Ellzey, J.L. and Henneke, M.R., The shock-vortex interaction: The origins of the acoustic wave, *SAE Int. J. Engines*, 21(3):171–184, 1997.